



UNIVERSITA' DEGLI STUDI DI MILANO

SCUOLA DI DOTTORATO
FISICA, ASTROFISICA E FISICA APPLICATA

DIPARTIMENTO
DI FISICA

CORSO DI DOTTORATO DI RICERCA IN
FISICA, ASTROFISICA E FISICA APPLICATA
CICLO XXV

Two-dimensional and novel quasi-two-dimensional quantum liquids

SETTORE SCIENTIFICO DISCIPLINARE FIS/03

Tesi di Dottorato di:
MARCO NAVA

Supervisore: DOTT. DAVIDE EMILIO GALLI
Coordinatore: PROF. MARCO BERSANELLI

A.A. 2012-2013

Acknowledgements

I would like to thank and dedicate this work to friends and foes. To friends for the time shared together, in both bliss and woe. To foes for their opposition that gives me fuel to improve myself. Well, actually I have no foes but rather friends with different views and friends with more different views; anyway, I like the opening effect of the previous sentences. Now, to acknowledgements: as almost everyone does in acknowledgements, I wish to thank my parents for the support that they have been giving till now. I hope to have the opportunity to pay back. Of course, it's not that everyone who writes acknowledgements says "thank you" to *my* parents, but I'm sure a lot of phd students owe much to *theirs*. Particular thanks also to Natasha, my beloved girlfriend, and no, she's not threatening me with dagger and sword to write something cute for her. I'm really happy with her and I wish to thank her for her patience with me when I had to write this never ending document. Indeed, my struggles with blank pages that somehow had to be filled with something brought me to discover new original ways to launch curses and imprecations; in such moments, she has been very kind and brought me cats (I thank them to, for their *furriness*), tea, biscuits and her sweet eyes to calm me down.

A lot of thanks to my collaborators, I would not have made it till now if not for the deep physical insight of Luciano, the everlasting "holiness" of Maurizio (and His nemesis that can't be named), the hyperfine mathematic formalism of Ettore (the section about the mathematics of Markov chains has been possible only thanks to him). Thanks also to Filippo, he has been using the QMC++ library since September and has been very kind to report various minor bugs and also a "thank you" to Mario; no, not because I don't want to exclude him. He's the new entry of the group but we have had chance to do some work together with Jellium and I enjoyed the time spent. But he should learn to be less shy and take freely the tea leaves that I leave in lab for everyone's tea time.

Finally, particular and sincere acknowledgements to Davide, he has been a superb advisor and I hope I'll have the opportunity to work again with him and learn even more. His guidance led me to work on very exciting projects and his wisdom and cunning contributed a lot in the developments of the works presented here. In these years I've come to know him (at least for what regards academic life): his passion for research and his dedication to be a collaborator instead of a competitor should be taken as example. I'm very proud to know people like him. Indeed, I really mean it. I swear that it's not because he's gonna examine me !

Who else to thank? I'm surely forgetting an awful lot of people, but to excuse myself I write here that I offer a beer to anyone shows me that has been forgotten in this section; at only one condition: he has to answer correctly to a question of my choice that concerns this work.

Contents

Acknowledgements	ii
1 Introduction	1
1.0.1 Motivations	1
1.1 Implemented Methodologies	4
1.2 Thesis Outline	6
2 Path Integral Methods	12
2.1 Path Integral Ground State	12
2.1.1 Quantum–Classical Isomorphism	15
2.2 Path Integral at finite temperature	30
3 Polarization energy of two–dimensional ^3He	37
3.0.1 QMC simulation	38
3.0.2 The Bosonic System	42
3.0.3 The Twist Averages	43
3.0.4 Analytic Continuation	47
3.0.5 Results	48
4 Dynamics of two–dimensional ^3He	58
5 Study of ^4He adsorbed on Graphene–Fluoryde and Graphene–Hydrate	72
5.0.6 Adsorption potential	73
5.0.7 The QMC parameters	79
5.0.8 A single Helium atom on the substrates	82
5.0.9 Equilibrium density of submonolayer ^4He on GF	85
5.0.10 Properties at high coverages	95
5.0.11 Equation of state of ^3He on GF and GH	100
5.0.12 Discussion	103
6 Conclusions	108
7 Computational details	111
7.1 Monte Carlo integration: the strategy	111
7.1.1 Mathematics of Markov chains	113
7.1.2 The Metropolis algorithm	119

7.1.3	Sampling and expectation values	121
7.1.4	Metropolis sampling	121
7.1.5	Estimators	130
7.1.6	The Worm algorithm	142
A	Estimators	151
A.0.7	Total Energy	151
A.0.8	Kinetic Energy	152
A.0.9	Pressure	152
A.0.10	T=0 limit	153
A.0.11	Virial Energy Estimator	153
B	Higher order approximations for the density matrix	156
B.0.12	The Pair Product	157
B.0.13	The Multi Product Expansion	157

Chapter 1

Introduction

1.0.1 Motivations

Strongly interacting quantum many-body systems have been one of the main challenges of quantum physics and are still not well understood in many aspects; many novel intriguing phenomena may in fact be originated from the strong interactions among particles in these systems[1]. A strongly interacting system can be described as a system where one can not define a small parameter on which a perturbative theory can be built. This complication inspired the development of numerical approaches based on the variational principle[2] and also quantum simulations[3, 4] that, in the case of bosonic systems, are in principle “exact”. In this work we have considered two systems that can be regarded as the archetype for neutral strongly interacting systems: ^4He , which is a bosonic system, and its fermionic counterpart, ^3He . More specifically, in this work we employed Quantum Monte Carlo (QMC) techniques at zero and at finite temperature, respectively the Path Integral Ground State[3] (PIGS) and the Path Integral Monte Carlo[4] (PIMC), to the study of a system of two dimensional ^3He ($2d\text{-}^3\text{He}$) and to the study of ^4He adsorbed on Graphene-Fluoride (GF, called also Fluorographene) and Graphane (GH), namely two corrugated substrates that can be derived[6] from Graphene. Our main purpose in the case of adsorbed ^4He was the research of new physical phenomena, whereas in the case of $2d\text{-}^3\text{He}$ it was the application of novel methodologies[7] for the study of static properties of Fermi systems and the extension of such methodologies for an *ab-initio* study of the low energy excitations of a strongly interacting fermionic system.

Apart from being both strongly interacting, the systems that we have considered are interesting also from a methodological point of view, as they can be used to test the limits of the employed techniques. In the case of $2d\text{-}^3\text{He}$ the main technical difficulty relies in the well known *sign problem*[5], which, on one side, poses a severe limit on the number of particles that can be simulated by QMC and, on the other side, limits the study of imaginary-time dynamics to small values of imaginary-time. For ^4He on GF and GH the geometry of the confinement gives rise to rare tunneling events that are relevant in both the static and dynamic properties of the system and must thus be correctly described by the used QMC technique. The relevance of these system is also increased by the fact that experiments are feasible on both systems, indeed for

$2d$ - ^3He there is already a number of experimental works in literature and comparison with experiments has been done wherever possible; our study of ^4He on GF and GH instead is novel and up to now there is no experimental data with which we can compare our predictions, however it has been shown in Ref. [6] that the substrates that were considered are available to the experimentalists and we hope that this work will inspire some new experiments on this topic.

In the remnant of this section we give a first introduction of the systems that have been considered.

Two dimensional ^3He

Two dimensional bulk ^3He at zero temperature is a model well suited for the study of strongly correlated Fermi systems. This is because, as shown in Ref. [8], the model is a good approximation for liquid ^3He adsorbed on preplated graphite substrates. Indeed, much experimental work has been done on such systems, we mention heat capacity measurements in Ref. [9, 10] and more recently [11], the study of the thermodynamic behavior of the second layer of ^3He has been done in Ref. [12], the study of magnetic properties of liquid ^3He films[13, 14] and the study of low energy excitations with neutron scattering experiments[15, 16]; another feature of such systems is also the possibility to realize small clusters with a controlled number of particles[17]; this is appealing because those systems can possibly be simulated with “exact” QMC techniques.

Also from the theoretical side, $2d$ ^3He has been the subject of many works, we mention the thermodynamic study of $2d$ Fermi liquid with and without external magnetic field[18, 19], a many-body study of elementary excitations is reported in Ref. [20], a QMC computation of the zero temperature equation state of pure $2d$ ^3He [21] and an estimation of its effective mass[22];

The experimental works in Ref. [8] revealed that quasi-two-dimensional ^3He has a nearly perfect Fermi liquid behavior, in particular, they showed that the effective mass m^* and the spin susceptibility χ/χ_0 increase with the density. This behavior, consistent with a divergence of m^* near the freezing density, has been interpreted[23] as a signal of Mott transition to an insulating crystal. On the other hand, quasi-two-dimensional ^3He has been studied by theoretical means[22] that suggested that the freezing and the divergence of m^* may not have the same physical origin, in particular the freezing density is influenced by the preplated substrate. In this context, the study of the strictly $2d$ ^3He becomes valuable in order to isolate the effect of correlations on the system near freezing density. A further advantage in the theoretical study of this system is that the properties of the liquid phase are largely independent on the choice of the substrate and thus it is possible to make a comparison with experimental data[8]. An even greater interest in $2d$ ^3He has been also inspired by the recent work in Ref. [20, 24] in which, *for the first time*, the collective zero-sound mode has been observed as a well defined excitation crossing and possibly reemerging from the particle-hole continuum.

We have thus performed a Quantum Monte Carlo study of a two-dimensional bulk sample of ^3He using the unbiased Fermionic Correlations (FC) technique that

has been successfully employed in the $2d$ electron gas in Ref. [7]. This technique is a formally exact method that makes use of bosonic imaginary-time correlation functions of operators suitably chosen in order to extract fermionic energies. In this work we computed the energy per particle as function of the polarization of the system at different fluid densities, from this data we obtained a spin susceptibility that is in very good agreement with experiments. As a further study of the system, we have extended the FC method to study dynamical properties; we computed an *ab-initio* low-energy excitation spectrum of $2d$ ^3He obtaining a well defined zero-sound mode in remarkably good agreement with Ref. [24].

^4He on Graphane and Graphene-Fluoride

Experiments on the adsorption of Helium on Graphite have been carried out in the seventies at the University of Washington; those experiments revealed for the first time a behavior corresponding to a two-dimensional gas. Moreover, the appearance of a peak in the specific heat of ^4He near a critical temperature $T_c = 3$ K showed evidence of a phase transition from a high T fluid to a low T commensurate ($\sqrt{3} \times \sqrt{3}$ R30°) phase, an ordered phase in which the ^4He atoms are localized on second-nearest neighbors hexagons. Following this discovery, a number of experimental and theoretical works followed and now the Helium monolayer on Graphite is probably one of the most studied adsorbed quantum systems.

On the experimental side we mention specific heat measurements in Ref. [25, 26], chemical potential measurements in Ref. [27] and neutron scattering experiments in Ref. [28]. The phase diagram of the first layer of ^4He on Graphite has been inspected in Ref. [29, 30, 31]. As for the second layer, we mention the experimental work in Ref. [32]. Superfluid properties of Helium on Graphite were investigated in Ref. [33, 34, 35].

On the theoretical side we mention the work on the interaction potential of He on Graphite by Carlos and Cole[36] and a study on the possible commensurate solid phases of the second layer presented in Ref. [37, 38]. There are also many simulations[39, 40, 41, 42, 43, 44] on strictly $2d$ ^4He . As for Helium on Graphite, the role of corrugation has been studied with Path Integral in Ref. [45] whereas the properties of the adsorbed layers have been studied with Monte Carlo simulations in Ref. [8, 46, 47, 48] and more recently in Ref. [49]. There has also been works on Helium on Graphene, the phase diagram has been calculated in Ref. [50] and superfluid properties in Ref. [51].

The availability of Graphene and especially its derivatives like Graphane and Graphene-Fluoride makes possible the study of new adsorbed systems. No special phenomenon is expected for Helium adsorbed on Graphene because the interaction is geometrically similar to that on graphite, but in the case of GF and GH the adsorption potential is qualitatively different from the case of Graphite and indeed we found a unique behavior of the adsorption system. The difference of GF and GH from Graphite is due to their conformation; GF and GH are respectively Graphene sheets to which are chemically bonded planes of either Fluorine or Hydrogen atoms; in the case of GH, for example, the substrate is made of a Graphene sheet with Hydrogen

atoms attached above and below the C atoms, in an alternating pattern. Such atomic structure provides an Helium–substrate interaction potential which, compared with the Helium–Graphite potential, has twice the number of adsorption minima located on an honeycomb lattice; compared with Graphite, the tunneling between the adsorption sites of GF and GH is also enhanced along three spatial directions that cross saddle points of the potentials. These properties of the GF(GH) adsorption potential, as shown in Sec. 5, not only confine Helium in a multi–connected space but also destabilize the analogue of the $\sqrt{3} \times \sqrt{3}$ R30° on Graphite: we found that the ground state at equilibrium density, for both GF and GH, is indeed a *modulated superfluid* that in GF has anisotropic rotons in the excitation spectrum. Also high coverages of ^4He monolayer on GF and GH show novel properties that have been described in Sec. 5; we found in fact a stable commensurate solid phase that is the analogue of the theoretically predicted 4/7 phase on Graphite, moreover we have preliminary evidence that this solid phase possesses also a relevant superfluid fraction.

1.1 Implemented Methodologies

Quantum Monte Carlo methods are largely employed in the study of strongly interacting quantum systems; the main reason for that is because they can provide expectation values that can be in principle “exact” in the case of Bose systems. In the case of Fermi systems, QMC methods are still an highly accurate tool. The word “exact” here means that the used approximations may be reduced below the statistical error of the QMC method. To make a few examples of successful applications of QMC methods, we mention the quantitative evaluation[52] of the Bose–Einstein condensate fraction in liquid ^4He at zero temperature, the phase diagram of ^4He adsorbed on Graphite[49] and, more recently, the low energy excitation spectrum[53] of ^4He at zero temperature and the computation of the normal–state equation of a Fermi ultra–cold gas at unitary regime[54].

The first QMC method that appeared was a variational technique named Variational Monte Carlo[2] (VMC). This technique expresses a zero temperature expectation value on a given family of variational wave functions as a multi–dimensional integral and then compute the integral with the Metropolis algorithm[55]. Originally it was implemented with Jastrow wave functions[56], but better classes of trial wave functions were introduced; it is worth to mention here the Shadow Wave Functions (SWF) for Bosons[57] and for Fermions[58], that introduce many–bodies correlations in an implicit way and is able to describe a system in both the liquid and the solid phases, without introducing explicitly any equilibrium lattice for the solid state. Beyond the variational level, the first introduced “exact” QMC technique was the Diffusion Monte Carlo[59] (DMC) that solves the Schrödinger equation for the ground state of a many–body system taking advantage of its similarity with the diffusion equation in imaginary time. Another exact technique valid at zero temperature that was developed soon after DMC is the Green’s Function Monte Carlo[60] (GFMC); this method exploits an integral formulation of the Schrödinger equation in order to express ground state quantum averages; on the same line, another very successful

method is the Path Integral Ground State[3] (PIGS) that expresses a ground state expectation value through Feynman’s path integrals as a sufficiently long imaginary–time evolution of a trial wave function; an improvement of DMC that had been introduced in the same years of PIGS is the Reptation Monte Carlo[61] (RMC). Like in the case of VMC, better trial wave functions have been constantly introduced in PIGS; one of the last advancements in zero temperature path integral simulations on Bose systems is the Shadow Path Integral Ground State[62] (SPIGS) which makes use of SWF as trial wave functions. A very strong feature of PIGS and SPIGS is that they are formally similar to the Path Integral Monte Carlo[4] (PIMC) method; PIMC, in fact, uses Feynman’s path integrals in order to compute quantum thermal averages; apart from that, its remarkable formal similarity with PIGS comes also from the similarity between the thermal density matrix and the quantum imaginary–time evolution operator. This feature has a practical value because the two methodologies can be implemented within the same framework.

The mentioned “exact” methodologies, if applied to Fermi systems, suffer from the *sign problem*[5]. This problem occurs because the Fermi symmetry introduces a nodal surface in the ground state wave function (or in the density matrix elements in the case of PIMC) that, as consequence, is no longer a probability density that can be sampled with Monte Carlo; the same problem is also present in Bosonic systems if an excited state instead of the ground state is considered. There are workarounds but they result in a signal to noise ratio that decreases exponentially with the number of particles; exact Fermi simulations, as well as the study of the excitations of Bosonic systems, are thus restricted to system with small number of particles. Among the adaptations that allow the QMC computation on Fermi systems there is the Fixed Node[63] approximation (FN), a variational technique that approximates the true nodal surface of the ground state with that of a trial wave function, and its evolution, the Released Node[64], that has shown to be exact for small systems[64]; we also mention the Restricted Path[65] method that extends PIMC to Fermi systems and a more recent evolution[66] of the DMC method that gives exact results for small systems.

The mentioned techniques work in real coordinates space; another rather new and promising approach to the study of Fermi systems is the formulation of novel QMC techniques; we mention here the Auxiliary Fields Quantum Monte Carlo[67] (AFQMC) and the Bold Diagrammatic Monte Carlo[68] (BDMC).

In this work we have studied Fermi systems with SPIGS; for this purpose we have adopted another recently developed technique named Fermionic Correlations[7] (FC). FC can be defined as a “cross–over” technique because its basic idea is to obtain informations on a Fermi system through the computation of an imaginary–time correlation function on a fictitious Bose system; with this approach, the sign problem is avoided and the simulation is in principle exact. However, to obtain the informations on the Fermi system from the imaginary–time correlation function one has to compute a numerical inversion of the Laplace transform in ill–posed conditions, this is a difficult inverse problem that, again, results in severe limits on the number of particles that can be studied. If the number of particles is small enough, however, the FC technique is an unbiased, *ab–initio* method that gives access to the energy

(and possibly its derivatives) of strong interacting Fermi systems; moreover, the FC technique has been extended in this work to study collective excitations of Fermi systems.

1.2 Thesis Outline

In this work we have made an "unconventional" choice: instead of making a single chapter devoted to the full theoretical introduction of the methodologies, we have introduced the essentials in chapter 2 and the technical details of the methodologies in the chapter *after* the conclusions. With this choice, a reader that is not interested in technical details can safely ignore anything written after the conclusions.

This document is organized as follows.

- The present section provides a background on both the studied physical systems and the employed methodologies.
- In chapter 2 we provide a basic description of the PIGS and PIMC techniques. In this chapter, a methodological work is also presented. We show that, on a realistic model potential for ${}^4\text{He}$, the PIGS method does not suffer from any bias deriving from the choice of the trial wave function.

This work has been published on *J. Chem. Phys.*, **131**, 154108 (2009).

- In chapter 3 is presented the study of $2d$ ${}^3\text{He}$ at zero temperature with the FC technique. The energy of the system for various densities and polarizations is reported as well as the resulting spin susceptibility as function of the density.

The work includes also comparison with experimental data and Fixed Node simulations and has been published on *Phys. Rev. B*, **85**, 184401 (2012).

- In chapter 4 we adapted the FC technique to study the excitations of a Fermi system. The reader can find an *ab-initio* computation of the dynamic structure factor of $2d$ ${}^3\text{He}$ at zero temperature compared with recent experimental data, the static response function and the approximate static structure factor.

These results are in preparation for submission to *Phys. Rev. B*.

- In chapter 5 we present the study of Helium adsorbed on Graphene-Fluoride (GF) and Graphane (GH). The section will present one body properties, such as the ground state energy of one atom of ${}^3\text{He}$ and ${}^4\text{He}$ on GF and GH and the first energy band in the four cases; it will treat then many-body properties of the first layer of ${}^4\text{He}$, such as the stability of various commensurate phases, the equation of state at zero temperature, the condensate fraction in the liquid phases, the zero temperature low energy excitation spectrum at the equilibrium density and superfluid properties at both zero and finite temperature. We also present preliminary data on a possible supersolid phase present at high coverages on both GF and GH.

Many of these results have been published on:

J. Phys.: Conference Series **400**, 012010 (2012) - proceedings of the LT26 conference.

J. Low. Temp. Phys. - proceedings of the QFS2012 conference. DOI: 10.1007/s10909-012-0770-9

Phys. Rev. B. **86**, 174509 (2012).

- In chapter 6 we draw the conclusions of this work.
- in chapter 7 the computational details of the PIGS and PIMC methods are thoroughly described, from the mathematics of the Markov chain to the implementation of the Metropolis algorithm and the derivation of estimators that compute expectation values of various physical quantities.

Bibliography

- [1] P. W. Anderson, *Science* **177** 393(1972).
- [2] W. L. McMillan, *Phys. Rev.* **138** 442(1965).
- [3] A. Sarsa, K. E. Schmidt and W. R. Magro, *J. Chem. Phys.* **113** 1366(2000).
- [4] D. M. Ceperley, *Rev. Mod. Phys.* **67** 279(1995).
- [5] R. P. Feynman and A. R. Hibbs, in *Quantum Mechanics and Path Integrals* Ed. McGraw-Hill, (1965), p. 292-293.
- [6] J. O. Sofo, A. S. Chaudharu and G. D. Barber, *Phys. Rev. B* **75** 153401(2007).
- [7] G. Carleo, S. Moroni, F. Becca and S. Baroni, *Phys. Rev. B* **83** 060411(2011).
- [8] P. A. Whitlock, G. V. Chester and B. Krishnamachari, *Phys. Rev. B* **58** 8704(1998).
- [9] D. S. Greywall, *Phys. Rev. B* **41** 1842(1990).
- [10] Y. Matsumoto, D. Tsuji, S. Murakawa, H. Akisato, H. Kambara and H. Fukuyama, *J. Low Temp. Phys.* **138** 271(2005).
- [11] M. Morishita, *J. Phys.: Conf. Ser.* **150** 032066(2009).
- [12] M. Neumann, J. Nyeki, B. Cowan and J. Saunders, *Science* **317** 1356(2007).
- [13] C. Bäuerle, Yu. M. Bunkov, A. S. Chen, S. N. Fisher and H. Godfrin, *J. Low Temp. Phys.* **110** 333(1998).
- [14] K. D. Morhard, C. Bäuerle, J. Bossy, Yu. Bunkov, S. N. Fischer and H. Godfrin, *Phys. Rev. B* **53** 2658(1996).
- [15] A. Sultan, H. Godfrin, M. Meschke, H. J. Lauter, H. Schober, H. Böhm, R. Holler, E. Krotscheck and M Panholzer, *J. Phys.: Conf. Ser.* **340** 012078(2012).
- [16] H. Godfrin, M. Meschke, H. J. Lauter, A. Sultan, H. M. Böhm, E. Krotscheck and M. Panholzer, *Nature* **483** 576(2012).
- [17] E. Collin, C. Bäuerle, Yu. M. Bunkov and H. Godfrin, *Phys. Rev. B* **73** 125421(2006).

- [18] J. Betouras, D. Efremov and A. Chubukov, *Phys. Rev. B* **72** 115112(2005).
- [19] D. Coffey and K. S. Bedell, *Phys. Rev. Lett.* **71** 1043(1993).
- [20] H. M. Böhm, E. Krotscheck, M. Panholzer, H. Godfrin, H. J. Lauter and M. Meschke, *J. Low Temp. Phys.* **158** 194(2010).
- [21] V. Grau, J. Boronat and J. Casulleras, *Phys. Rev. Lett.* **89** 045301(2002).
- [22] J. Boronat, J. Casulleras, V. Grau, E. Krotscheck and J. Springer, *Phys. Rev. Lett.* **91** 085302(2003).
- [23] C. P. Lusher, B. P. Cowan and J. Saunders, *Phys. Rev. Lett.* **67** 2497(1991).
- [24] H. Godfrin, M. Meschke, H. J. Lauter, A. Sultan, H. M. Bohm, E. Krotscheck and M. Panholzer, *Nat. Phys.* **483** 576(2012).
- [25] M. Bretz, J. G. Dash, D. C. Hickernell, E. O. McLean, *Phys. Rev. A* **8** 1589(1973).
- [26] D. S. Greywall, *Phys. Rev. B* **47** 309 (1993).
- [27] M. Bretz, J. G. Dash, D. C. Hickernell, E. O. McLean, *Phys. Rev. A* **8** 1589(1973).
- [28] H. J. Lauter, H. Godfrin, in *Phase transition in Surface Films 2* (Plenum, New York, 1991).
- [29] M. Schick, in *Phase transitions in surface films* (Plenum, New York, 1973).
- [30] D. S. Greywall, *Phys. Rev. B* **47** 309(1993).
- [31] D. S. Greywall and P. A. Busch, *Phys. Rev. Lett.* **67** 3535(1991).
- [32] M. Bertz, in *Monolayer and Submonolayer Helium Films* (Plenum, New York, 1973).
- [33] G. Zimmerli, G. Mistura and M. H. W. Chan, *Phys. Rev. Lett.* **68** 60(1992).
- [34] P. A. Crowell and J. D. Reppy, *Phys. Rev. Lett.* **70** 21(1993).
- [35] P. A. Crowell and J. D. Reppy, *Phys. Rev. B* **53** 5(1996).
- [36] W. E. Carlos and M. W. Cole, *Surface Science* **91** 339(1980).
- [37] M. Pierce and E. Manousakis, *Phys. Rev. B* **59** 3802(1999).
- [38] G. V. Chester, M. E. Fisher and N. D. Mermin, *Phys. Rev.* **185** 760(1969).
- [39] D. M. Ceperley and E. L. Pollock, *Phys. Rev. B* **39** 2084(1989).
- [40] S. Giorgini, J. Boronat and J. Casulleras, *Phys. Rev. B* **54** 6099(1996).
- [41] M. C. Gordillo and D. M. Ceperley, *Phys. Rev. B* **58** 6447(1998).

- [42] B. Krishnamachari and G. V. Chester, *Phys. Rev. B* **61** 9677(2000).
- [43] P. A. Whitlock, G. V. Chester and M. H. Kalos, *Phys. Rev. B* **38** 2418(1988).
- [44] M. Rossi, E. Vitali, D. E. Galli and L. Reatto, *J. Phys.:Condens. Matter* **22** 145401(2010).
- [45] M. E. Pierce and E. Manousakis, *Phys. Rev. B* **62** 5228(2000).
- [46] P. A. Whitlock, G. V. Chester and B. Krishnamachari, *Comput. Phys. Comm.* **121-122** 460(1999).
- [47] M. E. Pierce and E. Manousakis, *Phys. Rev. Lett.* **83** 5314(1999).
- [48] M. E. Pierce and E. Manousakis, *Phys. Rev. B* **63** 144524(2001).
- [49] P. Corboz, M. Boninsegni, L. Pollet and M. Troyer *Phys. Rev. B* **78** 245414(2008).
- [50] M. C. Gordillo and J. Boronat, *Phys. Rev. Lett.* **102** 085303(2009).
- [51] M. C. Gordillo, C. Cazorla and J. Boronat, *Phys. Rev. B* **83** 121406(2011).
- [52] S. Moroni and M. Boninsegni, *J. Low Temp. Phys.* **136** 129(2004).
- [53] E. Vitali, M. Rossi, D. E. Galli and L. Reatto, *Phys. Rev. B* **82** 174510(2010).
- [54] K. Van Houcke, F. Werner, E. Kozik, N. Prokof'ev, B. Svistunov, M. J. H. Ku, A. T. Sommer, L. W. Cheuk, A. Schirotzek and M. W. Zwierlein, *Nat. Phys.* **8** 366(2012).
- [55] N. Metropolis, A. W. Rosenbluth, M. N. Rosenbluth, A. H. Teller and E. Teller, *J. Chem. Phys.* **21** 1087(1953).
- [56] R. Jastrow, *Phys. Rev.* **98** 1479(1955).
- [57] T. MacFarland, S. A. Vitiello, L. Reatto, G. V. Chester and M. H. Kalos, *Phys. Rev. B* **50** 13577(1994).
- [58] F. Pederiva, S. A. Vitiello, K. Gernoth, S. Fantoni and L. Reatto, *Phys. Rev. B* **53** 15129(1996).
- [59] J. B. Anderson, *J. Chem. Phys.* **63** 1499(1975).
- [60] M. H. Kalos, *Phys. Rev.* **128** 1791(1962).
- [61] S. Baroni and S. Moroni, *Phys. Rev. Lett.* **82** 4745(1999).
- [62] D. E. Galli and L. Reatto, *J. Low Temp. Phys.* **136** 343(2004).
- [63] Y. Kwon, D. M. Ceperley and R. M. Martin, *Phys. Rev. B* **48** 12037(1993).
- [64] D. M. Ceperley and B. J. Alder, *J. Chem. Phys.* **81** 5833(1984).

- [65] D. M. Ceperley, in *Monte Carlo and Molecular Dynamics of Condensed Matter Systems*, Ed. K. Binder and G. Ciccotti (Bologna,Italy,1996).
- [66] M. H. Kalos and F. Pederiva, *Phys. Rev. Lett.* **85** 3547(2000).
- [67] S. Zhang and H. Krakauer, *Phys. Rev. Lett.* **90** 136401(2003).
- [68] N. Prokof'ev and B. Svistunov, *Phys. Rev. Lett.* **99** 250201(2007).

Chapter 2

Path Integral Methods

In this Chapter the general basis of two Monte Carlo techniques will be described; the technical details will instead be discussed in Chapter 7. The method used for zero temperature simulations is the Path Integral Ground State[1] (PIGS) whereas, that used for finite temperature simulations is the Path Integral Monte Carlo[2] (PIMC). The PIGS and the PIMC techniques are “exact” methods if the studied system has the Bose symmetry; the word “exact” in the context of Quantum Monte Carlo (QMC) means that the systematic errors due to the used approximations can be arbitrarily reduced below the Monte Carlo statistical uncertainty. The two techniques have also a similar formalism. For this reason, they are easily implementable in a unified computer library.

2.1 Path Integral Ground State

In Sec. 7 we show that, using Monte Carlo techniques, it is indeed possible to sample an arbitrary probability distribution and that with the resulting sampling it is possible to evaluate N -dimensional integrals. We now specialize that methodology to the problem of calculating the expectation values of a bosonic N -particle system.

Let's thus consider a system of N atoms of mass m at a temperature $T = 0$ K, in a box of volume V_b in periodic boundaries conditions, with an interatomic potential $V(r)$, the Hamiltonian operator is

$$\hat{H} = \hat{T} + \hat{V} \tag{2.1}$$

where the kinetic term is

$$\hat{T} = -\frac{\hbar^2}{2m} \sum_{i=1}^N \nabla_i^2 \tag{2.2}$$

and the potential term is

$$\hat{V} = \sum_{i < j} v(|\vec{r}_i - \vec{r}_j|) \tag{2.3}$$

this Hamiltonian is used for ease of writing, but a more general Hamiltonian with anisotropic interactions and external potential can be used as well. Defined $\Psi(R)$ as the ground state wave function, we want to compute the quantity

$$\langle \hat{O} \rangle = \int dR O(R) \Psi^2(R) \quad (2.4)$$

where $R = \{\vec{r}_i\}_{i=1}^N$ is a many-body variable and \vec{r}_i is the position of the i -th particle of the system and \hat{O} is an operator that is diagonal in the coordinate representation. The square of the wave function, $\Psi^2(R)$, real and nodeless because we are considering a bosonic system, is proportional to the probability distribution to be sampled with the Metropolis algorithm (see Chapter 7). The quantity $\Psi^2(R)$ is in general unknown but a workaround that has been very successful among $T=0$ K methods is to exploit the quantum evolution in imaginary time.

Given an initial state $|\Psi(0)\rangle$, the quantum time-evolution is determined by the Schrödinger's equation and

$$|\Psi(t)\rangle = e^{-\frac{i}{\hbar}t\hat{H}} |\Psi(0)\rangle \quad (2.5)$$

where the time evolution operator $\hat{U}(t) = e^{-\frac{i}{\hbar}t\hat{H}}$. If $|\Phi_i\rangle$ is an eigenvector of \hat{H} , its overlap with the state $|\Psi(\tau)\rangle$ can be expressed as

$$\langle \Phi_i | \Psi(\tau) \rangle = \sum_j \langle \Phi_i | e^{-\tau\hat{H}} | \Phi_j \rangle \langle \Phi_j | \Psi(0) \rangle \quad (2.6)$$

where we have defined the quantum imaginary-time evolution operator $\hat{U}(\tau) = e^{-\tau\hat{H}}$ by substituting $\tau = \frac{i}{\hbar}t$. Eq. (2.6) can be rewritten as $\langle \Phi_i | \Psi(\tau) \rangle = e^{-\tau E_i} \langle \Phi_i | \Psi(0) \rangle$. For a sufficiently long τ , if the initial state $\Psi(0)$ is not orthogonal to the ground state, only the eigenstate corresponding to the lowest eigenvalue has a relevant overlap on the evolved trial wave function $|\Psi(\tau)\rangle$. The ground state wave function Ψ_0 in coordinate representation can be thus expressed as the $\tau \rightarrow \infty$ limit of an imaginary time evolution of an arbitrary trial wave function Ψ_T provided that $\langle \Psi_0 | \Psi_T \rangle \neq 0$

$$\Psi_0 = \lim_{\tau \rightarrow \infty} \frac{e^{-\tau(\hat{H}-E_0)} \Psi_T}{\langle \Psi_0 | \Psi_T \rangle} \quad (2.7)$$

The normalization factor is not involved in the Monte Carlo sampling; within the Green's function formalism, the ground state wave function can be approximated with $\tilde{\Psi}_\tau(R)$,

$$\tilde{\Psi}_\tau(R) = \frac{1}{\mathcal{N}} \int dR' G(R, R', \tau) \Psi_T(R) \quad (2.8)$$

where \mathcal{N} is the normalization constant and the term $G(R, R', \tau) = \langle R | e^{-\tau\hat{H}} | R' \rangle$ is the Green's function or density matrix. Here, the expectation value has just merely

been rewritten in term of the Green's function, but the Green's function for a sufficiently large τ is still a generally unknown quantity. There are, however, known analytic approximations of the Green's function that are valid for small imaginary time $\delta\tau$ and the Path Integral formalism provides a way to express a large τ Green's function as a convolution of smaller imaginary-time Green's functions. This comes from an important property of the density matrix,

$$e^{-\tau\hat{H}} = \left(e^{-\delta\tau\hat{H}} \right)^M \quad (2.9)$$

where $\delta\tau = \frac{\tau}{M}$. In the coordinate representation, the product becomes a convolution

$$G(R_1, R_{M+1}, \tau) = \int \dots \int dR_2 \dots dR_M \prod_{j=1}^{M-1} G(R_j, R_{j+1}, \delta\tau) \quad . \quad (2.10)$$

A density matrix at imaginary time τ can be represented as a convolution of M density matrices at smaller imaginary time τ/M . This convolution is the Path Integral and, as the name *Path Integral Ground State* may suggest, it is a fundamental element for the quantum simulation techniques that have been used throughout this work.

Combining Eq. (2.4) with (2.7) and (2.8), a quantum average on the ground state thus becomes

$$\begin{aligned} \langle \hat{O} \rangle &= \frac{1}{\mathcal{N}} \int \left(\prod_{i=1}^M dR_i \right) \Psi_T(R_1) O(R_{M/2}) \times \\ &\quad \times \prod_{j=1}^{M-1} G(R_j, R_{j+1}, \delta\tau) \Psi_T(R_M) \quad . \end{aligned} \quad (2.11)$$

In the case that $\tau/2$ is sufficiently large to have a good approximation of Eq. (2.7), if the operator \hat{O} commutes with $e^{-\tau\hat{H}}$, then it can be applied at any position k of the path integral and it will give the ground state expectation value, if otherwise, $[\hat{O}, \hat{H}] \neq 0$, then the operator applied at positions $k = 1$ and $k = M$ will give mixed expectation values $\langle \Psi_T | \hat{O} | \Psi_0 \rangle$ and for $k = 2 \dots M/2$ the expectation values $\langle \Psi_T | e^{-(k-1)\delta\tau\hat{H}} | \hat{O} | \Psi(0) \rangle$ will converge to the ground state value. To go further and obtain an explicit definition of the quantum expectation value, an analytic approximation of the small imaginary-time Green's function must be used. The simplest one is the Primitive Approximation (PA); more advanced approximations are illustrated in Appendix. B. The PA consists in neglecting the commutator between \hat{T} and \hat{V} when factorizing the density matrix $e^{-\delta\tau\hat{H}}$, the error associated with this approximation is of the order $\delta\tau^2$.

$$e^{-\delta\tau\hat{H}} \simeq e^{-\delta\tau\hat{T}} e^{-\delta\tau\hat{V}} \quad . \quad (2.12)$$

In this approximation the matrix elements of the two factors are easy to obtain,

$$\langle R_i | e^{-\delta\tau\hat{T}} | R_{i+1} \rangle = \frac{1}{(4\pi\lambda\delta\tau)^{\frac{dN}{2}}} e^{\left[-\frac{|R_i - R_{i+1}|^2}{4\lambda\delta\tau}\right]} \quad (2.13)$$

$$\langle R_i | e^{-\delta\tau\hat{V}} | R_{i+1} \rangle = e^{-\delta\tau V(R_i)} \delta(R_i, R_{i+1}) \quad (2.14)$$

where we have defined $\lambda = \frac{\hbar^2}{2m}$, $|R_i - R_{i+1}|^2 = \sum_{j=1}^N |\vec{r}_j^i - \vec{r}_j^{i+1}|^2$ and $V(R_m) = \sum_{i < j}^N v(r_{ij}^m)$. We use the shorthand notation $r_{ij}^m = |\vec{r}_i^m - \vec{r}_j^m|$.

The ground state expectation value of an operator \hat{O} that is diagonal in the coordinate representation becomes

$$\langle \hat{O} \rangle \simeq \frac{1}{\mathcal{N}} \int \prod_{i=1}^{M-1} dR_i \Psi_T(R_1) e^{-\frac{\delta\tau}{2}V(R_i)} e^{-\frac{(R_i - R_{i+1})^2}{4\lambda\delta\tau}} e^{-\frac{\tau}{2}V(R_{i+1})} O(R_{M/2}) \Psi_T(R_M) \quad (2.15)$$

where the primitive approximation has been written in a symmetric form, namely

$$G_{PA}(R_i, R_{i+1}, \delta\tau) = e^{-\frac{\delta\tau}{2}V(R_i)} e^{-\frac{(R_i - R_{i+1})^2}{4\lambda\delta\tau}} e^{-\frac{\delta\tau}{2}V(R_{i+1})} \quad . \quad (2.16)$$

In the limit $M \rightarrow \infty$, Eq. (2.15) becomes exact due to the Trotter formula :

$$e^{-\tau\hat{H}} = \lim_{M \rightarrow \infty} \left[e^{(-\delta\tau\hat{T})} e^{(-\delta\tau\hat{V})} \right]^M \quad . \quad (2.17)$$

Chosen a sufficiently high M , then, the error in Eq. (2.15) can be arbitrarily reduced, and, chosen a sufficiently high τ , an arbitrary precise description of the ground state can be obtained. The integral can be evaluated with Monte Carlo and the multi-dimensional probability distribution to sample with the Metropolis algorithm is

$$p(\{R_n\}) = \Psi_T(R_1) \prod_{j=1}^{M-1} G(R_j, R_{j+1}, \delta\tau) G(R_M, R, \delta\tau) \Psi_T(R_M) \quad . \quad (2.18)$$

The value of τ that is sufficiently high to have convergence depends by a good degree on the choice of the trial wave function Ψ_T . A trial wave function that has an high overlap on the ground state could, in fact, enhance the convergence of Eq. (2.7). We emphasize that this, however, is not necessary to obtain unbiased results: a very strong feature of PIGS, as we have shown in Ref. [3], is that, indeed, the results of a PIGS calculation do not depend on the choice of the trial wave function. This is what we are going to show in Sec. 2.1.1, the practical implementation of the Metropolis algorithm will be instead described in Sec. 7.1.4.

2.1.1 Quantum–Classical Isomorphism

Although path integrals and quantum evolution in imaginary time are very abstract topics, there is a simple interpretation of the probability distribution (2.18) that allows

for an easy visualization of the Metropolis sampling; besides the practical advantages, it is also an interesting example in which many aspects of both the mathematics of Markov chains and the physics of the system take life in a fictitious classical system made of beads that have very special interactions between each other; this is why this correspondence is called *quantum-classical isomorphism*. More specifically, Eq. (2.18) is the partition function of a *classical* system of N *polymers* composed by M *beads* that have special interactions. The kinetic term of the Hamiltonian represents the interaction between adjacent beads of the same polymer whereas the potential term of the Hamiltonian maps onto the interactions between beads of different polymers. A polymer is essentially a set of beads corresponding to some integration variables in Eq. (2.18), namely the i -th polymer is $\{\vec{r}_i^j\}_{j=1}^M$. The length of the polymer is τ ; due to the analogy with the quantum evolution operator $e^{-i\tau\hat{H}}$, this length is an imaginary time. The index j represents the position of the bead in the polymer, this position corresponds to a discrete imaginary time $\tau_j = j\delta\tau = j\frac{\tau}{M}$. The discretization of the polymer in the imaginary time is named *time-step*. The mean square displacement of the beads in a polymer represents the indetermination of the position of the corresponding particle in the quantum system. A configuration of these special interacting polymers is thus defined by a set of coordinates $\{\vec{r}_i^j\}$, where i represents the polymer and j represents the bead in the i -th polymer; Figure 2.1 shows a schematic representation of the polymers in PIGS and their correlations. A quantum observable is mapped to an operator that acts on such configurations that in this context shall be referred as *estimator*.

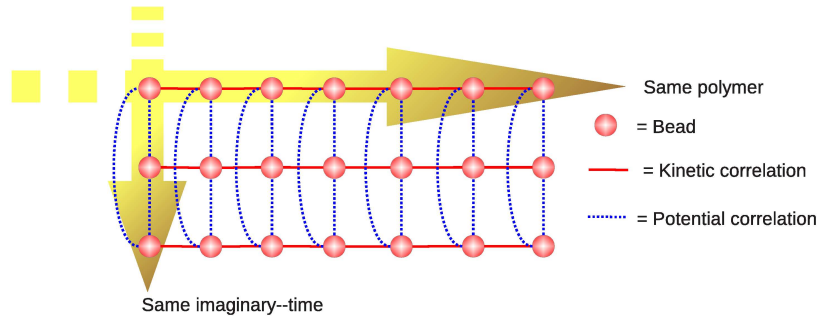


Figure 2.1: Schematic representation of the polymers in PIGS and their correlations.

Here on, we will focus on Bose systems. In Sec. 7.1.4 the practical implementation of the Metropolis algorithm will be described; in that section, two different Monte Carlo algorithms used to sample the space of permutations will also be shown.

Path Integral Ground State in action

In my work for the Master degree I developed a library that can run PIGS simulations as well as Path Integral simulations at finite temperature (Path Integral Monte Carlo, PIMC, see Sec. 2.2). The work presented in this section is one of the early employments of the library and it is a benchmark for both the library itself and the

PIGS technique. A benchmark for the library because the library came through extensive testing during this work, a benchmark for the PIGS technique because this work shows that PIGS is really unbiased, in other words, the choice of the trial wave function does not affect the final results, provided that the projection time is large enough and the time-step $\delta\tau$ is sufficiently small. This is a very strong feature of PIGS and is a necessary condition for a truly *ab-initio* method because it allows the study of a quantum system even if we don't know *anything* about its many-body ground state wave function.

Test systems We have considered two bulk phases of a many-body strongly interacting Boson system: liquid and solid ^4He . Dealing with low temperature properties, ^4He atoms are described as structureless zero-spin bosons, interacting through a realistic two-body potential, that we assume to be the HFDHE2 Aziz potential [4]; we remark here that our results are thus valid on this interaction potential and have not general validity.

For the liquid phase, we have considered a cubic box with periodic boundary conditions, containing $N = 64$ atoms at the equilibrium density $\rho_l = 0.0218\text{\AA}^{-3}$. For the solid phase we have considered a cubic box with periodic boundary conditions designed to house a fcc crystal of $N = 32$ atoms at the density $\rho_s = 0.0313\text{\AA}^{-3}$. In both cases we add standard tail corrections to the potential energy to account for the finite size of the system by assuming the medium homogeneous (i.e. $g(r) = 1$) beyond $L/2$, where L is the size of the box. Obviously, this is not an accurate assumption specially for the solid phase in such a small box, but our main purpose here is to show that PIGS method is able to reach the same results independently on the considered initial wave function. Computations of ground state properties of bulk ^4He with accurate tail corrections can be found in the current literature.[5, 6]

Trial wave functions The trial wave functions commonly used within the PIGS method[1] are the variational Jastrow wave function (JWF) for the liquid and the Jastrow-Nosonow (J-NWF) for the solid. A JWF represents the simplest possible choice of wave function for strongly interacting Bosons[7] and it contains only two-body correlations. Using a McMillan pseudopotential[8], the unnormalized JWF reads as

$$\psi_{\text{JWF}}(R) = \prod_{i<j=1}^N e^{-\frac{1}{2}\left(\frac{b}{r_{ij}}\right)^m}. \quad (2.19)$$

The physical meaning of this JWF is that, due to the sharp repulsive part of the interaction potential V in the Hamiltonian \hat{H} , ^4He atoms prefer to avoid each other. In the J-NWF the JWF is multiplied by a term like the one in Eq. (2.22) below, that localizes the particles in a crystalline order. In this work, however, in order to explore the convergence properties of the PIGS method, we have considered two wave functions of “opposite” quality: the best available one, that is the shadow wave function, and the poorest imaginable one, i.e. the constant wave function. As we shall see, JWF will be considered only when computing the one-body density matrix in the liquid phase.

The constant wave function is the ground state wave function of the ideal Bose gas,

$$\psi_{\text{CWF}}(R) = 1. \quad (2.20)$$

It carries no correlation at all. We choose this wave function because, allowing an unrestricted sampling of the full configurational space, it results in no importance sampling. Then the whole imaginary time projection procedure is driven only by the short imaginary time Green's function $G(R, R', \delta\tau)$, without any input, and then any bias, from the initial state. Thus at the starting point the system is made up by free particles; if after a long enough imaginary time projection, PIGS turns out to be able to reach a strong correlated quantum liquid and quantum crystal by itself we can safely believe that no variational bias affects PIGS results.

On the other hand, we choose as ψ_T a SWF optimized with a variational computation in order to have as reference results the ones coming from the projection of an initial wave function that is more accurate as possible, i.e. from a wave function whose overlap with the exact ground state is known to be large. In the SWF, additional correlations besides the standard two body terms are introduced via auxiliary variables which are integrated out[9]. This is done so efficiently that the crystalline phase emerges as a spontaneously broken symmetry process, induced by the inter-particles correlations as the density is increased, without the need of any a priori knowledge of the equilibrium positions and without losing the translationally invariant form of the wave function. Thus SWF is able to describe both the liquid and the solid phase with the same functional form and it is explicitly Bose symmetric. The standard SWF functional form reads

$$\psi_{\text{SWF}}(R) = \phi_r(R) \int dS K(R, S) \phi_s(S) \quad (2.21)$$

where $S = (\vec{s}_1, \vec{s}_2, \dots, \vec{s}_N)$ is the set of auxiliary shadow variables, $\phi_r(R)$ is the standard Jastrow two body correlation term (2.19), $K(R, S)$ is a kernel coupling each shadow to the corresponding real variable, and $\phi_s(S)$ is another Jastrow term describing the inter-shadow correlations. Due to its analytical expression, the introduction of the SWF defined by Eq. (2.21) in a PIGS simulation consists in adding a timeslice at each extremity of every polymer. These newly added timeslices have special correlations; namely there are *real-shadow* intrapolymer correlations defined by $K(R, S)$ and *shadow-shadow* interpolymer correlations defined by $\phi_s(S)$. As consequence, the PIGS method has to be extended with Metropolis moves that accordingly involve the introduced shadow timeslices.

As usual[10], we take $K(R, S)$ Gaussian and, as pseudopotential in $\phi_s(S)$, we use the He-He potential V rescaled in both amplitude and distances. The variational parameters we use were chosen in order to minimize the expectation value of the Hamiltonian \hat{H} and are reported in Ref. [10]. Nowadays the SWF represents the best available variational wave function for ${}^4\text{He}$ systems.[6] Recently, it has been estimated[11] that, when describing a two dimensional solid, the overlap of the SWF with the true ground state is of about $(0.998)^N$, which ensures a fast convergence rate when projected within the PIGS method. The properties of the SWF are so peculiar

that the PIGS method that has a SWF as ψ_T deserves an its own name and is dubbed SPIGS: Shadow Path Integral Ground State method.[12, 13]

In order to test how robust PIGS is, we consider also a wave function that describes the wrong phase: for the liquid phase we consider a Gaussian wave function, where each particle is harmonically localized around fixed positions $\{\vec{r}_{0i}\}$

$$\psi_{\text{GWF}}(R) = \prod_{i=1}^N e^{-C|\vec{r}_i - \vec{r}_{0i}|^2}, \quad (2.22)$$

i.e. ψ_T it the wave function of an Einstein harmonic solid. The parameter $C = 8 \text{ \AA}^{-2}$ is arbitrary and it is was chosen to ensure a strong localization of the particles around the positions $\{\vec{r}_{0i}\}$ that were taken over a regular cubic lattice within the simulation box. This wave function is evidently not translationally invariant and not Bose symmetric. Furthermore it does not contain any correlation between the particles, and all the information that it carries is that of a crystalline system, i.e. GWF is an extremely poor wave function for the liquid phase. This “bad” initial wave function will provide a stringent test on the convergence properties of the PIGS methods.

As far as the one-body density matrix computation in the liquid phase is concerned, the values of the parameters b and m in the JWF have been chosen equal to the ones of the corresponding Jastrow term in the SWF.

Small time Green’s function One of the fundamental elements of path integral projection Monte Carlo methods is the imaginary time Green’s function $G(R, R', \tau)$, whose accuracy turns out to be crucial to the convergence to the exact results. The functional form of G for a generic τ is unfortunately not known with exception of few particular cases, such as, for example, the free particle and the harmonic oscillator, but accurate approximations of G are obtainable in the small τ regime[2, 14, 15]. In this work, we have chosen the Pair–Suzuki approximation[16] for the imaginary time propagator, which is a pair–approximation of the fourth–order Suzuki–Chin density matrix.[14]

The Suzuki–Chin approximation is based on the following factorization of the density matrix:

$$e^{-2\delta\tau\hat{H}} \simeq e^{-\frac{\delta\tau}{3}\hat{V}_e} e^{-\delta\tau\hat{T}} e^{-\frac{4\delta\tau}{3}\hat{V}_c} e^{-\delta\tau\hat{T}} e^{-\frac{\delta\tau}{3}\hat{V}_e} \quad (2.23)$$

where \hat{T} is the kinetic operator and \hat{V}_e and \hat{V}_c are given by

$$\hat{V}_e = \hat{V} + \frac{\alpha\delta\tau^2\lambda}{3} \sum_{i=1}^N (\mathbf{F}_i)^2 \quad (2.24)$$

and

$$\hat{V}_c = \hat{V} + \frac{(1-\alpha)\delta\tau^2\lambda}{6} \sum_{i=1}^N (\mathbf{F}_i)^2 \quad (2.25)$$

respectively, with \hat{V} the potential operator, α an arbitrary constant in the range $[0, 1]$, $\lambda = \hbar^2/2m$ and $\mathbf{F}_i = \nabla_i V$. The resulting imaginary time propagator is accurate to order $\delta\tau^4$, and has been successfully applied to liquid ${}^4\text{He}$ in two and three dimensions.[14] This approximation offers also the advantage that adjusting the parameter α it is possible to optimize the convergence, and a standard choice for a quantum system is $\alpha = 0$.[14] A strategy to obtain a simpler, but equally accurate, approximation consists in applying a pair product assumption.[16] For sufficiently short time steps, in fact, the many-body propagator (in imaginary time) is well approximated by the product of two-body propagators.[2] In this approximation, the small time propagator reads

$$G(R_m, R_{m+1}; \delta\tau) = (4\pi\lambda\delta\tau)^{-3N/2} \times \prod_{i=1}^N \exp\left(-\frac{(\vec{r}_{i,m} - \vec{r}_{i,m+1})^2}{4\lambda\delta\tau}\right) \times \exp(-u(r_{ij,m}, r_{ij,m+1})) \quad (2.26)$$

where u is given as

$$u(r_m, r_{m+1}) = \begin{cases} \frac{\delta\tau}{3} [v_e(r_m) + 2v_c(r_{m+1})] & m \text{ odd} \\ \frac{\delta\tau}{3} [2v_c(r_m) + v_e(r_{m+1})] & m \text{ even.} \end{cases} \quad (2.27)$$

The potentials $v_e(r)$ and $v_c(r)$ are defined as

$$v_e(r) = V(r) + \alpha \frac{2}{3} \delta\tau^2 \lambda \left(\frac{\partial V}{\partial r}\right)^2$$

$$v_c(r) = V(r) + (1 - \alpha) \frac{1}{3} \delta\tau^2 \lambda \left(\frac{\partial V}{\partial r}\right)^2 \quad (2.28)$$

where $V(r)$ is the potential experienced by two ${}^4\text{He}$ atoms at a distance r . The advantage is that there is no need to calculate \mathbf{F}_i . As for the full Suzuki–Chin approximation,[14] also for the Pair–Suzuki the operators corresponding to physical observables must be inserted only on odd time slices in the imaginary time path.

In order to fix the optimal small imaginary time step value, we have performed PIGS simulations with different initial wave functions. By considering decreasing $\delta\tau$ values with a fixed total projection time, τ , we have taken the energy per particle $E(\tau)$ as observable of reference. As an example, our results for SWF and CWF in the liquid phase are plotted in Fig. 2.2. We choose as optimal value $\delta\tau = 1/640 \text{ K}^{-1}$; in fact, further reductions do not change the energy in a detectable way, i.e. within the statistical uncertainty. In Fig. 2.2 SWF and CWF do not converge to the same value simply because the considered total projection time τ in this test is not enough to ensure convergence of $E(\tau)$ to the ground state energy for CWF (see Fig. 2.3). Similarly, in the solid phase we take $\delta\tau = 1/960 \text{ K}^{-1}$.

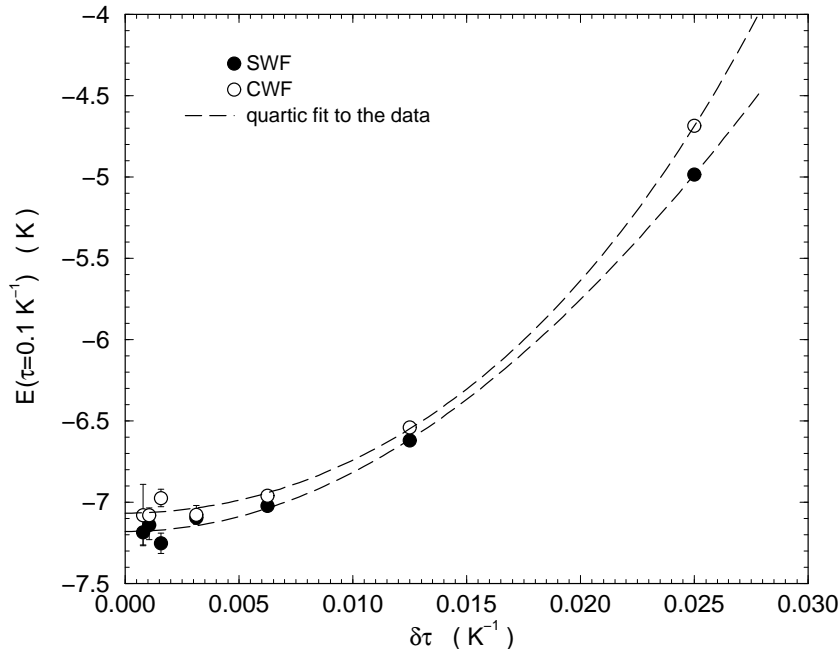


Figure 2.2: Energy per ${}^4\text{He}$ atom $E(\tau)$ vs. imaginary time step $\delta\tau$. The total projection time is $\tau = 0.1 \text{ K}^{-1}$. The calculations were carried out by projecting a SWF and a CWF for a system of 64 particles at the equilibrium density $\rho = 0.0218 \text{ \AA}^{-3}$. Dashed lines are quartic fits to the data. Error bars, when not shown, are smaller than the used symbols.

Once set the optimal $\delta\tau$ value, we have computed the diagonal properties of the system for increasing total projection time τ until we reached convergence to a value that corresponds to the exact ground state result both for the liquid and for the solid phase. In the liquid phase we have computed also the one-body density matrix.

PIGS results without importance sampling For the liquid phase we have projected a SWF and a CWF. The energy per particle as a function of the total projection time τ for both the wave functions is plotted in Fig. 2.3. We find that the energy converges, independently from the considered initial wave function, to the same value $E = -7.17 \pm 0.02 \text{ K}$. This value, in spite of the small size of the considered system, is close to the experimental[17] result $E = -7.14 \text{ K}$. SWF converges very quickly, in fact $\tau = 0.05 \text{ K}^{-1}$ is already enough to ensure convergence. CWF instead, requires a three times larger imaginary time, i.e. $\tau = 0.15 \text{ K}^{-1}$. Nevertheless, the quick convergence of also CWF is a really remarkable result. In fact, this means that PIGS efficiently includes the exact interparticle correlations through the imaginary time projections, without any need of importance sampling. Then, the choice of a good wave function, within the PIGS method, becomes a matter of convenience rather than of principle, since better initial wave functions only allow for a smaller total projection time τ , and thus less CPU consuming simulations.

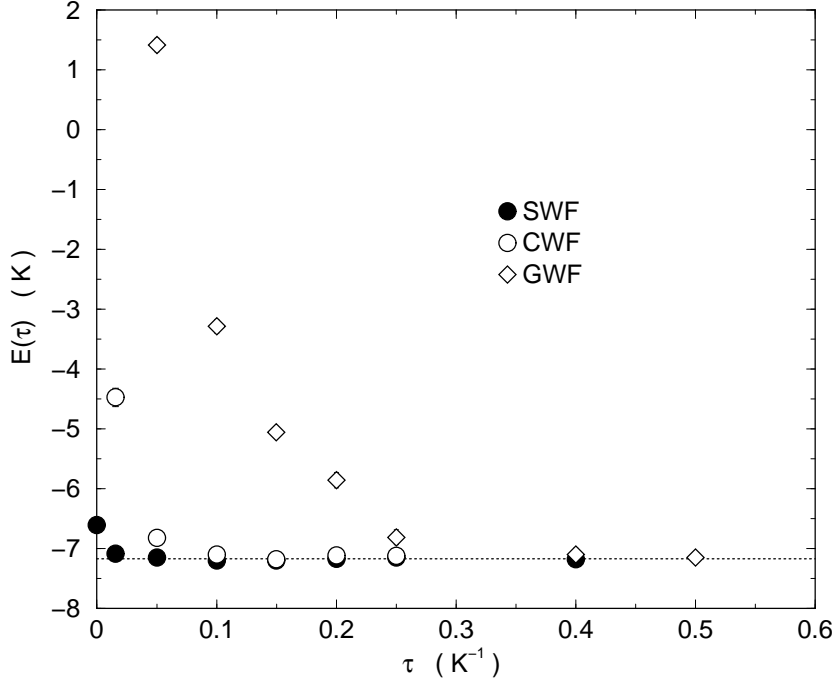


Figure 2.3: Energy per particle E as a function of the total projection time τ obtained from PIGS simulations for liquid ${}^4\text{He}$ at the equilibrium density $\rho = 0.0218 \text{ \AA}^{-3}$ by projecting a SWF (filled circles) and a CWF (open circles) and a GWF (open diamonds). $\tau = 0$ result (filled circle) corresponds to the SWF variational estimate of E , the $\tau = 0$ for the GWF is $E = 122.08 \pm 0.06 \text{ K}$ and for CWF E is essentially infinite. Error bars are smaller than the used symbols. Dotted line indicates the convergence value $E = -7.17 \pm 0.02 \text{ K}$.

This convergence is confirmed also by the radial distribution function $g(r)$ and the static structure factor $S(k)$. For such quantities, the convergence rate is found to be similar to the energy one. In Fig. 2.4 we report the radial distribution function $g(r)$ obtained by projecting both a SWF and a CWF at different imaginary time values. For $\tau > 0.05 \text{ K}^{-1}$, SWF results at different τ are indistinguishable within the statistical uncertainty (see Fig. 2.4a). In fact, with SWF the exact result is reached within very few projection steps and then it is no more affected by further projections. As already pointed out, also CWF displays a fast convergence, as shown in Fig. 2.4c, where $\Delta g^\tau(r) = g_{\text{SWF}}^\tau(r) - g_{\text{CWF}}^\tau(r)$ is shown. For increasing τ , Δg^τ evolves toward a flat function, meaning that the systems described starting from the two different wave functions, i.e the strongly correlated quantum liquid of SWF and the ideal gas of CWF, are evolving into the same quantum liquid, which is the best reachable representation of the exact ground state of the simulated system. The same conclusion is inferred from the evolution of the static structure factor $S(k)$, which is plotted in Fig. 2.5.

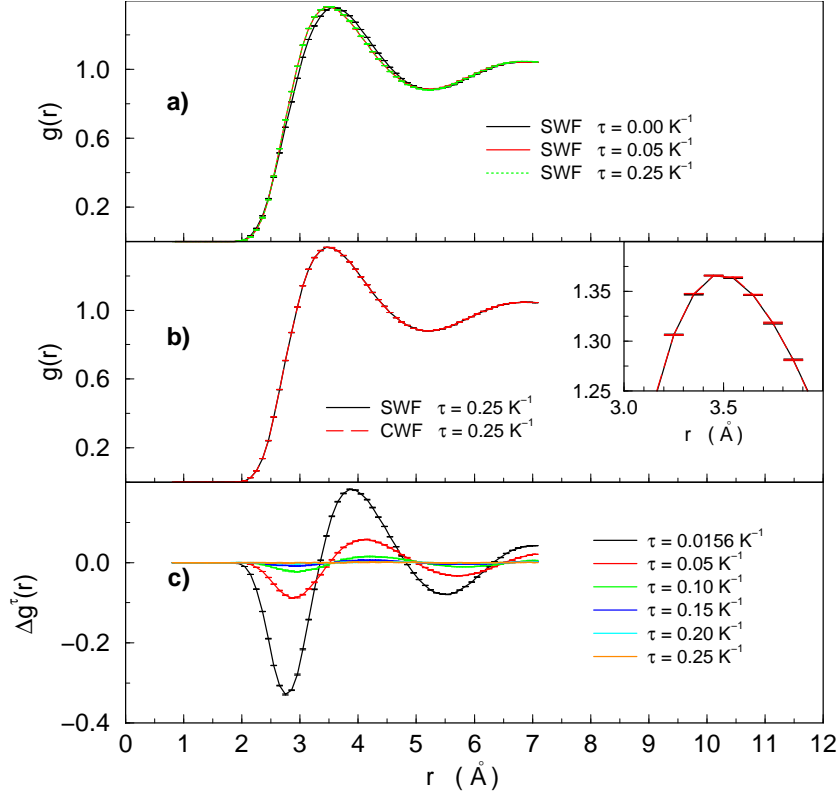


Figure 2.4: Radial distribution function $g(r)$ for bulk liquid ${}^4\text{He}$ computed in a cubic box with $N = 64$ at the density $\rho = 0.0218 \text{ \AA}^{-3}$ with the PIGS method. a) $g(r)$ obtained by projecting a SWF for $\tau = 0.00, 0.05$ and 0.25 K^{-1} . The $\tau = 0.00$ result corresponds to the variational SWF estimate of $g(r)$. b) $g(r)$ obtained by projecting a SWF for $\tau = 0.25 \text{ K}^{-1}$ and a CWF for $\tau = 0.25 \text{ K}^{-1}$. In the inset a zoom of the first maximum region. c) $\Delta g^\tau(r) = g_{\text{SWF}}^\tau(r) - g_{\text{CWF}}^\tau(r)$ at different τ values, where $g_{\text{SWF}}^\tau(r)$ is the $g(r)$ computed by projecting a SWF for an imaginary time equal to τ , and $g_{\text{CWF}}^\tau(r)$ is the same but by projecting a CWF. Note the smaller scale on the vertical axis

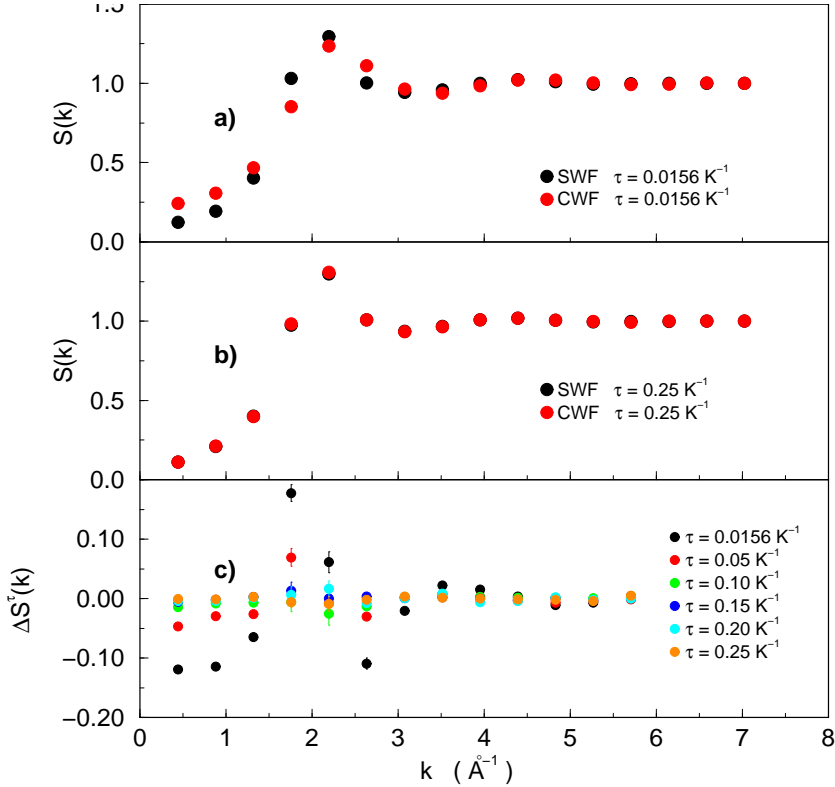


Figure 2.5: Static structure factor $S(k)$ for bulk liquid ${}^4\text{He}$ computed in a cubic box with $N = 64$ at the density $\rho = 0.0218 \text{ \AA}^{-3}$ with the PIGS method. a) $S(k)$ obtained by projecting a SWF and a CWF for $\tau = 0.05 \text{ K}^{-1}$. b) $S(k)$ obtained by projecting a SWF and a CWF for $\tau = 0.40 \text{ K}^{-1}$. c) $\Delta S^\tau(k) = S_{\text{SWF}}^\tau(k) - S_{\text{CWF}}^\tau(k)$ at different τ values, where $S_{\text{SWF}}^\tau(k)$ is the $S(k)$ computed by projecting a SWF for an imaginary time equal to τ , and $S_{\text{CWF}}^\tau(k)$ is the same but by projecting a CWF. Note the smaller scale on the vertical axis.

PIGS results from a “bad” initial function In order to put a more stringent check on the PIGS method ability to converge to the exact ground state without any variational bias, we have considered also a “bad” initial wave function by projecting a GWF. Thus at the starting point of the imaginary time path there is now a strongly localized Einstein crystal. We note that, differently from the other considered cases, the GWF is *not* Bose symmetric; as consequence of this choice, the projection relation (2.8) is not Bose symmetric and thus requires symmetrization. The symmetrization has been introduced with the sampling of the permutations between polymers; this is a standard technique used in Path Integral simulations and will be described in Sec. 7.1.4.

With this initial function, we find even in this case that the energy converges to the same value as before (see Fig. 2.3). Thus PIGS is able not only to drop from the initial wave function the wrong information of localization, but also to generate at the same time the correct correlations among the particles. GWF needs $\tau = 0.5 \text{ K}^{-1}$ to converge, which is ten times larger than the SWF value.

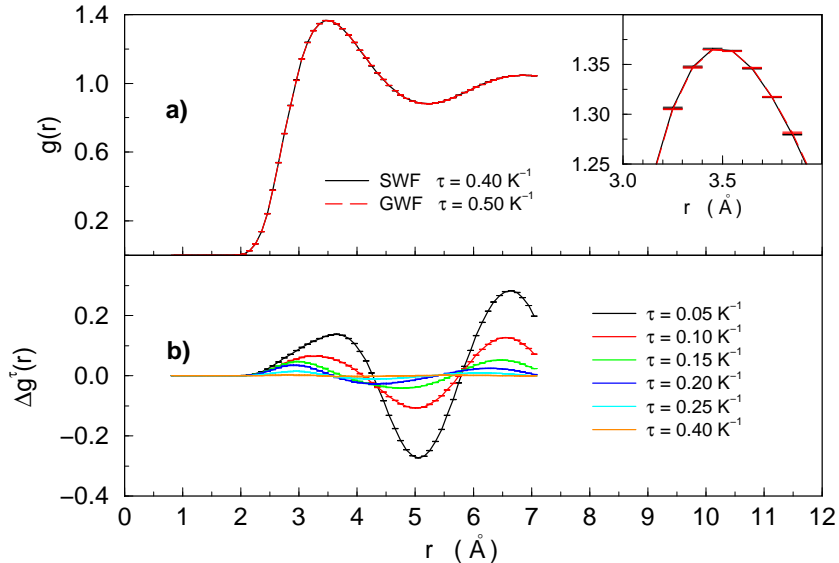


Figure 2.6: Radial distribution function $g(r)$ for bulk liquid ${}^4\text{He}$ computed in a cubic box with $N = 64$ at the density $\rho = 0.0218 \text{ \AA}^{-3}$ with the PIGS method. a) $g(r)$ obtained by projecting a SWF for $\tau = 0.40 \text{ K}^{-1}$ and a GWF for $\tau = 0.50 \text{ K}^{-1}$. In the inset a zoom of the first maximum region. b) $\Delta g^\tau(r) = g_{\text{SWF}}^\tau(r) - g_{\text{GWF}}^\tau(r)$ at different τ values, where $g_{\text{SWF}}^\tau(r)$ is the $g(r)$ computed by projecting a SWF for an imaginary time equal to τ , and $g_{\text{GWF}}^\tau(r)$ is the same but by projecting a GWF. Note the smaller scale on the vertical axis.

Again this convergence is confirmed also by the radial distribution function $g(r)$ and the static structure factor $S(k)$. In Fig. 2.6 we report the radial distribution function $g(r)$ obtained by projecting a GWF at different imaginary time values compared with the ones coming from the projection of SWF. It is evident that small imaginary time is not enough to leave out the wrong information in the GWF. For lower τ values, there are still reminiscences of the starting harmonic solid, which are progressively lost as the projection time increases. This is made clearer in Fig. 2.6b where we plot the difference $\Delta g^\tau(r)$, at fixed imaginary time τ , between the $g(r)$ computed by projecting the SWF and the one obtained by projecting the GWF. A similar behavior is observed in the evolution static structure factor $S(k)$, plotted in Fig. 2.7. For the GWF, the Bragg peak shown at small τ values (Fig. 2.7a), which is typical of the solid phase, becomes lower and lower as the projection time is increased (Fig. 2.7b), until convergence is reached (see Fig. 2.7c).

From the plot of the energy per particle vs. the total imaginary time τ it is possible to estimate the overlap per particle of the initial wave function on the exact ground state.[18] By using the results in Fig. 2.3 we find that the overlap of SWF is about 99%, while the GWF one is about 10%. That SWF has an high overlap with the ground state is not a surprise; it was qualitatively expected since SWF is presently the best available wave function for ${}^4\text{He}$. [6] However a 99% overlap is really remarkable and provides a further argument on the goodness of SWF. On the other

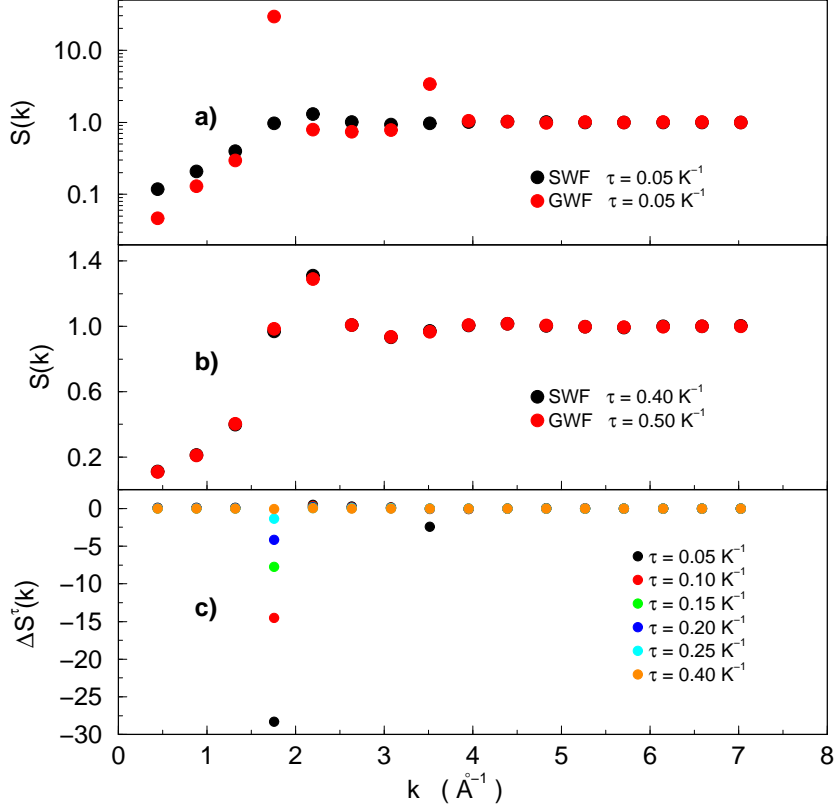


Figure 2.7: Static structure factor $S(k)$ for bulk liquid ^4He computed in a cubic box with $N = 64$ at the density $\rho = 0.0218 \text{ \AA}^{-3}$ with the PIGS method. a) $S(k)$ obtained by projecting a SWF and a GWF for $\tau = 0.05 \text{ K}^{-1}$. It is evident in the GWF result the presence of the Bragg peak. Note the logarithmic scale. b) $S(k)$ obtained by projecting a SWF for $\tau = 0.40 \text{ K}^{-1}$ and a GWF for $\tau = 0.50 \text{ K}^{-1}$. The Bragg peak is no more present in the GWF result. c) $\Delta S^\tau(k) = S_{\text{SWF}}^\tau(k) - S_{\text{GWF}}^\tau(k)$ at different τ values, where $S_{\text{SWF}}^\tau(k)$ is the $S(k)$ computed by projecting a SWF for an imaginary time equal to τ , and $S_{\text{GWF}}^\tau(k)$ is the same but by projecting a GWF. Note the change of the vertical scale. Error bars are smaller than the used symbols.

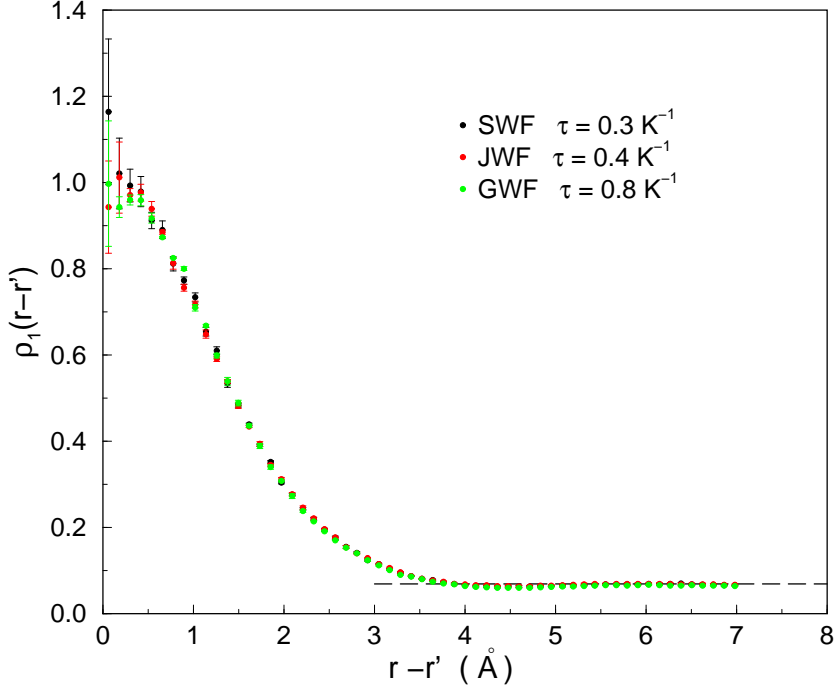


Figure 2.8: One-body density matrix ρ_1 obtained from PIGS simulations for liquid ${}^4\text{He}$ at the equilibrium density $\rho = 0.0218 \text{ \AA}^{-3}$ by projecting a SWF, a JWF and a GWF for an imaginary time $\tau = 0.30, 0.40$ and 0.80 K^{-1} respectively. The dotted line indicates the condensate value $n_0 = 0.069$ obtained from an independent PIGS simulation.[19]

hand, a poor overlap of GWF was somehow expected, since the parameter C was chosen to strongly localize the atoms of the bulk liquid around fictitious equilibrium positions on a regular lattice.

Off-diagonal properties Besides the diagonal ones, also off-diagonal properties, such as the one-body density matrix, are accessible within PIGS simulations. The one-body density matrix $\rho_1(\vec{r}, \vec{r}')$ represents the probability amplitude of destroying a particle in \vec{r} and creating one in \vec{r}' . Its Fourier transformation represents the momentum distribution. In first quantization ρ_1 is given by the overlap between the normalized many-body ground state wave functions $\psi_0(R)$ and $\psi_0(R')$, where the configuration $R' = (\vec{r}', \vec{r}_2, \dots, \vec{r}_N)$ differs from $R = (\vec{r}, \vec{r}_2, \dots, \vec{r}_N)$ only by the position of one of the N atoms in the system. If $\psi_0(R)$ is translationally invariant, ρ_1 only depends on the difference $|\vec{r} - \vec{r}'|$, thus

$$\rho_1(\vec{r} - \vec{r}') = N \int d\vec{r}_2 \dots d\vec{r}_N \psi_0^*(R) \psi_0(R'). \quad (2.29)$$

The Bose-Einstein condensate fraction n_0 is equal to the large distance limit of $\rho_1(\vec{r} - \vec{r}')$. In fact, if ρ_1 has a nonzero plateau at large distance, the so called off-diagonal

long-range order (ODLRO), its FT contains a Dirac delta function, which indicates a macroscopic occupation of a single momentum state, i.e. Bose–Einstein condensation.

The exact ρ_1 can be obtained in PIGS simulation by substituting ψ_0 in (2.29) with ψ_τ with τ large enough. This corresponds to the simulation of a system of $N - 1$ linear polymers plus a polymer which is cut into two halves, called half-polymers, one departing from \vec{r} and the other from \vec{r}' . Thus ρ_1 is obtained by collecting the relative distances among the cut ends of the two half-polymers during the Monte Carlo sampling. The present computation of ρ_1 has been obtained by implementing a zero temperature version of the worm algorithm.[20] We have worked with a fixed number of particles and not in the grand canonical ensemble, similarly to what has been done at finite temperature in Ref. [16]. In practice this corresponds to a usual PIGS calculation of ρ_1 where “open” and “close” moves have been implemented[20] in order to visit diagonal and off-diagonal sectors within the same simulation. The advantage of doing this does not come from the efficiency of the worm algorithm to explore off-diagonal configurations, because similar efficiency is obtained with PIGS when “swap” moves are implemented.[11] The benefit in using a worm-like algorithm here instead comes from the automatic normalization of ρ_1 which is a peculiarity of this method.[20] In Fig. 2.8 we report ρ_1 obtained in PIGS simulations of bulk liquid ^4He at $\rho = 0.0218 \text{ \AA}^{-3}$ by projecting either a SWF, a JWF and a GWF. All the simulations give the same result, shown in Fig. 2.8 which turns out to be compatible with the recent estimate obtained with PIGS given in Ref. [19] of $n_0 = 0.069 \pm 0.005$.

Results on the solid system We have performed the computation at density $\rho = 0.0313 \text{ \AA}^{-3}$, where ^4He is in the solid phase, by projecting a SWF and a CWF. Our results for the energy per particle are plotted in Fig. 2.9 as a function of τ . In both cases we find convergence to the value $E = -5.34 \pm 0.02 \text{ K}$. Even in this phase the convergence of SWF is faster, being $\tau = 0.05 \text{ K}^{-1}$ enough to reach convergence. In the case of CWF convergence is reached only for a much larger imaginary time $\tau = 0.80 \text{ K}^{-1}$.

Also in this case convergence is obtained for the radial distribution function and for the static structure factor, reported in Fig. 2.10 and Fig. 2.11 respectively. From Fig. 2.10a it is evident that SWF has reached the true ground state with few projection steps, since the results for $g(r)$ at $\tau = 0.05 \text{ K}^{-1}$ and $\tau = 0.80 \text{ K}^{-1}$ are indistinguishable. The evolution toward the correct ground state of the projected CWF is instead detectable. The presence of the crystalline structure is mainly evident in the static structure factor, where a Bragg peak grows with increasing τ (see Fig. 2.11a,b). The emerging of the correct solid structure by projecting a really poor wave function such as the CWF is made evident by the trend toward a flat function of the differences $\Delta g^\tau(r)$ and $\Delta S^\tau(k)$ plotted in Fig. 2.10c and Fig. 2.11c respectively.

Conclusions of the test phase In this section we have studied with the Path Integral Ground State method diagonal and off-diagonal properties of a strongly interacting quantum Bose system like the bulk liquid and solid phases of ^4He . We have obtained convergence to the ground state values of quantities like the total energy,

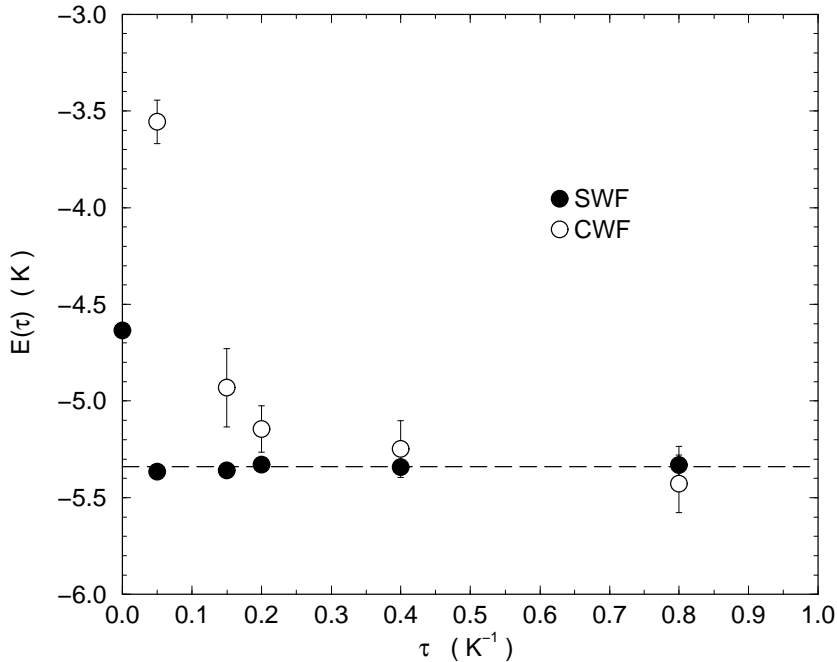


Figure 2.9: Energy per particle E as a function of the total projection time τ obtained from PIGS simulations of an fcc ${}^4\text{He}$ crystal at the density $\rho = 0.0313 \text{ \AA}^{-3}$ by projecting a SWF (filled circles) and a CWF (open circles). Dashed line indicates the convergence value $E = -5.34 \pm 0.02 \text{ K}$.

the radial distribution function, the static structure factor and the one-body density matrix projecting radically different wave functions: equivalent expectation values in the liquid phase have been obtained using as initial wave function a shadow wave function, a Gaussian wave function with strongly localized particles of an Einstein solid without interparticle correlations and also a constant wave function where all configurations of the particles are equally probable. Similarly in the solid phase equivalent expectation values have been obtained by considering a shadow wave function, which describes a solid, and a constant wave function which describes an ideal Bose gas. The present analysis demonstrates the absence of any variational bias in PIGS; a method that can be thus considered as unbiased as the finite temperature PIMC. This remarkable property comes from the accurate imaginary time propagators, exactly the same used with PIMC, that do not depend on the initial trial state. It remains true that the use of a good variational initial wave function greatly improves the rate of convergence to the exact results.

We have addressed here only the case of a realistic interaction potential among Helium atoms. However one can reasonably expect that this conclusion holds even for very different kinds of interaction, once an accurate approximation for the imaginary time propagator is known (for example hard-spheres[21] or hydrogen plasma[22]). As far as pathological potentials like the attractive Coulomb one are concerned, PIGS would suffer the same limitations of PIMC if inaccurate approximations of the propagator were used.[23]

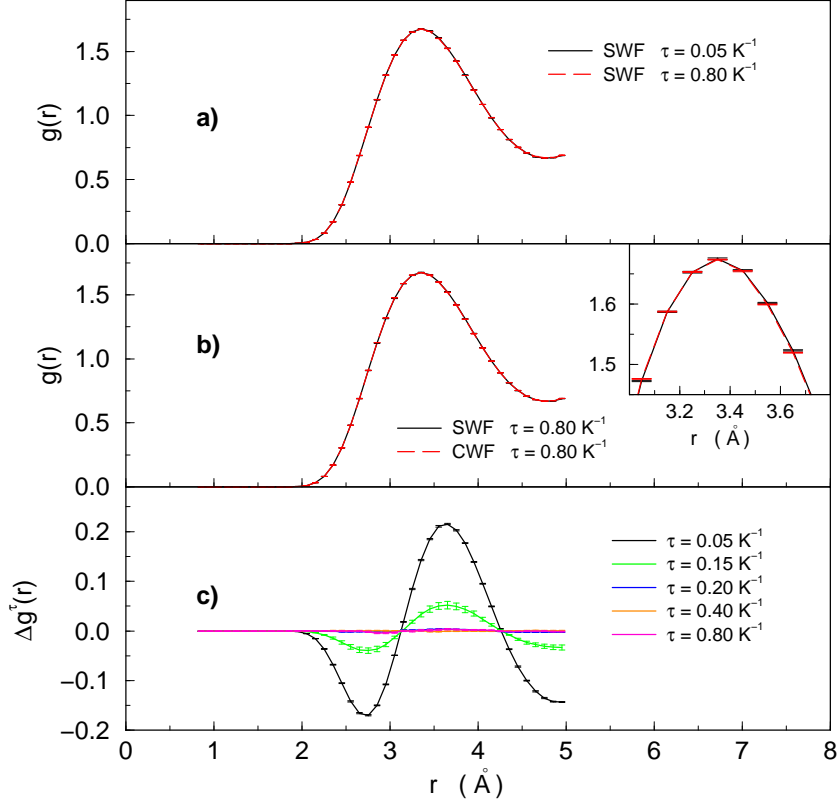


Figure 2.10: Radial distribution function $g(r)$ for bulk solid ${}^4\text{He}$ computed in a cubic box with $N = 32$ at the density $\rho = 0.0313 \text{ \AA}^{-3}$ with the PIGS method. a) $g(r)$ obtained by projecting a SWF for $\tau = 0.05$ and 0.80 K^{-1} . b) $g(r)$ obtained by projecting a SWF and a CWF for $\tau = 0.80 \text{ K}^{-1}$. In the inset a zoom of the first maximum region. c) $\Delta g^\tau(r) = g_{\text{SWF}}^\tau(r) - g_{\text{CWF}}^\tau(r)$ at different τ values, where $g_{\text{SWF}}^\tau(r)$ is the $g(r)$ computed by projecting a SWF for an imaginary time equal to τ , and $g_{\text{CWF}}^\tau(r)$ is the same but by projecting a CWF.

2.2 Path Integral at finite temperature

Up to now we have focused on the problem of evaluating $T = 0 \text{ K}$ expectation values; the formalism of the previous section, however, can be used with very small modifications also for quantum thermal averages, the resulting methodology is named Path Integral Monte Carlo (PIMC). This methodology was developed well before PIGS in the work in Ref. [24]. The physical properties of the system are obtained from the thermal density matrix

$$\hat{\rho} = \frac{e^{-\beta\hat{H}}}{\mathbf{Z}} \quad (2.30)$$

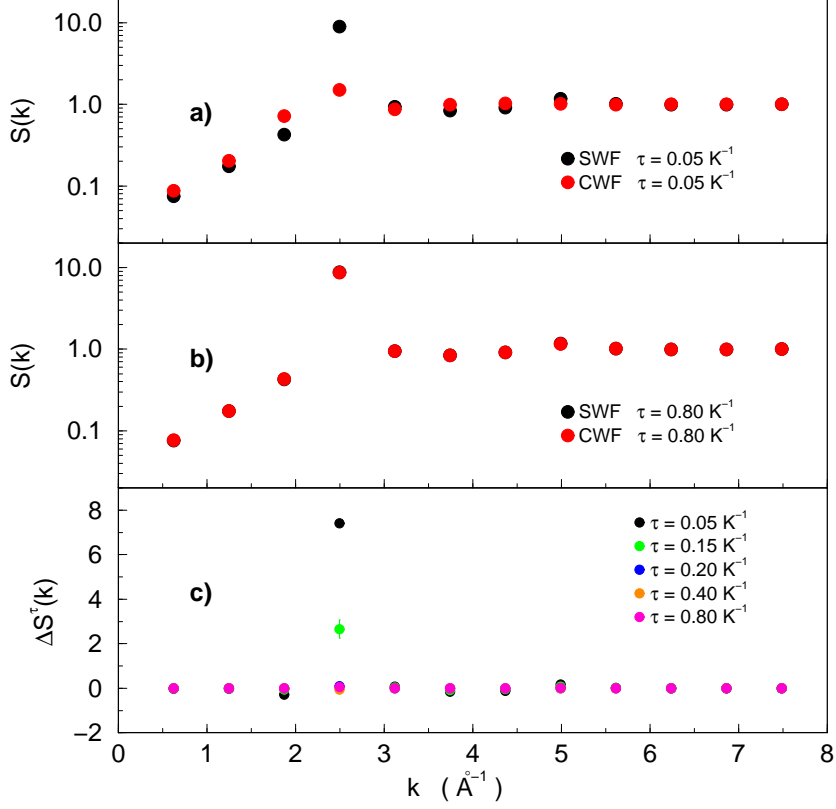


Figure 2.11: Static structure factor $S(k)$ for bulk solid ${}^4\text{He}$ computed in a cubic box with $N = 32$ at the density $\rho = 0.0313 \text{ \AA}^{-3}$ with the PIGS method. a) $S(k)$ obtained by projecting a SWF and a CWF for $\tau = 0.05 \text{ K}^{-1}$. b) $S(k)$ obtained by projecting a SWF and a CWF for $\tau = 0.80 \text{ K}^{-1}$. The black dots are under the red ones. c) $\Delta S^\tau(k) = S_{\text{SWF}}^\tau(k) - S_{\text{CWF}}^\tau(k)$ at different τ values, where $S_{\text{SWF}}^\tau(k)$ is the $S(k)$ computed by projecting a SWF for an imaginary time equal to τ , and $S_{\text{CWF}}^\tau(k)$ is the same but by projecting a CWF. Error bars are smaller than the used symbols. Notice the logarithmic scale in panels a) and b).

where $\beta = \frac{1}{k_b T}$, k_b is the Boltzmann constant and the normalization $\mathcal{Z} = \mathbf{Tr}(\hat{\rho})$ is the partition function of the system. The expectation value of an observable \hat{O} is

$$\langle \hat{O} \rangle = \frac{\mathbf{Tr}(\hat{O}\hat{\rho})}{\mathcal{Z}} . \quad (2.31)$$

It is evident in Eq. (2.30) that the unnormalized density matrix operator is formally identical to the quantum imaginary time operator appearing in Eq. (2.5) if one chooses $\tau = \beta$. The density matrix $\hat{\rho}$ in coordinate representation becomes

$$G(R, R', \beta) = \langle R | e^{(-\beta\hat{H})} | R' \rangle . \quad (2.32)$$

Fixed this set of basis, $|R\rangle\langle R| = \int dR$, the trace operator acts on the density matrix as follows

$$\mathbf{Tr}(\hat{\rho}) = \int dR G(R, R, \beta) = \mathcal{Z} \quad (2.33)$$

$$\langle \hat{O} \rangle = \frac{1}{\mathcal{Z}} \int dR O(R) G(R, R, \beta) \quad (2.34)$$

where \hat{O} is diagonal in the coordinate representation.

Using the Path Integral notation and following the same procedure employed for PIGS, Eq. (2.31) becomes

$$\langle \hat{O} \rangle = \frac{1}{\mathcal{Z}} \int \prod_{i=1}^M dR_i O(R_k) \prod_{j=1}^{M-1} G(R_j, R_{j+1}, \delta\tau) G(R_M, R_1, \delta\tau) \quad (2.35)$$

where here $\delta\tau = \beta/M$; the cyclic property of the trace operation allows $O(R)$ to be evaluated at any position in the path integral, in other words $1 \leq k \leq M$.

Eq. (2.18), however, does not possess the Bose symmetry; in order to introduce either the Bose or the Fermi statistics one has to symmetrize the density matrix (2.35) over the permutations of the particle labels.

$$G_B(R, R', \beta) = \frac{1}{N!} \sum_P G(R', \hat{P}R, \beta) \quad (2.36)$$

$$G_F(R, R', \beta) = \frac{1}{N!} \sum_P (-)^{n_P} G(R', \hat{P}R, \beta) \quad (2.37)$$

the first equation holds for the Bose statistics and the second for the Fermi statistics. The permutation operator \hat{P} acts on the many-body coordinate $R = \{\vec{r}_i\}_{i=1}^N$ by applying a cycle of n_P exchanges between particle indices, $\hat{P}R = \{\vec{r}_{P(i)}\}_{i=1}^N$. The sum in the two equations is meant as a sum over all the $N!$ possible permutations.

The Fermi symmetrization introduces negative density matrices that no longer can be directly interpreted as probability densities; there are different techniques[25]

that can re-express the density matrix as a definite positive object with a weight on the sampled configurations that introduces the sign given by the Fermi symmetry, however these techniques yield a signal to noise ratio[26] that dramatically decreases as $e^{-\gamma N}$; as consequence of this *sign problem*, these methodologies are restricted to small particle numbers.

Due to its affinity with Eq. (2.11), \mathcal{Z} is also the partition function of a system of classical *closed* polymers.

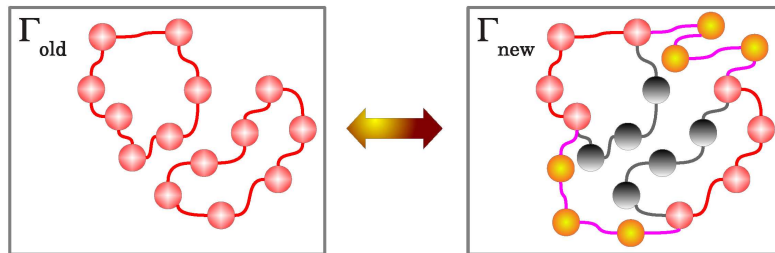


Figure 2.12: Representation of the polymers in PIMC and the effect of a permutation; a permutation between two polymers results in a new compound polymer with twice the length in imaginary time. This is a configuration that can not be sampled with moves that involve only a single polymer. Grey beads and lines represent the removed segment of the polymer. This picture can also be viewed from right to left: in this case, grey beads and lines represent the new segment of the polymer; this permutation splits a ring polymer of length 2β into two ring polymers of length β .

The differences between PIGS and PIMC in “polymer language” are minimal; first, in PIMC does not appear any trial wave function and the quantum imaginary–time is proportional to $\beta = 1/(k_B T)$; a more subtle difference that has deep consequences, however, is the different topology of the polymers. Due to the trace operation, in fact, the polymers in PIMC are represented by Eq. (2.33); these polymers close on themselves (for this reason they are also called *ring polymers*, see Fig. 2.12) and the role of permutations becomes more important than in the PIGS case. This is so because Eq. (2.33) is not yet Bose–symmetrized and the effect of the symmetrization (2.36) is that the polymers representing the particles of the system no longer close on themselves but, instead, are allowed to close on another ring polymer; this is explicitly shown in Fig. 2.12. The relevance of the symmetrization in PIMC is also noted by the fact that permutations explore topologically different configurations of the system that could not be obtained with single polymer sampling. This situation is different from the PIGS case; in PIGS, in fact, permutations between polymers will simply yield another configuration of open polymers that is topologically identical and can be obtained with single polymer moves; this implies that the sampling of permutations is not necessary if the Bose symmetry is already introduced by the chosen trial wave function. Another difference is that open polymers have less constraints on their structure and, compared to ring polymers, can be moved more efficiently by the Metropolis sampling; this is especially true when the probability distribution to

sample has many local maxima: in this case, with open polymers is generally easier to satisfy the ergodicity of the sampling.

Bibliography

- [1] A. Sarsa, k.E. Schmidt and W.R. Magro, *J. Chem. Phys.* **113**, 1366 (2000).
- [2] D.M. Ceperley, *Rev. Mod. Phys.* **67**, 279 (1995).
- [3] M. Rossi, M. Nava, L. Reatto and D. E. Galli, *J. Chem. Phys.* **131**, 154108 (2009).
- [4] R.A. Aziz, V.P.S. Nain, J.S. Carley, W.L. Taylor and G.T. McConville, *J. Chem. Phys.* **70**, 4330 (1979).
- [5] See for example J. Boronat and J. Casulleras, *Phys. Rev. B* **49**, 8920 (1994).
- [6] S. Moroni, D.E. Galli, S. Fantoni and L. Reatto, *Phys. Rev. B* **58**, 909 (1998).
- [7] see for instance, E. Feenberg, *Theory of Quantum Fluids* (Academic, New York, 1969).
- [8] W.L. McMillan, *Phys. Rev.* **138**, A442 (1965).
- [9] S.A. Vitiello, K. Runge and M.H. Kalos, *Phys. Rev. Lett.* **60**, 1970 (1988).
- [10] T. MacFarland, S.A. Vitiello, L. Reatto and G.V. Chester, *Phys. Rev. B* **50**, 13577 (1994).
- [11] E. Vitali, M. Rossi, F. Tramonto, D.E. Galli and L. Reatto, *Phys. Rev. B* **77**,180505(R) (2008).
- [12] D.E. Galli and L. Reatto, *Mol. Phys.* **101**, 1697 (2003); *J. Low Temp. Phys.*
- [13] D.E. Galli and L. Reatto, *J. Low Temp. Phys.* **136**, 343 (2004).
- [14] J.E. Cuervo, P.-N. Roy and M. Boninsegni, *J. Chem. Phys.* **122**, 114504 (2005).
- [15] K. Sakkos, J. Casulleras and J. Boronat, arXiv:0903.2763.
- [16] S. Pilati, *PhD thesis* p. 18, Trento University, Italy (2008).
- [17] P.T. Roach, J.B. Ketterson and C.W. Woo, *Phys. Rev. A* **2**, 543 (1970).
- [18] C. Mora and X. Waintal, *Phys. Rev. Lett.* **99**, 030403 (2007).

- [19] S. Moroni and M. Boninsegni, *J. Low Temp. Phys.* **136**, 129 (2004).
- [20] M. Boninsegni, N.V. Prokof'ev and B.V. Svistunov, *Phys. Rev. Lett.* **96**, 070601 (2006); *Phys. Rev. E* **74**, 036701 (2006).
- [21] J. Cao and B.J. Berne, *J. Chem. Phys.* **97**, 2382 (1992); L.M. Sesè and R. Ledesma, *J. Chem. Phys.* **102**, 3776 (1995); P. Grüter, D.M. Ceperley and F. Laloë, *Phys. Rev. Lett.* **79**, 3549 (1997).
- [22] C. Pierleoni, D.M. Ceperley, B. Bernu and W.R. Magro, *Phys. Rev. Lett.* **73**, 2145 (1994).
- [23] M.H. Müser and B.J. Berne, *J. Chem. Phys.* **107**, 571 (1997).
- [24] E. L. Pollock and D.M. Ceperley, *Phys. Rev. B* **30**, 2555 (1984).
- [25] Y. Kwon, D. M. Ceperley and R. M. Martin, *Phys. Rev. B* **48** 12037(1993); D. M. Ceperley and B. J. Alder, *J. Chem. Phys.* **81** 5833(1984); M. H. Kalos and F. Pederiva, *Phys. Rev. Lett.* **85** 3547(2000);
- [26] R. P. Feynman and A. R. Hibbs, in *Quantum Mechanics and Path Integrals* Ed. McGraw-Hill, (1965), p. 292-293.

Chapter 3

Polarization energy of two-dimensional ^3He

In this chapter, the subject under study is a system of two-dimensional ^3He ($2d\ ^3\text{He}$) in a wide range of densities in the liquid region and up to freezing. This subject is of interest because, as it has been shown in Ref. [1], a pure $2d\ ^3\text{He}$ system is a good approximation of a quasi-two-dimensional ^3He sample. Such system can be experimentally realized over a wide range of liquid densities by adsorbing ^3He on a variety of preplated graphite substrates[2, 3, 4]. Regarding the effective mass m^* and the spin susceptibility χ/χ_0 , the system behaves in good approximation like a perfect Fermi liquid[1]: the enhancement of χ/χ_0 increases with the density and m^* is consistent with a divergence near freezing density. This behavior at freezing has been interpreted[4] as a signature of a Mott transition leading to an insulating crystal. Theoretical studies[5], however, suggest that the singularity of m^* and freezing could not have the same origin and the freezing density is influenced by the preplated substrate. In this context, it is relevant the study of the effect of correlations without any effect induced by the external potential of the substrate.

Bulk $2d\ ^3\text{He}$ is interesting also from the theoretical point of view because, being a strongly interacting system at high densities, it provides a severe test case for microscopic calculations[6]. Some of the most powerful tools to study strongly interacting systems are QMC methods. The so-called fixed-node (FN) approximation[7], used in most Fermionic QMC calculations, however, has been argued to give a significant bias in the polarization energy of three-dimensional liquid ^3He [8] at high density. We have thus performed QMC simulations beyond the FN level, following a formally exact method[9] that is referred here as *Fermionic Correlations* (FC). With both the FN and FC methods we have calculated the ground-state energy per particle $e = \frac{E}{N}$ of the $2d\ ^3\text{He}$ liquid at zero temperature as a function of the number density ρ and the spin polarization ζ .

The FC method is slightly different from the well known transient estimate (TE) technique[10], the basic idea is to perform simulations relying on the basic Hamiltonian in an enlarged, unphysical space of states of any symmetry, including those with Fermi and Bose statistics. The ground state energy of the physical fermionic ^3He is considered as an excitation energy of the absolute bosonic ground state, which

is sampled exactly with QMC. In this approach one ‘trades’ (in a sense which we will explain below) the sign problem faced by TE[10] for the analytic continuation needed to extract excitation energies from suitable imaginary–time correlation functions. A mixed approach, devised to ease detection of the asymptotic convergence of TE by a Bayesian analysis of imaginary–time correlation functions, was proposed By Caffarel and Ceperley[11].

We compared our results also with a previous FN QMC calculation[12] that however is limited to low densities and only considers the paramagnetic fluid phase. We find indeed that the FN level of the theory and the exact calculation predict a qualitatively different behavior. This is rather expected because the accuracy of the FN approximation in the high density regime is questionable[8]. In fact, within FN the system becomes ferromagnetic well before crystallization takes place upon increasing the density, whereas the unbiased calculation shows that the spin polarization of the fluid is preempted by freezing, as observed experimentally. From the estimated curve $e(\zeta)$ we obtain a spin susceptibility enhancement in quantitative agreement with the available measurements.

3.0.1 QMC simulation

We simulate N particles with the mass m_3 of ^3He atoms, interacting with the HFDHE2 pair potential[13] in periodic boundary conditions, which is the most accurate two–body potential for Helium systems[14]. The simulation box, of area Ω , is a square of side L for the liquid phase; for the solid it is a rectangle which accommodates a triangular lattice. The Hamiltonian is

$$\hat{H} = -\frac{\hbar^2}{2m_3} \sum_{i=1}^N \nabla_i^2 + \sum_{i<j=1}^N v(\vec{r}_i - \vec{r}_j) \quad (3.1)$$

The simulations of the bosonic ^3He were made with the SPIGS technique, using the Pair Product approximation for the propagator at short imaginary times. For this system, we have verified that, using a Shadow Wave Function, a projection time of $\tau = 0.2 \text{ K}^{-1}$ is enough to yield an accurate description of the ground state. As for the time–step, we used $\delta\tau = 1/160 \text{ K}^{-1}$ and verified that it is small enough to be an accurate approximation.

Fixed–Node approach

The fixed–node approximation[7] is one of the most commonly used approaches in the QMC simulation of Fermi systems. FN stochastically solves the imaginary–time Schrödinger equation subject to the boundary conditions implied by the nodal structure of a given trial function Ψ_T . This approach gives a rigorous upper bound to the ground state energy, which often turns out to be extremely accurate.

For a given spin polarization, i.e. considering N_\uparrow spin-up and $N_\downarrow = N - N_\uparrow$ spin-down ^3He atoms, Ψ_T is chosen of the form

$$\Psi_T(\mathcal{R}) = \mathcal{D}(\mathcal{R}_\uparrow)\mathcal{D}(\mathcal{R}_\downarrow)\Psi_J(\mathcal{R})\chi_\zeta \quad (3.2)$$

where $\mathcal{R} \equiv (\vec{r}_1, \dots, \vec{r}_N)$, $\mathcal{R}_\uparrow \equiv (\vec{r}_1, \dots, \vec{r}_{N_\uparrow})$, $\mathcal{R}_\downarrow \equiv (\vec{r}_{N_\uparrow+1}, \dots, \vec{r}_N)$, and the whole dependence on the spin degrees of freedom is contained in χ_ζ , a spin eigenfunction for the given polarization

$$\zeta = \frac{N_\uparrow - N_\downarrow}{N} \quad , \quad (3.3)$$

The Jastrow factor,

$$\Psi_J(\mathcal{R}) = \prod_{i < j} \exp\left(-\frac{1}{2}u(|\vec{r}_i - \vec{r}_j|)\right), \quad (3.4)$$

describes pair correlations arising from the interaction potential; we use a simple pseudopotential of the McMillan form $u(r) = (b/r)^5$. Finally, the simplest form of the antisymmetric factors $\mathcal{D}(\mathcal{R}_{\uparrow,\downarrow})$ is in the form of Slater Determinants of plane waves:

$$\mathcal{D}(\mathcal{R}_{\uparrow,\downarrow}) = \det\left(\left\{\exp(i\vec{k}_i \cdot \vec{r}_j)\right\}_{i,j}\right) \quad (3.5)$$

More accuracy in the FN results is achieved by introducing also backflow correlations[15] via quasi-particles vector positions:

$$\begin{aligned} \mathcal{D}(\mathcal{R}_{\uparrow,\downarrow}) &= \det\left(\left\{\exp(i\vec{k}_i \cdot \vec{x}_j)\right\}_{i,j}\right) \quad (3.6) \\ \vec{x}_j &\stackrel{def}{=} \vec{r}_j + \sum_{i \neq j=1}^N \eta(|\vec{r}_j - \vec{r}_i|)(\vec{r}_j - \vec{r}_i). \end{aligned}$$

For the backflow correlation function $\eta(r)$ we adopt the simple form:

$$\eta(r) = Ae^{-B(r-C)^2} \quad . \quad (3.7)$$

We will refer to the two choices respectively as plane waves fixed-node (PW-FN) and backflow fixed-node (BF-FN). For each density, the variational parameters b , A , B and C are optimized using correlated sampling[16] at $\zeta = 0$, and left unchanged at different polarizations. The backflow parameters, for each density, are shown in Table 3.1

Part of the bias related to the finite size of the simulated system arises from shell effects in the filling of single-particle orbitals[17]. This bias can be substantially reduced adopting twisted boundary conditions[17], i.e. choosing \vec{k} appearing in (3.5) and (3.6) inside the set:

$$\vec{k}_{\vec{n}} = \frac{2\pi\vec{n} + \vec{\theta}}{L} \quad (3.8)$$

Table 3.1: Backflow parameters used for each density

Density (\AA^{-2})	A	B (\AA^{-1})	C (\AA)
0.020	1.90393	0.117865	-1.89877
0.050	1.124523	0.112559	-0.94888
0.060	1.017654	0.147372	-0.51614

where \vec{n} is an integer vector, L is the side of the simulation box Ω and $\vec{\theta}$ is a *twist parameter* $\theta_i \in [0, \pi]$ which, at the end of the calculations, is averaged over.

In the solid phase, quantum exchanges are strongly suppressed and the energy difference between a Fermionic and a Bosonic crystal is negligibly small for the purpose of locating the liquid–solid transition. We will therefore replace the energy of ^3He with that of a fictitious bosonic Helium of mass m_3 , which can be calculated exactly[18, 19, 20]. The small error incurred by such replacement is bound by the difference between the fermionic Fixed–Node (FN) energy and the unbiased bosonic energy. This difference, calculated[21] as a check at the melting density where it is expected to be largest, is indeed in the sub–milliKelvin range.

We stress that we actually made a particular choice of trial wave functions; the obtained results depend on such a choice: when we will speak about ‘fixed–node level’ of the theory or about ‘fixed–node approximation’ we will always implicitly refer to the above mentioned trial wave functions. Naturally it could be possible to improve the fixed–node results using more sophisticated wave functions; instead, we have chosen to follow another way with the FC method; this method is in principle exact and does not depend on a particular choice of the wave function.

Fermionic correlations approach

As mentioned before, for the fluid phases the FN approximation may not be accurate enough, particularly at high density where correlations are stronger and the energy balance between different polarization states is more delicate.

In order to go beyond the FN level and obtain accurate data, we use the FC technique[9] which is in principle exact, even if limited to small system sizes.

The idea, with similarities with the transient estimate formalism[10, 11], is that of viewing (3.1) as an operator acting inside the Hilbert space $\mathcal{H}(N) \equiv (L^2(\Omega))^{\otimes N}$, that has no constraints on spin and statistics: one can use Quantum Monte Carlo to sample the lowest energy eigenfunction $\psi_0(\mathcal{R})$ of \hat{H} among the states of both Bose and Fermi symmetry.

It is known [22] that ψ_0 must share the *Bose symmetry* of the Hamiltonian, so that:

$$E_0^B \equiv \frac{\langle \psi_0 | \hat{H} \psi_0 \rangle_{\mathcal{H}(N)}}{\langle \psi_0 | \psi_0 \rangle_{\mathcal{H}(N)}} \quad (3.9)$$

is the Ground State energy of a fictitious system of N Bosons of mass m_3 interacting via the potential $v(r)$.

The connection between the fermionic energies is retrieved in the following way: let us fix a spin polarization, it is surely a good quantum number since the basic Hamiltonian is spin-independent. As discussed in Ref. [9], if we are able to define an operator $\hat{\mathcal{A}}_F$ such that, inside $\mathcal{H}(N)$,

$$\psi_F(\mathcal{R}) = \left(\hat{\mathcal{A}}_F \psi_0 \right) (\mathcal{R}) \quad (3.10)$$

has *non-zero overlap* with the configurational part of any *exact fermionic* Ground State of \hat{H} for the given ζ , we can define the *imaginary-time correlation function*:

$$\mathcal{C}_F(\tau) \equiv \frac{\langle \psi_0 | \left(e^{\tau \hat{H}} \hat{\mathcal{A}}_F^\dagger e^{-\tau \hat{H}} \right) \hat{\mathcal{A}}_F \psi_0 \rangle_{\mathcal{H}(N)}}{\langle \psi_0 | \psi_0 \rangle_{\mathcal{H}(N)}}, \quad \tau \geq 0 \quad (3.11)$$

which can be straightforwardly evaluated in a bosonic QMC simulation[18, 20, 23]. This is readily made because the evaluation of Eq. (3.11) at a certain discrete imaginary time $\tau_l = l\delta\tau$ can be done with the evaluation of the Slater determinant \mathcal{A}_F on two time sectors located at different imaginary times $\tau_0 = m\delta\tau$ and $\tau_1 = (m+l)\delta\tau$. The actual calculation has been done using the Path Integral Ground State with Shadow Wave Functions (SPIGS) that has been described in chapter 2. The lowest energy contribution in $\mathcal{C}_F(\tau)$ provides the *exact gap* between the fermionic and the bosonic ground states of the two-dimensional Fermi liquid; this can be readily seen by formally expressing (3.11) on the basis $\{\psi_n\}_{n \geq 0}$ of eigenvectors of \hat{H} corresponding to the eigenvalues $\{E_n\}_{n \geq 0}$:

$$\mathcal{C}_F(\tau) = \sum_{n=0}^{+\infty} e^{-\tau(E_n - E_0^B)} \frac{|\langle \hat{\mathcal{A}}_F \psi_0 | \psi_n \rangle_{\mathcal{H}(N)}|^2}{\langle \psi_0 | \psi_0 \rangle_{\mathcal{H}(N)}} \quad (3.12)$$

A quite natural choice[9] is to define $\hat{\mathcal{A}}_F$ borrowing suggestions from the form of the trial wave function for the FN calculation, i.e.:

$$\left(\hat{\mathcal{A}}_F \psi_0 \right) (\mathcal{R}) \stackrel{def}{=} \mathcal{D}(\mathcal{R}_\uparrow) \mathcal{D}(\mathcal{R}_\downarrow) \psi_0(\mathcal{R}) \quad (3.13)$$

where we can choose either the definition (3.5) of \mathcal{D} or the definition (3.6). We will refer to such choices simply as the plane waves fermionic correlations (PW-FC) and the backflow fermionic correlations (BF-FC). Naturally the final results for the Bose-Fermi gap should coincide within statistical uncertainties, and the actual comparison can be a good test for the robustness of the approach.

We observe that the sign problem is not really avoided as it manifests itself in two ways: on one hand poor choices of the wave functions appearing in the correlation functions imply the necessity to consider very large τ regions of the correlation function; on the other hand, since the gap energy is an extensive quantity, the exponential decay of the correlation functions increases in the limit $N \rightarrow \infty$, making impractical the extraction of meaningful information.

3.0.2 The Bosonic System

Figure 3.1 shows the state equation of both the solid and the liquid phases of the system; in Table 3.2 the values of the energies at each density are shown.

Table 3.2: Potential (E_{pot}), Kinetic (E_{kin}) and Total (E_{tot}) Energy per particle of “bosonic” $2d$ ^3He at each studied density. The system has $N = 26$ atoms in a square box of side $L = (N/\rho)^{1/2}$. Tail corrections to the potential energy to account for the finite size of the system have been applied only to E_{tot}/N ; instead, for a more direct comparison, E_{pot}/N is exactly the output of the simulations.

Density (\AA^{-2})	E_{pot}/N (K)	E_{kin}/N (K)	E_{tot}/N (K)
0.015	-1.176 (5)	1.107 (7)	-0.10 (1)
0.020	-1.640 (6)	1.58 (1)	-0.10 (2)
0.025	-2.150 (6)	2.12 (1)	-0.09 (2)
0.030	2.75 (2)	-2.709 (9)	-0.04 (2)
0.035	3.47 (2)	-3.318 (7)	0.06 (4)
0.040	4.29 (2)	-3.97 (1)	0.22 (4)
0.045	5.26 (2)	-4.71 (1)	0.45 (4)
0.050	6.35 (2)	-5.47 (1)	0.78 (4)
0.055	7.62 (3)	-6.28 (1)	1.25 (4)
0.060	9.16 (3)	-7.12 (1)	1.86 (4)
0.065	10.81 (3)	-7.98 (2)	2.67 (5)
0.070	12.75 (4)	-8.91 (2)	3.66 (7)
0.075	15.00 (3)	-9.94 (3)	4.77 (6)
0.080	17.27 (4)	-10.84 (2)	6.12 (7)
0.085	19.70 (4)	-11.65 (2)	7.81 (7)
0.090	22.32 (5)	-12.28 (3)	9.90 (9)
0.095	25.19 (6)	-12.72 (3)	12.5 (1)
0.100	28.31 (7)	-12.88 (3)	15.7 (1)

The agreement with data in Ref. [12] is good (Fig. 3.2), although the comparison must take into account the slight difference coming from the interaction potential used in our simulation (Aziz ‘79, Ref. [13]), and that used in Ref. [12] (Aziz ‘87, Ref. [24]). This difference, $E_{87} - E_{79}$, depends on the density ρ and can be estimated with the following computation if one neglects the dependence of the radial distribution function, $g(r)$, on the interaction potential $v(r)$:

$$E_{87} - E_{79} \simeq \pi\rho \int_0^\infty dr [v_{87}(r) - v_{79}(r)]g(r) \quad (3.14)$$

With the Maxwell construction obtained from the polynomial fit of the equation of state in the liquid and the solid phase (see Table 3.3 for the fitting parameters), the freezing point is estimated at a density of 0.069\AA^{-2} , while the melting point is approximately at a density of 0.073\AA^{-2} .

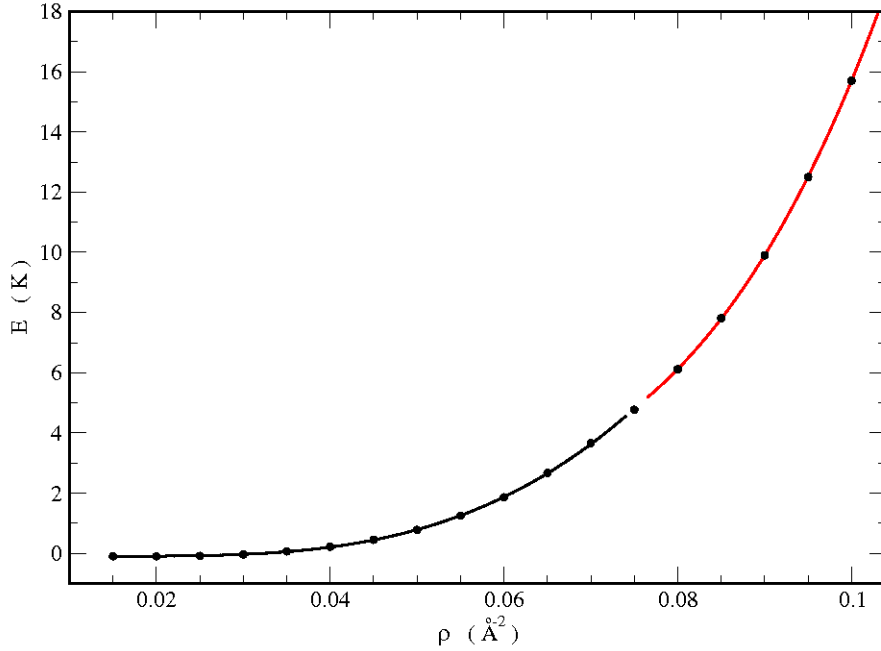


Figure 3.1: State equation of the bosonic system used to calculate the correlation functions. The lines represent a fit of the data in both the solid (red line) and the liquid (black line) phase. The error bars are hidden inside the symbols. These results are in good agreement with Ref. [12]

Table 3.3: Fitting parameters for the solid and the liquid phases. The polynomial that has been fitted to the data is of the form $E/N = a\rho^5 + b\rho^4 + c\rho^3 + d\rho^2 + e\rho$.

Phase	a ($\text{K}\text{\AA}^{10}$)	b ($\text{K}\text{\AA}^8$)	c ($\text{K}\text{\AA}^6$)	d ($\text{K}\text{\AA}^4$)	e ($\text{K}\text{\AA}^2$)
liquid	1745632.16048	-66748.2524	9553.61311	-61.70852	-7.51343
solid	3063129.8758	-532201.7865	58695.29501	-2598.78493	57.3547

High accuracy in these computations is very important for two reasons: first, even though the bosonic system is unphysical in itself, its energy is required for the evaluation of the energy of the real ${}^3\text{He}$ system, and finally, high quality of data is essential for a successful inversion of the Laplace Transform.

3.0.3 The Twist Averages

One of the main differences between the TE and the FC methods is the way in which twisted boundary conditions (TBC) are used. In FC, TBC are not applied whenever

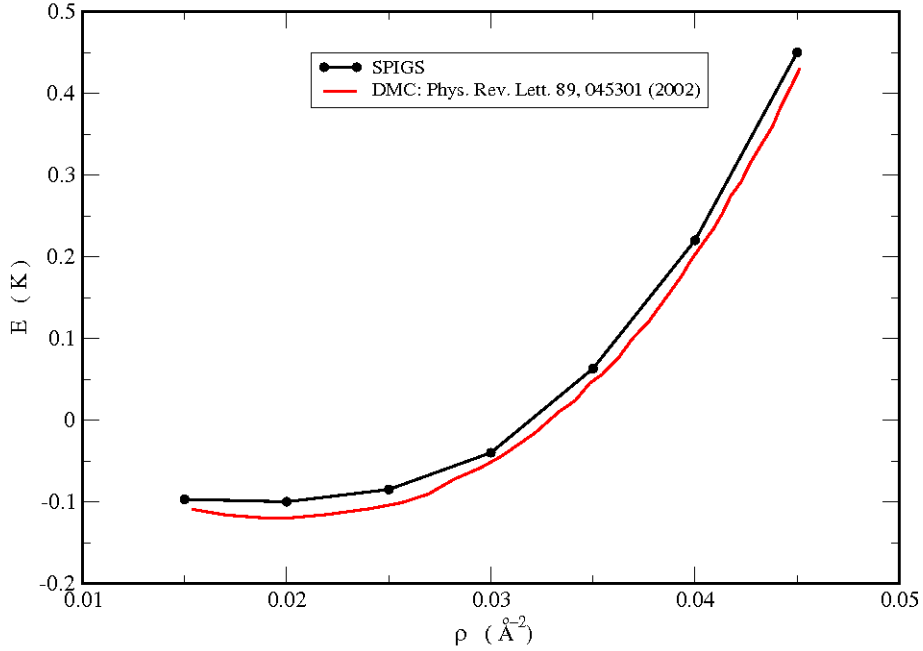


Figure 3.2: Comparison between the equation of state of mass-3 bosons obtained with the Diffusion Monte Carlo and that obtained with the SPIGS. The systematic difference of roughly 0.03K is due to the different interaction potential that has been employed.

a particle crosses a boundary of the simulation box but are taken into account during the evaluation of the correlation function; more precisely, the twist angle is introduced during the preparation of the Slater matrices, namely:

$$S_{N_{\uparrow}} = \begin{pmatrix} e^{i\left(\vec{k}_1 + \frac{\theta_1}{L}\right) \cdot \vec{r}_1} & \dots & e^{i\left(\vec{k}_1 + \frac{\theta_1}{L}\right) \cdot \vec{r}_{N_{\uparrow}}} \\ \dots & \dots & \dots \\ e^{i\left(\vec{k}_{N_{\uparrow}} + \frac{\theta_1}{L}\right) \cdot \vec{r}_1} & \dots & e^{i\left(\vec{k}_{N_{\uparrow}} + \frac{\theta_1}{L}\right) \cdot \vec{r}_{N_{\uparrow}}} \end{pmatrix} \quad (3.15)$$

where θ_1 is a given twist angle and N_{\uparrow} is the number of spin up particles; naturally the same applies for the spin down particles. The coordinates \vec{r}_i can be, like in the FN case, with or without backflow correlations, in the latter case we place $\vec{r}_i = \vec{r}_i^{abs}$, where the superscript means that the coordinates of the i -th particle are obtained without invoking the periodic boundary conditions (pbc); this is done in the following way: each particle has two coordinate systems, the first are coordinates inside the simulation box, which we refer here with the superscript “pbc”, these are obtained by

invoking the pbc whenever the particle crosses a boundary of the simulation box, the second coordinate system is made with absolute coordinates that are not constrained in the simulation cell: if a particle moves from a position \vec{x}_1^{pbc} to a position \vec{x}_2^{pbc} , its absolute coordinate changes accordingly $\vec{x}_2^{abs} = \vec{x}_1^{abs} + (\vec{x}_2^{pbc} - \vec{x}_1^{pbc})_{pbc}$, where the last subscript means that the displacement $(\vec{x}_2^{pbc} - \vec{x}_1^{pbc})$ is calculated with periodic boundary conditions. The other choice for \vec{r}_i is with backflow correlations,

$$\vec{r}_i = \vec{r}_i^{abs} + \sum_{j=1; j \neq i}^N \eta \left(|\vec{r}_j - \vec{r}_i|_{pbc} \right) (\vec{r}_j - \vec{r}_i)_{pbc} \quad (3.16)$$

where $\eta(r)$ is defined in Eq. (3.7).

Another delicate point in the construction of the Slater matrix (3.15) is the choice of the values $\{\vec{k}_n + \theta_1/L\}_{n=1}^{N_\uparrow}$; for $\theta_1 = 0$ the choice would reduce to the wave vectors $\{\vec{k}_n\}$ inside the Fermi surface corresponding to N_\uparrow particles, however it may not be the case for certain choices of the twist angle θ_1 ; the procedure to follow is that, for a given twist angle θ_1 , the wave vectors are those that give the first N_\uparrow lowest energies E_n ,

$$E_n = \lambda \left| \vec{k}_n + \frac{\theta_1}{L} \right|^2 \quad (3.17)$$

where $\lambda = \hbar^2/(2m_{3He})$.

For the evaluation of a single energy gap, 15 different correlation functions have been used for every Monte Carlo block. Each correlation function corresponds to a twist angle. This choice leads to a uniform distribution of the twist angles in an area of the first Brillouin zone of the simulation box that contains no symmetries. This area is shown in Fig. 3.0.3.

Following the prescription in Eq. (3.13), once the Slater matrices have been prepared, the Slater determinant has to be computed. This operation will be invoked many times during a Monte Carlo step and an efficient algorithm is advised. Our choice has been the LU decomposition that writes a matrix A as a product of an upper triangular matrix U and a lower triangular matrix L . The determinant of A is then the product of the diagonal elements of U and L . The LU decomposition is extensively described in Ref. [25] for real matrices, the case of complex matrices is easily generalizable: from the algorithm in Ref. [25] it is enough to redefine the matrices L and U to complex matrices $L = \Re L + \Im L$ and $U = \Re U + \Im U$; all the algebraic operations have then to be ambiented in the complex field and the resulting determinant will be a complex number. A complex number for the Slater determinant will yield a complex imaginary time correlation function; however, due to Eq. (3.12), this correlation function will have, on average, an imaginary part compatible with zero.

The procedure to obtain the polarization curves may be schematized in the following steps:

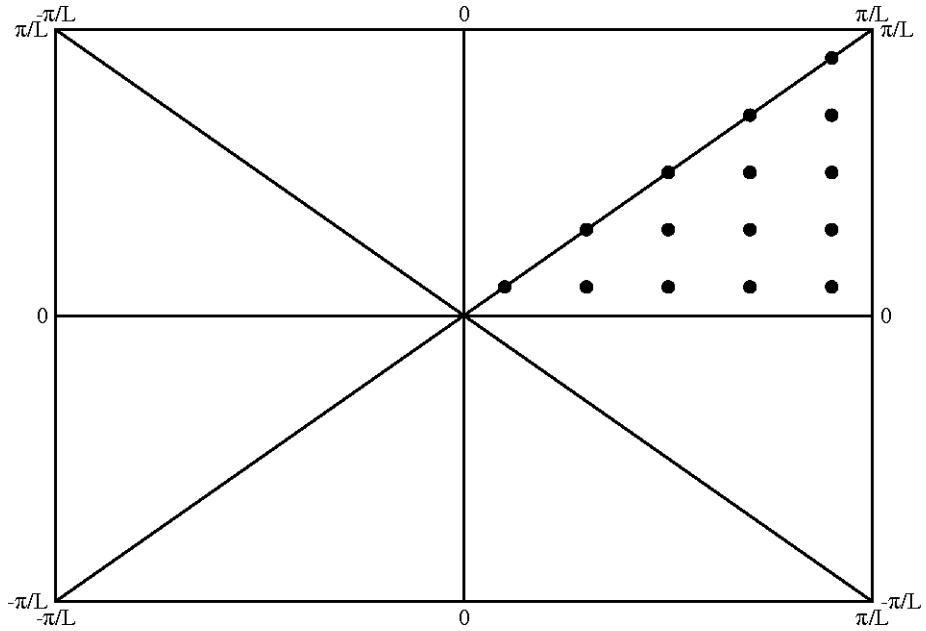


Figure 3.3: Schematic representation of the chosen twist angles in the first Brillouin zone of the simulation box. The simulation box is a square of late L .

- Consider all of the correlation functions corresponding to a given twist angle that have been computed for each block of the simulation. Calculate the error using the central limit theorem.
- From the previously calculated error, infer the error of the correlation function relative to a single block.
- Apply the inversion method and localize the position of the first peak. In this work we used the GIFT method but we obtained compatible results also with a fit of the long imaginary-time part of the imaginary-time correlation function.
- Repeat the previous steps for every twist angle and hence perform a weighted average according with the symmetries of the first Brillouin zone. This yields a single-block estimate of the energy gap.
- The final energy-gap value for a given polarization is the block average of the single-block estimates that have thus been obtained.

The described procedure has been applied for every polarization. This implies thousands of Laplace transforms to be inverted with relative peaks to be localized; it

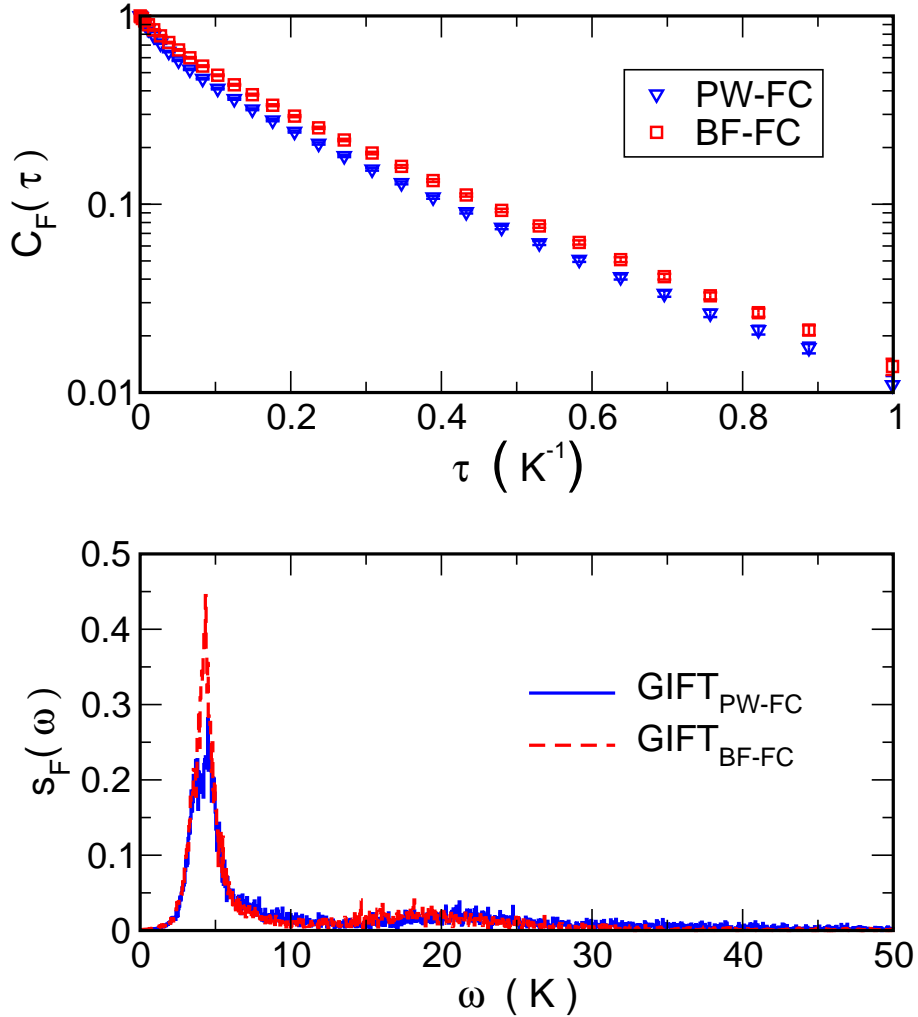


Figure 3.4: (Color online) Upper panel: Imaginary time correlation functions, $\mathcal{C}_F(\tau)$, corresponding to the two different choices of the operator in (3.13). Lower panel: reconstructed spectral functions $s_F(\omega)$ obtained with the GIFT method.

is a task that is unlikely to be done manually and an automated procedure was implemented. However, particular attention must be paid in the automatic localization of the peaks in order to avoid false values and thus systematic errors. Possibly, different localization algorithms must be applied and a check by eye of a random selection of the inversion results is highly advised. We would like to emphasize again that the most delicate part of this method lies in the numerical inversion of the Laplace transform of the correlation functions but also in the data analysis of the results.

3.0.4 Analytic Continuation

Once we have achieved a QMC evaluation of $\mathcal{C}_F(\tau)$, the information about the Bose-Fermi gap $\Delta_{BF} = E_0 - E_0^B$ is contained in the resulting correlation functions. The

results for $\mathcal{C}_F(\tau)$ appear as simple smooth decreasing functions, whose values can be evaluated only in correspondence with a finite number of imaginary–time values, say $\{\tau_0, \tau_1, \tau_2, \dots, \tau_l\}$; moreover the data are perturbed by unavoidable statistical uncertainties. The Bose–Fermi gap Δ_{BF} is thus hidden inside the sets of limited and noisy data. How can we extract it?

In the upper panel of Fig. 3.4 we show two imaginary time correlation functions $\mathcal{C}_F(\tau)$, respectively a PW–FC and a BF–FC, corresponding to the same spin polarization and twist parameter. The long– τ tails of the two curves tend towards a linear behavior (in logarithmic scale) with the same slope, and this is a general feature shared by all the functions we have evaluated. This indicates that, because of the finite–size of the system (and selection rules on the total momentum), the fermionic spectrum has a sufficiently defined gap, i.e. the lowest–energy term $\exp(-\Delta_{BF}\tau)$ in the correlation function (3.12) appears to be quite well resolved with respect to contributions from higher fermionic energies. The difference between the two curves (in particular the rigid shift between their asymptotic tails) arises from the spectral weight of the Ground State contribution, which is higher when backflow correlations are taken into account, as expected.

In this favorable situation, the Bose–Fermi gap can be reliably extracted by simply fitting an exponential to the long–time tail of the correlation function.

This key result is strongly supported by a more sophisticated approach, which evaluates Δ_{BF} by performing the full Laplace transform inversion of $\mathcal{C}_F(\tau)$, i.e. solving

$$\mathcal{C}_F(\tau) = \int_0^{+\infty} d\omega e^{-\tau\omega} s_F(\omega) \quad , \quad (3.18)$$

for the unknown *spectral function* $s_F(\omega)$. Recently a new method, the genetic inversion via falsification of theories (GIFT) method[26], has been developed to face general inverse problems and in particular it has allowed to reconstruct the excitation spectrum of superfluid ^4He starting from QMC evaluations of the intermediate scattering function in imaginary–time[26]; the results were in close agreement with experimental data[26]. Moreover the method has allowed to extract also multiphonon energies with a good accuracy level. When applied to the two curves depicted in the upper panel of Fig. 3.4, we find the two spectral functions in the lower panel of Fig. 3.4; it is apparent that the lowest– ω peak is indeed well resolved from higher–energy contributions. Crucially, its position does not depend on the actual choice of the operator $\hat{\mathcal{A}}_F$, and it is in excellent agreement with the smallest decay constant found by the simple exponential fit. The spectral weight instead is different, consistently with the differences between PW–FC and BF–FC.

3.0.5 Results

We fit a fifth order polynomial to the density dependence of the energies of the triangular crystal and of the paramagnetic and the ferromagnetic fluids, listed in Table 3.0.5. The resulting equation of state of two–dimensional ^3He is shown in Figure 3.0.5. With the fermionic correlations method, we find a transition between

Table 3.4: The equations of state of ${}^3\text{He}$ for the paramagnetic fluid and the solid (solid lines in Figure 3.0.5) are of the form $\alpha_1\rho + \alpha_2\rho^2 + \alpha_3\rho^3 + \alpha_4\rho^4 + \alpha_5\rho^5$. This Table lists the values of the parameters α_i , with lengths in \AA .

	liquid	solid
α_1	21.23782	57.35474
α_2	-1344.413	-2598.784
α_3	45093.37	58695.29
α_4	-569306.0	-532201.7
α_5	4383507	3063129

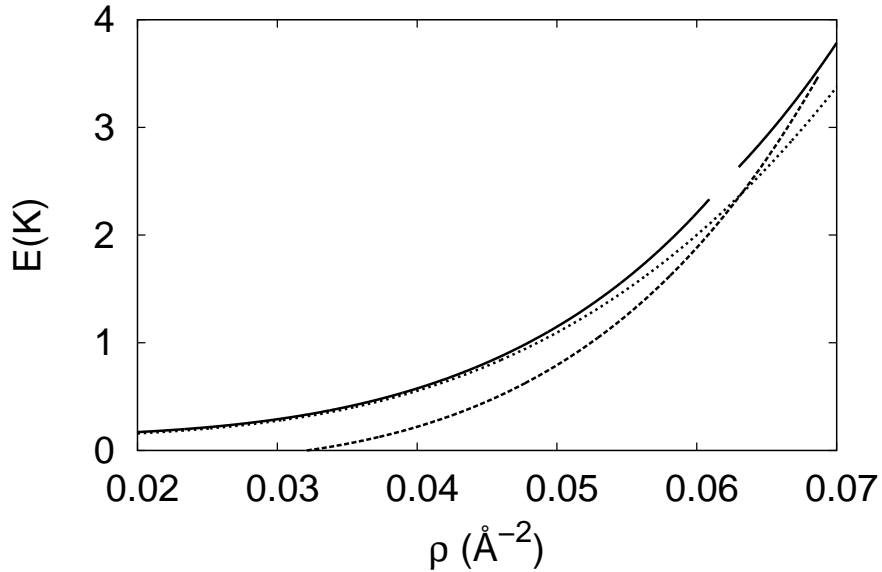


Figure 3.5: Equation of state of ${}^3\text{He}$ in two dimensions. Solid line (broken across the coexistence region): liquid and solid ${}^3\text{He}$; dashed line: mass-3 boson fluid; dotted line: liquid ${}^3\text{He}$, after Ref. [12]. The latter is only reliable at low densities.

the paramagnetic fluid and the triangular crystal around $\rho = 0.061 \text{ \AA}^{-2}$, with a narrow coexistence of about 0.002 \AA^{-2} , while the ferromagnetic fluid is never stable (see Table 3.5). The obtained solidification density can not be directly compared with experimental data since we are studying a model of an ideal $2d$ -system. It could be interesting in future calculations to consider an adsorbing external potential representing the interaction of the ${}^3\text{He}$ atoms with a substrate.

The energy of the bosonic mass-3 liquid is also shown. This fictitious system, simulated to extract the PW-FC and BF-FC energies, crystallizes at $\rho = 0.069 \text{ \AA}^{-2}$. The freezing density of ${}^3\text{He}$ is considerably higher than the highest density simulated in Ref. [12]. Correspondingly, the equation of state given in Ref. [12] is only reliable at relatively low density. In particular, while it is only slightly below our results for

Table 3.5: Ground state energy of ^3He in K, calculated by the FC method for the fluid phases and assumed to equal the bosonic energy for the solid phase.

density	liquid $\zeta = 0$	liquid $\zeta = 1$	solid
0.020	0.1707(18)	0.3218(25)	
0.045	0.8168(86)	0.9075(86)	
0.050	1.1500(81)	1.2123(88)	
0.055	1.5972(93)	1.6574(91)	
0.060	2.2069(68)	2.2493(54)	2.2506(54)
0.065	3.0065(73)	3.0359(45)	2.9195(26)
0.070	4.0644(33)	4.0915(34)	3.7878(35)
0.075			4.8728(44)
0.080			6.2445(35)
0.085			7.9589(39)
0.090			10.0661(46)
0.095			12.6739(39)
0.100			15.8536(45)

$\rho \lesssim 0.045 \text{ \AA}^{-2}$ as a consequence of the difference of interparticle potential adopted[24], it becomes even lower than the bosonic equation of state near the melting density, by an amount far larger than what could be due to the different employed potential.

The treatment of the spin polarization state requires a special care[27, 8, 28, 9]. In contrast to Ref. [12], we find that the BF–FN energy can be significantly higher than the unbiased Fermionic correlations (FC) energy. Starting from negligible values at low density, the BF-FN error quickly increases approaching the strongly correlated regime. As expected[8], it is larger for the paramagnetic than for the ferromagnetic fluid. This happens, because the available variational wave function for ferromagnetic states are more accurate than those for paramagnetic states. These findings are exemplified in Figure 3.6. The inadequacy of the BF–FN is striking in the phase diagram: Figure 3.7 shows that BF–FN incorrectly predicts a transition to a ferromagnetic fluid well before crystallization takes place. Such a transition is also evident from Figure 3.8, which shows the BF–FN results for the polarization energy $e(\zeta)$ at various densities. The unbiased results, shown in Figure 3.9, display instead a paramagnetic behavior even in a metastable fluid phase well beyond the freezing density.

From the FC polarization energy $e(\zeta)$ we can estimate the spin susceptibility enhancement χ/χ_0 . Assuming a quadratic dependence over the whole polarization range, which is generally consistent with the data of Figure 3.9, we find an excellent agreement with the measured susceptibility. Figure 3.10 shows the comparison between the calculated χ/χ_0 and the experimental data. We display only the results obtained in the second layer of ^3He on graphite[3] since they extend to the highest density in the fluid phase, but experiments carried on with differently preplated substrates lead to equivalent results in their respective density ranges. The agreement among the results obtained using different substrates induces us to expect that our

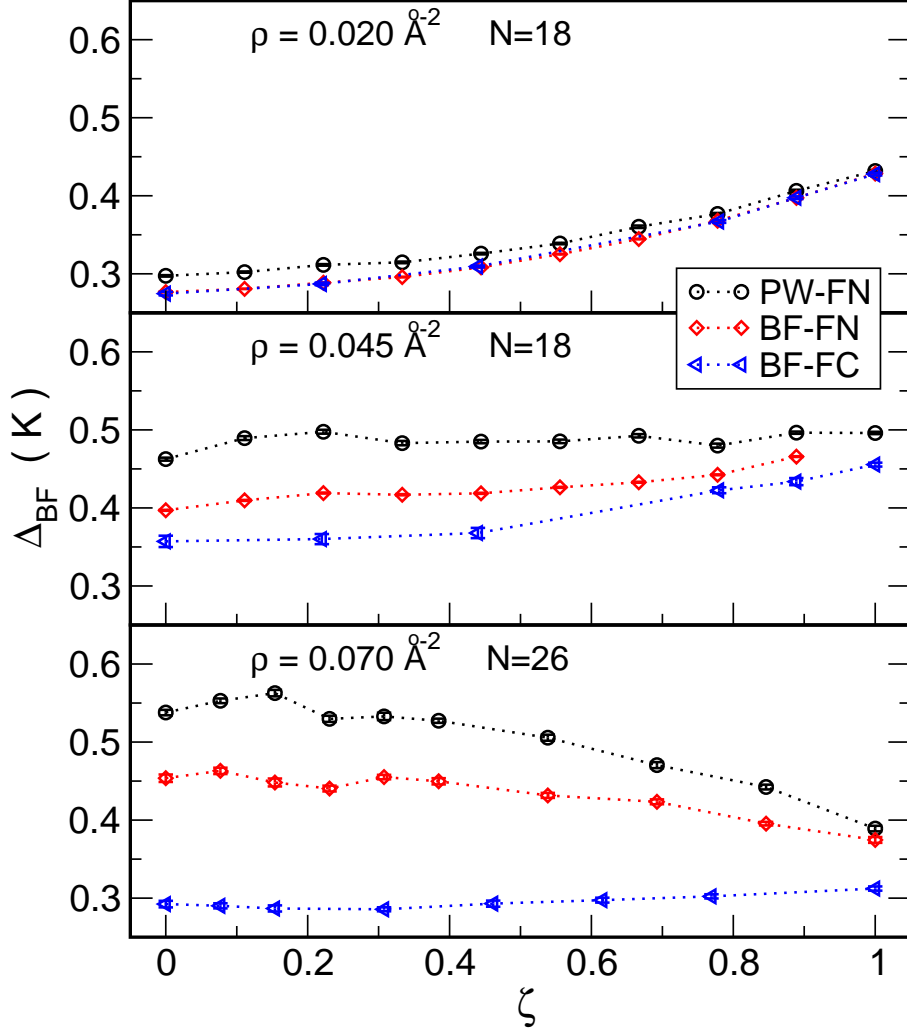


Figure 3.6: (Color online) Upper panel: Bose–Fermi gap, Δ_{BF} , as a function of the spin polarization, ζ , at density $\rho = 0.020 \text{ \AA}^{-2}$ evaluated via PW–FN, BF–FN, and BF–FC with $N = 18$ particles. Middle panel: Bose–Fermi gap, Δ_{BF} , as a function of the spin polarization, ζ , at density $\rho = 0.045 \text{ \AA}^{-2}$ evaluated via PW–FN, BF–FN, and BF–FC with $N = 18$ particles. Lower panel: Bose–Fermi gap, Δ_{BF} , as a function of the spin polarization, ζ , at density $\rho = 0.070 \text{ \AA}^{-2}$ evaluated via PW–FN, BF–FN, and BF–FC with $N = 26$ particles. The statistical uncertainties are below the symbols size.

ideal model actually captures the physical mechanisms underlying the behavior of χ/χ_0 .

The results for χ/χ_0 evaluated with BF–FN calculations diverge at a density around 0.050 \AA^{-2} , consistently with the BF–FN prediction of a phase transition taking place around the above mentioned density. The need for an exact QMC approach is thus witnessed by the failure of the BF–FN approximation to predict the lack of a polarization transition experimentally observed in the fluid phase, let alone an

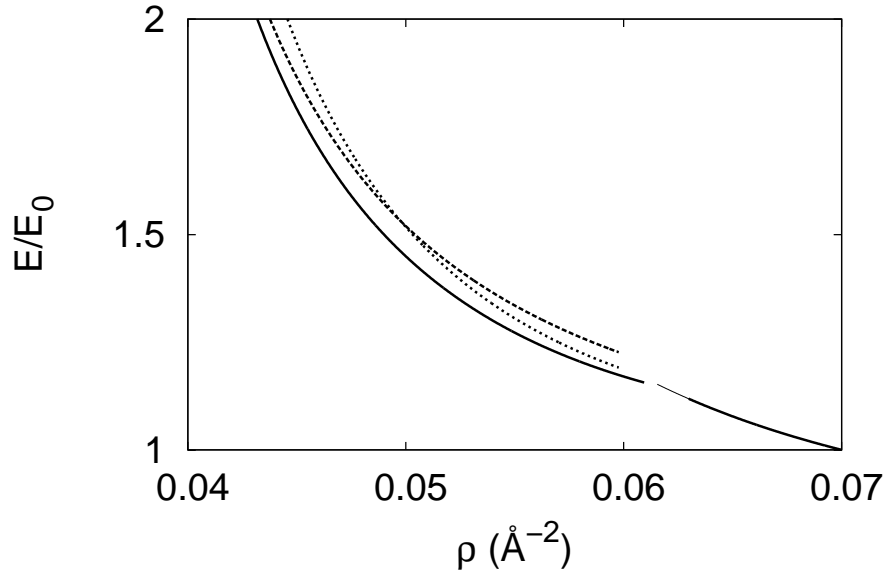


Figure 3.7: Unbiased FC versus Fixed-Node equation of state. Thick solid line (broken across the coexistence region): paramagnetic liquid and solid ${}^3\text{He}$ (FC); dashed line: paramagnetic liquid (FN); dotted line: ferromagnetic liquid (FN); the dashed and dotted lines terminate at the FN freezing density; thin solid line: energy of the solid, down to the FN melting density. For each density, the energy is relative to the energy E_0 of the mass-3 boson fluid.

accurate value for the spin susceptibility. We emphasize that in principle it is possible to improve the fixed node results working on the choice of the trial wave function. Our purpose in this work was to follow a methodology which is unbiased, that is independent on the choice of the wave function; such methodology gives access only to the energy and its derivatives. Here we have shown the improvements with respect to the results obtained with a particular fixed-node approximation that has already been used[12] for ${}^3\text{He}$.

In conclusion, we have calculated the equation of state and the polarization energy of ${}^3\text{He}$ in two dimensions by means of an unbiased QMC method. The system crystallizes into a triangular lattice from the paramagnetic fluid at a density of 0.061 \AA^{-2} , with a narrow coexistence region of about 0.002 \AA^{-2} ; the ferromagnetic fluid is never stable. From the polarization energy we obtain a spin susceptibility enhancement in excellent agreement with the experimental values.

We remark that, although the Fermionic correlation technique is in principle unbiased, to obtain the estimation of the Bose-Fermi gap one has to face an ill-posed inverse problem: the inversion of the Laplace transform at the presence of a limited set of noisy data; the quality of the results of the inversion procedure cannot be guaranteed *a priori*, in this work we have found empirically that the obtained correlation

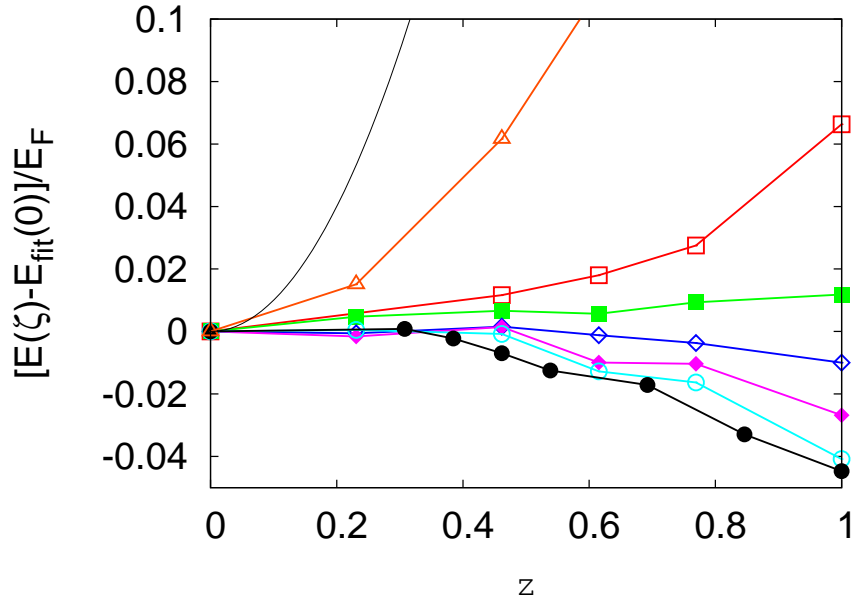


Figure 3.8: (Color online) Fixed-node results for the polarization energy $E(\zeta) - E_{\text{fit}}(0)$ relative to the Fermi energy E_F at $\rho = 0.020$ (open triangles), 0.045 (open squares), 0.050 (filled squares), 0.055 (open diamonds), 0.060 (filled diamonds), 0.065 (open circles), 0.070 (filled circles) \AA^{-2} , i.e. from top to bottom. The function $E_{\text{fit}}(\zeta)$ is a quadratic polynomial in ζ^2 fitted to the simulation data; the solid line is the density-independent result for non-interacting particles.

functions could be safely inverted obtaining robust results, which has been checked using different techniques.

Moreover, the estimation of the Bose-Fermi gap via the Fermionic correlation method is limited to relatively small systems: the present results are obtained with either 18 or (in most cases) 26 particles. While the size effect remains the main source of uncertainty of the present calculation, the agreement of the calculated and measured spin susceptibility suggests that finite-size errors are relatively small.

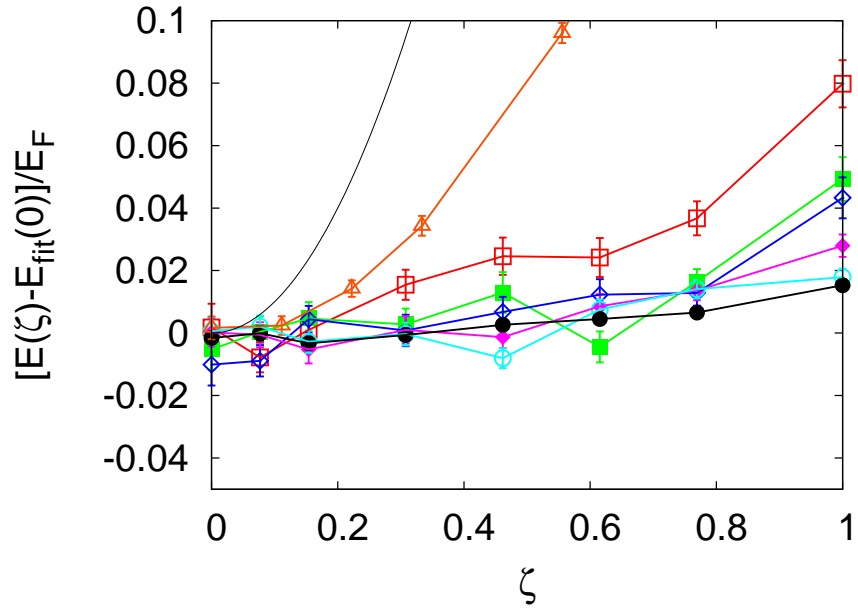


Figure 3.9: (Color online) Exact results for the polarization energy $E(\zeta) - E_{\text{fit}}(0)$ relative to the Fermi energy E_F at $\rho = 0.020$ (open triangles), 0.045 (open squares), 0.050 (filled squares), 0.055 (open diamonds), 0.060 (filled diamonds), 0.065 (open circles), 0.070 (filled circles) \AA^{-2} , in order of decreasing dispersion. The function $E_{\text{fit}}(\zeta)$ is a quadratic polynomial in ζ^2 fitted to the simulation data; the solid line is the density-independent result for non-interacting particles.

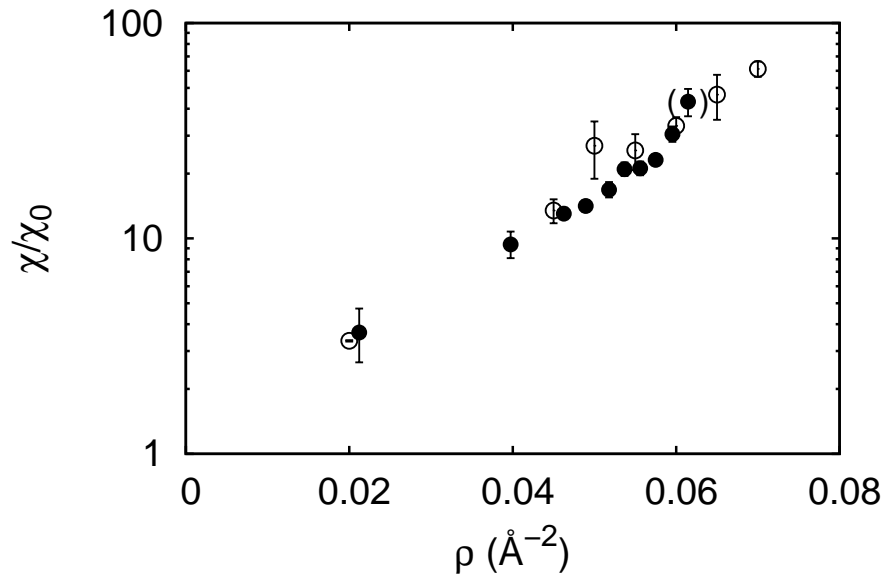


Figure 3.10: Enhancement of the spin susceptibility as a function of the density: (filled circles) as measured in the second layer of ${}^3\text{He}$ on graphite[3]; (open circles) as calculated assuming a quadratic dispersion over the whole polarization range in Fig. 3.9. The corresponding Fixed-node result from Fig. 3.8 would diverge at $\rho \simeq 0.050 \text{ \AA}^{-2}$.

Bibliography

- [1] P. A. Whitlock, G. V. Chester and B. Krishnamachari, *Phys. Rev. B*, **58**, 8704 (1998).
- [2] C. P. Lusher, B. P. Cowan, and J. Saunders, *Phys. Rev. Lett.*, **67**, 18 (1991).
- [3] K.-D. Morhard, C. Bauerle, J. Bossy, Yu. Bunkov, S. N. Fisher, and H. Godfrin, *Phys. Rev. B*, **53**, 2658 (1996).
- [4] A. Casey, H. Patel, J. Nyeki, B. P. Cowan, and J. Saunders, *Phys. Rev. Lett.*, **90**, 11 (2003).
- [5] J. Boronat, J. Casulleras, V. Grau, E. Krotscheck, and J. Springer, *Phys. Rev. Lett.*, **91**, 8 (2003).
- [6] H. M. Bohm, E. Krotscheck, M. Panholzer, H. Godfrin, H. J. Lauter, M. Meschke, *J. Low. Temp. Phys.*, **158**, 194-200 (2010).
- [7] P.J. Reynolds, D.M. Ceperley, B.J. Alder, and W.A. Lester, *J. Chem. Phys.* **77**, 5593 (1982).
- [8] M. Holzmann, B. Bernu and D. M. Ceperley, *Phys. Rev. B* **74**, 104510 (2006).
- [9] G. Carleo, S. Moroni, F. Becca, and S. Baroni, *Phys. Rev. B* **83**, 060411 (2011).
- [10] M. A. Lee, K. E. Schmidt, M. H. Kalos, and G. V. Chester, *Phys. Rev. Lett.* **46**, 728-731 (1981); K. E. Schmidt and M. H. Kalos, in *Monte Carlo Methods in Statistical Physics II*, ed. K. Binder (Springer Verlag, Berlin, 1984).
- [11] M. Caffarel and D. M. Ceperley, *J. Chem. Phys.* **97**, 8415 (1992).
- [12] V. Grau, J. Boronat and J. Casulleras, *Phys. Rev. Lett.* **89**, 045301 (2002).
- [13] R. A. Aziz, V. P. S. Nain, J. S. Carley, W. L. Taylor and G. T. McConville, *J. Chem. Phys.* **70**, 4330 (1979).
- [14] M. Rossi, E. Vitali, L. Reatto, and D. E. Galli, *Phys. Rev. B* **85**, 014525 (2012).
- [15] K. E. Schmidt, Michael A. Lee, M. H. Kalos, and G. V. Chester, *Phys. Rev. Lett.* **47**, 807 (1981).

- [16] D. M. Ceperley and M. H. Kalos, in *Monte Carlo Methods in Statistical Physics*, ed. K. Binder (Springer, New York, 1979).
- [17] C. Lin, H. Zong and D. M. Ceperley, *Phys. Rev. E* **64**, 016702 (2001).
- [18] S. Baroni and S. Moroni, *Phys. Rev. Lett.* **82**, 4745 (1999).
- [19] A. Sarsa, K.E. Schmidt and W.R. Magro, *J. Chem. Phys.* **113**, 1366 (2000).
- [20] D. E. Galli and L. Reatto, *Mol. Phys.* **101**, 1697 (2003).
- [21] For the bosonic crystal, the trial function is of the Jastrow-Nosanow form; see L. H. Nosanow, *Phys. Rev. Lett.* **13**, 270 (1964). For the fermionic crystal, the trial function is of the Jastrow-Slater form, with Slater determinants of Gaussians centered at lattice sites.
- [22] E. Vitali, D.E. Galli and L. Reatto, *Series of advances in Quantum Many Body Theory* **11** (2008).
- [23] M. Rossi, M. Nava, L. Reatto, and D.E. Galli, *J. Chem. Phys.* **131**, 154108 (2009).
- [24] R. A. Aziz, F. R. W. McCourt and C. C. K. Wong, *Mol. Phys.* **61**, 1487 (1987).
- [25] *Numerical Recipes in C: The Art of Scientific Computing*, second edition, p. 43.
- [26] E. Vitali, M. Rossi, L. Reatto and D. E. Galli, *Phys. Rev. B* **82**, 174510 (2010).
- [27] F. H. Zong, C. Lin, and D. M. Ceperley, *Phys. Rev. E*, **66**, 036703 (2002).
- [28] N. D. Drummond, R. J. Needs, *Phys. Rev. Lett.*, **102**, 126402 (2009).

Chapter 4

Dynamics of two-dimensional ^3He

In the previous chapter we have studied static properties of $2d$ ^3He ; in particular we have inspected the dependence of the energy versus spin polarization at different densities, showing that $2d$ ^3He remains a paramagnetic fluid up to the freezing density. In this chapter we focus on the dynamical properties of this system. In fact, the low energy dynamics of ^3He is of outstanding importance in condensed matter physics to understand the thermodynamic behavior of quantum strongly correlated systems[1].

Recently inelastic neutron scattering experiments have been performed on a monolayer of liquid ^3He adsorbed on suitably preplated graphite: for the first time the collective *zero-sound* mode has been detected as a well defined excitation crossing and possibly reemerging from the particle-hole continuum typical of a Fermi fluid[14, 6]. In this chapter, we undertake an *ab-initio* study of the low-energy collective excitations, in particular the zero-sound mode, of a strictly two-dimensional ($2d$) ^3He sample relying on Quantum Monte Carlo (QMC) methods. This is particularly appealing since it has been shown that the strictly $2d$ model is often a realistic representation of the adsorbed liquid layer, as far as the liquid phase properties are concerned[2, 3]. The key quantity to be computed to compare with neutron scattering experiments is the dynamical structure factor $S(\vec{q}, \omega)$, which, apart from kinematical factors, is related to the differential cross section and contains informations about low-energy dynamics of the sample; in the case of ^3He , the dynamic structure factor is a sum of a coherent term $S_c(\vec{q}, \omega)$ and an incoherent contribution due to the coupling of the nuclear spin with the neutron beam[4], $S_i(\vec{q}, \omega)$

$$S(\vec{q}, \omega) = S_c(\vec{q}, \omega) + (\sigma_i/\sigma_c)S_I(\vec{q}, \omega) \quad (4.1)$$

$$S_c(\vec{q}, \omega) = \frac{1}{2\pi N b} \int_{-\infty}^{+\infty} dt e^{i\omega t} \langle e^{i\frac{t}{\hbar}\hat{H}} \hat{\rho}_{\vec{q}} e^{-i\frac{t}{\hbar}\hat{H}} \hat{\rho}_{-\vec{q}} \rangle \quad (4.2)$$

$$S_i(\vec{q}, \omega) = \frac{1}{2\pi N} \int_{-\infty}^{+\infty} dt e^{i\omega t} \langle e^{i\frac{t}{\hbar}\hat{H}} \hat{\rho}_{z\vec{q}} e^{-i\frac{t}{\hbar}\hat{H}} \hat{\rho}_{z-\vec{q}} \rangle \quad (4.3)$$

The brackets indicate a Ground state or thermal average, \hat{H} is the Hamiltonian operator, $\hat{\rho}_{\vec{q}} = \sum_{i=1}^N e^{-i\vec{q}\cdot\vec{r}_i}$ and $\hat{\rho}_{z\vec{q}} = \sum_{i=1}^{N_{\uparrow}} e^{-i\vec{q}\cdot\vec{r}_i^{\uparrow}} - \sum_{i=1}^{N_{\downarrow}} e^{-i\vec{q}\cdot\vec{r}_i^{\downarrow}}$ are respectively the local particle and spin densities in Fourier space. The parameter b is the coherent

scattering length and σ_c and σ_i are the scattering cross sections for the coherent and incoherent scattering. Similarly to the previous chapter, we are interested here only in zero temperature properties. The excitations of the system manifest themselves in the shape of $S(\vec{q}, \omega)$, appearing either as sharp peaks if they are long-lived or as broad structures if strong damping is present. In particular, the zero sound mode, which is the main target of this work, is related with $S_c(\vec{q}, \omega)$; the ratio σ_i/σ_c has been shown[5] to be 0.20(5); moreover, in the experimental data in Ref. [6] there is a well defined signal from the zero-sound mode but possible excitations from the incoherent part of $S(\vec{q}, \omega)$ (i.e. spin waves) are much harder to discern. Given these considerations, the data in Ref. [6] is dominated by $S_c(\vec{q}, \omega)$; we focus here on the coherent dynamical structure factor, $S_c(\vec{q}, \omega)$. QMC methods may indeed give access indirectly to the dynamic structure factor, $S_c(\vec{q}, \omega)$, because they allow to evaluate the intermediate scattering function:

$$F(\vec{q}, \tau) = \langle e^{\tau \hat{H}} \hat{\rho}_{\vec{q}} e^{-\tau \hat{H}} \hat{\rho}_{-\vec{q}} \rangle \quad (4.4)$$

by simulating a stochastic dynamics in imaginary time driven by the simple Hamiltonian:

$$\hat{H} = -\frac{\hbar^2}{2m_3} \sum_{i=1}^N \nabla_i^2 + \sum_{i < j=1}^N v(\vec{r}_i - \vec{r}_j) \quad . \quad (4.5)$$

Here m_3 is the mass of ^3He atoms and the pair interaction $v(r)$ is a realistic effective potential among ^3He atoms[7].

Since the ground state is not known, a QMC calculation of (4.4) requires an additional time $\tilde{\tau}$ to project a trial wave function ψ_T^F onto the exact ground state ψ_0^F (see chapter 2):

$$F(\vec{q}, \tau) = \frac{\langle \psi_T^F | e^{-\tilde{\tau} \hat{H}} \hat{\rho}_{\vec{q}} e^{-\tau \hat{H}} \hat{\rho}_{-\vec{q}} e^{-\tilde{\tau} \hat{H}} | \psi_T^F \rangle}{\langle \psi_T^F | e^{-(2\tilde{\tau} + \tau)} | \psi_T^F \rangle} \quad (4.6)$$

The correlation function (4.4) is the Laplace transform of $S_c(\vec{q}, \omega)$. Despite the well known difficulties related to the inversion of the Laplace transform in ill-posed conditions, the evaluation of $S_c(\vec{q}, \omega)$ starting from the QMC estimation of $F(\vec{q}, \tau)$ (4.6) has been proved to be fruitful for several bosonic systems[8, 9, 10].

For a Fermi liquid, the difficulty is further enhanced by the famous *sign problem*, thereby the computational effort grows exponentially with the projection time (as well as with the number of particles). The total projection time $2\tilde{\tau} + \tau$ in Eq. (4.6) is too large for all practical purposes.

While accurate approximations exist to circumvent this problem in the calculation of static ground-state properties[11], we are aware of no applications of approximate schemes such as the restricted path[12] or constrained path[13] methods to the calculation of imaginary-time correlation functions.

We thus resort to the following approximation:

$$\psi_0^F = e^{-\tilde{\tau} \hat{H}} \psi_T^F \simeq \mathcal{D} e^{-\tilde{\tau} \hat{H}} \psi_T^B = \mathcal{D} \psi_0^B \quad (4.7)$$

where a superscript $F(B)$ indicates Fermi(Bose) statistics and \mathcal{D} is a Slater determinant. In the resulting approximate correlation function

$$F_A(\vec{q}, \tau) = \frac{\langle \psi_0^B | \mathcal{D}^* \hat{\rho}_{\vec{q}} e^{-\tau \hat{H}} \hat{\rho}_{-\vec{q}} \mathcal{D} | \psi_0^B \rangle}{\langle \psi_0^B | \mathcal{D}^* e^{-\tau \hat{H}} \mathcal{D} | \psi_0^B \rangle} \quad (4.8)$$

the projection time between the determinants, which determines the severity of the sign problem, is limited to τ ; F_A is an approximation of the intermediate scattering function in imaginary time (4.4), which would be exact if $\mathcal{D}\psi_0^B$ were the exact Fermi ground state. Its inverse Laplace transform is an approximation of the dynamical structure factor (4.2). For a given wave vector, the positions of the peaks in $S(\vec{q}, \omega)$ provide the energy of the excitations, while their shape is related to the life-time of the excited states. In general, the approximation (4.7) introduces biases both in the excitation energies and in the shape of $S_c(\vec{q}, \omega)$. In order to enhance the robustness of this approach, we introduce also another correlation function, F_B , which is defined on the bosonic ground state:

$$F_B(\vec{q}, \tau) = \frac{\langle \psi_0^B | e^{\tau \hat{H}} \mathcal{D}^* \hat{\rho}_{\vec{q}} e^{-\tau \hat{H}} \hat{\rho}_{-\vec{q}} \mathcal{D} | \psi_0^B \rangle}{\langle \psi_0^B | \psi_0^B \rangle}. \quad (4.9)$$

Despite F_B is not directly related to the dynamical structure factor of the Fermi liquid, this function has some useful features: on one hand, it contains the *exact* fermionic spectrum, as can be seen from the spectral resolution:

$$F_B(\vec{q}, \tau) = \sum_{n=0}^{+\infty} e^{-\tau(E_n^F - E_0^B)} b_n, \quad b_n = \frac{|\langle \hat{\rho}_{-\vec{q}} \mathcal{D} \psi_0^B | \psi_n^F \rangle|^2}{\langle \psi_0^B | \psi_0^B \rangle} \quad (4.10)$$

On the other hand, it is a bosonic correlation function and thus it can be evaluated with great accuracy by means of exact bosonic QMC methods. If, moreover, the approximation (4.7) is accurate enough, the coefficients b_n become, apart from an unessential normalization, the spectral weights f_n of the exact intermediate scattering function (4.4).

$$f_n = \frac{|\langle \hat{\rho}_{-\vec{q}} \psi_0^F | \psi_n^F \rangle|^2}{\langle \psi_0^F | \psi_0^F \rangle} \quad (4.11)$$

We note finally that F_B arises as a natural generalization of the Fermionic correlations method: in fact, F_B has the same form of Eq. (3.11) that has been used in the previous chapter about the ground state of an ${}^3\text{He}$ film: in that context, the Fermionic correlations method provided results for the magnetic properties of the system in impressive agreement with experimental data.

We argue that a comparison between dynamical properties evaluated with F_A and F_B might provide a strong indication of the robustness of our approach.

We studied a system of $N = 26$ structureless 1/2-spin fermions of mass m_3 , interacting via the Aziz potential described by ref. [7], a very accurate model for the effective interactions among ${}^3\text{He}$ atoms. The choice of the particle number was inspired by our previous work in Ref. [3]: such number of atoms was chosen to be a

closed-shell number; this choice minimizes size effects related to the discrete Fermi sea, but still allows to extract physical information from the imaginary time correlation functions, which rapidly become steeper as the size of the system is increased.

Differently from the work described in the previous chapter, we have not used twisted boundary conditions (TBC). This choice is motivated by the fact that the effect of TBC enters in the estimation of both the Fermi–Bose gap and the energy of the excited state with respect to the bosonic ground state; being the energy of the excitation a difference between these two quantities, we assumed that, as a first approximation, the effects of TBC cancel out. In conclusion, considering that the evaluation of the necessary correlation functions are required with high quality data, neglecting TBC is a good compromise between accuracy and practical computing times.

We have focused on a density around 0.047 \AA^{-2} , close to the experimental conditions[14]. Moreover, we have explored the behavior of the sample at the densities 0.038 and 0.060 \AA^{-2} in order to investigate the possible density-dependence of the excitations of the system. In particular, the highest density was chosen very close to the freezing point. The QMC evaluation of F_B requires a simple generalization of the methodology that we have followed in the previous Chapter: a fictitious system of *bosons* of mass m_3 is simulated with the Shadow Path Integral Ground State method. The imaginary-time propagation was 1.3125 K^{-1} and the density matrix approximation was a Pair Product[15] with imaginary-time-step of $1/160 \text{ K}^{-1}$.

The Shadow Path Integral Ground State[16] technique was chosen in the computation of both the bosonic ground-state energy and the correlation functions.

Performing such a QMC simulation, we have computed $F_B(\vec{q}, \tau)$ for each wave-vector \vec{q} , together with the correlation function:

$$F_0(\tau) = \frac{\langle \psi_0^B | \mathcal{D}^* e^{-\tau \hat{H}} \mathcal{D} | \psi_0^B \rangle}{\langle \psi_0^B | \psi_0^B \rangle} \quad (4.12)$$

which is precisely the correlation function that was used in the previous chapter in order to estimate the energy gap between the bosonic fictitious system and the fermionic ground state. F_A has been then estimated from the exact identity:

$$F_A(\vec{q}, \tau) = \frac{F_B(\vec{q}, \tau)}{F_0(\tau)} \quad (4.13)$$

It is well known that, in order to extract information from imaginary time correlation function, an inversion of the Laplace transform in ill-posed conditions is necessary. This can be carried out by means of the Genetic Inversion via Falsification of Theories (GIFT) [9], which has already provided very accurate results in the study of low energy excitations of Bose superfluids[9] and supersolids[10]. Naturally the problem is unavoidably ill-posed: the quality of the results of the inversion procedure cannot be guaranteed *a priori*; however, a test of reliability of the inversion procedure can be obtained by comparing our estimations of the dynamic structure factor with experimental data; Fig. 4.3 shows a remarkable agreement.

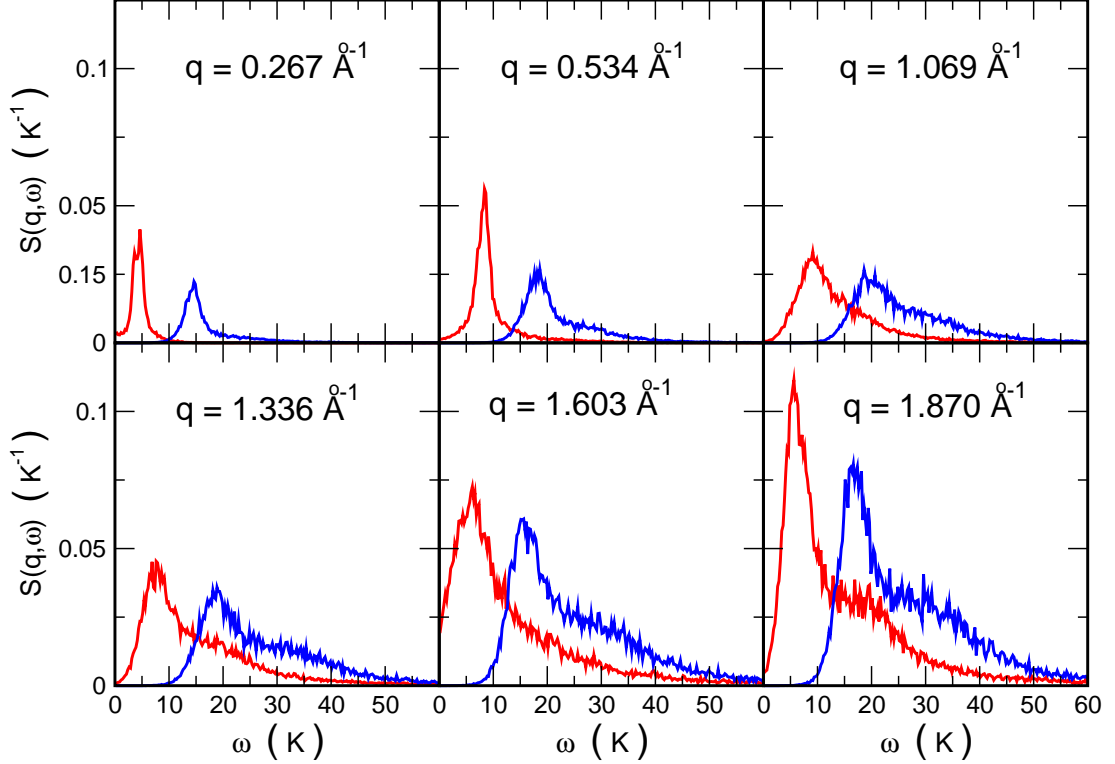


Figure 4.1: Comparison between the spectral functions obtained from F_A and those obtained from F_B for some wave-vectors q . The two spectral functions have a compatible shape, with a shift in energy of $E_0^F - E_0^B$. The data for F_A , differently from Fig. 4.3, has been obtained from the average of six different evaluations of $F_A(\tau)$.

In Fig.4.1 we show a comparison between the estimated inverse Laplace transforms of F_A and F_B : apart from a rigid shift in energy, due to the difference $E_0^F - E_0^B$ which we have estimated in the previous chapter, the reconstructions coincides within the “algorithmic resolution” of the GIFT methodology. This represents a confirmation for the robustness of our approach. We remark that F_B is much easier to handle than F_A , since it does not suffer of long- τ large fluctuations due to the presence of the τ -dependent denominator in (4.13).

The shape of the reconstructed spectral functions depends on the lowest-energy fermionic exact eigenstates not orthogonal to the wave function $\hat{\rho}_{-\vec{q}} \mathcal{D} \psi_0^B$, a state containing a density modulation of wave vector \vec{q} .

Our assumption (4.7) asserts that such wave function is very similar to $\hat{\rho}_{-\vec{q}} \psi_0^F$. As appears evident in Fig.4.2, at low wave vectors the inversions of $F_B(\vec{q}, \tau)$ provide spectral functions with sharp peaks; this provides our microscopic estimation of the *zero-sound mode* dispersion relation, with an “algorithmic resolution” similar to that found in the previous chapter, where the Fermi Ground State signal was detected, at higher wave vectors the peaks become much broader. We interpret such a broadening as a damping of density fluctuations due to the presence of other excitations, in particular the particle-hole excitations.

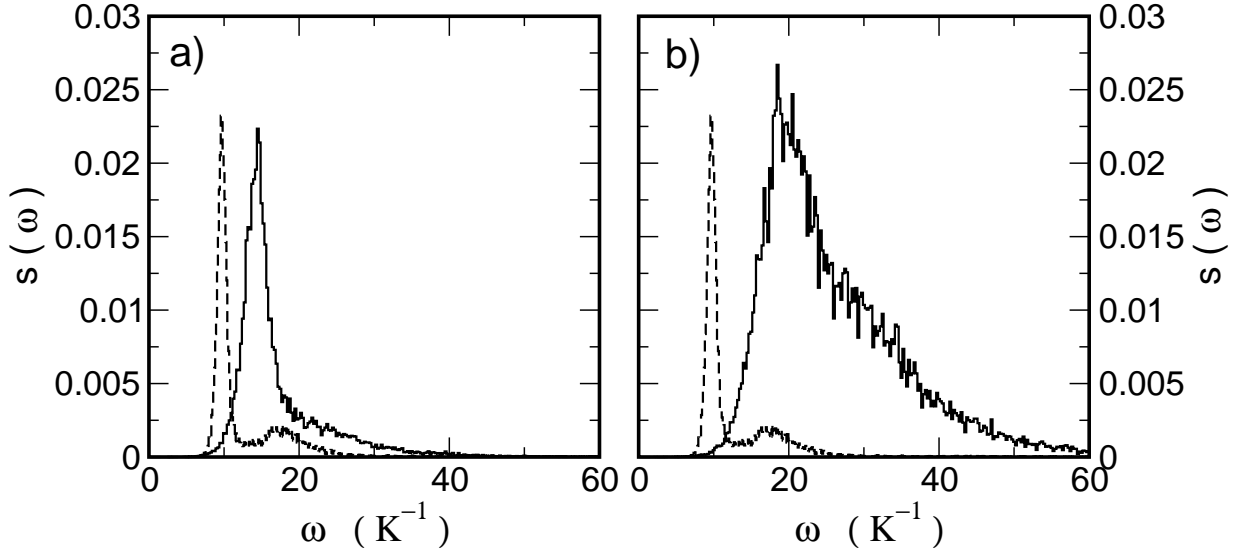


Figure 4.2: Panel a) the gap between the Bosonic and the Fermionic ground state (dashed line) and the inversion of eq. (4.10) for $q = 0.0267 \text{ \AA}^{-1}$ (filled line). Panel b) the same of panel a), but with $q = 0.801 \text{ \AA}^{-1}$

In Fig.4.3 we show the comparison between our estimation of the dynamic structure factor of the ^3He film and the experimental data[14]. The agreement is impressive and gives a strong support to the approximation (4.7); it is also clear from this comparison that Eq. (4.7) describes accurately also the mechanisms which give rise to a broadening of the dynamic structure factor; this is displayed even better in Fig.4.4, where we report, in a color plot, the estimated $S_B(\vec{q}, \omega)$. At low q we find well defined excitation energies, while, as the wave vector increases, we observe the sharp mode becoming damped.

What kind of excitation provide the damping of the zero-sound mode? Any expert in Fermi liquid theory would immediately answer: the particle-hole continuum. But what does it mean in an *ab-initio* approach to a strongly correlated fermion fluid? Our idea is to exploit the correlation functions formalism to build up a “Fermi–liquid like” function:

$$F_{ph}(\tau) = \frac{\langle \psi_0^B | \mathcal{D}_{ph}^* e^{-\tau \hat{H}} \mathcal{D}_{ph} | \psi_0^B \rangle}{\langle \psi_0^B | e^{-\tau \hat{H}} | \psi_0^B \rangle} \quad (4.14)$$

where \mathcal{D}_{ph} is simply a Slater Determinant like that employed in the previous chapter (see Eq. (3.15)), with $\theta_1 = 0$. Differently from Eq. (3.15), in the enumeration of the wave–vectors $\{\vec{k}_n\}$, one element has been taken out of the ideal gas Fermi sea; the bosonic ground state and the backflow correlations provide a “dressing” for the *ph-wave function* $\mathcal{D}_{ph}\psi_0^B$. In Fig. 4.5 we show both the particle-hole excitation energies for the ideal Fermi gas, which do not form a continuum since the system is finite, and the estimated energies extracted from the inversions of $F_{ph}(\tau)$, which have been evaluated for wave vectors at the high- q borderline of the structure; we focused on

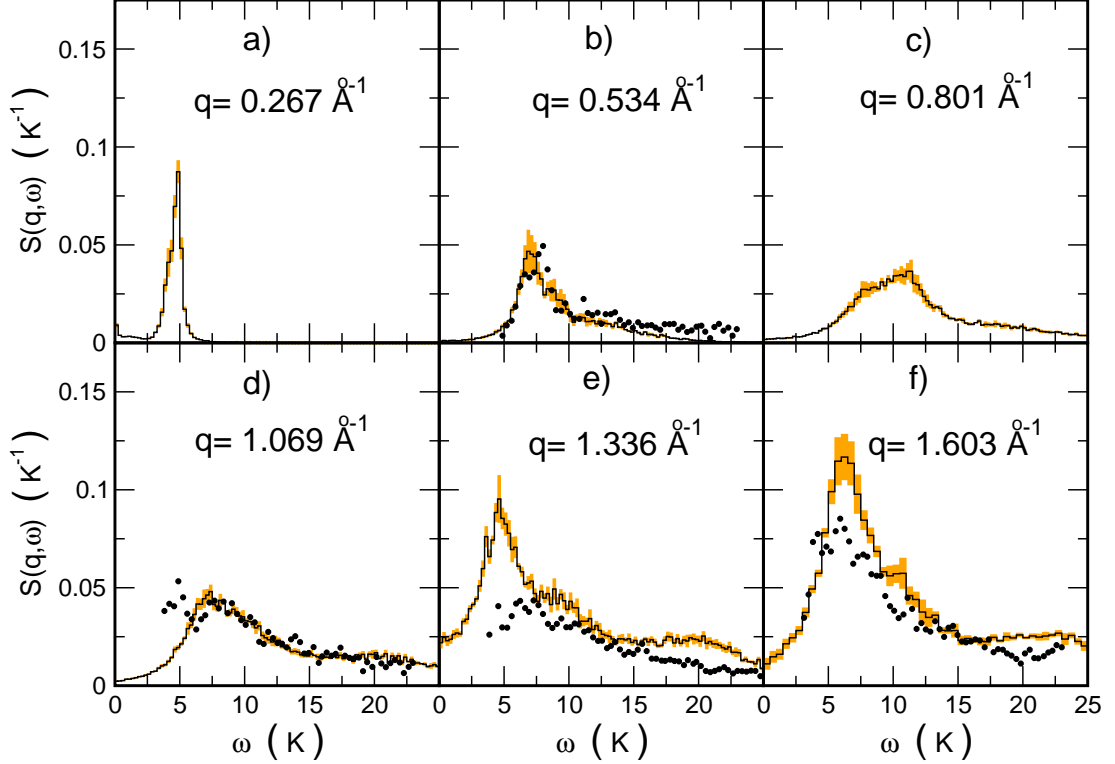


Figure 4.3: From left to right the obtained dynamic structure factor for increasing wave vectors at $\rho = 0.047 \text{ \AA}^{-2}$. The yellow shadow represents statistical uncertainties obtained from six different evaluations of the dynamic structure factor at each wave-vector; filled circles are the available experimental data from Ref. ([14]). The wave-vector shown in picture are those accessible from our simulation, the experimental wave vectors are $q = 0.55 \text{ \AA}^{-1}$ (b), $q = 1.15 \text{ \AA}^{-1}$ (d), $q = 1.25 \text{ \AA}^{-1}$ (e) and $q = 1.65 \text{ \AA}^{-1}$ (f).

the high- q borderline in order to verify whether the roton states reemerges from the particle-hole band or not. The particle-hole band of the ideal Fermi gas has been computed following the definition of particle-hole energy: from an ideal Fermi gas of N particles of mass m in a square box of late L , the Fermi Sea is labeled by quantum numbers that define the wave vector of each state, $\vec{k}_{ij} = (2\pi i/L, 2\pi j/L)$; a particle-hole excitation characterized by a hole at (i_0, j_0) , corresponding to a wave-vector \vec{k}_0 inside the Fermi sphere, and a particle at (i_1, j_1) with wave-vector \vec{k}_1 outside the Fermi sphere, has a wave-vector \vec{q} and an energy $E_{\vec{q}}^{ideal}$ defined as:

$$\vec{q} = \frac{2\pi}{L} \sqrt{(i_1 - i_0)^2 + (j_1 - j_0)^2} \quad (4.15)$$

$$E_{\vec{q}}^{ideal} = \left(E_F + \frac{\hbar^2}{2m} |\vec{k}_2|^2 \right) - \left(E_F - \frac{\hbar^2}{2m} |\vec{k}_1|^2 \right) = \frac{\hbar^2}{2m} \left(|\vec{k}_2|^2 + |\vec{k}_1|^2 \right) \quad (4.16)$$

where E_F is the Fermi energy of the system. The particle-hole band of the ideal Fermi gas in Fig. 4.5 has been obtained following this prescription; all the possible particle-

hole combinations which gave a wave vector \vec{q} in the displayed range were considered. Comparing the ideal particle–hole band with that of the interacting system one can also estimate the effective mass m^* ; in this context, the effective mass is a parameter of the Landau Fermi liquid theory which gives the mass of the quasi–particle; m^* is obtained from the ratio of the particle–hole energies of the interacting and the non–interacting systems at the same wave–vector,

$$E_{\vec{q}}^{ideal} = \frac{\hbar^2}{2m} |\vec{q}|^2 \quad (4.17)$$

$$E_{\vec{q}}^{int} = \frac{\hbar^2}{2m^*} |\vec{q}|^2 \quad (4.18)$$

$$\frac{m^*}{m} = \frac{E_{\vec{q}}^{ideal}}{E_{\vec{q}}^{int}} \quad (4.19)$$

This relation, however, is valid only in the range of applicability of the Landau Fermi liquid theory; in particular, this evaluation of the effective–mass holds for small wave–vectors; in this work we give a rough estimate of the effective mass as the average of $E_{\vec{q}}^{ideal}/E_{\vec{q}}^{int}$ for each particle–hole wave–vector \vec{q} computed in our simulations. In the interacting system, we find in general that the particle–hole energies become smaller, resulting in an higher effective mass (see Tab. 4.1). In particular this has important consequence as far as the re–emergence of the zero–sound mode from the particle–hole band is concerned: in contrast to what the authors of Ref. [6] argue, using the non–interacting estimation of the particle–hole band, we do *not* observe such re–emergence in the roton region at any density (see Fig.4.2).

Table 4.1: Effective to bare mass ratio estimated from the computed particle–hole excitations in a system of $N = 26$ particles at the studied densities.

Density (\AA^{-2})	$\frac{m^*}{m}$
0.038	1.3(3)
0.045	1.8(1)
0.060	2.0(1)

We point out that this evaluation of the particle hole excitations gives only a first evidence that the roton mode is still inside the particle–hole band; a further step on this topic consists in a size scaling analysis that has been planned for future works.

The static response function can be obtained from the knowledge of the dynamic structure function. The described method can thus be viewed also as a new and very accurate way to compute the static response function of a fermion system. From six independent evaluations of the dynamic structure factor we computed the static response function defined as $\chi_{\vec{q}} = -2\rho \int d\omega \frac{S(\vec{q},\omega)}{\omega}$ and the result is displayed in figure 4.3. To our knowledge, this is the first microscopic *ab–initio* computation of the static response function of two–dimensional ^3He .

As a last result, we note that Eq. (4.8), for $\tau = 0$ is the definition of the static structure factor evaluated on a Fermi state $|\mathcal{D}\Psi_0^B\rangle$. This state, as shown in Fig. 4.3,

is a good approximation of the true fermionic ground state; this is at least true for the low-energy dynamical properties; we assume that this holds also for the static structure factor. In Fig. 4.6 we show the static structure factor of $2d$ ^3He compared with that of the fictitious “bosonic” ^3He . The similarity between the two static structure factors is evident; this indicates that the structural properties of Helium are dominated by the inter-atomic potential rather than the quantum symmetry.

In conclusion, we have presented the first *ab-initio* computation of the zero-sound excitation energy. We have also proposed an approximate evaluation from first principles of the dynamic structure factor that is found to be in very good agreement with experimental data[14]. We employed a well tested methodology involving the Laplace inversion of imaginary-time correlation functions [17, 3] and extended it in order to handle the excited states. Our results are in agreement with the experimental data and show that our variational estimation of the dynamic structure factor is accurate enough to represent the broadening of the zero-sound mode in the particle-hole band. At the studied densities we did not observe the re-emergence of the roton mode from the particle-hole band, however our data on particle-hole excitations is not yet conclusive: possible finite size effects on the particle-hole band have still to be studied with simulations of bigger systems.

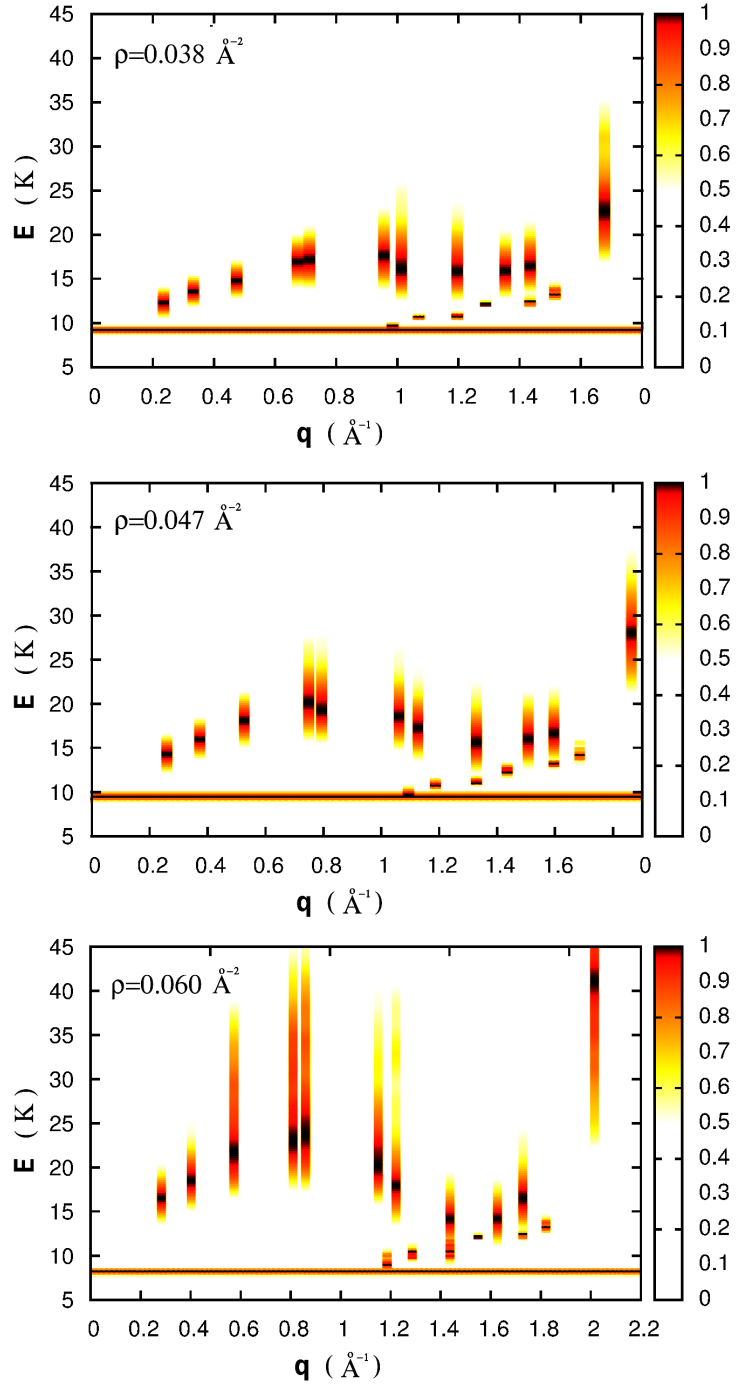


Figure 4.4: The horizontal continuous line represents the energy gap between the Fermionic and the Bosonic ground state, slightly above - at wave vectors ranging roughly between 1 and 2 \AA^{-1} - the discrete particle-hole right boundary is shown; the remaining and larger vertical bands are the density-density collective excitations. The bands are centered on the corresponding values and their width has been enlarged for a better visibility.

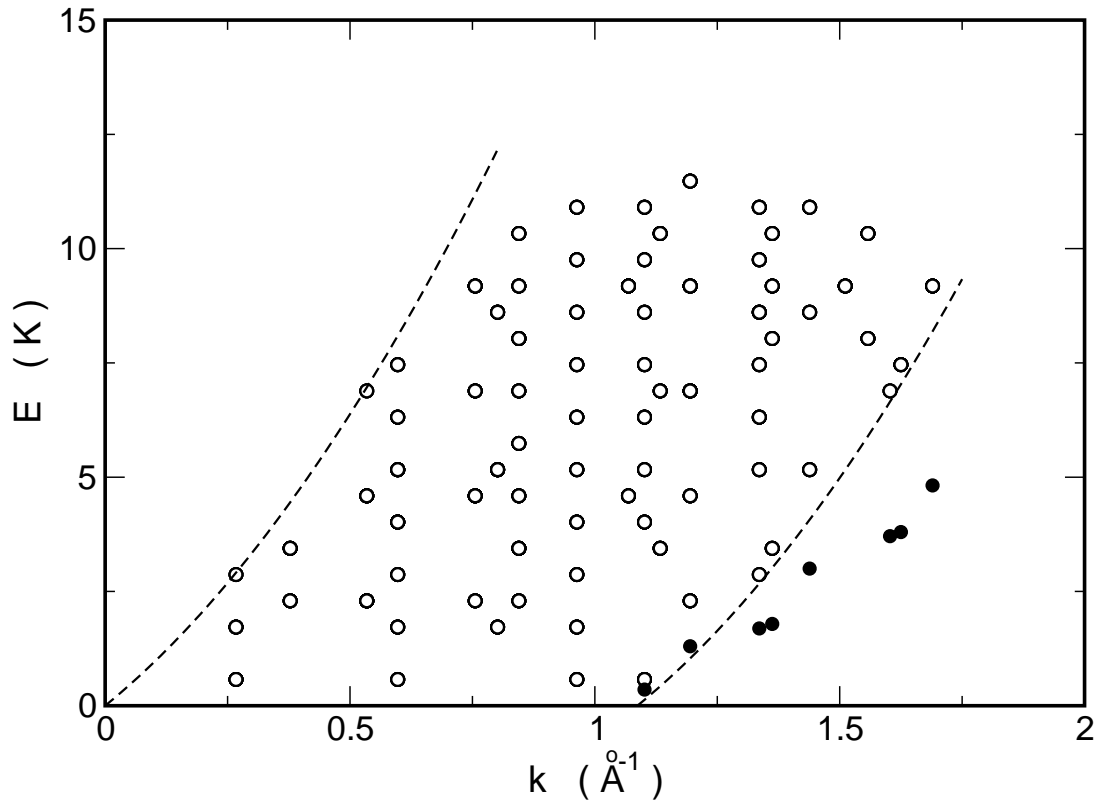


Figure 4.5: (Circles) Particle-hole excitations for $N=26$ non-interacting atoms of ${}^4\text{He}$ mass. (Dashed lines) Particle-hole band for the ideal gas in the thermodynamic limit. (Filled circles) Particle-hole excitations for $N=26$ atoms of interacting ${}^4\text{He}$.

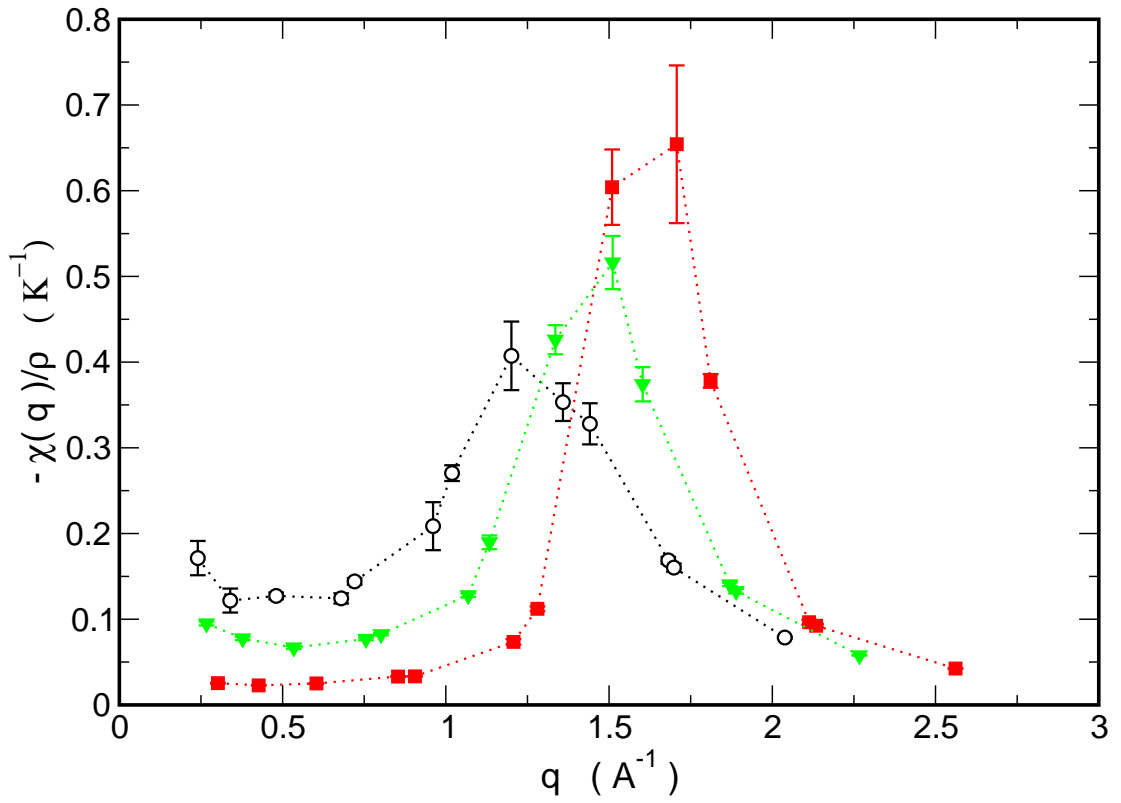


Figure 4.6: The static response function of ${}^3\text{He}$ obtained from eq. (4.10). (Circles) $\rho = 0.038 \text{ \AA}^{-2}$. (Triangles) $\rho = 0.047 \text{ \AA}^{-2}$. (Squares) $\rho = 0.060 \text{ \AA}^{-2}$.

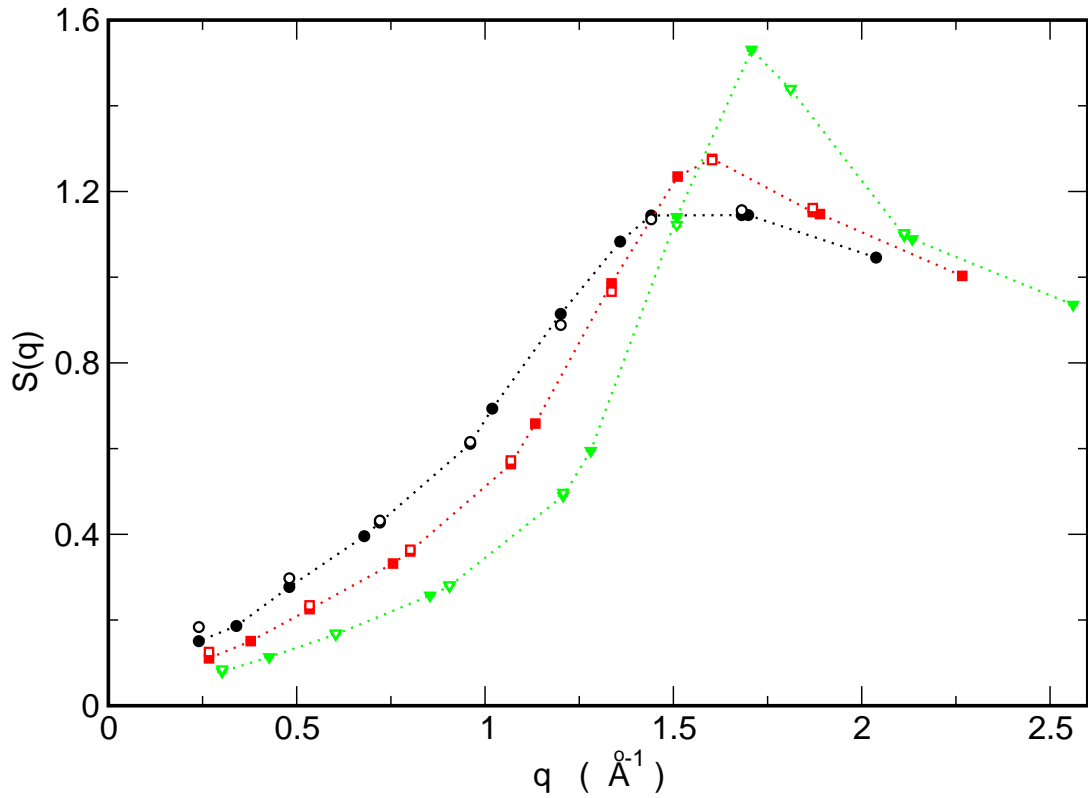


Figure 4.7: The Static Structure Factor of $2d$ ${}^3\text{He}$ (filled symbols) compared with that of “bosonic” $2d$ ${}^3\text{He}$ (empty symbols). Data is relative to three densities: $\rho = 0.038 \text{ \AA}^{-2}$ (Circles); $\rho = 0.047 \text{ \AA}^{-2}$ (Squares) and $\rho = 0.060 \text{ \AA}^{-2}$ (Triangles). The dashed lines are guides to the eye.

Bibliography

- [1] H. M. Bohm, E. Krotscheck, M. Panholzer, H. Godfrin, H. J. Lauter, M. Meschke, *J. Low. Temp. Phys.*, **158**, 194-200 (2010).
- [2] P. A. Whitlock, G. V. Chester and B. Krishnamachari, *Phys. Rev. B*, **58**, 13 (1998).
- [3] M. Nava, E. Vitali, D. E. Galli and S. Moroni *Phys. Rev. B*, **85**, 184401 (2012)
- [4] R. H. Glyde, in *Excitations in liquid and solid Helium*, Oxford University Press (New York, 1994).
- [5] K. Sköld and C. A. Pelizzari, *Philos. Trans. R. Soc. London, Ser. B*, **290**, 605 (1980)
- [6] H. Godfrin, M. Meschke, H. J. Lauter, A. Sultan, H. M. Bohm, E. Krotscheck and M. Panholzer, *Nat. Phys.*, **483**, 576-579 (2012)
- [7] R. A. Aziz, V. P. S. Nain, J. S. Carley, W. L. Taylor and G. T. McConville, *J. Chem. Phys* **70**, 4330 (1979).
- [8] M. Caffarel and D. M. Ceperley, *J. Chem. Phys.* **97**, 11 (1992).
- [9] E. Vitali, M. Rossi, L. Reatto and D. E. Galli *Phys. Rev. B*, **82**, 174510 (2010)
- [10] S. Saccani, S. Moroni and M. Boninsegni, *Phys. Rev. Lett.* **108**, 175301 (2012).
- [11] P.J. Reynolds, D.M. Ceperley, B.J. Alder, and W.A. Lester, *J. Chem. Phys.* **77**, 5593 (1982).
- [12] D. M. Ceperley, in *Monte Carlo and Molecular Dynamics of Condensed Matter Systems*, Ed. K. Binder and G. Ciccotti (Bologna, Italy, 1996).
- [13] S. Zhang, J. Carlson and J. E. Gubernatis, *Phys. Rev. Lett.* **74**, 3652 (1995).
- [14] H. M. Bohm, E. Krotscheck, M. Panholzer, H. Godfrin, H. J. Lauter, M. Meschke, *J. Low. Temp. Phys.*, **158**, 147-154 (2010).
- [15] D. M. Ceperley, *Rev. Mod. Phys.* **67**, 279 (1995).
- [16] D. E. Galli and L. Reatto, *Mol. Phys.* **101**, 1697 (2003).
- [17] E. Vitali, G. Carleo, S. Moroni and S. Baroni, *to be published*.

Chapter 5

Study of ^4He adsorbed on Graphene–Fluoryde and Graphene–Hydrate

At the forefront of current research in condensed matter physics is the study of strongly interacting systems, with a remarkable variety of phase transitions [1]. The effects of fluctuations are enhanced in low dimensions and in the presence of frustration [2]. These represent some of the motivations for studying adsorption phenomena, where important roles are played by the gas–gas interaction and the “tunable” effect of the substrate. The surface of graphite has long been a playground for studying two–dimensional (2D) monolayer phases of classical and quantum gases [3].

Probably the best understood adsorption system is the He monolayer on graphite [4]. Experiments carried out at the University of Washington ca. 1970 revealed *for the first time* behavior corresponding to a two–dimensional (2D) gas. More dramatic was the appearance of a spectacular peak in the specific heat of ^4He near $T_c = 3$ K. This peak, well described by the 3 state Potts model, manifested a 2D transition from a high T fluid to a low T commensurate ($\sqrt{3} \times \sqrt{3}$ R30 $^\circ$) phase, providing a benchmark measure of coverage, not seen in previous adsorption experiments. This ordered phase (at density $\rho_{\sqrt{3}} = 0.0636\text{\AA}^{-2}$) corresponds to atoms localized on second–nearest neighbor hexagons. At higher densities near completion of the first monolayer ($\rho = 0.11\text{\AA}^{-2}$) an incommensurate 2D triangular solid phase is present; the phase diagram at intermediate densities is not yet completely determined. A quantitative understanding of the He–graphite interaction was made possible by precise scattering measurements of surface bound states and band structures [5, 6].

The availability of graphene (Gr) and its derivatives like graphane (GH) [7] and graphene–fluoride (GF) [8] offers the prospect of novel adsorption phenomena.

Since Gr is just a single plane of graphite, the symmetry and corrugation are expected to be very similar in the two cases. If Gr is rigid, no new phenomena are expected for adsorption on one side of Gr, in comparison with graphite, [5] and this has been verified by recent quantum simulations of ^4He [8]. The situation is different for the derivatives of Gr, graphene–fluoride (GF) [7] and graphane (GH) [7, 9] that have been recently obtained experimentally. Because GF and GH have surface symmetries

and compositions which are quite different from Gr, adsorbed gases will have very different properties.

In the next section we show a model adsorption potential for He on GF and GH. We will then show the study of a single ^4He and ^3He atom on these substrates, as well as submonolayer films of ^4He at coverages similar to that ($\rho = 0.064\text{\AA}^{-2}$) of the $\sqrt{3} \times \sqrt{3}$ R30 $^\circ$ state on graphite. In the last section the properties at high coverages will be described.

5.0.6 Adsorption potential

Graphane and graphene–fluoride have a similar geometry; half of the H (F) atoms are attached on one side of the graphene sheet to the carbon atoms forming one of the two sublattices of graphene. The other half are attached on the other side to the C atoms forming the other sublattice. The H (F) atoms are located on two planes (see left of Fig. 5.2); one is an overlayer located at a distance h above the pristine graphene plane while the other is an underlayer at a distance h below the graphene plane. In addition, as seen in Fig. 5.1 there is a buckling of the C–plane with the C atoms of one sublattice moving upward by a distance b while the other sublattice moves downward by the same amount. A He atom approaching GH (GF) from above will interact primarily with the H (F) overlayer, but it will interact also with the C atoms and the H (F) atoms of the underlayer.

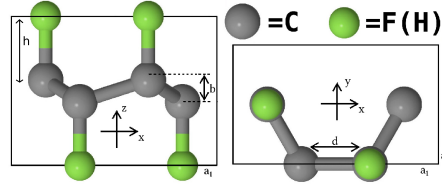


Figure 5.1: Geometry of the substrate with the definitions of the buckling parameter b , the interplane distance h and d , the carbon–carbon distance on the plane

We have adopted a traditional, semi–empirical model to construct the potential energy $V(\vec{r})$ of a single He atom at position \vec{r} near a surface [10, 11, 12, 13]. The potential is written $V(\vec{r}) = V_{\text{rep}}(\vec{r}) + V_{\text{att}}(\vec{r})$, a sum of a Hartree–Fock repulsion derived from effective medium theory, and an attraction, $V_{\text{att}}(\vec{r})$, which is a sum of damped He atom van der Waals (VDW) interactions and the polarization interaction with the surface electric field. The first term is $V_{\text{rep}}(\vec{r}) = \alpha\rho(\vec{r})$. Here $\alpha = 364 \text{ eV}\text{-bohr}^3$ is a value derived by several workers as the coefficient of proportionality between the repulsive interaction and the substrate’s electronic charge density $\rho(\vec{r})$ *prior* to adsorption. The geometry of GH and GF, their electronic charge density and the electrostatic potential have been obtained using Density Functional Theory with an all–electron triple numerical plus polarization basis set with an orbital cutoff of 3.7 \AA as implemented in the DMol3 code[14]. The exchange and correlation potential was treated in a Generalized Gradient Approximation parameterized by Perdew, Burke,

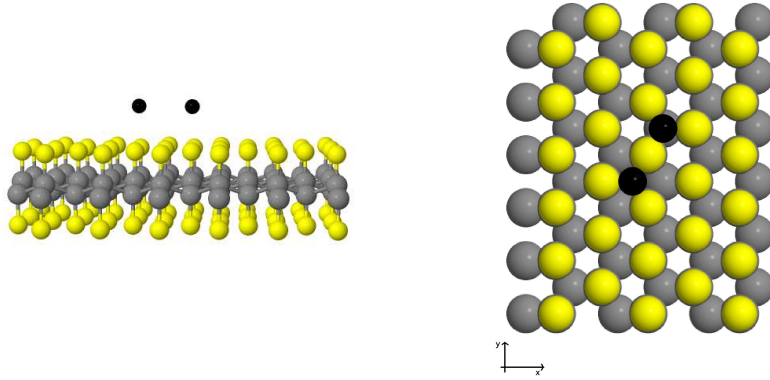


Figure 5.2: Two schematic views of GF. F (C) atoms are light (dark) gray. Positions of atoms are to scale but their sizes are arbitrary. The black balls represent two adsorption sites for He, one of each kind. GH is similar.

and Ernzerhof [15]. We use a tetragonal unit cell containing four C atoms and four H (F) atoms for GH and GF, respectively. The cell dimensions for GF are $a_1 = 2.59$ Å, $a_2 = 4.48$ Å, and $a_3 = 12$ Å, while for GH we use $a_1 = 2.52$ Å, $a_2 = 4.36$ Å, and $a_3 = 12$ Å. The Brillouin zone was sampled with a Monkhorst–Pack grid of $6 \times 3 \times 1$ \vec{k} points in both cases. The self-consistent cycles were run until the energy difference was less than 10^{-6} eV. The atomic positions were relaxed until the forces on all atoms were lower than 0.01 eV/Å. As a result, the C–F distance is 1.38 Å, the C–C distance 1.57 Å, the C–C distance projected on the $x-y$ plane is $d = 1.495$ Å and the buckling displacement $b = 0.484$ Å; while in GH, the C–H distance is 1.11 Å, the C–C distance 1.52 Å, $d = 1.453$ Å and $b = 0.45$ Å.

The attraction is a sum of contributions; for GH,

$$V_{\text{att}}(\vec{r}) = V_{\text{H}^+}(\vec{r}) + V_{\text{gr}}(\vec{r}) + V_{\text{H}^-}(\vec{r}) - \alpha_{\text{He}} E^2(\vec{r})/2 \quad (5.1)$$

The right-most term is the induced dipole energy, where $\alpha_{\text{He}} = 0.205$ Å³ is the static polarizability of the He atom and $\vec{E}(\vec{r})$ is the electric field due to the substrate. This term gives a minor contribution to the adsorption potential (see Fig. 5.3) and has been neglected in this work.

The three VDW terms for GH originate from the H overlayer, the graphene sheet (we are neglecting in this term the small buckling of the graphene sheet) and the H underlayer, respectively. These terms are described by the attractive part of a

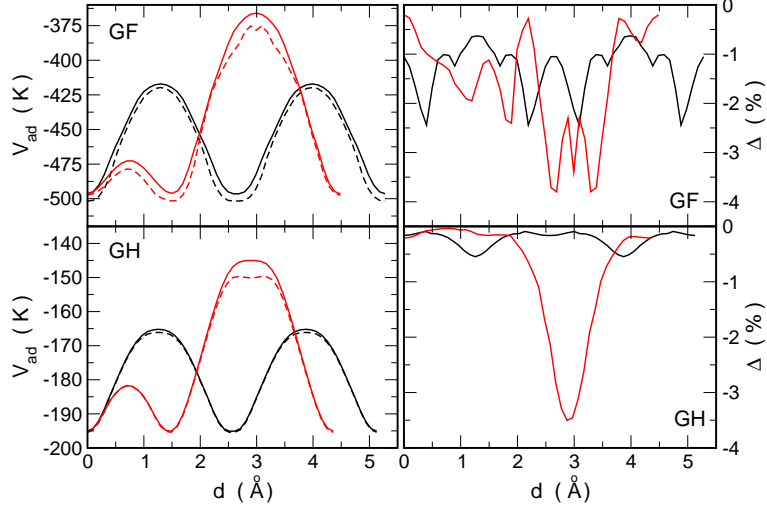


Figure 5.3: Upper figures: ^4He on GF. (Left) minimum value with respect to z of $V_{ads}(\vec{r})$ along the direction $(x, 0)$ (black) and $(0, y)$ (red). Full lines represent the adsorption potential, V_a , obtained using Eq. (5.1) for the attractive part, dashed lines the adsorption potential, V_b , obtained neglecting the induced dipole energy. (Right) the relative difference (in percentage) between V_a and V_b with respect to V_a , namely $100 * (V_b - V_a)/V_a$. Lower figures: the same for GH.

Lennard–Jones potential,

$$V_{H-}(\vec{r}) = - \sum_j \frac{C_{6H}}{|\vec{r} - \vec{r}_j^{H-}|^6} \quad (5.2)$$

$$V_{gr}(\vec{r}) = - \sum_j \frac{C_{6C}}{|\vec{r} - \vec{r}_j^{gr}|^6} \quad (5.3)$$

$$V_{H+}(\vec{r}) = - \sum_j \frac{C_{6H}}{|\vec{r} - \vec{r}_j^{H+}|^6} \quad (5.4)$$

where the sum spans over the carbon or hydrogen positions; C_{6C} and C_{6H} are respectively the Helium–Carbon and the Helium–Hydrogen VDW coefficients. Due to the distance between the helium monolayer and the graphene plane, Eq. (5.2) can be integrated over the x – y plane

$$\begin{aligned} V_{H-}(\vec{r}) &= -\theta_H C_{6H} \int d^2\vec{R} \frac{1}{\left((z + \tilde{h})^2 + |\vec{R}|^2\right)^3} = \\ &= - \left(\frac{\theta_H - \pi C_{6H}}{2}\right) (z + \tilde{h})^{-4} = - \frac{A_C}{(z + \tilde{h})^4} \end{aligned} \quad (5.5)$$

where θ_{H-} is the Hydrogen density of the sublayer on the x - y plane and $\tilde{h} = h + b/2$ is the distance between the Hydrogen underlayer and the mean Carbon plane (see Fig. 5.1). The He-H VDW coefficient, C_{6H} , is obtained from the VDW interaction of He-H₂. In Ref. [16], the potential energy between He and H₂ is written as a sum of potential terms regarding the interaction of Helium with each single Hydrogen,

$$U_{He-H_2}(\vec{r}, \vec{R}_1, \vec{R}_2) = U_{He-H}(|\vec{r} - \vec{R}_1|) + U_{He-H}(|\vec{r} - \vec{R}_2|) \quad (5.6)$$

where \vec{R}_1 and \vec{R}_2 are the positions of the Hydrogen atoms. Considering an attractive VDW term, $-C_{6H}/r^6$, for each Hydrogen atom and neglecting the structure of the H₂ molecule, we approximate the attractive part of U_{He-H_2} as an isotropic VDW interaction C_{6H_2}/r^6 . We then have:

$$C_{6H} = \frac{C_{6H_2}}{2} \quad (5.7)$$

The value of C_{6H_2} is obtained from Ref. [17]; in that work the anisotropy of U_{He-H_2} is also studied. The work shows that the leading term of the long range attractive part of the He-H₂ potential is

$$U_{He-H_2}^{att}(\vec{R}, \gamma) = - \sum_{n \geq 3} \frac{C_{2nH_2}}{|\vec{R}|^{2n}} [1 + \Gamma_{2n} P_2(\cos \gamma)] \quad (5.8)$$

where \vec{R} is the distance from the center of mass of H₂ and γ the angle between \vec{R} and the axis of the molecule. The leading term of Eq. (5.8) is exactly the VDW term C_{6H_2}/r^6 ; the anisotropy is described by the Legendre term P_2 ; in particular, Ref. [18] shows that the leading anisotropic correction involves Γ_6 which is of order 0.1. This quantity, even though might have some relevance, has been neglected: its effects can be taken into account; however, the results in this chapter may not change qualitatively; this has been checked with an arbitrary change of the VDW parameters for the interaction potential of both He-GF and He-GH. Moreover, this work is based on a semi-empirical adsorption potential and it is not aimed to obtain quantitative data.

The term $V_{gr}(\vec{r})$ can be treated in an analogous way of the term $V_{H-}(\vec{r})$,

$$V_{gr}(\vec{r}) = -\theta_{gr} C_{6C} \int d^2 \vec{R} \frac{1}{\left(z^2 + |\vec{R}|^2\right)^3} = - \left(\frac{\theta_{gr} \pi C_{6C}}{2}\right) z^{-4} = -\frac{A_C}{z^4}. \quad (5.9)$$

This approximation, however, neglects the buckling of the Carbon atoms and gives rise to variations of 8% in the case of GH (see Fig. 5.4). Apart from a shift in energy, we don't expect that this approximation would change the qualitative behavior of the system; in fact, as can be seen in Fig. 5.4, the larger differences are at the maxima of the adsorption potential, where the Helium density is lower. Nevertheless, in this work we preferred to use directly Eq. (5.3). The Helium-Carbon VDW coefficient appearing in this equation, C_{6C} , can be determined from the known[12] VDW coefficient $C_3 =$

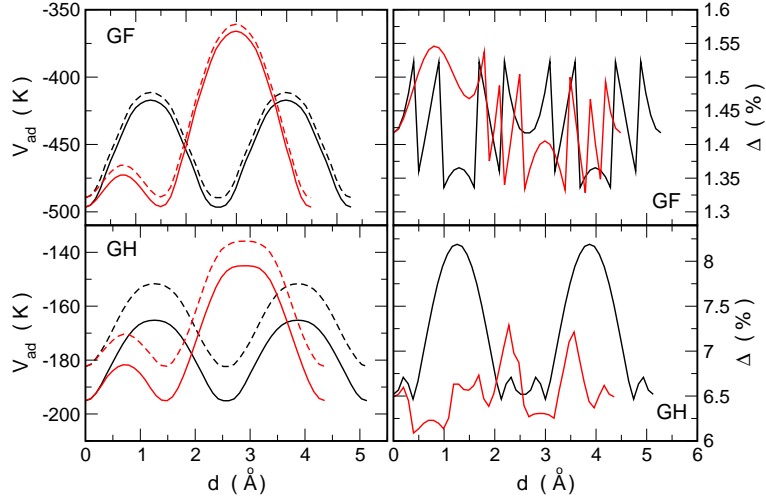


Figure 5.4: Upper figures: ${}^4\text{He}$ on GF. (Left) minimum value with respect to z of $V_{ads}(\vec{r})$ along the direction $(x, 0)$ (black) and $(0, y)$ (red). Full lines represent the adsorption potential, V_a , obtained using Eq. (5.3), dashed lines the adsorption potential, V_b , obtained with the approximation (5.9). (Right) the relative difference (in percentage) between V_a and V_b with respect to V_a , namely $100 * (V_b - V_a)/V_a$. Lower figures: the same for GH.

$180 \text{ meV}\text{-}\text{\AA}^3$ for an Helium atom interacting with a half-space of graphite, $V(z) \simeq -C_3 z^{-3}$. This is connected to the VDW interaction $\simeq -C_{6C} r^{-6}$ by an integral over the half-space; in a way similar to Eq. (5.5) we find the relationship between C_3 and C_{6C} ,

$$C_3 = \frac{\pi}{6} n C_{6C} \quad (5.10)$$

where $d = 3.4 \text{ \AA}$ is the distance between two carbon planes of Graphite; $n = \theta/d$ is the three dimensional density of the half plane of Graphite. Using Eq. (5.3) and Eq. (5.10) one obtains that $A_C = 3C_3 d = 1.84 \text{ eV}\text{-}\text{\AA}^4$.

The term in Eq. (5.4), $V_{H+}(\vec{r})$, gives the main attractive contribution; not only this term can not be integrated along the x - y plane but its proximity with the Helium monolayer requires the use of damping; we have adopted the Tang-Toennies damping procedure for this situation [13]; the term in Eq. (5.4) thus becomes

$$V_{H+}(\vec{r}) = - \sum_j V_{damp}(|\vec{r} - \vec{r}_j|)$$

$$V_{damp}(x) = C_{6H} \frac{1 - e^{-\beta x} \sum_{n=0}^6 \frac{(\beta x)^n}{n!}}{x^6}. \quad (5.11)$$

The function V_{damp} has an asymptotic x^{-6} behavior; for small values of x the divergence is cured; this can be seen with a Taylor expansion of $e^{-\beta x}$. Following Ref. [13],

the parameter β is the decay coefficient in the asymptotic charge density $\rho_H(r) \simeq e^{-\beta r}$ due to the H atom; for Hydrogen $\beta = 3.78 \text{ \AA}^{-1}$.

In the case of GF, $V_{\text{att}}(\vec{r})$ has an expression similar to Eq. (5.1) with V_{H+} and V_{H-} replaced by V_{F+} and by V_{F-} . The same procedure used for GH applies with the coefficient $C_{6F} = 4.2 \text{ eV}\text{-}\text{\AA}^6$ as given by Frigo et al [19], $\beta = 3.2 \text{ \AA}^{-1}$ and $A_F = 1.1 \text{ eV}\text{-}\text{\AA}^4$.

Table 5.1: Parameters for the adsorption potential of He on GH and GF

Parameter	Value	Type
C_{6F}	$4.2 \text{ eV}\text{\AA}^6$	GF
C_{6H}	$1.206 \text{ eV}\text{\AA}^6$	GH
C_{6C}	$3.447 \text{ eV}\text{\AA}^6$	GF/GH
A_F	$1.1 \text{ eV}\text{\AA}^4$	GF
A_H	$0.3455 \text{ eV}\text{\AA}^4$	GH
β_F	3.2125 \AA^{-1}	GF
β_H	3.77945 \AA^{-1}	GH
γ	$53.9392 \text{ eV}\text{\AA}^3$	GF/GH

The obtained adsorption potential relies on the electron density of the substrate. This quantity is the output of a DFT computation and is in the form of a $3d$ table formatted as $i\delta x, j\delta y, k\delta z, value$, where $\delta x, \delta y, \delta z$ is the spatial discretization of the electron density table. The adsorption potential that enters as input in the QMC simulations is thus a $3d$ table; this table is read in the simplest way: if the simulation box is a cube in the region with positive coordinates, a position $\vec{r} = (x, y, z)$ corresponds to a bin in the table defined by (a, b, c) , where $a = x/dx$, $b = y/dy$ and $c = z/dz$.

With such model potentials the adsorption sites (see Fig. 5.6) are above the centers of each triplets of H (F) atoms of the overlayer, forming a honeycomb lattice with the number of sites equal to the number of C atoms, twice as many as those on Gr. Half of the sites are above H (F) of the underlayer but the difference between the well depths for the two kinds of adsorption sites is very small, below 1%. For GF the well depth is 498 K and for GH it is 195 K. These values do not include the induced dipole energy which gives a contribution below 1%. The inter-site energy barrier is 24 K for GF and 13 K for GH. Both values are significantly smaller than the barrier height 41K for graphite. In this last case, as shown in Fig. 5.7, the energy barrier does not depend much on the direction in the $x - y$ plane whereas in the case of GF and GH the ratio between maximum and minimum barrier height in the $x - y$ plane is of order of 4–5: the energy landscape of the two last substrates is characterized by a very large corrugation with narrow channels along which low potential barriers are present. The motion of the He atom, especially in the case of GF, essentially visits only these channels, as though the atom moves in a multiconnected space; this is seen in Fig. 5.0.6. Another significant difference is that the distance between two neighboring sites is 1.49 \AA for GF and 1.45 \AA for GH whereas it is 2.46 \AA for

graphite and for Gr. Prior to these studies, graphite was believed to be the most attractive surface for He, with a well–depth a factor of 10 greater than that on the least attractive surface (Cs). The present results reveal GF to replace graphite, since its well is a factor of 3 more attractive.

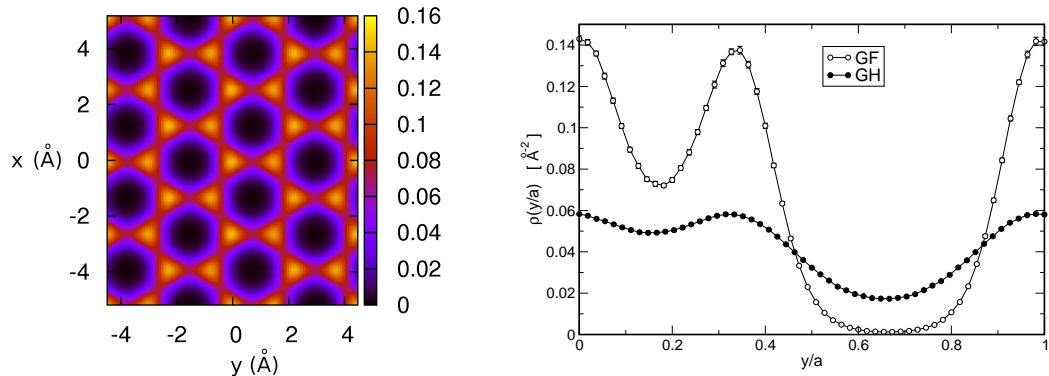


Figure 5.5: Upper panel: local density $\rho(x, y)$ (in units of \AA^{-2}) as function of x – y for ${}^4\text{He}$ at equilibrium density on GF. Lower panel: local density $\rho(x = 0, y)$ (in units of \AA^{-2}) in the unit cell (with side $a = 4.486 \text{ \AA}$ in the GF case and $a = 4.347 \text{ \AA}$ in the GH case) along the y direction for ${}^4\text{He}$ at equilibrium density on GF and GH; note the logarithmic scale used for $\rho(x = 0, y)$. Error bars are below the symbol size; lines are guides to the eye.

5.0.7 The QMC parameters

The computations in this chapter are based on the Path Integral Ground State[20] (PIGS) and the Path Integral Monte Carlo (PIMC) methods[21]. As widely explained in the first chapter, with these methods we can compute quantum averages of the system at respectively zero and finite temperature; the PIGS method uses the quantum evolution in imaginary–time τ of a trial wave function Ψ_t . If Ψ_t is not orthogonal to the ground state, and τ is sufficiently long, the quantum evolution purges from Ψ_t the contributions of the excited states, yielding the ground state energy and wave function. A valuable feature of the PIGS method is that it is exact, in principle; the results are independent of Ψ_t [22] and systematic errors may be reduced below the statistical uncertainty. The PIMC method applies the Path Integral formalism to the quantum thermal average expressed in coordinates representation; this expression is then evaluated with Monte Carlo methods; these methods are extensively explained in Chapter 2.

Both the zero and finite temperature simulations on GF and GH have been performed with the eight order Multi Product Expansion of the small imaginary–time propagator; the imaginary–time discretization is $\delta\tau = 1/160 \text{ K}^{-1}$, which gives a sufficiently accurate approximation of the propagator; an example in the case of GF is given in Fig. 5.8. Due to the computational complexity of PIMC, especially at low

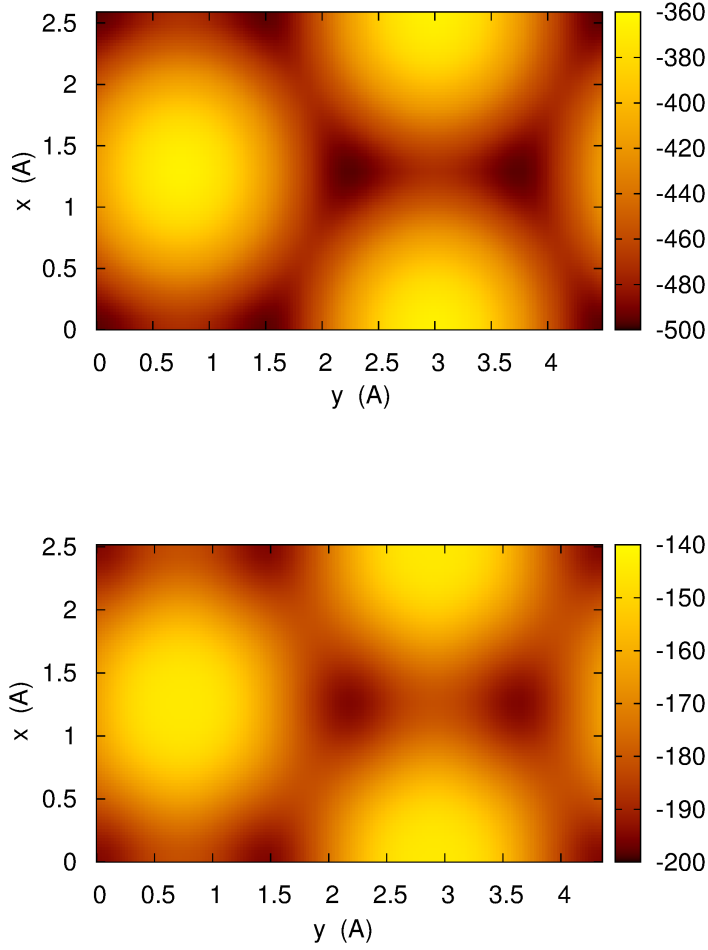


Figure 5.6: Upper panel: plot of the minimum value with respect to z of the adsorption potential He–GF, $V(\vec{r})$, in K as function of x – y . Lower panel: the same for GH.

temperatures (i.e. 0.5 K), the simulations at finite temperature performed in order to obtain an estimation of the superfluid density were carried out with $\delta\tau = \frac{1}{60} \text{ K}^{-1}$; this choice does not lead to quantitative results, however we note once again that this work is based on a semi-empirical adsorption potential; moreover, a quantitative study of the superfluid fraction would require extensive size scaling in order to determine the normal–to–superfluid transition; the aim of these simulation is thus to give a preliminary estimate of the superfluid fraction in order to determine *if* there is superfluidity rather than the exact density.

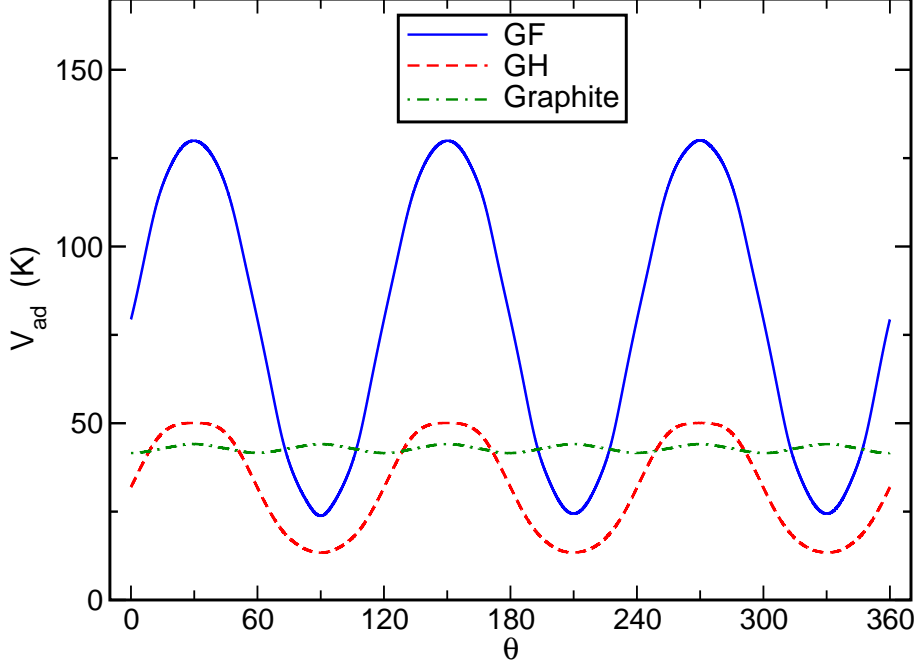


Figure 5.7: Energy barrier in GF, GH and graphite as atom moves along a line making an angle θ with the horizontal direction and following the height $z(x, y)$ giving the minimum of $V(\vec{r})$. Plotted energy is relative to energy at the adsorption site.

The trial wave function Ψ_t that we have used in PIGS is the product of a Jastrow-McMillan wave function and a Gaussian along the z -direction

$$\Psi_t = e^{-\sum_{i<j=1}^N \left(\frac{b}{r_{ij}}\right)^m} e^{-A \sum_{i=1}^N (z_0 - z_i)^2} \quad (5.12)$$

where N is the particle number and $r_{ij} = |\vec{r}_i - \vec{r}_j|$ is the distance between two atoms labeled i and j . The Jastrow parameters are $b = 2.84\text{\AA}$ and $m = 5$. The Gaussian along the z -direction (i.e. the direction perpendicular to the substrate plane) was used only far away from the layer promotion density; its parameters have been obtained with a fit of the density along the z -direction, for GF $A = 5.6\text{\AA}^{-2}$, $z_0 = 3.72\text{\AA}$, for GH $A = 3.0\text{\AA}^{-2}$ and $z_0 = 3.85\text{\AA}$.

At high densities, where the probability to occupy the second layer is not negligible, a Jastrow wave function has been used,

$$\Psi_t^{hd} = e^{-\sum_{i<j=1}^N \left(\frac{b}{r_{ij}}\right)^m}. \quad (5.13)$$

With these trial wave functions, we allowed a $\delta\tau = 0.15 \text{ K}^{-1}$ imaginary-time projection before computing the ground-state expectation values. The total imaginary-time sampled in our calculations was $\tau = 0.4 \text{ K}^{-1}$. The value of τ has been chosen following a convergence test of the total energy versus the imaginary-time projection.

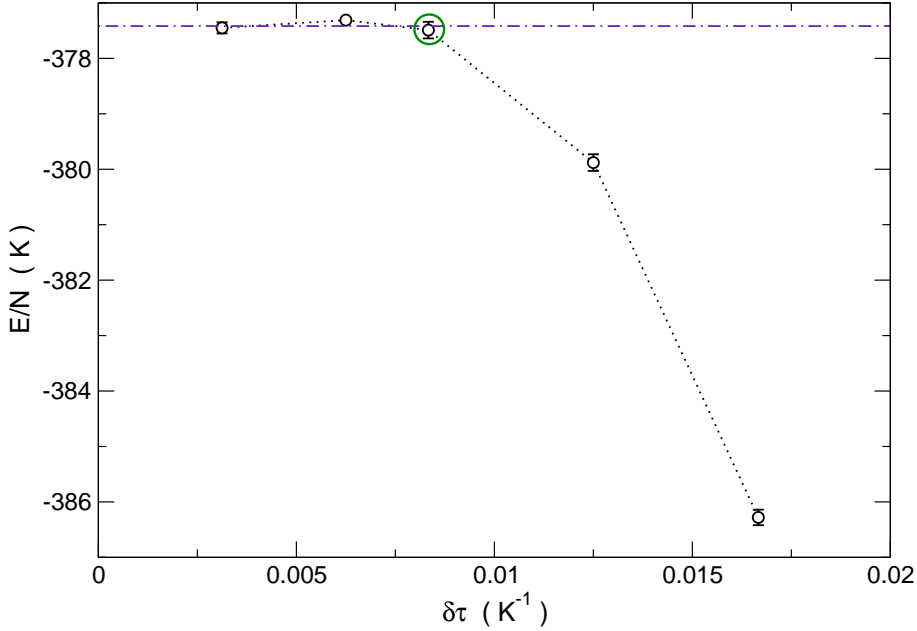


Figure 5.8: Convergence of the total energy per particle versus time-step $\delta\tau$ for a system of $N = 26$ atoms of ${}^4\text{He}$ on GF at equilibrium density. The horizontal line is the convergence value taken as the average of the energy at the three smallest timesteps. The green circle represents the used time-step, $\delta\tau = 1/160 \text{ K}^{-1}$.

The Worm algorithm[23] was used at both finite and zero temperature respectively for the sampling of the permutations and the computation of the one body density matrix.

The computations required on average 10^5 Monte Carlo steps, the heaviest computations were those made for the superfluid fraction at zero temperature and required approximately 10^7 Monte Carlo steps.

5.0.8 A single Helium atom on the substrates

We computed the exact ground state energy of one ${}^4\text{He}$ atom or one ${}^3\text{He}$ atom on GF and GH, see Table 5.2. The binding energy on GH is similar to that on graphite, whereas that on GF is about three times that on graphite. In both cases the ground state is delocalized over the full substrate and both kinds of adsorption sites are occupied with comparable probability.

We have also computed the density-density imaginary time correlation function in Fourier space; in the case $N = 1$, at an imaginary-time τ , this function takes the form: $F(\vec{k}, \tau) = \langle \rho_{\vec{k}}(\tau) \rho_{-\vec{k}}(0) \rangle$, $\rho_{\vec{k}}(\tau) = \exp[i\vec{k} \cdot \vec{r}(\tau)]$. Here $\vec{r}(\tau)$ is the position of the atom at imaginary time τ . $F(\vec{k}, \tau)$ contains informations on the excited states of the system; these informations can be extracted through an inversion of the Laplace

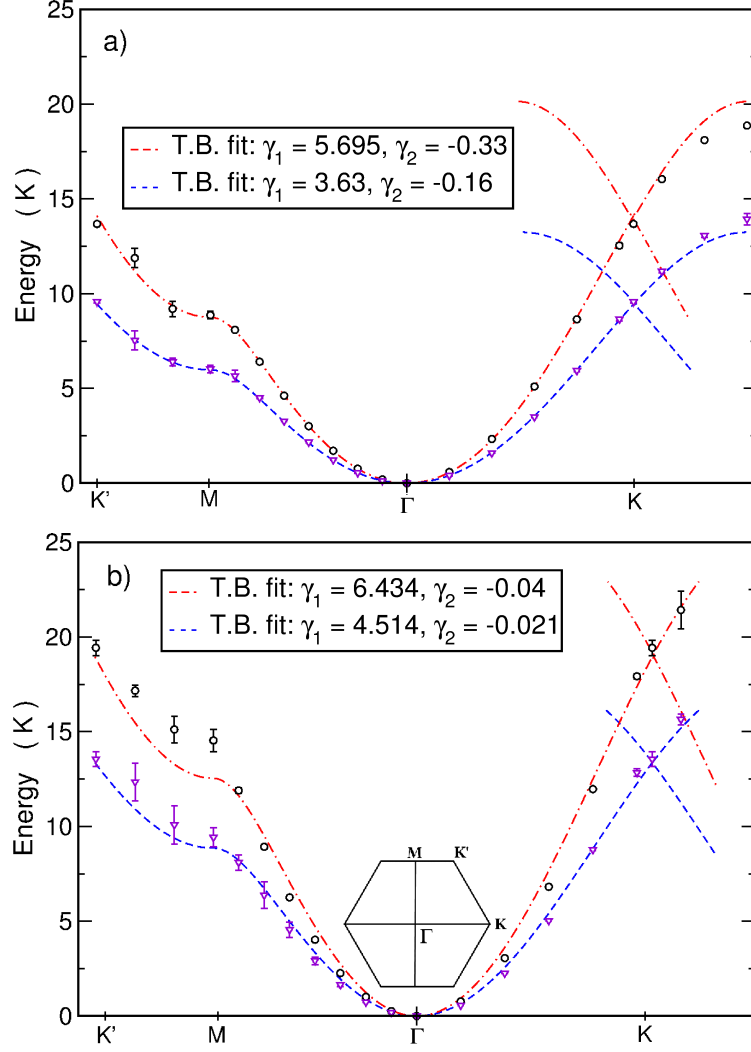


Figure 5.9: Panel a) Energy of the first band along two directions of the first Brillouin zone for ${}^4\text{He}$ (triangles) and ${}^3\text{He}$ (circles) on GF. Data along ΓK beyond the Dirac point K give the results in the II Brillouin zone. The dashed lines are fits made with the tight binding model on a honeycomb lattice with nearest neighbor parameter γ_1 and next nearest neighbor parameter γ_2 as in legend. Panel b) Same as for panel a) for ${}^4\text{He}$ and ${}^3\text{He}$ on GH.

transform that gives the dynamic structure factor $S(\vec{k}, \omega)$:

$$F(\vec{k}, \tau) = \int d\omega e^{-\omega\tau} S(\vec{k}, \omega). \quad (5.14)$$

However, $F(\vec{k}, \tau)$ is known only at discrete imaginary-times τ_m with a statistical uncertainty; the inversion of the Laplace transform in such conditions is an ill-posed inverse problem; as consequence, the quality of the extracted informations can not

Table 5.2: Kinetic, potential and total energies for the ground state of He on GF, on GH and on graphite. In the last column the bandwidth Δ is shown. Numbers in parentheses represent statistical uncertainty in the last digit.

System	E_{kin} (K)	E_{pot} (K)	E_{tot} (K)	Δ (K)
$^4\text{He}+\text{GF}$	46.78(4)	-422.94(1)	-376.15(2)	9.6(1)
$^3\text{He}+\text{GF}$	51.08(1)	-413.41(1)	-362.33(1)	13.7(1)
$^4\text{He}+\text{GH}$	20.51(1)	-153.58(1)	-133.06(1)	13.6(4)
$^3\text{He}+\text{GH}$	22.53(2)	-149.50(1)	-126.97(2)	19.4(4)
$^4\text{He}+\text{Gr}$	25.30(4)	-168.49(1)	-143.19(4)	9.6(2)
$^3\text{He}+\text{Gr}$	27.05(2)	-162.87(1)	-135.82(2)	15.7(4)

be guaranteed. The inversion of the Laplace transform has been computed with the GIFT method explained in Ref. [24]. Basically, the GIFT method uses a Genetic Algorithm to explore a space of solutions $\{S_n(\vec{k}, \omega)\}$; the solutions that can reproduce $F(\vec{k}, \tau)$ with an user-defined accuracy are averaged together to give the solution. In

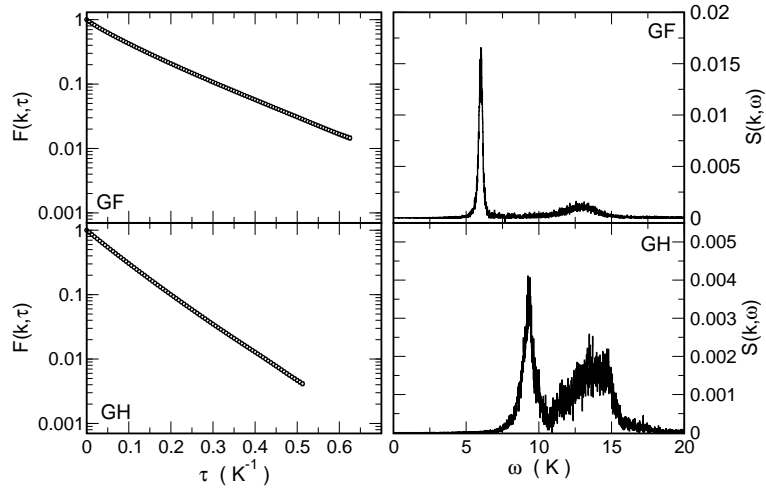


Figure 5.10: Left side: density-density correlation functions $F(\vec{k}, \tau)$ for a wave vector \vec{k} corresponding to the point M in the first Brillouin zone (see Fig. 5.9). On the right side the respective inversions of Laplace transform, $S(\vec{k}, \omega)$, are shown.

Fig. 5.10 an example of $F(\vec{k}, \tau)$ and its $S(\vec{k}, \omega)$ obtained with GIFT is given: in these functions $F(\vec{k}, \tau)$, the main contribution comes from the lowest energy band; moreover, the excitation appears in $S(\vec{k}, \omega)$ as a well defined peak; it is thus possible to obtain the energy spectrum of the first energy band; we interpret the width of the peaks as the uncertainty associated to the excitation energy at that wave-vector. The computed energy spectrum along the directions ΓK and ΓM for He on GF and

on GH is shown in Fig. 5.9. These bands are represented rather accurately by a tight binding model with nearest and next nearest coupling [25].

substrate and $N=1$ properties		
Property	GF	GH
U_0	498 K	195 K
BA	24 K	13 K
d_s	1.49 Å	1.45 Å
E_0 for ^4He	-376.15(2) K	-133.06(1) K
E_0 for ^3He	-362.33(1) K	-126.97(2) K
BW of ^4He	9.6 K	13.6K
BW of ^3He	13.7 K	19.4 K
m^*/m of ^4He	1.40	1.05
m^*/m of ^3He	1.26	1.01

Table 5.3: Substrate and $N=1$ properties, with: U_0) Depth of potential well; BA) Inter-site energy barrier; d_s) Inter-site distance; E_0) Ground state energy; BW) Bandwidth; m^*/m effective mass to bare mass ratio.

For comparison we have computed with this same method the band energy for He on graphite finding substantial agreement with the Carlos and Cole result for the lowest band [26]. The bandwidths Δ of He on these three substrates are given in Table 5.2.

From the first energy band it is possible to obtain an estimate of the effective mass of one atom of Helium on GF(GH); this is done with a fit of the energy band at small wave-vectors (in Fig. 5.9 it is the region around the point Γ); in fact, for small wave-vectors the first energy band $E_k \simeq \hbar^2 k^2 / (2m^*)$. The effective masses m^* of the various systems reflect the varying corrugations of the potentials. For ^4He (^3He), the ratios of m^* to the bare mass are 1.40 (1.25), 1.10 (1.08) and 1.05 (1.01) on GF, graphite and GH, respectively. The smaller mass enhancement of ^3He than ^4He reflects the smaller ratio of the corrugation potential to the translational zero-point energy.

5.0.9 Equilibrium density of submonolayer ^4He on GF

We have studied a ^4He submonolayer on GF. Some of the obtained properties are in Tab. 5.4. As He-He interaction we have used an Aziz potential [27]. The ground state has been computed for a number of ^4He atoms from 22 to about 120 spanning the density range $\rho=0.04\text{--}0.09 \text{ \AA}^{-2}$. On graphite the ground state is the commensurate $\sqrt{3} \times \sqrt{3}$ R30° state with filling factor 1/3 of the adsorption sites. A similar state on GF is obtained by populating fourth neighbor sites (this corresponds to second neighbors in one of the sublattices of the honeycomb at a distance 4.482 Å) with a filling factor of the adsorption sites equal to 1/6 and it corresponds to a density $\rho_{1/6}^{\text{GF}} = 0.0574 \text{ \AA}^{-2}$. Notice that this density is smaller than the $\rho_{\sqrt{3}} = 0.0636 \text{ \AA}^{-2}$ on graphite due to the dilation of the C plane in GF.

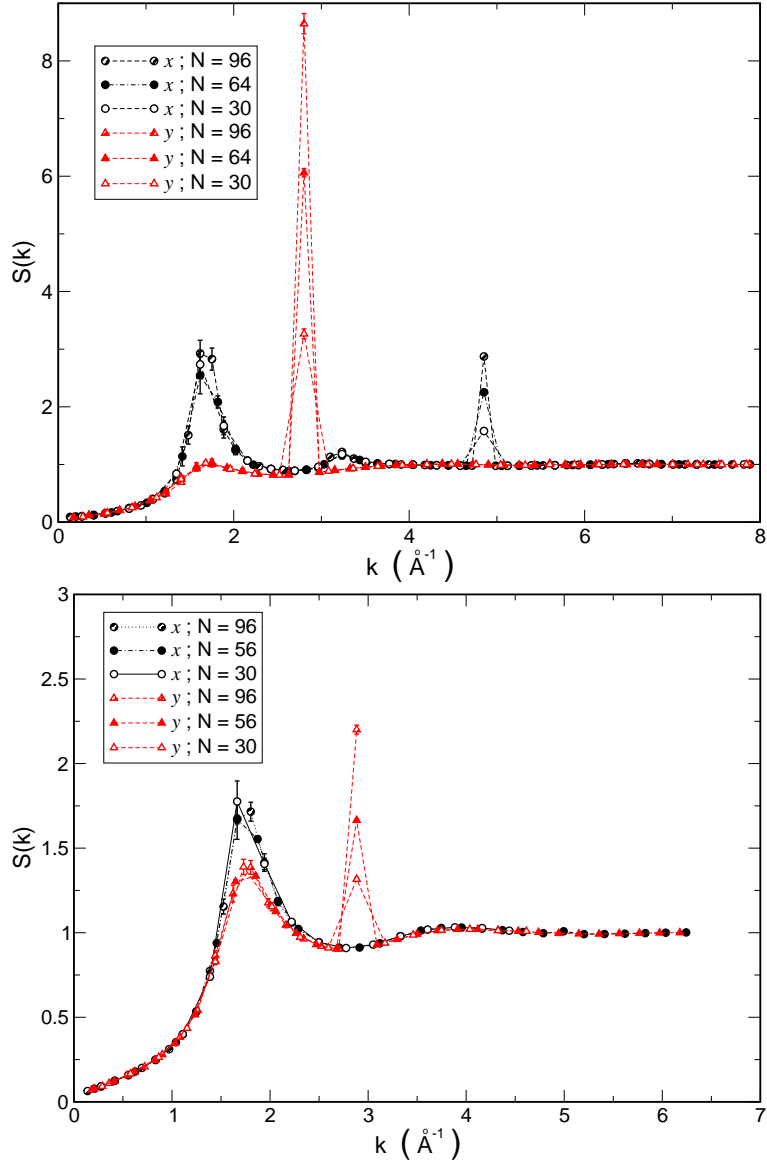


Figure 5.11: Upper panel: static structure factor for GF at density $\rho_{1/6}^{\text{GF}}$. Lower panel: the same for GH, at density $\rho_{1/6}^{\text{GH}}$. Lines are guides to the eyes.

A simple consideration suggests the instability of a similar commensurate state. Using the curvature of the He–substrate potential at an adsorption site, the two-dimensional zero point energy is estimated to be 55(40) K on GF (GH), much larger than the minimum potential barrier 23(13) K, so that such a localized state might be unstable. We find indeed that this ordered state is unstable: starting the simulation from an ordered configuration after a short Monte Carlo evolution the Bragg peaks corresponding to the $\sqrt{3} \times \sqrt{3}$ R30° state disappear and the system evolves into a disordered fluid state modulated by the substrate potential. $S(k)$ at this density is plotted in Fig. 5.11 as function of k_x and k_y for two numbers N of particles: the

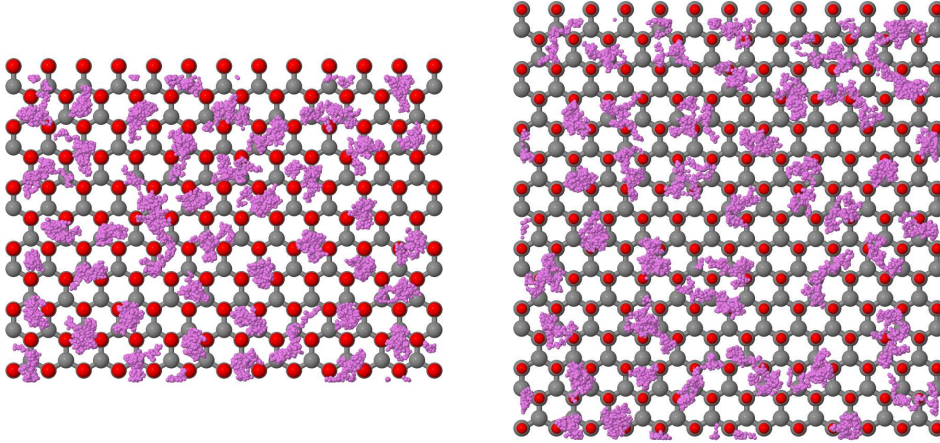


Figure 5.12: Polymer configurations for a liquid system of $N = 43$ atoms of ${}^4\text{He}$ on GF (left) and $N = 41$ atoms of ${}^4\text{He}$ on GH (right) at equilibrium density. Each polymer represents the evolution up to 0.4 K^{-1} in imaginary time of its correspondent ${}^4\text{He}$ atom. The substrate is represented in the background with carbon atoms marked in gray and the F(H) overlayer marked in red.

intensity of some of the peaks do not depend on N so they are due to short range order, others scale roughly as N and arise from the modulation of the density due to the adsorption potential.

Many-body properties		
Property	GF	GH
ρ_{eq}	0.049 \AA^{-2}	0.042 \AA^{-2}
x	0.142	0.115
E_0	$-377.71(4) \text{ K}$	$-134.02(5) \text{ K}$
E_b	$1.55(6) \text{ K}$	$0.95(6) \text{ K}$
n_0	$11 \pm 1 \%$	$22.6 \pm 1.3 \%$
ρ_s/ρ	$0.60(3)$	$0.95(3)$
T_c	$0.2\text{--}0.3 \text{ K}$	$1.0\text{--}1.2 \text{ K}$
ρ_{sat}	0.136 \AA^{-2}	0.108 \AA^{-2}

Table 5.4: Many-body properties, with: ρ_{eq}) Equilibrium density; x) coverage; E_0) Ground state energy per particle; E_b) Binding energy; n_0) Condensate fraction; ρ_s/ρ) $T=0 \text{ K}$ superfluid fraction; T_c) Transition temperature; ρ_{sat}) Completion density

Fig. 5.12 shows a sampled configuration of polymers for a system of ${}^4\text{He}$ on GF and GH at equilibrium density. The spread in space of a single polymer is related to the zero point motion, whereas the center of mass of each polymer gives an idea of the spatial order of that configuration. As expected, the polymers stay on average over the adsorption sites but, apart from the modulation of the external potential, there is not spacial order due to the He–He interaction. It is interesting to note that

sometimes zero point motion allows a polymer to stretch toward a near adsorption site by crossing a saddle point; this is a dynamic in imaginary time that eventually leads a polymer to connect with an adjacent one implementing quantum exchanges phenomena in a multi connected geometry. On average, such exchanges are more frequent in the configuration on the GH substrate rather than that on the GF, this is expected because of the strongest confinement given by the GF adsorption potential.

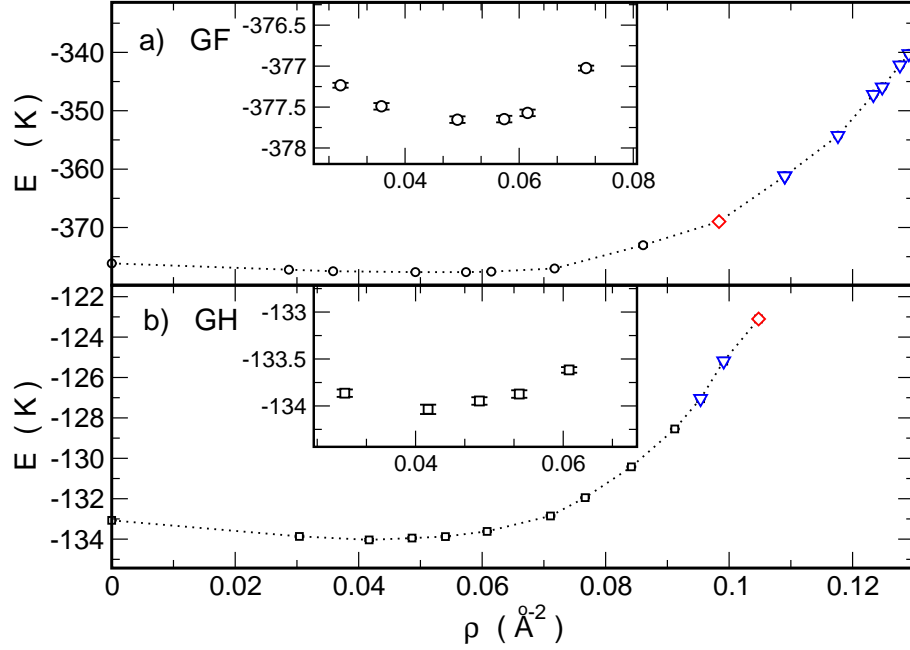


Figure 5.13: Panel (a): Energy per particle of ^4He on GF at $T = 0\text{K}$. Panel (b): Equation of state of ^4He on GH at $T = 0\text{K}$. The inset represents a zoom in the region around the energy minimum. In both cases, the used particle numbers ranged between $N = 60$ and $N = 120$. The dashed line represents a guide to the eye. Circles are liquid densities, Squares represent the commensurate $2/7$ phase and Triangles are incommensurate densities.

In Fig. 5.0.9 the energy per particle of ^4He on GF and ^4He on GH at the studied densities are reported. In the GF case, the energy per particle has a minimum value $E_0 = -377.71 \pm 0.04\text{ K}$ at the density $\rho_{eq} = 0.049\text{ \AA}^{-2}$. This lies $1.55(6)\text{ K}$ below the single particle energy, implying that the ground state is a self-bound liquid. In the GH case a similar state is obtained, with $E_0 = -134.02 \pm 0.05\text{ K}$ and a binding energy per atom of $0.95(6)$. For comparison, we note that the strictly 2D cohesive energy of ^4He [28] is just 0.84 K and the equilibrium density is $\rho = 0.0436\text{ \AA}^{-2}$. In both the cases a liquid phase has been found at least for densities up to filling factors $x = 1/4$ that for the GF case correspond to a density $\rho_{1/4}^{GF} = 0.0861\text{ \AA}^{-2}$, and for the GH case to a density $\rho_{1/4}^{GF} = 0.0912\text{ \AA}^{-2}$.

In Fig. 5.0.9 the local density on the x - y plane is shown for ^4He on GF (left) and GH (right) at equilibrium density. These local densities clearly reflect the geometry

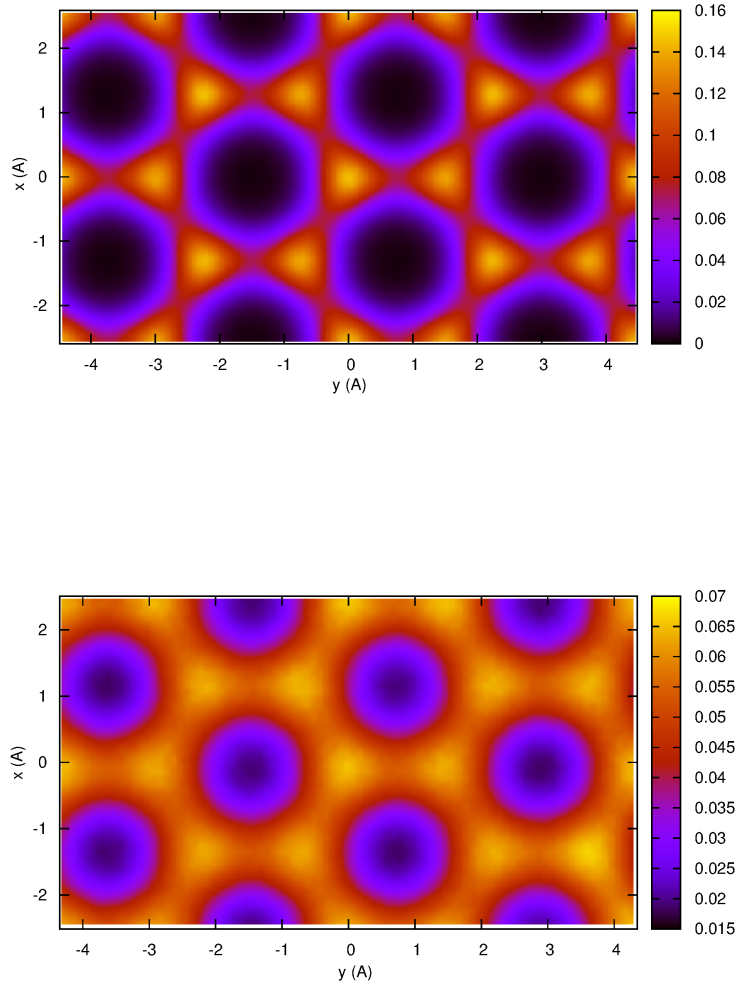


Figure 5.14: Local density (in \AA^{-2} units) on the x-y plane integrated along the z direction of $N = 33$ atoms of ${}^4\text{He}$ on GF (left) and $N = 41$ atoms of ${}^4\text{He}$ on GH (right) at equilibrium density.

of the adsorption potential shown in Fig. 5.6. The system is energetically allowed to stay in a multi-connected space in which adsorption minima are reachable through channels that cross a saddle point of the adsorption potential. Note that although the geometry in the two cases is the same, the potential barrier above the F (H) overlayer is much lower in the GH case (see Fig. 5.7), this produces an higher degree of anisotropy in the GF case and reflects in the local density as a non-zero probability to occupy an adsorption maximum in the GH case.

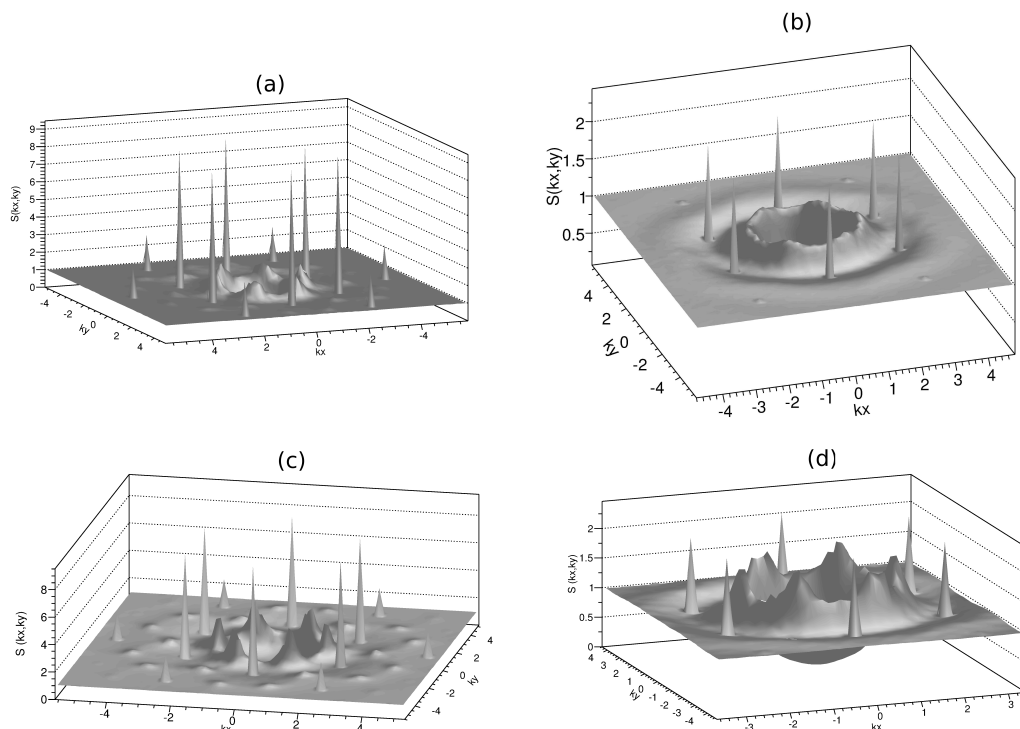


Figure 5.15: Static structure factor on the x - y plane of $N = 96$ atoms of ${}^4\text{He}$ on GF at equilibrium density (upper left), on GH at equilibrium density (upper right), on GH at filling factor $x = 1/6$ (lower left), on GH at $x = 1/6$ (lower right).

The static structure factor of ${}^4\text{He}$ on GF and GH at equilibrium density as well as that at filling factor $x = 1/6$ are shown in Fig. (5.0.9). The sharp peaks reflect the density modulation due to the corrugation of the adsorption potential. The crater like structure at smaller k represents short range He-He correlations. It can be noticed that short range correlations in the GH case are much less anisotropic than that in the GF case, this reflects the smaller corrugation of the adsorption potential of GH.

We have computed the off diagonal one body density matrix $\rho_1(r - r')$. As can be seen in Fig. 5.0.9 ρ_1 reaches a plateau at large $r - r'$ and the Bose Einstein condensate (BEC) fraction is $10.3 \pm 0.4 \%$ at $\rho = 0.049 \text{ \AA}^{-2}$ and $7.3 \pm 1.5 \%$ at $\rho_{1/6}$; the system is superfluid. We reach a similar conclusion in the case of the GH substrate: the ground state is a liquid with density $\rho_{eq} = 0.045 \text{ \AA}^{-2}$ and $E_0 = -134.28 \pm 0.02 \text{ K}$ per atom and the BEC fraction is $22.6 \pm 1.3 \%$ at the equilibrium density and $6.8 \pm 0.5 \%$ at $\rho_{1/6}^{\text{GH}} = 0.0608 \text{ \AA}^{-2}$. Note that this condensate fraction is significantly smaller than the value ($\simeq 40 \%$) for ${}^4\text{He}$ in 2D [28]. The smaller value is a consequence of the spatial order, albeit imperfect, induced by the substrate potential and of the smaller effective surface available to the atoms due to the strong channeling induced by that potential.

In Fig. (5.0.9) the superfluid fraction ρ_s/ρ is shown in function of the temperature for a system of $N = 26$ atoms of ${}^4\text{He}$ on GF and $N = 20$ atoms of ${}^4\text{He}$ on GH at their

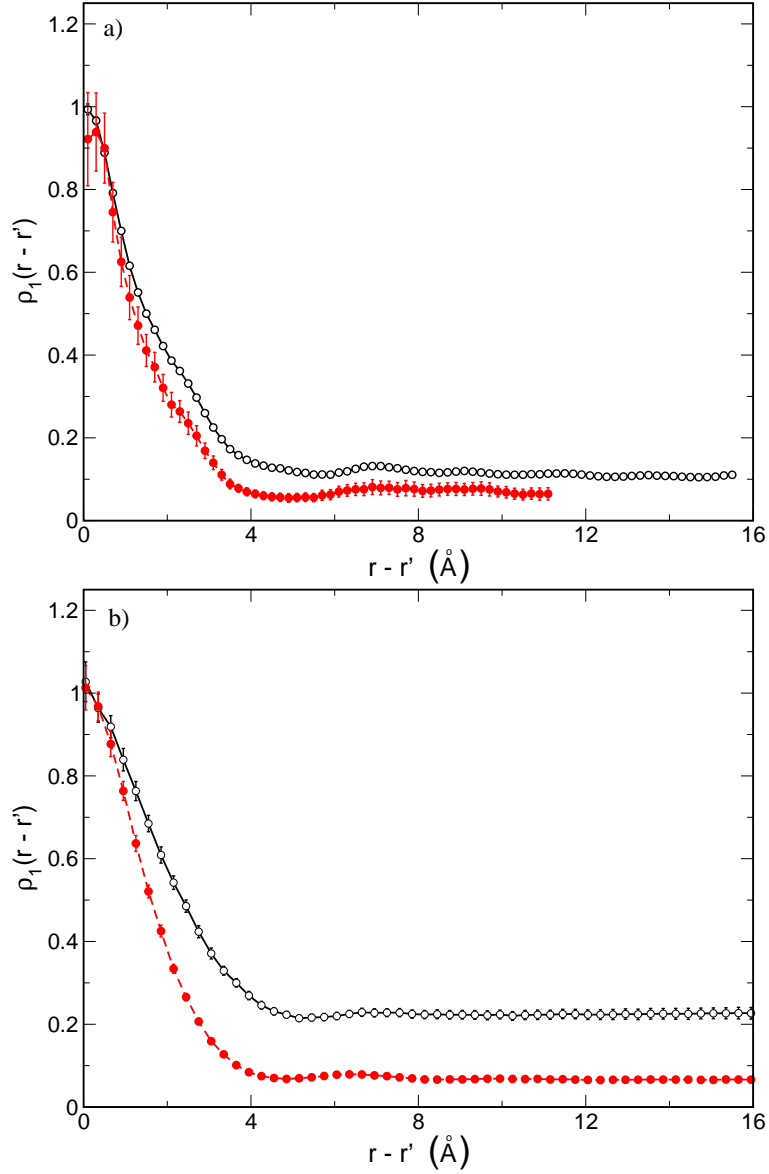


Figure 5.16: Panel a) Off diagonal one body density matrix for ${}^4\text{He}$ on GF at $\rho_{eq}^{\text{GF}} = 0.049 \text{ \AA}^{-2}$ (open circles) and $\rho_{1/6}^{\text{GF}} = 0.0574 \text{ \AA}^{-2}$ (filled circles). Panel b) the same for GH, with $\rho_{eq}^{\text{GH}} = 0.042 \text{ \AA}^{-2}$ and $\rho_{1/6}^{\text{GH}} = 0.0608 \text{ \AA}^{-2}$. Lines are guides to the eyes.

respective equilibrium densities. At finite temperature, the superfluid fraction has been estimated with the winding number method. The data at zero temperature has been obtained with the evolution of the center of mass of the system for sufficiently

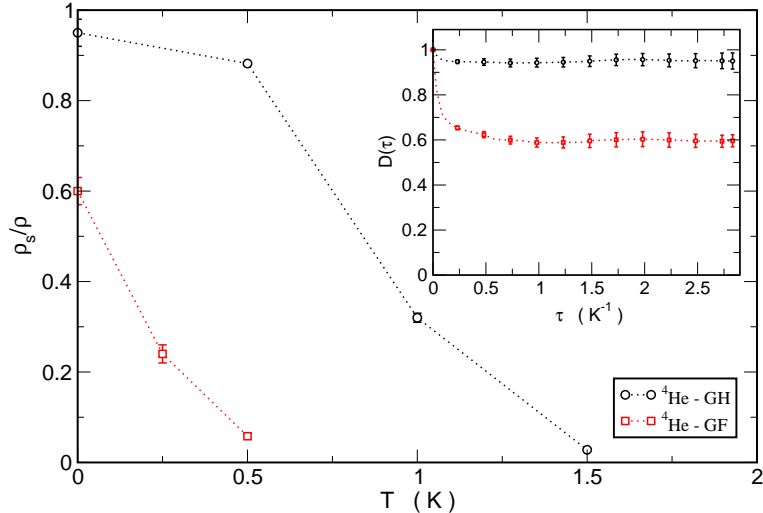


Figure 5.17: The superfluid fraction as function of temperature for a system of $N = 20$ atoms of ${}^4\text{He}$ on GH and a system of $N = 26$ atoms of ${}^4\text{He}$ on GF. The transition temperature can be roughly estimated in the range $1.0 - 1.2$ K for ${}^4\text{He}$ -GH and $0.2 - 0.3$ K for ${}^4\text{He}$ -GF. In the inset is displayed the diffusion of the center of mass from which the zero-temperature estimation of the superfluidity has been extrapolated.

large imaginary-time[29] τ :

$$\frac{\rho_s}{\rho} = \lim_{\tau \rightarrow +\infty} D(\tau)$$

$$D(\tau) = \frac{N}{2d\lambda} \frac{\left\langle \left[\vec{R}_{CM}(\tau) - \vec{R}_{CM}(0) \right]^2 \right\rangle}{\tau}, \quad (5.15)$$

where $\lambda = \hbar^2/2m$, N is the number of particles, d is the number of dimensions along which the contribution to the superfluid fraction is considered, and the squared distance $[\vec{R}_{CM}(\tau) - \vec{R}_{CM}(0)]$ is evaluated without invoking periodic boundary conditions, i.e. including boundary crossing if $\vec{R}_{CM}(\tau)$ leaves the main simulation box. Note that in general the estimator for the superfluid fraction in equation 5.15 can be used with a PIGS algorithm only when the Hamiltonian of the system explicitly breaks the translational symmetry as in the present case. This is a necessary condition because even if one starts from a trial state Ψ_T in which the translational symmetry is broken, the imaginary-time evolution of Ψ_T obtained via PIGS (i.e. $\Psi_\tau = \hat{G}(\tau)\Psi_T$) immediately, for every imaginary time τ restore the translational invariance unavoidably disturbing the estimation of $D(\tau)$. This is due to the fact that the imaginary time evolution depends only on the Hamiltonian via $\hat{G}(\tau) = \exp(-\tau\hat{H})$.

It is noticeable that ρ_s/ρ for ${}^4\text{He}$ on GH joins smoothly with the $T = 0\text{K}$ value. This is a strong test on our algorithms since these values come from completely different computations, however, in the case of GF, the low transition temperature does not allow to reach the $T \ll T_c$ regime. From ρ_s/ρ at finite T and taking into

account size effect we estimate the superfluid transition temperature $T_c \simeq 0.2 - 0.3$ K for GF and $1.0 - 1.2$ K for GH. From the zero temperature computation of the superfluid density we predict that a submonolayer of ^4He film on GF (GH) is an *anisotropic* superfluid with superfluid fraction $\rho_s/\rho = 0.95(3)$ for GH and $0.60(3)$ for GF. Remarkably, this quantity is less than unity and this is in agreement with the predictions by Leggett for a nonuniform superfluid [30].

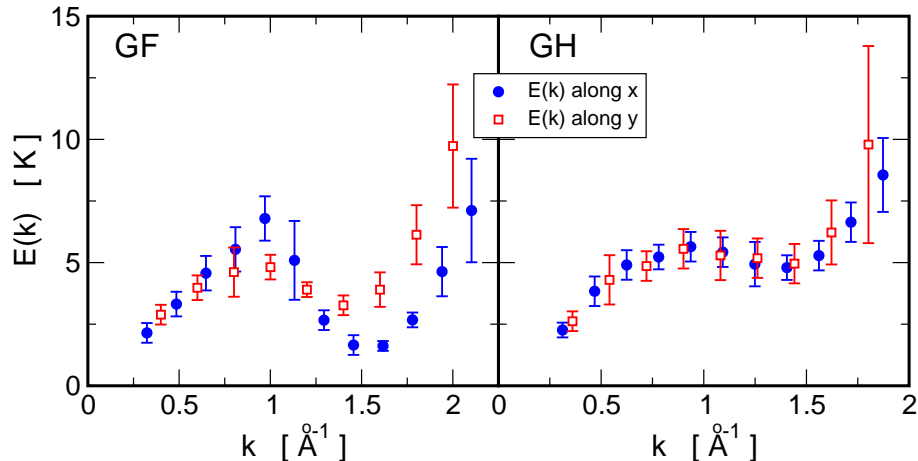


Figure 5.18: Left: Excitation spectrum, $E(k)$, of ^4He on GF at equilibrium density along x and y directions extracted from the position of the quasi-particle excitation peaks in the dynamical structure factors obtained via the GIFT algorithm. The error-bars represent the 1/2-height widths. The Bijl-Feynman spectrum, $E_F(k)$, is also shown. Right: The same for ^4He on GH. Lines are guides to the eye.

Dynamics at equilibrium density

Information about dynamical properties can, in principle, be extracted from imaginary time correlation functions, without relying on any approximation, focusing on an ill-posed inverse problem, i.e. the inversion of the Laplace transform which connects a suitable imaginary time correlations function $f(\tau)$ to the relevant spectral function. If one consider the dynamical structure factor $S(\vec{k}, \omega)$, which is measurable in an inelastic neutron scattering experiment, the related imaginary-time correlation function is the so called “intermediate scattering function” $F(\vec{k}, \tau)$:

$$F(\vec{k}, \tau) = \frac{1}{N} \langle e^{\tau \hat{H}} \hat{\rho}_{\vec{k}} e^{-\tau \hat{H}} \hat{\rho}_{-\vec{k}} \rangle = \int d\omega e^{-\omega\tau} S(\vec{k}, \omega) \quad . \quad (5.16)$$

The expression of $F(\vec{k}, \tau_i) = \langle e^{\tau_i \hat{H}} \hat{\rho}_{\vec{k}} e^{-\tau_i \hat{H}} \hat{\rho}_{-\vec{k}} \rangle / N$ can be estimated via “exact” Quantum Monte Carlo methods for a discrete set of imaginary time instants τ_i . However, the extraction of $S(\vec{k}, \omega)$ from the above integral equation, based on the limited and noisy knowledge of $F(\vec{k}, \tau)$, is an ill-posed inverse problem; in fact, the kernel $e^{-\omega\tau}$

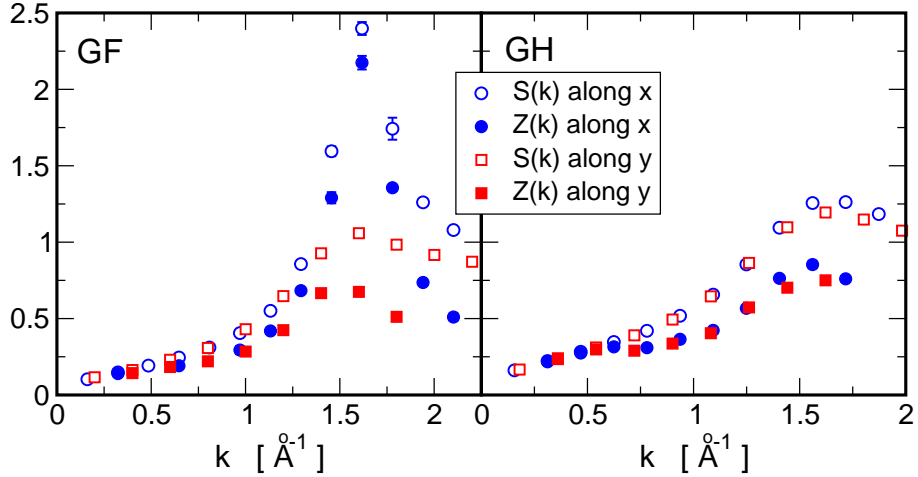


Figure 5.19: Left: Static structure factors $S(\vec{k})$ and strength of the quasi particle peak $Z(\vec{k})$ as function of q of ${}^4\text{He}$ on GF at equilibrium density along x and y directions. Right: The same for ${}^4\text{He}$ on GH.

is strongly smoothing and infinite dynamical structure factors turn out to be compatible with the information on the correlation function, i.e. with $F(\vec{k}, \tau_i)$ for the different τ_i . Recently, we have developed a technique to face such problems quite in general: the Genetic Inversion via Falsification of Theories (GIFT) method[31]. GIFT extracts information on spectral functions by averaging among models found compatible with observations (i.e. the correlation function for a discrete set of imaginary time instants: $f(\tau_i)$) via a genetic–algorithm–exploration of a given wide space of model spectral functions. When applied to bulk liquid ${}^4\text{He}$ at $T = 0$ K, GIFT has been found able to extract more information about $S(\vec{k}, \omega)$, separating quantitatively the elementary excitation peak from the multiphonon contributions[31, 32].

Here we have applied the GIFT algorithm to extract information on excited state properties of the equilibrium superfluid phases of ${}^4\text{He}$ on GF and GH. Intermediate scattering functions have been computed for different wave vectors with the PIGS method. Well–defined single excitation peaks and multiphonon contribution are present in the reconstructed dynamical structure factors via the GIFT algorithm. In Fig. 5.18 the position of these peaks as a function of the wave vectors in two different directions are shown. In the left panel, which correspond to the GF case, the spectrum is found to be highly anisotropic with roton excitations lower than 2 K along the x direction and of about 3.5 K along y . This is again a consequence of the strong and anisotropic corrugation of the GF substrate respect to the GH case where we found a much more isotropic spectrum, with a shallow roton minimum near 5 K.

Given the extracted single quasi–particle energies of the excitation spectrum one can estimate the Landau critical velocity, $v_c = \min(E(k)/\hbar k)$, for both cases and directions; in the GF case, these turn out to be $v_c \simeq 13$ m/s along x and $v_c \simeq 31$ m/s along y , in the GH case we obtain $v_c \simeq 45$ m/s along x and $v_c \simeq 51$ m/s along y .

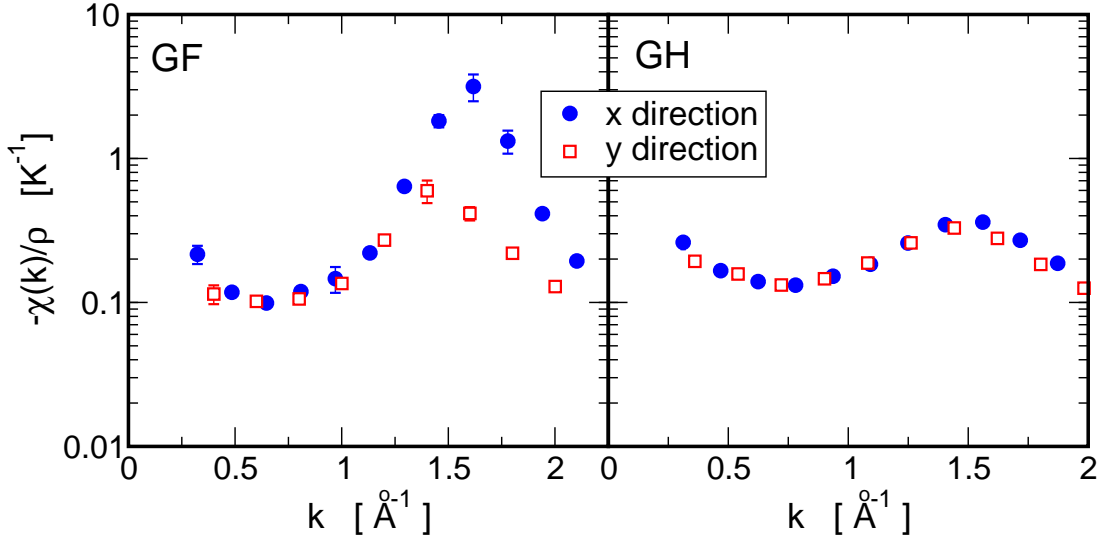


Figure 5.20: Left: Static density response function, $\chi(\vec{k})$, as function of q of ${}^4\text{He}$ on GF at equilibrium density along x and y directions. Right: The same for ${}^4\text{He}$ on GH.

By integrating $S(\vec{k}, \omega)$ with respect to ω in the range of the sharp peak and in the remaining frequency range we can determine the strength of the single quasi-particle peak, $Z(\vec{k})$, and to the contribution to the static structure factor, $S(\vec{k})$, coming from multiphonon excitations. The results for $Z(\vec{k})$ are shown in Fig. 5.19 for both cases, together with the static structure factor along the same direction; from the ratio between $Z(\vec{k})$ and $S(\vec{k})$ one can measure the efficiency of the single quasi-particle excitation channel.

The efficiency is specially high along the x direction of the GF case where we found the roton with the lower energy.

Also, through the relation

$$\chi(\vec{k}) = -2\rho \int_0^\infty d\omega \frac{S(\vec{k}, \omega)}{\omega} \quad (5.17)$$

one can compute the zero temperature static density response function $\chi(\vec{k})$. In Fig. 5.20 we present our results for $\chi(\vec{k})$ of ${}^4\text{He}$ on GF and GH computed along different directions respect to the substrates.

5.0.10 Properties at high coverages

The properties of the first layer at high density have been studied.

At $x = 2/7$ ($\rho = 0.0984 \text{ \AA}^{-2}$ on GF, $\rho = 0.105 \text{ \AA}^{-2}$ on GH) on both substrates we find that a commensurate triangular solid is stable, or at least metastable, containing 4 atoms in the unit cell of the triangular lattice rotated by 19.1° with respect to the substrate potential. In the unit cell one of the ${}^4\text{He}$ atoms is localized on an adsorption site in the middle of a graphene hexagonal ring, other two atoms approach adsorption

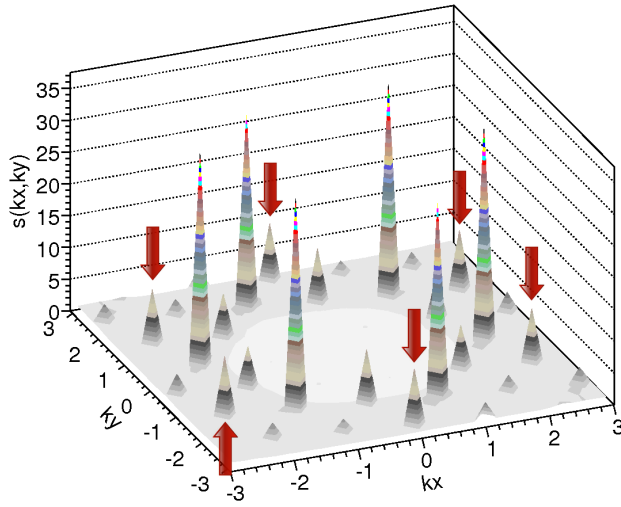
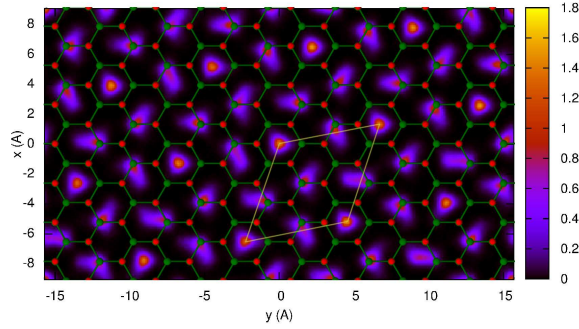


Figure 5.21: (Upper panel) Local density (in \AA^{-2} units) on the x - y plane of the $2/7$ phase of ${}^4\text{He}$ on GF compared with the geometry of the substrate. Red balls are centered on the position of Fluorine atoms and the green ones on the Carbon atoms. Thin white lines enclose the unit cell of the commensurate $2/7$ phase. (Lower panel) Static structure factor on the k_x - k_y plane of the $2/7$ phase of $N=112$ atoms of ${}^4\text{He}$ on GF. k_x and k_y axis are expressed in \AA^{-1} . Red arrows point to the peaks corresponding to the density modulation imposed by the adsorption potential.

sites of the other kind and finally the fourth one is centered on a saddle point of the potential. This state has some similarity with the $4/7$ commensurate state found for ${}^3\text{He}$ in the second layer on graphite[33]. The local density (Fig. 5.21 for ${}^4\text{He}$ on GF) displays the presence of a superlattice with four atoms in the unit cell of the triangular lattice. The static structure factor $S(k_x, k_y)$ has prominent Bragg peaks forming three stars. $S(k_x, k_y)$ for ${}^4\text{He}$ on GF is shown in Fig. 5.21. The star of the six highest peaks is the one of a triangular lattice with lattice parameter equal to that of

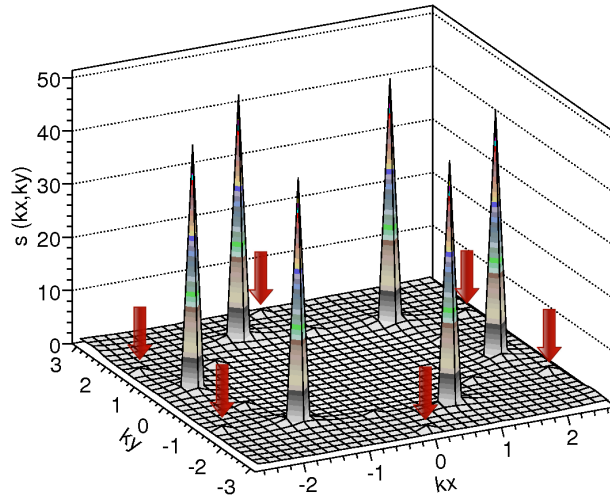
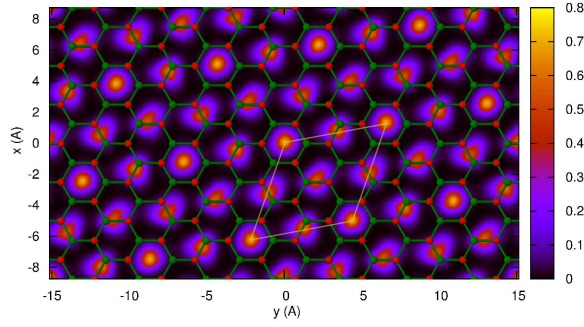


Figure 5.22: (Upper panel) Local density (in \AA^{-2} units) on the x - y plane of the $2/7$ phase of ${}^4\text{He}$ on GH compared with the geometry of the substrate. Red balls are centered on the position of Hydrogen atoms and the green ones on the Carbon atoms. Thin white lines enclose the unit cell of the commensurate $2/7$ phase. (Lower panel) Static structure factor on the k_x - k_y plane of the $2/7$ phase of $N=112$ atoms of ${}^4\text{He}$ on GH. k_x and k_y axis are expressed in \AA^{-1} . Red arrows point to the peaks corresponding to the density modulation imposed by the adsorption potential.

a triangular lattice at this density. Another star represents the density modulation due to the adsorption potential. The third star formed by six less intense peaks at a smaller wave vector is a combination of vectors of the two previous stars, thus corresponding to interference between the triangular and the honeycomb modulation. The intensity of all these peaks scale with the number of particles (data not shown). Additional peaks are present reflecting the superlattice but these peaks are very weak and hardly visible in the figure. Returning to the local density in Fig. 5.21 it can

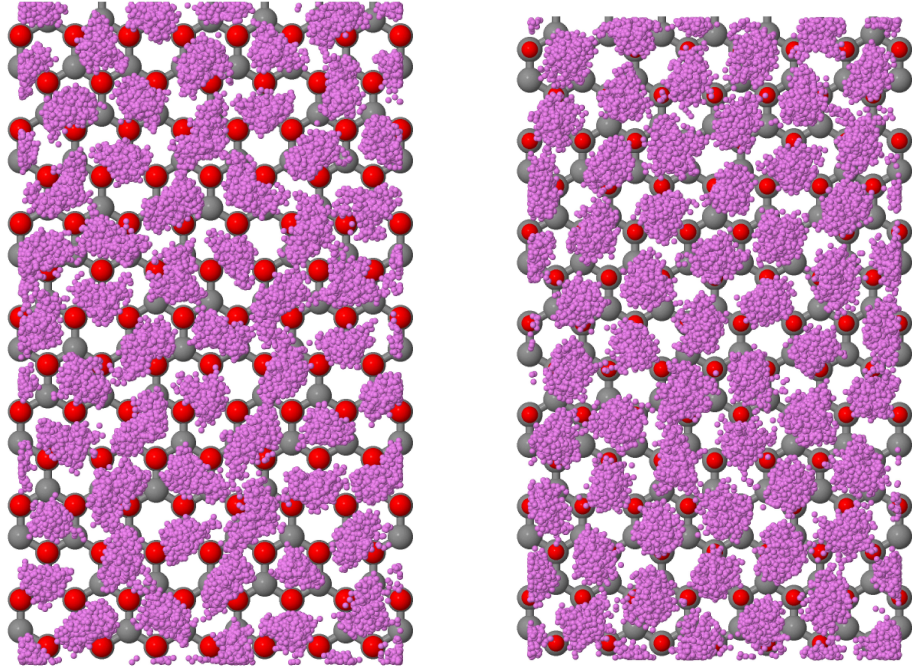


Figure 5.23: Polymer configurations for a system of $N = 56$ atoms of ${}^4\text{He}$ on GF (left) and GH (right) at filling $x = 2/7$. Each polymer represents the evolution up to 0.4 K^{-1} in imaginary time of its correspondent ${}^4\text{He}$ atom. The substrate is represented in the background with carbon atoms marked in gray and the F(H) overlayer marked in red.

be noticed that some of the spots, those located at a saddle point, are elongated indicating that the atoms visit also the neighboring adsorption sites. $S(k_x, k_y)$ and the local density of ${}^4\text{He}$ at coverage $2/7$ on GH are shown in Fig. 5.22. The results are similar to those on GF, it can be noticed the much smaller intensity of the Bragg peaks due to the adsorption potential in the case of GH as it can be expected due to the weaker corrugation of the adsorption potential of GH.

It should be noted that in this $2/7$ state not all atoms are localized around a single adsorption site but some atoms visit two or three neighboring sites, as consequence there is spatial order but the atoms are rather mobile and exchange easily so these solids might be supersolid. Evidence of this is indeed what we find at $T = 0\text{K}$ for both the substrates with the superfluidity estimation through the diffusion of the center of mass of the system in imaginary time (see Fig. 5.25). At the commensurate $2/7$ phase we estimate a superfluid fraction of 0.23 for GF and of 0.61 for GH.

At coverages around $2/7$ we find that ${}^4\text{He}$ has an incommensurate triangular order deformed by the substrate potential and defected because such order is not compatible with the periodic boundary conditions at the box sides. We discuss first ${}^4\text{He}$ on GF. We have investigated the density range between $\rho_{2/7}^{GF} = 0.0984 \text{ \AA}^{-2}$ and $\rho_{sat}^{GF} = 0.136 \text{ \AA}^{-2}$ and as an example $S(k_x, k_y)$ at $\rho = 0.123 \text{ \AA}^{-2}$ is shown in Fig. 5.27

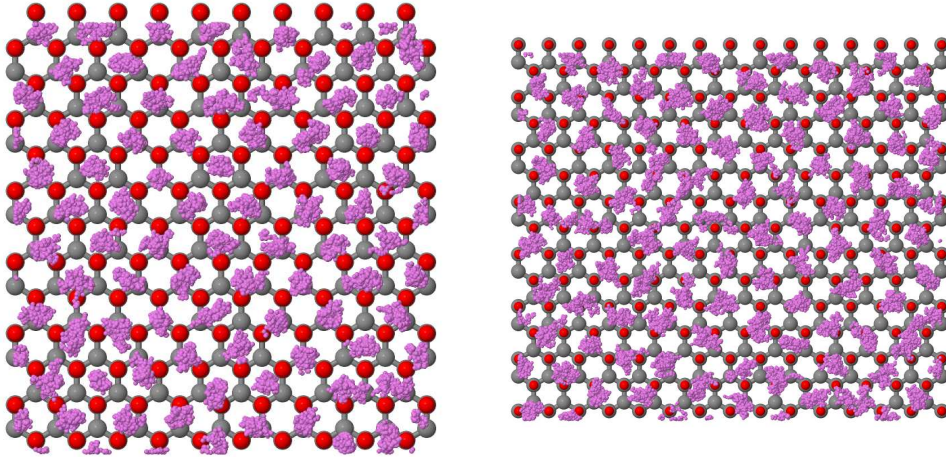


Figure 5.24: Polymer configurations in the incommensurate solid density range for a system of $N = 82$ atoms of ${}^4\text{He}$ on GF at density $\rho = 0.118 \text{ \AA}^{-2}$ (left) and a system of $N = 98$ atoms of ${}^4\text{He}$ on GH at density $\rho = 0.0916 \text{ \AA}^{-2}$ (right). Each polymer represents the evolution up to 0.4 K^{-1} in imaginary time of its correspondent ${}^4\text{He}$ atom. The substrate is represented in the background with carbon atoms marked in gray and the F(H) overlay marked in red.

and 5.26. As initial configuration we have used a disordered one as well as an ordered triangular configuration. The runs converge to the same results: $S(k_x, k_y)$ is dominated by a star of six peaks as expected for a triangular solid. The wave vectors of these peaks are not exactly equal to the value of an ideal triangular solid at this density implying that the triangular order is deformed in order to better fit within the simulation box. $S(k_x, k_y)$ has additional Bragg peaks corresponding to the modulation of the substrate potential and to the interference between the previous two sets of peaks. Additional smaller peaks are present presumably as consequence of the presence of defects. The modulus of the main Bragg peaks increases in a smooth way as the density is increased as expected for a triangular solid. The observed deviations from the value $k_B = 4\pi (\rho/2\sqrt{3})^{1/2}$ of an ideal triangular solid are explained by the deformations of the lattice and by the presence of some defects, mainly dislocations, that can be observed from the configuration of the atoms (data not shown).

In the case of GH we have investigated the density range $0.0916 \text{ \AA}^{-2} - \rho_{2/7}^{GH} = 0.105 \text{ \AA}^{-2}$. Again $S(k_x, k_y)$ is dominated by the Bragg peaks of a triangular lattice (see Fig. 5.27 for $S(k)$ at density $\rho = 0.102 \text{ \AA}^{-2}$) that is incommensurate with respect to the substrate periodicity.

In Fig. (5.23) and (5.24) we show a sampled configuration of polymers for a system of ${}^4\text{He}$ on GF and GH at respectively commensurate and incommensurate density. In the commensurate density case, Fig. 5.23, the adsorption potential has a greater influence in the GF case and causes the polymers on the saddle point to spread to neighboring adsorption sites; this effect is much less evident in the GH case where the shape of the polymer is more isotropic and the occupation of adsorption maxima

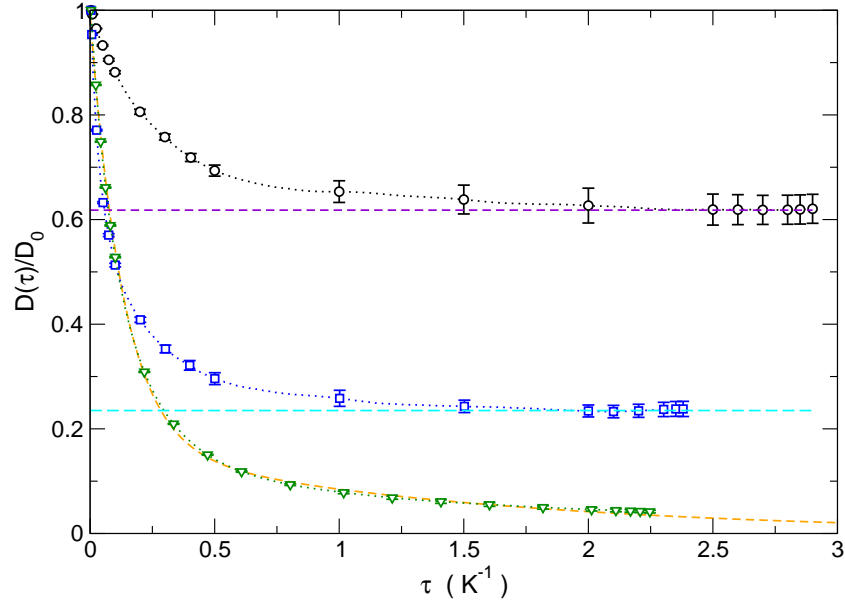


Figure 5.25: Center of mass diffusion for the 2/7 phase of GF (Circles) and GH (Squares) and the 1/3 phase of Graphite (Triangles). The superfluid fractions are obtained as the long- τ limit of the plotted functions. The horizontal dashed lines represent the value of the superfluid fraction, 0.23 for GF and 0.61 for GH. The dashed exponential curve is a fit to Graphite data and has a vanishing long τ behavior.

on top of the H overlayer is more likely. In the incommensurate case, Fig. 5.24, the presence of point dislocations are clearly visible in both the cases.

The static structure factors in the solid phase show a characteristic structure of three sets of six peaks that is represented in figure (5.26). The set that has the higher intensity represents the Bragg peaks of a triangular lattice. The six peaks that in figures 5.21, 5.22 and 5.27 are marked by the red arrows represent the density modulation induced by the adsorption potential like the peaks in Fig. 5.0.9. The third set of peaks is merely an interference pattern of the first two sets.

Increasing the number N , at some point some atoms spill out of the first layer and the density profile in the direction normal to the surface develops two well separated peaks. We have thus estimated the first layer's completion density, $\rho_{sat}^{GF(GH)}$. The promotion to the second layer takes place at a density $\rho_{sat}^{GF} = 0.136 \text{ \AA}^{-2}$ for the GF case and a density $\rho_{sat}^{GH} = 0.108 \text{ \AA}^{-2}$ for the GH case. Beyond such densities, the occupation of the second layer is clearly visible as a secondary peak in the local density along the z -direction displayed in Fig. 5.0.10.

5.0.11 Equation of state of ^3He on GF and GH

The ground state of ^3He on graphite is the $\sqrt{3} \times \sqrt{3}$ R30° state. We expect that the analogous commensurate state on GF and GH is unstable, as for ^4He , because the smaller mass makes ^3He localization more expensive.

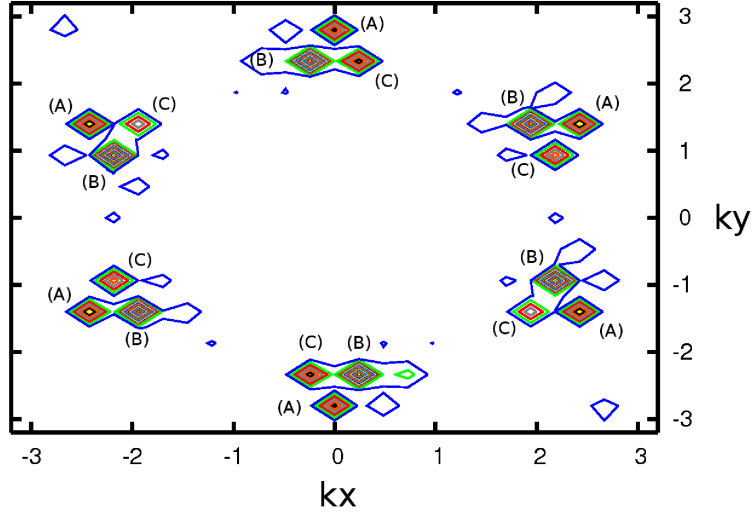


Figure 5.26: Level curves of the static structure factor of the $N=86$ incommensurate solid phase of ^4He on GF (Figure 5.27). The six peaks marked (A) reflect the density modulation due to the corrugation of the adsorption potential. The six peaks marked (B) represent the periodicity of a triangular lattice and the peaks marked (C) are interference patterns from the density modulations represented by (A) and (B). k_x and k_y axis are expressed in \AA^{-1} .

The ground state energy as function of density of mass 3 bosons and of the Fermionic ^3He on GF and on GH are plotted in Fig. 5.29 as function of density. In both cases, the system under study was composed of $N=18$ atoms of ^3He . In the figure we plot also the ^3He energy based on the crude approximation of taking as Fermi–Bose gap the kinetic energy $K_{free} = \hbar^2 \pi \rho / 2m^*$ of free fermions, where m^* is the effective mass of a ^3He atom on the substrate ($m^*/m = 1.26$ for GF, $m^*/m = 1.01$ for GH).

As shown in Fig. (5.29), the $\sqrt{3} \times \sqrt{3}$ R30° commensurate state for a mass 3 boson system is indeed unstable toward a fluid state on both substrates, in fact, the energy at the density corresponding to the $\sqrt{3} \times \sqrt{3}$ state is well above the energy at lower densities implying that this ordered commensurate state is indeed unstable and the system is in a fluid state. As a consequence we predict the existence of two new *anisotropic* Fermi fluids, in the sense that the local density is non-uniform and anisotropic, with a tunable density depending on the ^3He coverage. The density range depends on whether the ^3He atoms form a self-bound state. Such a self-bound state seems unlikely to occur for ^3He on GH on the basis of our computations. On the contrary a self-bound state might be present on GF. For mass 3 Bosons we find a bound state with a binding energy $E_0 = -0.22$ K at density $\rho_{eq} = 0.03 \text{\AA}^{-2}$. Adding to the boson energy the Fermi–Bose gap the energy yields a shallow minimum in the density range $0.015\text{--}0.025 \text{\AA}^{-2}$. The energy per particle at this minimum is equal

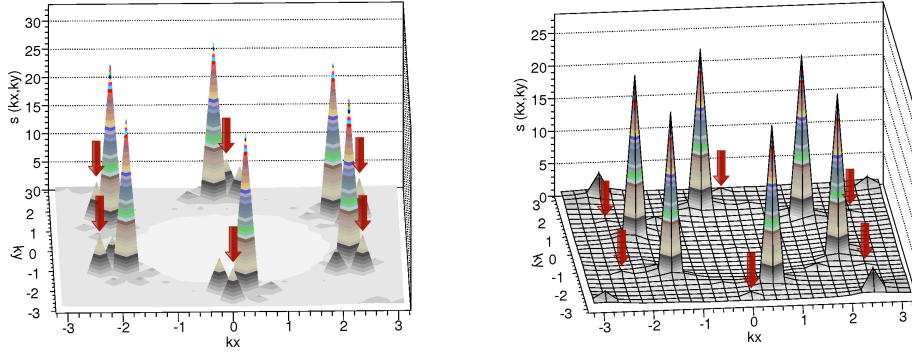


Figure 5.27: (Left) Static structure factor on the k_x - k_y plane of the incommensurate solid phase of $N=86$ atoms of ${}^4\text{He}$ on GF at density $\rho = 0.123 \text{ \AA}^{-2}$. k_x and k_y axis are expressed in \AA^{-1} . Red arrows point to the peaks corresponding to the density modulation imposed by the adsorption potential. (Right) Static structure factor on the k_x - k_y plane of the incommensurate solid phase of $N=66$ atoms of ${}^4\text{He}$ on GH at density $\rho = 0.102 \text{ \AA}^{-2}$. k_x and k_y axis are expressed in \AA^{-1} . Red arrows point to the peaks corresponding to the density modulation imposed by the adsorption potential.

within the statistical error to the energy of a single adsorbed ${}^3\text{He}$ on GF so that the existence of a self-bound state on GF is an unresolved possibility.

Remark: An accurate approximation for the energy per particle for ${}^3\text{He}$ on GF and GH has been obtained via the Fermionic Correlations technique[34, 35]. This methodology has been explained in Chapter 3: given a specific Hamiltonian, the Fermionic Correlations technique extracts the energy gap between the symmetric and antisymmetric ground state from a suitable Fermionic imaginary-time correlation function computed as an exact average on the Bose ground state:

$$\mathcal{C}_F(\tau) \equiv \frac{\langle \psi_0^B | \left(e^{\tau \hat{H}} \hat{\mathcal{A}}_F^\dagger e^{-\tau \hat{H}} \right) \hat{\mathcal{A}}_F \psi_0^B \rangle_{\mathcal{H}(N)}}{\langle \psi_0^B | \psi_0^B \rangle_{\mathcal{H}(N)}}, \quad \tau \geq 0 \quad (5.18)$$

where $\hat{\mathcal{A}}_F$ is, typically, a Slater determinant. The lowest energy contribution in $\mathcal{C}_F(\tau)$ yields the *exact gap* between the Fermionic and the Bosonic ground states, provided that one is able to obtain the inverse Laplace transform of $\mathcal{C}_F(\tau)$; this can be readily seen by formally expressing (5.18) on the basis $\{\psi_n^F\}_{n \geq 0}$ of eigenvectors of \hat{H} corresponding to the eigenvalues $\{E_n^F\}_{n \geq 0}$:

$$\mathcal{C}_F(\tau) = \sum_{n=0}^{+\infty} e^{-\tau(E_n^F - E_0^B)} \frac{|\langle \hat{\mathcal{A}}_F \psi_0^B | \psi_n^F \rangle_{\mathcal{H}(N)}|^2}{\langle \psi_0^B | \psi_0^B \rangle_{\mathcal{H}(N)}} \quad (5.19)$$

We have shown that this analytic continuation procedure can be handled efficiently with statistical inversion procedures, like the GIFT algorithm introduced in

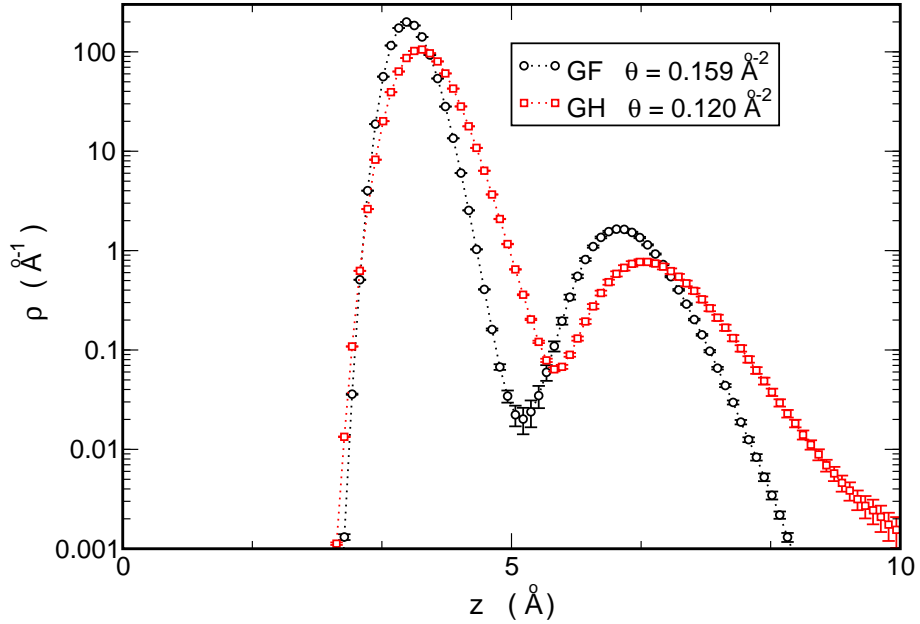


Figure 5.28: Local density along the z -direction of ${}^4\text{He}$ on GF (with $N=111$) and ${}^4\text{He}$ on GH (with $N=79$) at a density beyond the promotion density. The occupation of the first and the second layer are clearly visible as two peaks. The area under the peaks represents the number of ${}^4\text{He}$ atoms in the corresponding layer.

Ref.[31]. The Fermi-Bose gap $E_0^F - E_0^B$ is an extensive quantity, so this method can be applied provided that the system is not too large.

5.0.12 Discussion

He adsorption on new substrate materials is valuable because of the fundamental importance of helium in many-body physics, with a variety of phases seen in both 2D and 3D. Our results indicate that the GF substrate provides the strongest binding of any surface (since the previous record was held by graphite). Moreover, the novel symmetry, the smaller intersite distance and large corrugation imply that quite novel properties may be anticipated for this system. This is indeed the case. When many ${}^4\text{He}$ atoms are adsorbed on GF and on GH a very striking result is that the ground state is a low density liquid modulated by the substrate potential and the system has BEC, i.e. it is a superfluid. This is qualitatively different from graphite for which the lowest energy state is the $\sqrt{3} \times \sqrt{3}$ R30° commensurate one with no BEC [36]. We have verified that such an ordered state on GF and GH is unstable relative to the liquid phase. It should be noticed that some of the parameters in the adsorption potential are not known with high precision or they have been adopted from other systems. We have verified that even a change of parameters like α , C_{6F} and β by 20% does not modify the qualitative behavior of the adsorbed He atoms even if there can be a sizable change in the value, for instance, of the adsorption energy. Measurement

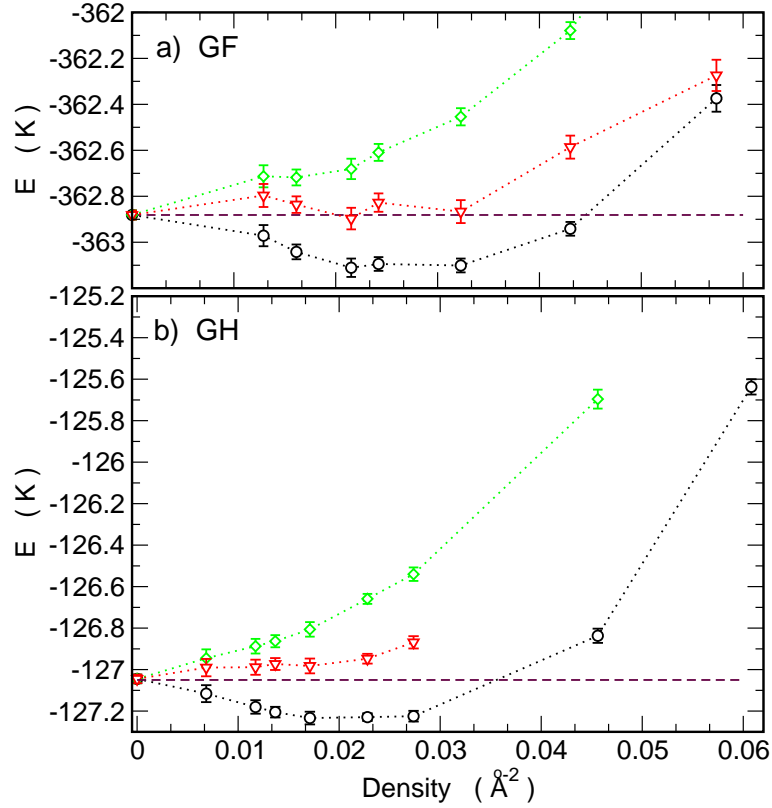


Figure 5.29: Panel a). Ground state energy as function of density of mass 3 bosons on GF (circles), Fermionic ^3He -GF obtained via the Fermionic correlations method (triangles) and Fermionic ^3He -GF obtained by approximating the Bose-Fermi gap with the kinetic energy of the free fermion gas (diamonds). Panel b). Same as for panel (a) for ^3He on GH.

of thermodynamic properties and He atomic beam scattering experiments from GF and GH will be important to test the accuracy of our model potentials. A remarkable result is the superfluid behavior of the $2/7$ phase that, however, might be a property of the system at strictly $T = 0\text{K}$ and is non reachable by experiments; on the other hand there might truly be a “supersolid” phase transition at a temperature in the $m\text{K}$ range that is not accessible by QMC computations. This, together with all the novel phenomena for He atoms on GF and GH that have been predicted in this work, calls for experimental verification. There is also an important aspect that should be considered in view of experiments; it might be difficult to have a 100% reacted graphene sheet with fluorine. However, the presence on GF of small regions of unreacted graphane should not affect the properties of the adsorbed film because the He or H_2 atoms are preferentially adsorbed on the F covered regions of graphene. This behavior, however, may change when coverages beyond the first layer completion on GF and GH are considered; in such cases it could be that the adsorbed atoms begin to populate the unreacted regions. The QMC techniques here employed may be used

to investigate also these interesting cases given that a suitable interaction potential is provided.

From the theoretical point of view many extensions of the present computations can be foreseen, for instance the characterization of the commensurate $2/7$ phases on GF and GH, of the system under rotation and the study the phase diagram of p-H₂ on GF. As a perspective of future work we plan to provide predictions concerning the phase diagrams and thermodynamic properties for both He/GF and He/GH, hoping to stimulate experimental studies of these systems.

Bibliography

- [1] S. Sachdev, *Nat. Phys* **4**, 173 (2008); I. Bloch, J. Dalibard, W. Zwerger, *Rev. Mod. Phys* **80**, 885 (2008).
- [2] R. G. Melko, A. Paramekanti, A. A. Burkov, A. Vishwanath, D. N. Sheng and L. Balents, *Phys. Rev. Lett.* **95**, 127207 (2005); E. Edlund, O. Lindgren, and M.N. Jacobi, *Phys. Rev. Lett.* **107**, 085503 (2011).
- [3] Sect. 6.1 of L.W. Brunch, M.W. Cole, and E. Zaremba, *Physical Adsorption: Forces and Phenomena*, (Dover Publishing, Mineola, NY, 2007).
- [4] J. G. Dash, M. Schick and O. E. Vilches, *Surf. Sci.* **299/300**, 405-414 (1994).
- [5] M. W. Cole, D. R. Frankl and D. L. Goodstein, *Rev. Mod. Phys.* **53**, 199 (1981).
- [6] G. Boato and P. Cantini, *Adv. Electronics and Electron Phys.* **60**, 95 (1983).
- [7] J. O. Sofo, A. S. Chaudhari and G. D. Barber, *Phys. Rev. B* **75**, 153401 (2007).
- [8] R. R. Nain et al., *Small* **6**, 2877 (2010); R. Zbořil et al., *Small* **6**, 2885 (2010).
- [9] D.C. Elias et al., *Science* **323**, 610 (2009).
- [10] M. J. Stott and E. Zaremba, *Phys. Rev. B* **22**, 1564 (1980).
- [11] M. W. Cole and F. Toigo, *Phys. Rev. B* **31**, 727 (1985).
- [12] G. Vidali, M. W. Cole and C. Schwartz, *Surf. Sci.* **87**, L273 (1979).
- [13] K. T. Tang and J. P. Toennies, *J. Chem. Phys.* **80**, 3726 (1984).
- [14] B. Delley, *J. Chem. Phys.* **92**, 508 (1990); B. Delley, *J. Chem. Phys.* **113**, 7756 (2000).
- [15] J. P. Perdew, K. Burke and N. Ernzerhof, *Phys. Rev. Lett.* **77**, 3865 (1996).
- [16] G. Vidali, M. W. Cole and W. H. Weinberg, *Phys. Rev. Lett.* **51**, 118 (1983).
- [17] K. T. Tang and J. P. Toennies, *J. Chem. Phys.* **68**, 5501 (1978).
- [18] W. Meyer, P. C. Hariharan and W. Kutzelnigg, *J. Chem. Phys.* **73**, 1880 (1980).

- [19] A. Frigo, F. Toigo, M. W. Cole and F. O. Goodman, *Phys. Rev. B* **33**, 4184 (1986).
- [20] A. Sarsa, K. E. Schmidt and W. R. Magro, *J. Chem. Phys.* **113**, 1366 (2000).
- [21] D. M. Ceperley, *Rev. Mod. Phys.* **67**, 279(1995).
- [22] M. Rossi, M. Nava, L. Reatto and D. E. Galli, *J. Chem. Phys.* **131**, 154108 (2009).
- [23] M. Boninsegni, N. V. Prokof'ev and B. V. Svistunov, *Phys. Rev. E* **74**, 036701 (2006).
- [24] E. Vitali, M. Rossi, L. Reatto and D. E. Galli, *Phys. Rev. B* **82**, 174510 (2010).
- [25] A. H. Castro Neto, F. Guinea, N. M. R. Peres, K. S. Novoselos and A. K. Geim, *Rev. Mod. Phys.* **81**, 109 (2009).
- [26] W. E. Carlos and M. W. Cole, *Phys. Rev. B* **21**, 3713 (1980).
- [27] R. A. Aziz, V. P. S. Nain, J. S. Carley, W. L. Taylor, and G. T. McConville, *J. Chem. Phys.* **70**, 4330 (1979).
- [28] P. A. Whitlock, G. V. Chester and M. H. Kalos, *Phys. Rev. B* **38**, 2418 (1988).
- [29] S. Zhang, N. Kawashima, J. Carlson, and J.E. Gubernatis, *Phys. Rev. Lett.* **74**, 1500 (1995).
- [30] A.J. Leggett, *J. Stat. Phys.* **93**, 927 (1998).
- [31] E. Vitali, M. Rossi, L. Reatto, and D.E. Galli, *Phys. Rev. B* **82**, 174510 (2010).
- [32] M. Rossi, E. Vitali, L. Reatto, and D. E. Galli, *Phys. Rev. B* **85**, 014525 (2012).
- [33] H. Fukuyama, *J. Phys. Soc. Japan* **77**, 111013 (2008).
- [34] M. Nava, E. Vitali, A. Motta, D.E. Galli, and S. Moroni, *Phys. Rev. B* **85**, 184401 (2012).
- [35] G. Carleo, S. Moroni, F. Becca, and S. Baroni, *Phys. Rev. B* **83**, 060411 (2011).
- [36] M. Buzzacchi, D. E. Galli and L. Reatto, *J. Low Temp. Phys.* **126**, 205 (2002).

Chapter 6

Conclusions

The idea underlying this work has been the study of strongly interacting quantum systems along with the development of new methodologies in the field of QMC. Strongly interacting quantum systems are indeed a fascinating field of research, much is yet unknown and indeed a proof of this assertion might be found in our results: we have studied new adsorbed phases of ^4He and also predicted the presence of a *modulated* superfluid given by the interplay between interatomic potentials and quantum tunneling. Strongly interacting Fermi systems are even more unexplored due to the sign problem. The methodological aspect of this work has been thus focused to develop a technique that can study the dynamics of such systems. This technique is an evolution of the Fermionic Correlations method; we have shown that, even though this methodology becomes unpractical for big numbers of particles, it indeed can compute an *ab-initio* low-energy excitation spectrum of two-dimensional ^3He .

In the conclusions of this work, we remind the main results obtained and presented throughout this work; we have already drawn conclusions in each chapter, here we will comment mostly the computations that are still in progress and even the “failed attempts”.

2d ^3He . Our simulation of two-dimensional ^3He gave a spin susceptibility as function of density that is in very good agreement with experimental data; our obtained polarization curves indicates that the ferromagnetic fluid is never stable and the system crystallizes into a triangular lattice from the paramagnetic fluid at a density of 0.061 \AA^{-2} . With an extension of the Fermionic Correlation (FC) technique, we have been able to obtain the first *ab-initio* evaluation of the zero-sound mode and the dynamic structure factor of 2d ^3He that is in remarkably good agreement with experiments. This excitation spectrum, moreover, turned out to have striking similarities with the phonon-maxon-roton spectrum of ^4He ; this indicates that the effects of the inter-atomic potential, in particular its strong repulsive part, dominate over the effects of the quantum symmetry. Another interesting question is whether the zero-sound mode, which is known to enter the particle-hole band, reemerges at wave vectors corresponding to the “roton” minimum of the spectrum; it is possible, with the FC method, to compute the particle-hole excitations and indeed we have presented preliminary results that show that the “roton” is still in the particle-hole

band. However, the re-emergence of the roton is a rather difficult question to answer with a simulation of a finite system. This is because there are relevant size effects on the particle–hole; these effects are due to the fact that we are far from the thermodynamic limit and the particle–hole is not a continuum; in order to obtain more conclusive data, a scaling analysis on bigger systems is in order. Such a study that is very demanding in term of computing resources and has been planned for future work.

We also attempted a study of the spin–waves excitations but in this case we found that the results were highly dependent on the direction of the wave vector. This anisotropy is a clear sign of size effects; unfortunately, these size effects for spin–waves are stronger than in the zero–sound or even the particle hole case and thus require the study of systems with particle numbers for which, like for most QMC methods, FC becomes unpractical.

An interesting perspective is the application of the FC technique to the study of elementary excitations of the $2d$ electron gas; possibly this would provide an *ab-initio* evaluation of the plasmon excitations.

^4He on Graphene-Fluoryde and Graphane. The study of ^4He adsorption on Graphene-Fluoryde (GF) and Graphane (GH) has been a comprehensive and articulated work. At the early stages of the project we showed that the commensurate $\sqrt{3} \times \sqrt{3} R30^\circ$ phase is unstable on both substrates. We then determined the equilibrium density at $T = 0$ K; our results indicated clearly that on both the substrates the equilibrium density has a condensate fraction and is thus a *modulated superfluid*. We determined the superfluid fraction at zero and finite temperature giving also a rough estimate of the fluid–superfluid transition temperature. The study of the equilibrium density at $T = 0$ K comprised also the excitation spectrum, and we have shown the phono–roton spectrum of ^4He on GF and GH. We focused then on high coverages of the monolayer and found a density range, not yet precisely determined, in which ^4He forms an incommensurate triangular solid; a remarkable result is that on both GF and GH a commensurate phase at filling factor $x = 2/7$ is stable or at least metastable. This result becomes even more interesting because we found a first evidence of superfluidity at zero temperature: at this density, the system may possibly be both solid and superfluid, in other words this system could posses the long sought property of supersolidity.

For the immediate future, we plan to study further this commensurate density with also a size scaling aimed to better estimate the finite size effects on the properties of the $2/7$ phase, in particular on the superfluid fraction. In our further studies, there are mainly two points to inspect: first, is the $2/7$ phase thermodynamically stable? This far, we have shown that it is mechanically stable, meaning that, at the density corresponding to $x = 2/7$, the configuration that gives the lowest energy is the $2/7$ triangular lattice; now we are planning to search for signatures of possible phase transitions between the incommensurate solid and the $2/7$ phase. Second, we are searching for more evidence of superfluidity in the commensurate phase, we already tried the computation of the superfluid density at finite temperature down to 0.5 K but

we did not find any superfluid signal, indeed, the very low rate of exchanges between atoms suggests that, if any, the transition temperature to the supersolid state would be too low to be reachable with PIMC with our current computing resources; another approach is the computation of the one body density matrix at zero temperature, in fact, the presence of even a small fraction of condensate would be a strong support for the supersolidity of this phase; this is very demanding in term of computing resources and is planned for the next future.

Besides the supersolidity, we have scheduled also a deeper study of the incommensurate density range with a quantitative characterization of the defects. This will prepare the background for the study of the second adsorbed layer that will be left for future works.

We conclude with a last remark. For the Helium-substrate interaction we have adopted a semi-empirical potential: its repulsive part has been obtained from a DFT calculation of the electron density of the substrate, on the other hand, the attractive part has been modeled with a Van der Waals type interaction with parameters taken from literature, adopted from the interaction potentials of Helium with similar chemical compounds. This study, as consequence, can be considered a semi-quantitative approach but the very fact that we find qualitatively the same behavior on two substrates that have completely different values of energies and corrugation is a strong proof of plausibility of our results; moreover, the robustness of the results has been explicitly tested at the $\sqrt{3} \times \sqrt{3}$ R30° density with a variation up to 20% of the parameters of the He-substrate potential. More exactly, this is an “exact” study on a semi-empirical Hamiltonian aimed to the research of new properties of adsorbed matter, our hope is that this predictive work will encourage, on one side, the development of more accurate Helium-substrate interaction potential and, on the other side, the experimental exploration of this subject so fascinating and full of surprises.

Chapter 7

Computational details

In this Chapter some technical details of the Monte Carlo techniques introduced in Sec. 2 will be described. Monte Carlo sampling will then be applied to the problem of evaluating physical properties of quantum systems at both zero and finite temperature.

The basic idea underlying the used path integral methods is that the computation of an expectation value in a quantum system can be viewed as an N -dimensional integral; in the case of a bosonic system, the ground state wave function can be chosen real and non-negative and this integral can be interpreted as the average of a random variable over a probability density[3].

7.1 Monte Carlo integration: the strategy

An effective way to compute an N -dimensional integral is to employ Monte Carlo (MC). Monte Carlo basically means “the use of random numbers in order to solve a problem”. In our case, the problem is the N -dimensional integral representing an expectation value for a quantum many-body system. In order to show how MC is employed in our context, consider, as an illustrative example, a function $f(\vec{x})$ that is a product of an arbitrary function $g(\vec{x})$ and a probability density $p(\vec{x})$

$$f(\vec{x}) = g(\vec{x}) \cdot p(\vec{x}) \text{ with} \quad (7.1)$$

$$p(\vec{x}) \geq 0 \forall \vec{x} \in \Gamma, \quad \int_{\Gamma} d\vec{x} p(\vec{x}) = 1 \quad (7.2)$$

The integral can be rewritten as[4],

$$\int_{\Gamma} d\vec{x} g(\vec{x})p(\vec{x}) = \lim_{N \rightarrow +\infty} \frac{1}{N} \sum_{i=1}^N g(\vec{x}_i) \simeq \langle g \rangle_p \quad (7.3)$$

where \vec{x}_i are elements sampled from the probability density $p(\vec{x})$. The integral value is thus the average of $g(\vec{x})$ over sets of values \vec{x} that are sampled from the probability density $p(\vec{x})$. The advantage of MC is that, given a way to sample $p(\vec{x})$, the computing

time required for the evaluation of the integral does not scale with the dimensionality; this is very important since, as will be clear further on, the integrals that are computed in this context have generally a very high dimensionality.

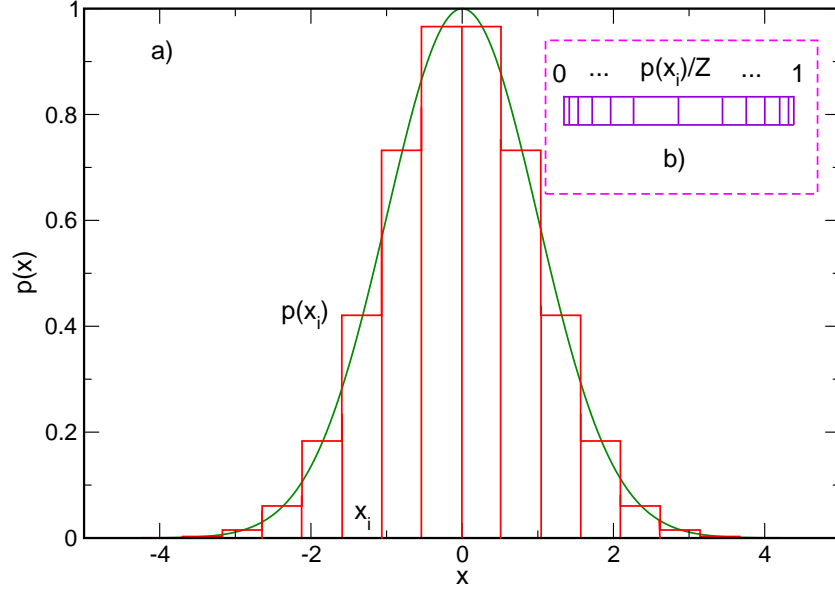


Figure 7.1: a) Schematic 1D representation of the sampling of a probability density and its discretization in N bins. b) The partition of the unity used in the faked roulette method: the interval $[0; 1)$ is divided into N bins, the m bin is the interval $I_m = \left[\sum_{j=1}^{m-1} p(x_j)/Z; \sum_{j=1}^m p(x_j)/Z \right)$, where the normalization $Z = \sum_{j=1}^N p(x_j)$. The faked roulette is a method to randomly chose m : a random number r uniformly distributed in $[0; 1)$ is generated, m corresponds to the interval I_m in which r falls, namely: I_m so that $I_m \cap \{r\} = \{r\}$

This however requires that one is able to sample an arbitrary N -dimensional probability distribution. Sampling means the generation of a random variable according to an arbitrary probability density $p(\vec{x})$; as sketched in Fig. 7.1, sampling can be done by dividing the domain of $p(\vec{x})$ in K^N bins with an assigned probability $p'_i = \frac{p(\vec{x}_i)}{Z}$, with Z a normalization constant and \vec{x}_i the central coordinate of the i -th bin. A simple way to extract a random variable value is through a *faked roulette* (see Fig. 7.1), however, the computational weight of this approach increases exponentially with the number of degrees of freedom and is thus unpractical for the evaluation of Eq. (7.1). A more sophisticated and efficient way to sample an arbitrary probability density is with Markov chains[5]. As is shown in the next section, a Markov chain has at least one invariant probability density and there is a sufficient condition for its uniqueness; the basic idea is thus to build a Markov chain that converges to the required unique invariant probability density. In the next section we provide a mathematical demonstration of the properties of the Markov chains used in this context, after that section an algorithm that can be used to build the required Markov chain, namely the Metropolis algorithm[6], will be described.

7.1.1 Mathematics of Markov chains

In this section, we follow Ref. [2] and show the mathematical basis of the Markov chains. Let's consider a given finite set $E = \{1, \dots, N\}$ and a probability space (Ω, \mathcal{F}, P) , where Ω is a sample space, \mathcal{F} is a σ -algebra on Ω and P a probability measure.

Definition 1. A Markov chain on a sample space E is a sequence of random variables $\{X_n\}_{n \in \mathbf{N}^0}$, $X_n : \Omega \rightarrow E$ such that there are non negative numbers $\mathcal{P}_{i \rightarrow j}(n)$, $n \in \mathbf{N}^0$ and $i, j \in E$ for which,

$$\begin{aligned} P(X_{n+1} = j | X_n = i, X_{n-1} = i_{n-1}, \dots, X_0 = i_0) = \\ P(X_{n+1} = j | X_n = i) = \mathcal{P}_{i \rightarrow j}(n) \end{aligned} \quad (7.4)$$

whenever the conditional probabilities $P(\cdot | \dots)$ are defined. From here on we focus on Markov chain that are independent on time translations, in this case $\mathcal{P}_{i \rightarrow j}(n)$ does not depend on n .

Transition matrix. The non-negative numbers $\mathcal{P}_{i \rightarrow j}$ can be represented in an $N \times N$ matrix $\underline{\mathcal{P}}$ that is referred as *transition matrix* of the Markov chain. Following from the definition of conditional probability, the sum of the element of a row is one, namely $\sum_{j=1}^N \mathcal{P}_{i \rightarrow j} = 1$ for $i = 1, \dots, N$. The probability distribution of the random variable X_0 is the starting probability of the chain and is defined by the numbers $v_k = P(X_0 = k)$, $k \in E$, this probability distribution can be identified by a row vector in \mathbf{R}^N , $\underline{v} = (v_1, \dots, v_N)$.

Statement: a Markov chain that is independent on time translations is defined by a starting probability and a transition matrix. This can be shown if, from the definition of conditional probability, we first obtain the probability distribution of X_1 :

$$P(X_1 = k) = \sum_{h=1}^N P(X_0 = h)P(X_1 = k | X_0 = h) = \sum_{h=1}^N v_h \mathcal{P}_{h \rightarrow k} \quad (7.5)$$

that in matrix notation becomes,

$$\underline{v}^{(1)} = \underline{v} \underline{\mathcal{P}} \quad (7.6)$$

where we define $\underline{v}^{(1)} = P(X_1 = k)$. Iterating to obtain the probability distribution for the next time step, $P(X_2)$,

$$\begin{aligned} P(X_2 = k) &= \sum_{l=1}^N P(X_1 = l)P(X_2 = k | X_1 = l) = \\ &= \sum_{l=1}^N P(X_1 = l) \mathcal{P}_{l \rightarrow k} = \sum_{l=1}^N \sum_{h=1}^N v_h \mathcal{P}_{h \rightarrow l} \mathcal{P}_{l \rightarrow k} = \\ &= \sum_{h=1}^N v_h \sum_{l=1}^N \mathcal{P}_{h \rightarrow l} \mathcal{P}_{l \rightarrow k} \end{aligned} \quad (7.7)$$

in matrix form:

$$\underline{v}^{(2)} = \underline{v} \underline{\mathcal{P}}^2 \quad (7.8)$$

iterating this rule the probability distribution at time step n can be obtained as the n -power of the transition matrix applied to the starting probability, $\underline{v}^{(n)} = \underline{v} \underline{\mathcal{P}}^n$. It will be used later on in this section the m steps transition probability, $\mathcal{P}_{i \rightarrow j}^{(m)} = P(X_{n+m} = j | X_n = i)$.

Statement: $\mathcal{P}_{i \rightarrow j}^{(m)}$ are the matrix elements of $\underline{\mathcal{P}}^m$. This, again, is shown by iteration:

$$\begin{aligned} P(X_{n+m} = j | X_n = i) &= \frac{P(X_{n+m} = j, X_n = i)}{P(X_n = i)} = \\ &= \sum_{h=1}^N \frac{P(X_{n+m} = j, X_{n+m-1} = h, X_n = i)}{P(X_n = i)} = \\ &= \sum_{h=1}^N \frac{P(X_{n+m} = j, X_{n+m-1} = h, X_n = i)}{P(X_{n+m-1} = h, X_n = i)} \frac{P(X_{n+m-1} = h, X_n = i)}{P(X_n = i)} = \\ &= \sum_{h=1}^N P(X_{n+m} = j | X_{n+m-1} = h, X_n = i) P(X_{n+m-1} = h | X_n = i) = \\ &= \sum_{h=1}^N \mathcal{P}_{h \rightarrow j} P(X_{n+m-1} = h | X_n = i). \end{aligned} \quad (7.9)$$

Repeating this passage with $P(X_{n+m-1} = h | X_n = i)$, and so on until $P(X_n = k | X_n = i)$, the statement is demonstrated.

Invariant probabilities. Given a probability distribution π on the set E identified by a row vector $\underline{\pi} = (\pi_1, \dots, \pi_N) \in \mathbf{R}^N$ and a Markov chain defined by a transition matrix $\underline{\mathcal{P}}$ and starting probability \underline{v} , π is *invariant* if:

$$\underline{\pi} = \underline{\pi} \underline{\mathcal{P}}, \quad (7.10)$$

in the particular case of $\underline{v} = \underline{\pi}$ we say that the Markov chain is *stationary*.

Theorem 1. (Markov-Kakutani) *There is always at least one invariant probability distribution.*

Proof. The probabilities on E are mapped onto the set

$$S = \left\{ \underline{x} \in \mathbf{R}^N : 0 \leq x_i \leq 1, \sum_{i=1}^N x_i = 1 \right\}, \quad (7.11)$$

this is a closed and limited set in \mathbf{R}^N and hence, by the Bolzano-Weierstrass theorem, it is a compact set; given a sequence of points in S , it is thus possible to define a subsequence that converges to a point in S . From a point \underline{x} of S , we define the

sequence:

$$\underline{x}_n = \frac{1}{n} \sum_{k=0}^{n-1} \underline{x} \mathcal{P}^k, \quad (7.12)$$

this vector has non negative components because is a product of elements with non negative components; \underline{x}_n also belongs to S , this is readily seen with a summation of its components $x_{n,i}$,

$$\sum_{i=1}^N x_{n,i} = \frac{1}{n} \sum_{k=0}^{n-1} \sum_{h=1}^N \sum_{i=1}^N x_h \mathcal{P}_{h \rightarrow i}^{(k)} = \frac{1}{n} \sum_{k=0}^{n-1} \sum_{h=1}^N x_h = 1 \quad (7.13)$$

where in the last passage the property of the transition probability $\sum_i \mathcal{P}_{h \rightarrow i}^{(m)} = 1$ was used. Having proved that $\underline{x}_n \in S$, there is a subsequence $\{\underline{x}_{n_k}\}$ converging to a point $\underline{\pi} \in S$. Now we write

$$\begin{aligned} & \underline{x}_{n_k} - \underline{x}_{n_k} \mathcal{P} = \\ & \frac{1}{n_k} \left(\sum_{h=0}^{n_k-1} \underline{x} \mathcal{P}^h - \sum_{h=0}^{n_k-1} \underline{x} \mathcal{P}^{h+1} \right) = \\ & = \frac{1}{n_k} (\underline{x} - \underline{x} \mathcal{P}^{n_k}) \end{aligned} \quad (7.14)$$

taking the limit for k to infinity, we observe that while n_k diverges, the quantity $\underline{x} - \underline{x} \mathcal{P}^{n_k}$ remains finite because is the difference between two elements of the limited set S . We thus obtain the following relation for $\underline{\pi}$:

$$\underline{\pi} - \underline{\pi} \mathcal{P} = \lim_{k \rightarrow +\infty} (\underline{x}_{n_k} - \underline{x}_{n_k} \mathcal{P}) = \lim_{k \rightarrow +\infty} \frac{1}{n_k} (\underline{x} - \underline{x} \mathcal{P}^{n_k}) = 0, \quad (7.15)$$

that demonstrates the theorem. \square

The invariant probability distributions of a Markov chain can be obtained from the solution of the linear system

$$\pi_j = \sum_{i=1}^N \pi_i \mathcal{P}_{i \rightarrow j}, \quad (7.16)$$

however, a *sufficient condition* for π to be invariant is that it satisfies the *detailed balance equation*:

$$\pi_i \mathcal{P}_{i \rightarrow j} = \pi_j \mathcal{P}_{j \rightarrow i} \quad (7.17)$$

for every $i, j \in E$. The demonstration of this statement comes directly from the definition of transition matrix

$$\sum_{i=1}^n \pi_i \mathcal{P}_{i \rightarrow j} = \sum_{i=1}^n \pi_j \mathcal{P}_{j \rightarrow i} = \pi_j \quad (7.18)$$

The detailed balance condition will be used in the next section when the Metropolis algorithm will be described. This algorithm is used to build a Markov chain that converges to an arbitrary invariant probability density.

Uniqueness of invariant probability distributions. Markov chains wouldn't be so much useful in Monte Carlo if there were not conditions of uniqueness of the invariant probability distribution. The uniqueness property is in fact what guarantees that the Metropolis algorithm converges to the wanted probability distribution. To state and prove this property some definitions are necessary.

Definition 2. Given the transition matrix $\underline{\mathcal{P}} = \{\mathcal{P}_{i \rightarrow j}\}_{i,j}$ of a time invariant Markov chain,

- $\underline{\mathcal{P}}$ is *irreducible* if for each $i, j \in E$ there is a positive integer number $m = m(i, j)$ so that $\mathcal{P}_{i \rightarrow j}^{(m)} > 0$.
- $\underline{\mathcal{P}}$ is *regular* if there is a positive integer number m for which $\mathcal{P}_{i \rightarrow j}^{(m)} > 0$ for every $i, j \in E$.

Clearly, a regular transition matrix is also irreducible but the opposite is not generally true, however if an irreducible transition matrix satisfies the following criterion, then we will show that it is also regular.

Statement. *If a transition matrix is irreducible and there is $h \in E$ such that $\mathcal{P}_{h \rightarrow h} > 0$, then that transition matrix is also regular.*

Proof. From the definition of irreducibility, for each $i, j \in E$ there is $m = m(i, j) > 0$ such that $\mathcal{P}_{i \rightarrow j}^{(m)} > 0$; defined $s = \max_{i,j \in E} m(i, j)$, then $\mathcal{P}_{l \rightarrow k}^{(2s)} > 0$ for each $l, k \in E$. In fact, one can always use iteratively the transition element $\mathcal{P}_{h \rightarrow h} > 0$ to express $\mathcal{P}_{l \rightarrow k}^{(2s)}$ as a chain of products: the irreducibility guarantees that given two elements $l, k \in E$ there are positive integer $n_1 = n(l, h)$ and $n_2 = n(h, k)$ such that $\mathcal{P}_{l \rightarrow h}^{(n_1)} > 0$ and $\mathcal{P}_{h \rightarrow k}^{(n_2)} > 0$; the element $\mathcal{P}_{l \rightarrow k}^{(2s)}$ will thus be expressed as:

$$\mathcal{P}_{l \rightarrow k}^{(2s)} \geq \mathcal{P}_{l \rightarrow h}^{(n_1 = n(l, h))} \mathcal{P}_{h \rightarrow h} \dots \mathcal{P}_{h \rightarrow h} \mathcal{P}_{h \rightarrow k}^{(n_2 = n(h, k))} > 0, \quad (7.19)$$

and this proves the statement. \square

We state now the uniqueness theorem.

Theorem 2. (Markov) *If a transition matrix is regular, then there is only one invariant probability π and, for any starting probability v , the following holds*

$$\pi_j = \lim_{n \rightarrow +\infty} (\underline{v} \underline{\mathcal{P}}^n)_j \quad (7.20)$$

Proof. From Markov-Kakutani theorem at least one invariant probability π exist and, by definition

$$\underline{\pi} = \underline{\pi} \mathcal{P}, \quad \sum_k \pi_k = 1, \quad 0 \leq \pi_k \leq 1 \quad (7.21)$$

Let's consider the one dimension vector subspace of \mathbf{C}^N generated by $\underline{\pi}$:

$$\mathcal{V}_\pi = \{ \underline{u} \in \mathbf{C}^N \mid \underline{u} = t \underline{\pi}, t \in \mathbf{C} \} \quad (7.22)$$

By the hypothesis and this definition follows respectively that $\underline{\pi}$ is an eigenvector of \mathcal{P} and $\underline{\pi} \in \mathcal{V}_\pi$. Define also the subspace \mathcal{V}_0 :

$$\mathcal{V}_0 = \left\{ \underline{y} \in \mathbf{C}^N \mid \sum_k y_k = 0 \right\}. \quad (7.23)$$

This subspace has dimension $M - 1$ and $\mathcal{V}_0 \cap \mathcal{V}_\pi = \{ \underline{0} \}$ because \mathcal{V}_π is made of elements \underline{u} for which $\sum_k u_k = t$. Following from this conditions, the vector space \mathbf{C}^N decomposes in the direct sum $\mathcal{V}_0 \oplus \mathcal{V}_\pi$. This implies that any element $\underline{v} \in \mathbf{C}^N$ can be uniquely written as:

$$\underline{v} = t \underline{\pi} + \underline{y}, \quad \underline{y} \in \mathcal{V}_0 \quad (7.24)$$

The eigenvalues equation for \mathcal{P} is:

$$\underline{v} \mathcal{P} = \lambda \underline{v}, \quad \lambda \in \mathbf{C} \quad (7.25)$$

Let's consider also that given an element $\underline{y} \in \mathcal{V}_0$, then also the element $\underline{y} \mathcal{P} \in \mathcal{V}_0$, this is seen in this passage:

$$\sum_k (\underline{y} \mathcal{P}_k) = \sum_k \sum_i y_i \mathcal{P}_{i \rightarrow k} = \sum_i y_i \sum_k \mathcal{P}_{i \rightarrow k} = \sum_i y_i = 0 \quad (7.26)$$

For an eigenvector $\underline{v} \in \mathbf{C}^N$ of \mathcal{P} , using Eq. (7.24),

$$\underline{v} \mathcal{P} = t \underline{\pi} \mathcal{P} + \underline{y} \mathcal{P} = \lambda t \underline{\pi} + \lambda \underline{y} \quad (7.27)$$

here, $\underline{y} \mathcal{P} \in \mathcal{V}_0$, and thus, for the decomposition of the vector space \mathbf{C}^N , it must necessarily be

$$\begin{cases} t \underline{\pi} \mathcal{P} = \lambda t \underline{\pi} \\ \underline{y} \mathcal{P} = \lambda \underline{y} \end{cases} \quad (7.28)$$

Let's consider the eigenvalue equation

$$\underline{y} \mathcal{P} = \lambda \underline{y}, \quad (7.29)$$

with $\underline{y} \in \mathcal{V}_0$ and $\underline{y} \neq 0$. Explicitating the matrix product and focusing on the i -th component,

$$\lambda y_i = \sum_k y_k \mathcal{P}_{k \rightarrow i} \quad (7.30)$$

Taking the absolute value, summing over the components, and considering that $\underline{\mathcal{P}}$ has non-negative elements.

$$|\lambda| \sum_i |y_i| = \sum_i \left| \sum_k y_k \mathcal{P}_{k \rightarrow i} \right| \leq \sum_i \sum_k |y_k| \mathcal{P}_{k \rightarrow i} = \sum_k |y_k|, \quad (7.31)$$

that implies

$$|\lambda| \leq 1 \quad (7.32)$$

If the transition matrix $\underline{\mathcal{P}}$ has the elements strictly positive, then Eq. (7.31) is strict inequality; this can be understood if we consider a summation of complex numbers $\sum_{n=1}^N r_n e^{i\phi_n}$, it is true that

$$\left| \sum_{i=1}^N r_n e^{i\phi_n} \right| = \sum_{i=1}^N |r_n e^{i\phi_n}| \quad (7.33)$$

if and only if $\phi_n = a \in \mathbf{R} \forall n \in [1, N]$; however, by hypothesis $\sum_k y_k = 0$ and $\underline{y} \neq 0$ and this necessarily implies that at least one component of \underline{y} must have a different phase; moreover, we have assumed that the matrix elements of $\mathcal{P}_{k \rightarrow i}$ are strictly positive so in a product they won't change the phases of the vector, meaning that $y_k \mathcal{P}_{k \rightarrow i}$ has the same phase of y_k . Hence, under the condition of strict positiveness of the matrix elements of $\underline{\mathcal{P}}$, holds that

$$|\lambda| < 1 \quad (7.34)$$

This is the crucial point of this demonstration. Using now the regularity condition we demonstrate the following statement.

Statement. For a regular transition matrix, $|\lambda| < 1$.

By definition of regularity, if $\underline{\mathcal{P}}$ is regular, then there is an integer $m > 0$ such that $\underline{\mathcal{P}}^m$ has strictly positive elements, $\underline{\mathcal{P}}^m$ is also a transition matrix, so the passages of the demonstration can be applied also to $\underline{\mathcal{P}}^m$ resulting in

$$|\lambda^m| < 1 \quad (7.35)$$

and this immediately implies that $|\lambda| < 1$. Consider now an arbitrary initial probability v , then

$$\underline{v} \underline{\mathcal{P}}^n = (\underline{\pi} + \underline{v} - \underline{\pi}) \underline{\mathcal{P}}^n = \underline{\pi} + (\underline{v} - \underline{\pi}) \underline{\mathcal{P}}^n \quad (7.36)$$

From Eq. (7.24) it is clear that $\underline{v} - \underline{\pi} \in \mathcal{V}_0$, but the linear operator $\underline{\mathcal{P}}$ defined on \mathcal{V}_0 has eigenvalues that in modulus are strictly lesser than 1; from Functional Analysis[8], given these conditions, it follows that

$$\lim_{n \rightarrow +\infty} \{(\underline{v} - \underline{\pi})\underline{\mathcal{P}}^n\} = 0. \quad (7.37)$$

In conclusion we have,

$$\lim_{n \rightarrow +\infty} \underline{v}\underline{\mathcal{P}}^n = \underline{\pi} + \lim_{n \rightarrow +\infty} \{(\underline{v} - \underline{\pi})\underline{\mathcal{P}}^n\} = \underline{\pi}, \quad (7.38)$$

this proves the theorem of uniqueness. \square

7.1.2 The Metropolis algorithm

Given a probability distribution π defined on a finite set $E = \{1, \dots, N\}$ we now show a recipe to obtain a transition matrix $\underline{\mathcal{P}}$ for which π is the only invariant probability, namely

$$\pi_j = \lim_{n \rightarrow +\infty} (\underline{v}\underline{\mathcal{P}}^n)_j \quad . \quad (7.39)$$

The recipe that we are going to show is the Metropolis algorithm[6] and it allows to sample any arbitrary probability density that satisfies some conditions. This algorithm is relevant in our context because it is used to evaluate N -dimensional integrals like the one in Eq. (7.3).

Theorem 3. (Metropolis). *Given a strictly positive probability distribution π , $\pi_j > 0 \forall j$, that is not the uniform probability density, for each probability distribution v , there is a Markov chain with initial probability v and regular transition matrix $\underline{\mathcal{P}}$ that has π as invariant distribution probability. The transition matrix $\underline{\mathcal{P}}$ is defined as:*

$$\mathcal{P}_{i \rightarrow j} = \begin{cases} \mathcal{L}_{i \rightarrow j}, & i \neq j, \pi_j \geq \pi_i \\ \mathcal{L}_{i \rightarrow j} \frac{\pi_j}{\pi_i}, & i \neq j, \pi_j < \pi_i \\ 1 - \sum_{j \neq i} \mathcal{P}_{i \rightarrow j}, & i = j \end{cases} \quad (7.40)$$

where $\underline{\mathcal{L}}$ is any symmetric and irreducible transition matrix.

Proof. With this choice of $\underline{\mathcal{P}}$, let's show that π satisfies the detailed balance condition; chose two elements i, j of E such that $\pi_j \leq \pi_i$, applying equation (7.40) we obtain,

$$\pi_i \mathcal{P}_{i \rightarrow j} = \pi_i \mathcal{L}_{i \rightarrow j} \frac{\pi_j}{\pi_i} = \mathcal{L}_{i \rightarrow j} \pi_j = \pi_j \mathcal{P}_{i \rightarrow j}, \quad (7.41)$$

where we used the symmetry of $\underline{\mathcal{L}}$; this shows that π is indeed an invariant probability associated to $\underline{\mathcal{P}}$. To prove the theorem we have to show that π is also the *unique* invariant probability of $\underline{\mathcal{P}}$; to this purpose, we will show then that $\underline{\mathcal{P}}$ is regular. Let's start from the irreducibility.

Statement. $\underline{\mathcal{P}}$ is irreducible. This follows directly from the irreducibility of $\underline{\mathcal{L}}$. The irreducibility is in fact related to the non-zero element of the transition matrix, this implies that if a transition matrix is irreducible, then it is also true for any transition matrix that has at least the same non-zero elements. This is exactly the case for $\underline{\mathcal{P}}$ as can be readily seen from its definition in Eq. (7.40). To show that $\underline{\mathcal{P}}$ is also regular, as shown in the previous section, it is enough to verify that there is an element $i_0 \in E$ such that $\mathcal{P}_{i_0 \rightarrow i_0} > 0$. By hypothesis, π is not the uniform probability distribution and thus there is a subset $M \subset E$ in which π is maximum, moreover, due to the irreducibility of $\underline{\mathcal{L}}$, there are two elements $i_0 \in M$ and $j_0 \in M^C$ such that $\mathcal{P}_{i_0 \rightarrow j_0} > 0$; remembering that, by definition, if $i \neq j$ then $\mathcal{P}_{i \rightarrow j} \leq \mathcal{L}_{i \rightarrow j}$, we have,

$$\begin{aligned}
\mathcal{P}_{i_0 \rightarrow i_0} &= 1 - \sum_{j \neq i_0} \mathcal{P}_{i_0 \rightarrow j} = 1 - \sum_{j \neq i_0, j_0} \mathcal{P}_{i_0 \rightarrow j} - \mathcal{P}_{i_0 \rightarrow j_0} \geq \\
&\geq 1 - \sum_{j \neq i_0, j_0} \mathcal{L}_{i_0 \rightarrow j} - \mathcal{L}_{i_0 \rightarrow j_0} \frac{\pi_{j_0}}{\pi_{i_0}} = \\
&= 1 - \sum_{j \neq i_0} \mathcal{L}_{i_0 \rightarrow j} + \mathcal{L}_{i_0 \rightarrow j_0} \left(1 - \frac{\pi_{j_0}}{\pi_{i_0}} \right) \geq \\
&\geq \mathcal{L}_{i_0 \rightarrow j_0} \left(1 - \frac{\pi_{j_0}}{\pi_{i_0}} \right) > 0 \quad . \tag{7.42}
\end{aligned}$$

And this proves the regularity of $\underline{\mathcal{P}}$; from the Markov theorem follows the uniqueness of the invariant probability distribution and this proves the theorem. \square

In most practical cases, Eq. (7.40) for $i \neq j$ is written in the form:

$$\mathcal{P}_{i \rightarrow j} = \mathcal{L}_{i \rightarrow j} \min \left(1, \frac{\pi_j}{\pi_i} \right) \quad . \tag{7.43}$$

The meaning of this relation is that the entire Markov chain can be built with pre-determined moves, $\mathcal{L}_{i \rightarrow j}$ that might be accepted with probability $\min \left(1, \frac{\pi_j}{\pi_i} \right)$. These moves, starting from a probability X_n propose a transition to a probability X_{n+1} : if this transition is accepted, X_{n+1} has been determined, in case of rejection $X_{n+1} = X_n$. The condition of irreducibility of $\underline{\mathcal{L}}$ means that the moves must be chosen so that their combination is able to explore the whole state space E , this property is called *ergodicity*. The symmetry of $\underline{\mathcal{L}}$ is a detailed balance condition on the Metropolis moves, this however can be dropped in favor of the weaker condition $\mathcal{L}_{i \rightarrow j} > 0$ whenever $\mathcal{L}_{j \rightarrow i} > 0$ if a new definition of $\mathcal{P}_{i \rightarrow j}$ is taken:

$$\mathcal{P}_{i \rightarrow j} = \mathcal{L}_{i \rightarrow j} \min \left(1, \frac{\pi_j \mathcal{L}_{j \rightarrow i}}{\pi_i \mathcal{L}_{i \rightarrow j}} \right) \quad . \tag{7.44}$$

A good choice of Metropolis moves will enhance the convergence of the Markov chain towards the equilibrium probability distribution.

7.1.3 Sampling and expectation values

In the previous section, we have seen a procedure to sample an arbitrary distribution probability such that in Eq. (7.3). In order to evaluate that N -dimensional integral, however, there are still two problems to take care of. First, the Monte Carlo evaluation of an integral is a statistical method and as such the results have an intrinsic statistical error due to the finite number of sampled values, and second, the Metropolis algorithm produces an highly correlated sampling of the probability distribution $p(\vec{x})$. To overcome these problems the block average technique can be used: if the summation in Eq. (7.1) is truncated after N_s terms, a block $I_{N_s} = \frac{1}{N_s} \sum_{i=1}^{N_s} g(\vec{x}_i)$ is defined. If N_s is long enough, each evaluated I_{N_s} can be considered statistical independent from the others; hence, by the central limit theorem, I_{N_s} is a Gaussian distributed random variable; if the set of values $I_N^1, I_N^2, \dots, I_N^{N_{blocks}}$ are generated with Eq. (7.1), then the average value I_{avg} and the standard deviation σ can be computed with the usual formulas:

$$I_{avg} = \frac{1}{N_{blocks}} \sum_{i=1}^{N_{blocks}} I_N^i \quad (7.45)$$

$$\sigma^2 = \frac{1}{N_{blocks} - 1} \sum_{i=1}^{N_{blocks}} (I_N^i - I_{avg})^2 \quad , \quad (7.46)$$

where the error of the estimation I_{avg} is $\sigma/\sqrt{N_{blocks}}$. This method for the evaluation of N -dimensional integrals is asymptotic, in fact the correct sampling of a distribution will be given only after that a long enough Markov chain has been built. This means that the probability distribution $p(\vec{x})$ is sampled only after a certain number of equilibration steps. This equilibration number can be evaluated by plotting on a graph the value of the integral averaged within a Monte Carlo block versus the index of the corresponding Monte Carlo block: equilibration is over as soon as transients disappear from the plot, provided that the chosen set of moves can efficiently explore the whole space of events. This might seem to be an easy condition to fulfill but in some cases a long equilibration is required, especially when the distribution density to sample has many local maxima separated by regions of low probability density. In Fig. 7.2 we show the value of an integrand evaluated at each MC step: the equilibration transient is clearly visible in the first twenty MC steps; the correlation of the Markov chain manifests here as a pattern in the values of the integrand.

7.1.4 Metropolis sampling

We now apply the Monte Carlo sampling to the problem of evaluating a quantum expectation value of a local operator \hat{O} introduced in Sec. 2.1; this quantum expectation value, from Eq. (2.11), can be written in compact form as

$$\langle \hat{O} \rangle = \int d\Gamma O(\Gamma)p(\Gamma) \quad (7.47)$$

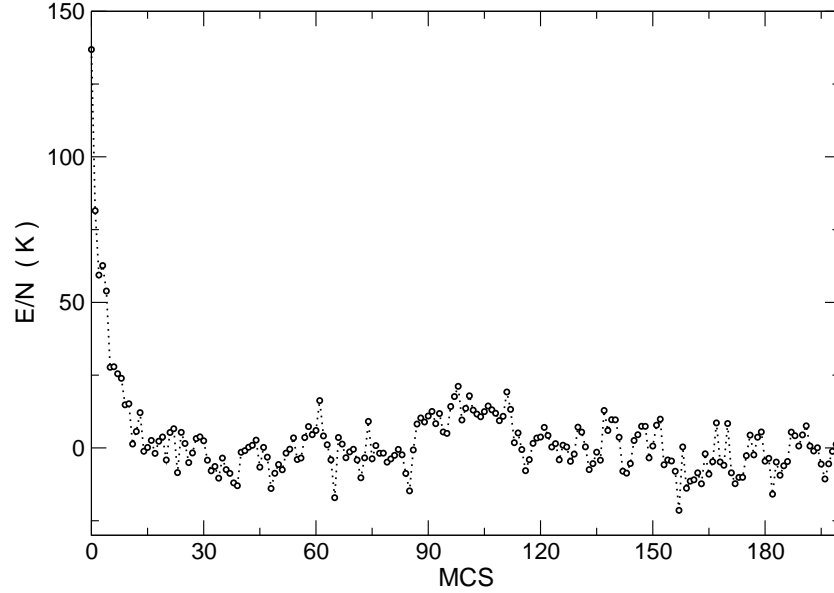


Figure 7.2: The “instantaneous” value of an integrand for each Monte Carlo Step. This integral represents the energy of one atom of ${}^4\text{He}$ in a 1D model potential defined by $V(x) = \sigma_1 x^4 - \sigma_2 x^2$, where $\sigma_1 = 8 \text{ K}\text{\AA}^{-4}$ and $\sigma_2 = 8 \text{ K}\text{\AA}^{-2}$. The methodology used to evaluate this integral is the Path Integral Ground State that will be described in Sec. 2.1.

where $\Gamma = \{R_1, \dots, R_M\}$. In this section we consider the PIGS case; the adaptation to quantum thermal averages is straightforward and will be considered contextually. The Metropolis algorithm is used to sample the multi-dimensional probability distribution $p(\Gamma)$ in Eq. (2.18), that, explicating the normalization constant \mathcal{N} , takes the form

$$p(\Gamma) = \frac{\Psi_T(R_1) \prod_{j=1}^{M-1} G(R_j, R_{j+1}, \delta\tau) \Psi_T(R_M)}{\int d\Gamma \Psi_T(R_0) \prod_{j=1}^{M-1} G(R_j, R_{j+1}, \tau) \Psi_T(R_M)} . \quad (7.48)$$

The sampling of $p(\Gamma)$ is made with a sequence of Metropolis “moves”. A move is a two-step process sketched in Fig. 7.3; this process, from a set of configurations Γ proposes a new set Γ_{new} and then evaluates whether to accept or reject the new set of configurations. The probability to accept the move is defined by Eq. (7.43), where the term $\mathcal{L}_{i \rightarrow j}$ represents the probability to try a move that from a configuration i proposes a new configuration j . From the *a-priori* knowledge of the system under study it is possible to use *guided* moves that are more likely able to sample physical configurations rather than highly improbable ones (in this case the probability to accept the move becomes Eq. (7.44); such a guided approach would enhance the convergence of the sampling, especially if the probability distribution has many local minima. The moves that will be described shortly are unguided, so that $\mathcal{L}_{i \rightarrow j} = \mathcal{L}_{j \rightarrow i}$

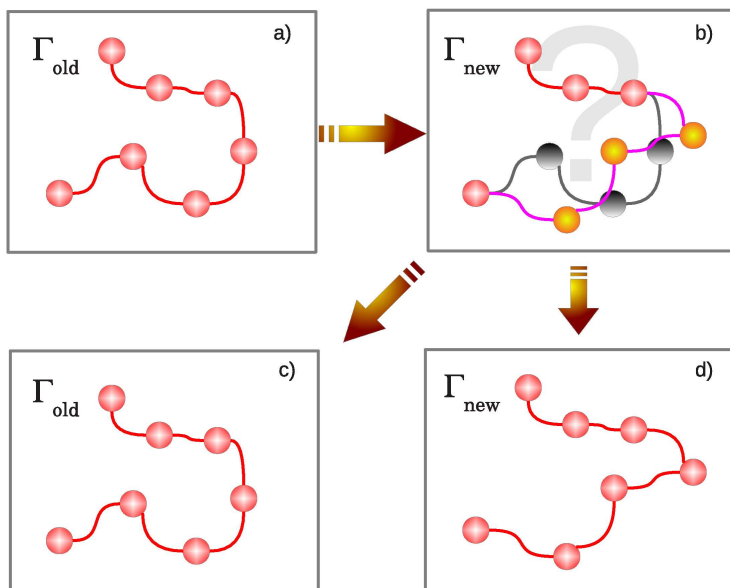


Figure 7.3: General scheme for a Metropolis move: from a configuration (a), a move is proposed (b). At this point the move can be accepted (c) or rejected (d). If the move is accepted, the new MC step will have a new configuration Γ_{new} ; otherwise the same configuration Γ_{old} is sampled again. Grey beads and lines represent the removed segment of the polymer.

and their probability to be accepted simplifies to the following relation

$$a(\Gamma_{new}) = \min \left(1, \frac{\Psi_T(R_1^{new}) \prod_{j=1}^{M-1} G(R_{j_{new}}, R_{j+1_{new}}, \delta\tau) \Psi_T(R_M^{new})}{\Psi_T(R_1) \prod_{j=1}^{M-1} G(R_j, R_{j+1}, \delta\tau) \Psi_T(R_M)} \right) . \quad (7.49)$$

In the context of quantum–classical isomorphism, a move can involve one or more different polymers. A move involving a single polymer is represented as a reconfiguration of some or all the beads of the polymer itself; the probability to accept such a move depends on the correlations of the beads at the same imaginary–time discretization (inter–polymer correlations) and on the correlations between adjacent beads that belong to the same polymer (intra–polymer correlation). This latter contribution is also referred as *kinetic spring* because comes from the kinetic term of the Hamiltonian (Eq. 2.13) and disfavors configurations in which two adjacent beads are placed far away from each other. A move involving many polymers is a generalization of a single polymer move; these moves can also involve permutations between polymers that can be employed to take into account the quantum statistics of the system.

A Monte Carlo simulation consists of a set of Monte Carlo Steps (MCS); in general, after each step the estimators can be evaluated. A MCS consists of a set of Metropolis moves that are tuned so that the effect of all the accepted moves modifies the positions of roughly half the beads that compose the system of polymers. The Metropolis moves

that are proposed here are the translation moves, the Brownian bridges and the permutation sampling. Later in this section will be introduced the Worm algorithm in the Canonical ensemble with its Metropolis moves. These moves can be also used for PIMC with a slight adaptation for the translation of a polymer.

In order to simplify the notation, we define the free particle propagator that appears in Eq. (2.13) as

$$G_0(\vec{r}, \vec{r}', \delta\tau) = \left(\frac{1}{4\pi\lambda\delta\tau} \right)^{\frac{d}{2}} e^{-\frac{|\vec{r}-\vec{r}'|^2}{4\lambda\delta\tau}} . \quad (7.50)$$

Translation of a single bead

In a PIGS simulation, this move, represented in Fig. 7.4 is generally applied to the first or the last bead of a polymer, namely \vec{r}_i^1 or \vec{r}_i^M . This is the simplest move for such beads: there are other, more performant, possibilities that allow to move a certain number of beads including \vec{r}_i^1 or \vec{r}_i^M ; one of those moves is a generalization of the Brownian bridge that takes into account the correlations from the trial wave function. The Brownian bridge will be introduced soon; however, in this work we did not implement the mentioned extension. Instead, we used the following move. Let's focus on the first bead of the i -th polymer, \vec{r}_i^1 ; the new configuration will have a translation of a vector \vec{d} applied to $\vec{r}_{i_{old}}^1 = \vec{r}_i^1$, namely $\vec{r}_{i_{new}}^1 = \vec{r}_i^1 + \vec{d}$.

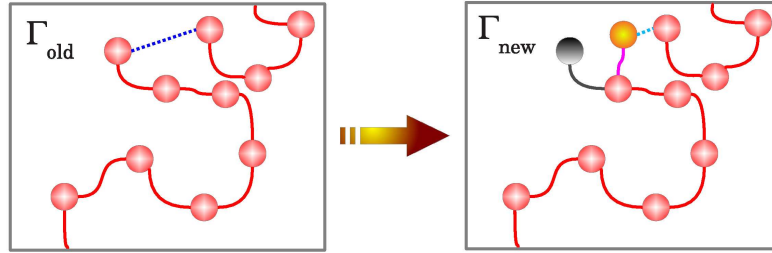


Figure 7.4: Scheme for the translation of an extremal bead of a polymer. Grey beads and lines represent the old position and kinetic correlation of the bead.

The probability to accept this move is

$$P_{sing} = \frac{a(\{R\}_{new}) \Psi_T(R_1^{new}) e^{-\frac{\delta\tau}{2} \sum_{k \neq i} v(|\vec{r}_{i_{new}}^1 - \vec{r}_k^1|)}}{a(\{R\}_{old}) \Psi_T(R_1^{old}) e^{-\frac{\delta\tau}{2} \sum_{k \neq i} v(|\vec{r}_{i_{old}}^1 - \vec{r}_k^1|)}} . \quad (7.51)$$

For the last bead, \vec{r}_i^M ,

$$P_{sing} = \frac{a(\{R\}_{new}) = \min(1, P_{tr})}{e^{-\frac{\delta\tau}{2} \sum_{k \neq i} v(|\vec{r}_{i_{new}}^M - \vec{r}_k^M|)} \Psi_T(R_M^{new})} \cdot \frac{e^{-\frac{\delta\tau}{2} \sum_{k \neq i} v(|\vec{r}_{i_{old}}^M - \vec{r}_k^M|)} \Psi_T(R_M^{old})}{1} \quad (7.52)$$

Translation of a polymer

In a translation (Fig. 7.5, a polymer i is rigidly moved by a vector. Kinetic springs remain unchanged and the probability to accept the move depends thus only on the interpolymer correlations.

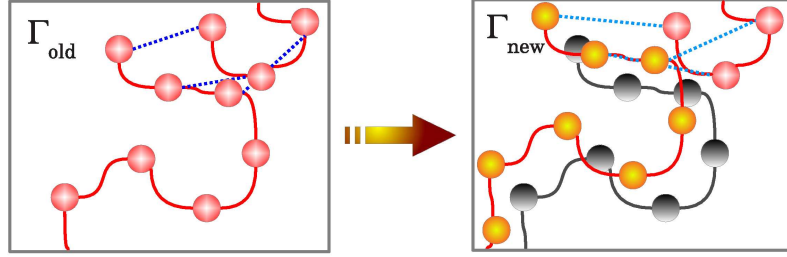


Figure 7.5: Scheme for the translation of an entire polymer. Grey beads and lines represent the old configuration of the polymer.

$$P_{tr} = \frac{a(\{R\}_{new}) = \min(1, P_{tr})}{\Psi_T(R_1^{old}) e^{-\frac{\delta\tau}{2} \sum_{k \neq i} v(|\vec{r}_{i_{old}}^1 - \vec{r}_k^1|)}} \times \frac{\Psi_T(R_1^{new}) e^{-\frac{\delta\tau}{2} \sum_{k \neq i} v(|\vec{r}_{i_{new}}^1 - \vec{r}_k^1|)}}{\Psi_T(R_1^{old}) e^{-\frac{\delta\tau}{2} \sum_{k \neq i} v(|\vec{r}_{i_{old}}^1 - \vec{r}_k^1|)}} \times \frac{\prod_{j=2}^{M-1} e^{-\delta\tau \sum_{k \neq i} v(|\vec{r}_{i_{new}}^j - \vec{r}_k^j|)} e^{-\frac{\delta\tau}{2} \sum_{k \neq i} v(|\vec{r}_{i_{new}}^M - \vec{r}_k^M|)} \Psi_T(R_M^{new})}{\prod_{j=2}^{M-1} e^{-\delta\tau \sum_{k \neq i} v(|\vec{r}_{i_{old}}^j - \vec{r}_k^j|)} e^{-\frac{\delta\tau}{2} \sum_{k \neq i} v(|\vec{r}_{i_{old}}^M - \vec{r}_k^M|)} \Psi_T(R_M^{old})} \quad (7.53)$$

In PIMC, the translation move has a probability to be accepted that is slightly different from Eq. (7.53):

$$P_{tr} = \frac{a(\{R\}_{new}) = \min(1, P_{tr})}{\prod_{j=1}^M e^{-\delta\tau \sum_{k \neq i} v(|\vec{r}_{i_{new}}^j - \vec{r}_k^j|)}} \cdot \frac{\prod_{j=1}^M e^{-\delta\tau \sum_{k \neq i} v(|\vec{r}_{i_{old}}^j - \vec{r}_k^j|)}}{\prod_{j=1}^M e^{-\delta\tau \sum_{k \neq i} v(|\vec{r}_{i_{old}}^j - \vec{r}_k^j|)}} \quad (7.54)$$

Brownian bridge

The Brownian bridge move is a very efficient way to reconstruct a segment composed of S adjacent beads. A schematic description of this move is shown in Fig. 7.6. The segment of polymer that the Brownian bridge re-creates represents the sampling of the free particle propagation in imaginary time between two time sectors. This propagation, as will be shown below, can be sampled exactly via the Box–Muller method[9]. This is a useful feature: the kinetic correlations of the reconstructed segment are sampled exactly, therefore the probability of acceptance of the move will depend only on the correlations between different polymers. This is readily seen if one considers the correlations of a segment of the i -th polymer $(\vec{r}_i^j, \dots, \vec{r}_i^{j+s})$ that is part of a configuration of polymers Γ :

$$\pi(\Gamma) = \prod_{m=j}^{j+s} e^{-\frac{1}{4\lambda\delta\tau} |\vec{r}_i^m - \vec{r}_i^{m+1}|^2} e^{-\delta\tau \sum_{l \neq i}^N v(|\vec{r}_i^m - \vec{r}_l^m|)} \quad (7.55)$$

the kinetic and potential parts are factorized. Recalling the Metropolis algorithm (Sec. 7.1.2), the general form of the transition matrix that represents the Markov chain is factorized in a “move” $\mathcal{L}_{i \rightarrow j}$ and an acceptance of the move:

$$\mathcal{P}_{i \rightarrow j} = \mathcal{L}_{i \rightarrow j} \min \left(1, \frac{\pi_j \mathcal{L}_{j \rightarrow i}}{\pi_i \mathcal{L}_{i \rightarrow j}} \right) . \quad (7.56)$$

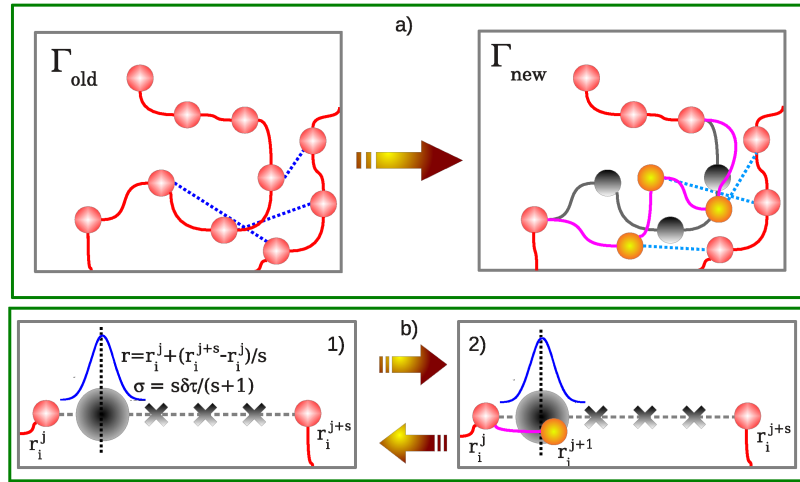


Figure 7.6: (Upper panel) The Brownian bridge: a segment of a polymer is reconstructed. (Lower panel) Iterative procedure used to sample a free particle propagation between two fixed extremities. Grey beads and lines represent the removed segment of the polymer.

In the case of the Brownian bridge, the move $\mathcal{L}_{i \rightarrow j} = \mathcal{L}_{j \rightarrow i}$ is the exact sampling of the free particle propagation in imaginary-time, $\pi_j = \pi(\Gamma_{new})$ is the correlation value of the new segment and $\pi_i = \pi(\Gamma_{old})$ is the correlation value of the segment before the move: the rest of the system is not changed by this move and the respective correlations, being unchanged, cancel out. From Eq. (7.55) it is clear that the free particle propagator that defines $\mathcal{L}_{i \rightarrow j}$ is a part of π_j ; therefore, the probability to accept a new segment becomes $a = \min(1, P_{bb})$, with:

$$P_{bb} = \frac{\prod_{m=j}^{j+s} e^{-\delta\tau \sum_{k \neq i} v(|\vec{r}_{i_{new}}^m - \vec{r}_k^m|)}}{\prod_{m=j}^{j+s} e^{-\delta\tau \sum_{k \neq i} v(|\vec{r}_{i_{old}}^m - \vec{r}_k^m|)}} \quad (7.57)$$

where the reconstruction starts from the $j + 1$ bead of the i -th polymer and the last reconstructed bead is at position $j + s - 1$.

The following operations, also illustrated in Fig. 7.6, are performed during the move:

- Remove the beads between j and $j + s$.
- Create a new timeslice at position $j + 1$: from the coordinates of the timeslices j and $j + s$, determine the coordinates of the new timeslice $j + 1$. These coordinates are determined in the following way: we first note that the bead at position $j + 1$ is the free propagation from the bead at position j , $p_1(\vec{r}_i^j, \vec{r}^*) = G_0(\vec{r}_i^j, \vec{r}^*, \delta\tau)$, and the free propagation from the bead at position $j + s$, $p_2(\vec{r}_i^{j+s}, \vec{r}^*) = G_0(\vec{r}_i^{j+s}, \vec{r}^*, s\delta\tau)$. The probability density from which the position \vec{r}_i^{j+1} is sampled is thus the joint probability $p_1 p_2$; with straightforward algebraic operations, this joint probability can be reconduced to the Gaussian form of Eq. (7.50) times a trivial normalization constant \mathcal{N}_t that won't affect the sampling; namely, the new bead is sampled from

$$p(\vec{r}^*) = p_1(\vec{r}_i^j, \vec{r}^*) p_2(\vec{r}_i^{j+s}, \vec{r}^*) = \mathcal{N}_t G_0(\vec{r}^*, \vec{r}_i^j + \frac{\vec{r}_i^{j+s} - \vec{r}_i^j}{s}, \frac{s}{s+1} \delta\tau) \quad (7.58)$$

- From the newly created bead, $j+1$, and the bead $j+s$, determine the coordinates of the bead $j + 2$. This is done by iteration, considering a segment of polymer that starts at $j + 1$ and has length $s - 1$. The procedure is iterated until the bead at position $j + s - 1$ has been determined.

This move samples the free particle propagation between two given extremities; it may happens that the two extremities are in different polymers that are connected at a timeslice j_p by a permutation cycle \hat{P} ; in this case the labels j , i and k must be permuted, so that $i \rightarrow \hat{P}_j i$ and $k \rightarrow \hat{P}_j k$, where $\hat{P}_j = \hat{I}$ for $j < j_p$ and $\hat{P}_j = \hat{P}$ otherwise.

The probability of acceptation can be varied modifying the length of the Brownian bridges. As an empirical rule, a good choice of this probability can be between 0.3 and 0.5. This is a reasonable trade-off between long moves and small moves: long

moves, on one hand, would yield an high rejection rate resulting in poor performance of the simulation; small moves, on the other hand, have an high acceptance ratio but might compromise the ergodicity of the simulation; this happens because improbable configurations would rarely be sampled.

Permutation sampling

The permutation sampling introduces the Bose symmetry in the system. In the polymer description, it is a move that involves a permutation between a variable number of polymers greater than one. As mentioned in Sec. 2.1.1, this move is necessary in PIGS when the trial wave function does not possess the Bose symmetry. This move is also necessary at finite temperature: in PIMC, in fact, the thermal average is not expressed through the quantum imaginary-time evolution of a trial wave function; as consequence, the Bose symmetry has to be explicitly introduced through permutation sampling.

Here we will show the algorithm described in Ref. [10]. The polymers involved in the permutation are selected with a kinetic test to be described soon. Once the polymers i_1 and i_2 have been selected, their beads between two time sectors j_0 and $j_0 + s$ are removed. At this point, a Brownian bridge is made from the bead at position j_0 of the polymer i_1 , to the bead at position $j_0 + s$ of the polymer i_2 . The permutation move follows the scheme in Figure 7.7: the iteration of this ‘swap’ procedure proceeds between polymers i_2 and i_3 , and so on until a polymer i_n closes on the polymer i_0 .

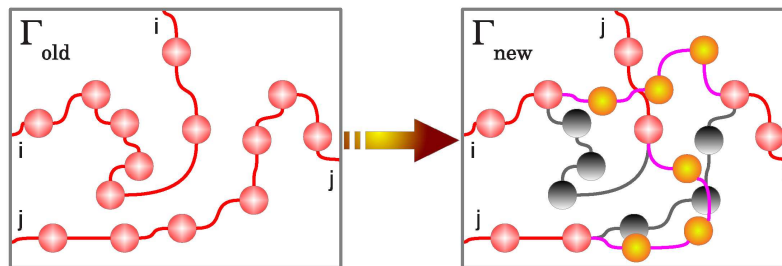


Figure 7.7: Permutation of two polymers i and j : the resulting configuration has still two polymers of the same length; it is thus topologically similar to the previous one. Grey beads and lines represent the removed segment of the polymer.

There are two main steps in permutation sampling: the kinetic test and the reconstruction step.

Kinetic Test step. Given a starting timeslices j_0 and a length of reconstructions s , this operation selects the polymers that are best suited for permutations and gives in output an ordered sequence of swaps between the polymers. The kinetic test starts from a random polymer i_1 that is chosen by generating an integer number between 1 and N from a uniform distribution probability. At this point, the following operations determine the next polymer which joins the permutation cycle.

- For the particle i_1 , build a table as follows

$$K_{i_1\omega}^1 = G_0(\vec{r}_{i_1}^{j_0}, \vec{r}_\omega^{j_0+s}, s\delta\tau) (1 - \delta_{i_1,\omega}) \quad (7.59)$$

where $\vec{r}_{i_1}^{j_0}$ are the coordinates of the polymer i_1 at timeslice j_0 .

- From Eq. (7.59), the probability to accept the particle i_1 in the permutation cycle is

$$C^{(1)} = \frac{\sum_\omega K_{i_1\omega}^1}{G_0(\vec{r}_{i_1}^{j_0}, \vec{r}_{i_1}^{j_0+s}, s\delta\tau) + \sum_\omega K_{i_1\omega}^1} . \quad (7.60)$$

Generate a random number p , uniformly distributed between 0 and 1. If $p > C^{(1)}$, the move is rejected; otherwise the process continues to the next step.

- From $K_{i_1\omega}^1$ a new particle is randomly chosen. The probability to chose a the particle ν is

$$\Pi_\nu = \frac{K_{i_1\nu}^1}{\sum_\omega K_{i_1\omega}^1} . \quad (7.61)$$

The new particle is selected with a ‘faked roulette’: the interval $[0, 1)$ is partitioned with bins of width Π_ν ; a bin Π_ν corresponds to the particle ν ; generate an uniformly distributed random number in the interval $[0, 1)$, the bin which contains this number corresponds to the particle that ‘wins’ the faked roulette; this particle is i_2 .

- Make an acceptance test on i_2 , similarly to that made on i_1

$$K_{i_2\omega}^2 = G_0(\vec{r}_{i_2}^{j_0}, \vec{r}_\omega^{j_0+s}, s\delta\tau) (1 - \delta_{i_2,\omega})$$

$$C^{(2)} = \frac{\sum_\omega K_{i_2\omega}^2}{G_0(\vec{r}_{i_2}^{j_0}, \vec{r}_{i_2}^{j_0+s}, s\delta\tau) + \sum_\omega K_{i_2\omega}^2} . \quad (7.62)$$

Again, generate a random number p , uniformly distributed between 0 and 1. If $p > C^{(2)}$, the move is rejected, else the particle i_2 is added to the permutation cycle.

These operations are repeated until either an acceptance test fails or a particle $i_\alpha = i_1$ is added to the permutation cycle.

The Dirac’s deltas that appears in $K_{i_n\omega}^n$ have two purposes:

- Exclude the possibility for a particle to swap with itself
- Exclude the possibility for a particle to swap with any other particle already added to the permutation cycle, except for the first particle of the permutation cycle.

The general definition for $K_{i_n\omega}^n$ is thus

$$K_{i_n\omega}^n = G_0(\vec{r}_{i_n}^{j_0}, \vec{r}_{\omega}^{j_0+s}, s\delta\tau) (1 - \delta_{i_2,\omega}) (1 - \delta_{i_3,\omega}) \dots (1 - \delta_{i_n,\omega}) \quad . \quad (7.63)$$

The output of the kinetic test step is a sequence of particles $(i_1, i_2, \dots, i_\alpha, i_1)$; from this output, the reconstruction step begins.

Reconstruction step. Starting from the previously obtained permutation cycle $(i_1, i_2, \dots, i_\alpha, i_{\alpha+1} \equiv i_1)$, α Brownian bridges are built from the j_0 bead of the i_1 polymer to the $j_0 + s$ bead of the i_2 , and so on until the last Brownian bridge from the j_0 bead of the i_α polymer to the $j_0 + s$ bead of the $i_{\alpha+1}$ closes the loop.

The obtained new configuration has a probability to be accepted that is the product of Eq. (7.57) for each reconstructed segment. If the move is accepted, this new configuration is kept, if this acceptance test fails the configuration prior to the permutation move has to be restored. The probability to accept exchanges is usually very low and in order to obtain an efficient permutation sampling one has to try thousands of permutation moves in a single MCS; moreover, in most cases, the probability to accept a permutation drops exponentially with the number of polymers involved in the permutation and thus the efficiency of this algorithm for permutation sampling get worse with increasing particle number N . Given a permutation cycle, the probability to accept the reconstruction step is roughly the product of the probability to accept each single Brownian bridge of the same length; this suggests that in most cases, a good choice of the length of reconstructions s can be roughly the same as that of a single Brownian bridge; this however may not be true if the polymers are distant each other; in this case the probability to accept a permutation is maximized if it involves a sufficiently large imaginary-time; this holds even though the Brownian bridges in the reconstruction step would have low acceptances.

7.1.5 Estimators

Let's consider again the expectation value of a local operator \hat{O}

$$\langle \hat{O} \rangle = \int d\Gamma \hat{O}(\Gamma_k) p(\Gamma) \quad (7.64)$$

where $\Gamma = \{R_1, \dots, R_M\}$ and $1 \leq k \leq M$ represents the position in the path integral at which the operator is applied. This equation holds for both PIGS and PIMC depending on the choice of the multi-dimensional probability distribution $p(\Gamma)$, to be more specific, in the PIMC case,

$$p(\Gamma) = p^{PIMC}(\Gamma) = \frac{\prod_{j=1}^M G(R_j, R_{j+1}, \delta\tau)}{\int d\Gamma \prod_{j=1}^M G(R_j, R_{j+1}, \delta\tau)} \quad (7.65)$$

where we set $R_{M+1} \equiv R_1$. In the PIGS case,

$$p(\Gamma) = p^{PIGS}(\Gamma) = \frac{\Psi_T(R_1) \prod_{j=1}^{M-1} G(R_j, R_{j+1}, \delta\tau) \Psi_T(R_M)}{\int d\Gamma \Psi_T(R_1) \prod_{j=1}^{M-1} G(R_j, R_{j+1}, \delta\tau) \Psi_T(R_M)} . \quad (7.66)$$

In the previous Sec we described a method to sample $p^{PIGS}(\Gamma)$ and $p^{PIMC}(\Gamma)$, here we focus on the application of the operator \hat{O} to the density matrix. We have already pointed out in Sec. 2.2 that in PIMC, due to the cyclic property of the trace operation, one can shift the position of \hat{O} along the path integral without changing the expectation value. This is useful because one can use all the configurations $\{R_1, \dots, R_M\}$ to compute the expectation values and then average the results. Also in PIGS an operator can be evaluated at any imaginary-time τ_i ; to be more explicit on the meaning of “application of an operator at an imaginary time τ_i ”:

$$\left\langle \Psi(\tau = l\delta\tau) \left| \hat{O} \right| \Psi(\tau = (M-l)\delta\tau) \right\rangle \simeq \quad (7.67)$$

$$\frac{\int dR_1 \dots dR_M \Psi_T(R_1) \dots G(R_{l-1}, R_l, \delta\tau) \hat{O}(R_l) G(R_l, R_{l+1}, \delta\tau) \dots \Psi_T(R_M)}{\int dR_1 \dots dR_M \Psi_T(R_1) G(R_1, R_2, \delta\tau) \dots G(R_{M-1}, R_M, \delta\tau) \Psi_T(R_M)}$$

with $2 \leq l \leq M-1$. Here $|\Psi(\tau)\rangle$ represents the evolution of the trial wave function $|\Psi_T\rangle$ at an imaginary-time τ , namely $|\Psi(\tau)\rangle = |e^{-\tau\hat{H}}\Psi_T\rangle$. Differently from PIMC, due to Eq. (2.7), only for $\tau_0 \leq \tau_l \leq \tau - \tau_0$ it is verified that, to a good approximation, $|\Psi(\tau = \tau_l = l\delta\tau)\rangle \simeq |0\rangle$ and $|\Psi(\tau = \tau_{M-l} = (M-l)\delta\tau)\rangle \simeq |0\rangle$; in this case, Eq. (7.67) becomes an expectation value on the ground state of the system. Outside the interval $[\tau_0; \tau - \tau_0]$ the expectation values are mixed, more specifically, for an imaginary-time index h so that $\tau_h < \tau_0$, $\left\langle \Psi(\tau = \tau_h) \left| \hat{O} \right| 0 \right\rangle$. For $\tau_h = 0$ and $\tau_h = \tau$ we obtain respectively the mixed expectation values $\left\langle \Psi_t \left| \hat{O} \right| 0 \right\rangle$ and $\left\langle 0 \left| \hat{O} \right| \Psi_T \right\rangle$ with the trial wave function Ψ_T . These expectation values are obtained by applying the operator directly on the trial wave function,

$$\left\langle \Psi_T \left| \hat{O} \right| \tilde{\Psi} \right\rangle \simeq \quad (7.68)$$

$$\frac{\int dR_1 \dots dR_M \hat{O}(R_1) \Psi_T(R_1) G(R_1, R_2, \delta\tau) \dots G(R_{M-1}, R_M, \delta\tau) \Psi_T(R_M)}{\int dR_1 \dots dR_M \Psi_T(R_1) G(R_1, R_2, \delta\tau) \dots G(R_{M-1}, R_M, \delta\tau) \Psi_T(R_M)}$$

an analogous relation holds for $\Psi_T(R_M)$. The mixed expectation value is very useful in the evaluation of the total energy. The Hamiltonian \hat{H} , commutes with the propagator $e^{-\delta\tau\hat{H}}$ and thus the total energy can be evaluated at any time-step; however, in Eq. (7.67), we are approximating $e^{-\delta\tau\hat{H}}$ with a propagator $G(R, R', \delta\tau)$; as consequence, the commutation rule that allows the evaluation of the total energy at any time-step, holds only if the small-time approximation of the propagator is accurate enough; this provides a useful check of convergence of PIGS for what concerns the choice of $\delta\tau$. Moreover, if an accurate trial wave function is available for the system to study, the evaluation of the total energy on the variational wave function

is more accurate than that at other imaginary times; this happens because the trial wave function introduces correlations that guide the Metropolis sampling in a more efficient way to explore physical configurations.

Now that the effect of the imaginary time evolution on the expectation values has been described, we show the application of the operator \hat{O} on a density matrix $G(R_j, R_{j+1}, \delta\tau)$ in the most common choices of \hat{O} . This, of course, is generally dependent on the particular choice of small imaginary-time approximation for G , exception made of the case of an operator that is diagonal in the coordinate representation, for example, the static structure factor, the density-density correlation function in imaginary time or the radial distribution function. Consider the general case for a density matrix that can be expressed as follows:

$$G(R_m, R_{m+1}, \delta\tau) = G_0(R_m, R_{m+1}, \delta\tau) e^{-U(R_m, R_{m+1}, \delta\tau)} \quad (7.69)$$

where G_0 is the density matrix for free particles. Some of these density matrices are illustrated in Appendix. B. Let's also consider, for simplicity, the PIMC case, so that the partition function of the system becomes

$$\mathcal{Z} \simeq \int \prod_{m=1}^M dR_m e^{-\frac{(R_m - R_{m+1})^2}{4\lambda\delta\tau}} e^{-\delta\tau U(R_m, R_{m+1}, \delta\tau)} \quad (7.70)$$

The following discussion applies also in the PIGS case with at worse slight modifications that will be described contextually.

Energy

The Energy per particle, E/N , is the expectation value of $\hat{O} = \hat{H}/N$. Apart from the physical importance of this quantity, the energy is one of the main expectation values that are used to tune the parameters of the simulations.

Hamiltonian estimators This estimator is obtained by applying the operator $\hat{H} = \hat{T} + \hat{V}$ to the density matrix (7.69).

The potential term $\hat{V} = \sum_{i<j} v(r_{ij})$ is diagonal on coordinates representation, so that

$$\hat{V}G(R_m, R_{m+1}, \delta\tau) = V(R_m)G(R_m, R_{m+1}, \delta\tau) \quad (7.71)$$

In Fig. 7.8 we show the potential energy obtained from a PIGS simulation of two-dimensional ${}^4\text{He}$.

The kinetic term is $\hat{T} = -\frac{\hbar^2}{2m} \sum_i \nabla_i^2$ and

$$\begin{aligned} \nabla_i^2 G(R_m, R_{m+1}, \delta\tau) &= G(R_m, R_{m+1}, \delta\tau) \quad (7.72) \\ \left[\delta\tau^2 \left| \vec{\nabla}_i U \right|^2 + \frac{(\vec{r}_i^m - \vec{r}_i^{m+1})^2}{4\lambda^2 \delta\tau^2} + \frac{1}{\lambda} (\vec{r}_i^m - \vec{r}_i^{m+1}) \cdot \vec{\nabla}_i U - \delta\tau \nabla_i^2 U - \frac{d}{2\lambda\delta\tau} \right] \end{aligned}$$

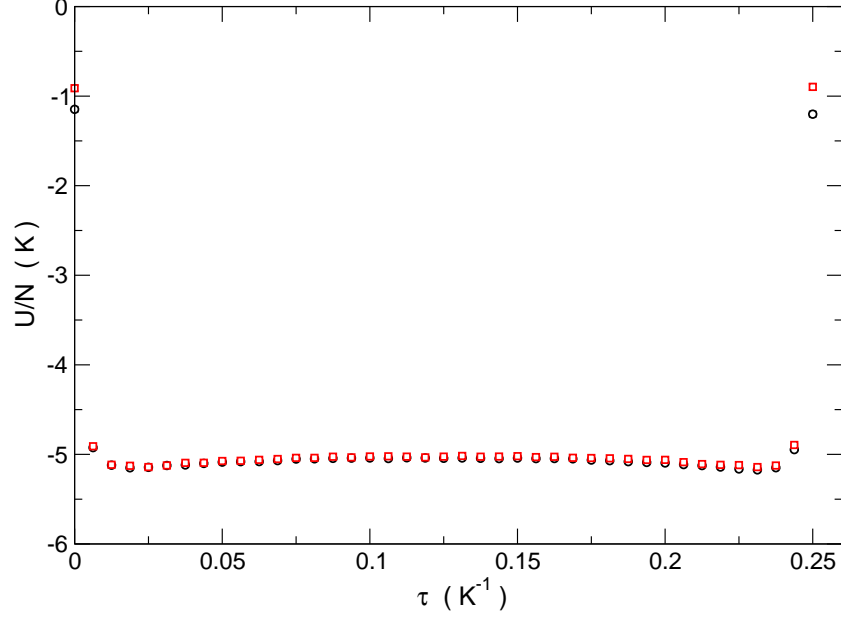


Figure 7.8: PIGS computation of the potential energy per particle versus imaginary-time for a 2D system of $N = 16$ atoms of ${}^4\text{He}$ at a density $\rho = 0.045 \text{ \AA}^{-2}$, interacting with the Aziz potential described in Ref. [7]. The trial wave function is $|\Psi_T\rangle = 1$ and the total projection time $\tau = 0.5 \text{ K}^{-1}$. Red squares are obtained with an 8-th order multi-product expansion (see Appendix B) at a timestep $6\delta\tau = 1/80 \text{ K}^{-1}$. Black circles are obtained with the primitive approximation at a timestep $\delta\tau = 1/480 \text{ K}^{-1}$; however, for comparison purposes, only points at $\tau_m = 6m/\delta\tau$ are shown.

where $U = U(R_m, R_{m+1}, \delta\tau)$ for simplicity, $\lambda = \frac{\hbar^2}{2m}$ and d is the dimensionality of the system.

Thermodynamic estimators The total energy per particle can be obtained also from the thermodynamic definition,

$$\frac{E(N, V, \beta)}{N} = -\frac{1}{N\mathcal{Z}} \frac{\partial \mathcal{Z}(N, V, \beta)}{\partial \beta} \quad (7.73)$$

where \mathcal{Z} is the partition function defined in Eq. (7.70). The thermodynamic estimator for the energy per particle is thus

$$\frac{E}{N} = \left\langle \frac{d}{2\delta\tau} - \frac{1}{4\lambda\delta\tau^2 MN} \sum_{m=1}^M (R_m - R_{m+1})^2 + \frac{1}{MN} \frac{\partial U(R_m, R_{m+1}, \delta\tau)}{\partial \delta\tau} \right\rangle. \quad (7.74)$$

In the same way, the kinetic energy per particle, K/N , can be obtained from the thermodynamic relation

$$\frac{K}{N} = \frac{m}{\beta \mathcal{Z}} \frac{\partial \mathcal{Z}(N, V, \beta)}{\partial m} \quad (7.75)$$

and the estimator becomes

$$\frac{K}{N} = \left\langle \frac{d}{2\delta\tau} - \frac{1}{4\lambda\delta\tau^2 MN} \sum_{m=1}^M (R_m - R_{m+1})^2 + \frac{m}{\delta\tau MN} \frac{\partial U(R_m, R_{m+1}, \delta\tau)}{\partial m} \right\rangle \quad (7.76)$$

where $\langle \dots \rangle$ is the average on the configurations $\{R_m\}_{m=1}^M$ that are sampled by the metropolis algorithm. An example of application of this estimator is shown in Fig. 7.9.

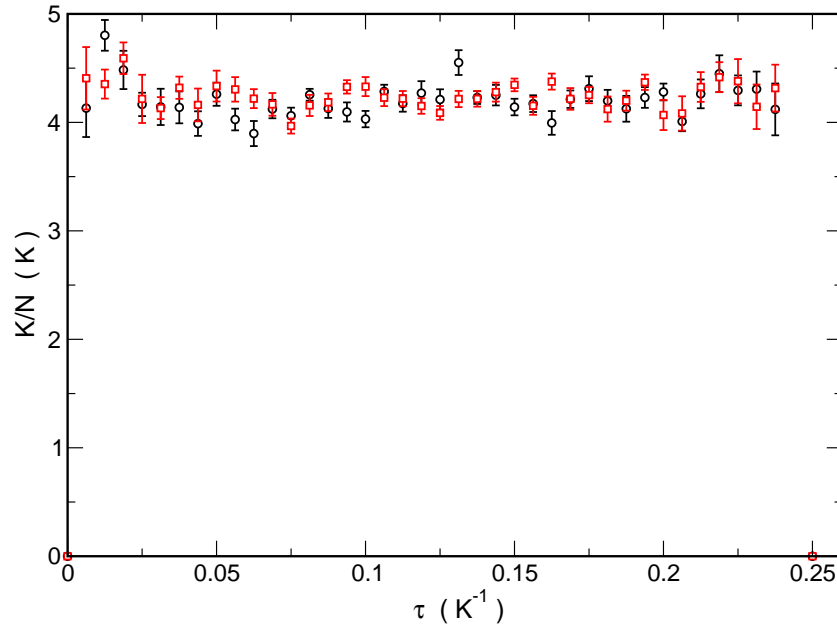


Figure 7.9: PIGS computation of the kinetic energy per particle versus imaginary-time for a 2D system of $N = 16$ atoms of ${}^4\text{He}$ at a density $\rho = 0.045 \text{ \AA}^{-2}$, interacting with the Aziz potential described in Ref. [7]. The trial wave function is $|\Psi_T\rangle = 1$ and the total projection time $\tau = 0.5 \text{ K}^{-1}$. Red squares are obtained with an 8-th order multi-product expansion (see Appendix B) at a timestep $6\delta\tau = 1/80 \text{ K}^{-1}$. Black circles are obtained with the primitive approximation at a timestep $\delta\tau = 1/480 \text{ K}^{-1}$; however, for comparison purposes, only points at $\tau_m = 6m/\delta\tau$ are shown.

The Hamiltonian and the thermodynamic estimators provide two different ways to obtain the energy, however they suffer from statistical fluctuations that increase with smaller values of $\delta\tau$, this is particularly true for the Hamiltonian estimator due to the presence of the laplacian operator, but happens in smaller degree also in the thermodynamic estimator because the first two terms in Eq. (7.74) and (7.76) are quantities that increase when $\delta\tau$ decreases and cancel each others. This requires

longer simulations when $\delta\tau$ is small and usually poses a computational limit for the evaluation of the total energy. There are at least two possibilities to overcome this problem: one can either use higher order estimators which achieve convergence at higher timestep or introduce a more advanced estimator. A choice for the latter possibility is the virial estimator[11]; the derivation of this estimator is shown in appendix A together with an explicit derivation of the thermodynamic estimators for the Pair Suzuki approximation. In this appendix we show also that although the thermodynamic estimators are obtained from a thermodynamic relation, because of the similar formalism of PIGS and PIMC, it is possible to use these estimators also in PIGS.

Radial distribution function

The pair correlation function $g(\vec{r}_1, \vec{r}_2)$ is the probability to have a particle at \vec{r}_1 and a particle at \vec{r}_2 . Within the path integral formalism,

$$g(\vec{r}_1, \vec{r}_2) = \frac{V^2}{\mathcal{Z}} \int d\vec{r}_3 \dots d\vec{r}_N G(R, R, \beta) \quad . \quad (7.77)$$

In a uniform system the pair distribution function depends only on the distance $r = |\vec{r}_1 - \vec{r}_2|$, with a change of integration variables in Eq. (7.77) and using the definition of thermal average (7.64), the estimator becomes

$$g(r) = \frac{V}{N^2 M} \left\langle \sum_{m=1}^M \sum_{i \neq j}^N \delta(|\vec{r}| - |\vec{r}_i^m - \vec{r}_j^m|) \right\rangle \quad (7.78)$$

where we have taken into account the symmetry under particle exchange and the estimator has been averaged over the timeslices m in order to employ larger statistics. In PIMC the sum over m covers all the timeslices; in PIGS, this sum must be intended only over the central timeslices, where Eq. (7.67) gives an accurate description of the ground state. To evaluate this estimator in a computer simulation one defines a partition P_n of the interval $[0; L_l/2]$ where L_l is the smallest size of the simulation box, and every element of the partition has a length Δr ; with $P_n = [n\Delta r; (n+1)\Delta r]$ then, construct an histogram of the frequencies of the relative distance r_{ij} between two particles of the system at the same imaginary-time index. This histogram has to be normalized with the number of particles that a free particles system of the same density would have at a bin n , namely for $d = 3$, $V_n = \frac{N}{V} \frac{4}{3} \pi [((n+1)\Delta r)^3 - (n\Delta r)^3]$. An example of QMC evaluation of the radial distribution function for a two-dimensional system of ^4He is provided in Fig. 7.10.

Static structure factor

The static structure factor is useful to study the spatial order of a system in the reciprocal lattice; it is in fact connected to the pair distribution function by a Fourier transform. This estimator is defined as a quantum average of the density operator

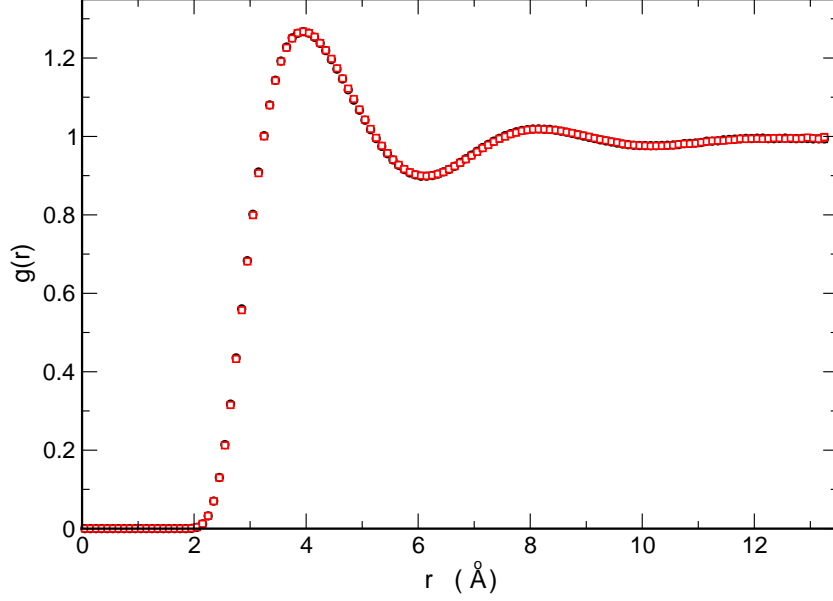


Figure 7.10: PIGS computation of the radial distribution function of a 2D system of $N = 16$ atoms of ${}^4\text{He}$ at a density $\rho = 0.045 \text{ \AA}^{-2}$, interacting with the Aziz potential described in Ref. [7]. The trial wave function is $|\Psi_T\rangle = 1$, the total projection time $\tau = 0.5 \text{ K}^{-1}$ and the averages were taken in the imaginary-time interval $0.2 \text{ K}^{-1} - 0.3 \text{ K}^{-1}$. Red squares are obtained with an 8-th order multi-product expansion (see Appendix B) at a timestep $6\delta\tau = 1/80 \text{ K}^{-1}$. Black circles are obtained with the primitive approximation at a timestep $\delta\tau = 1/480 \text{ K}^{-1}$. The simulation box is a square of side L ; the radial distribution function has been computed also in the range $(L/2; L\sqrt{2})$.

$\hat{\rho}_{\vec{k}}$,

$$S(\vec{k}) = \frac{1}{N} \langle \hat{\rho}_{\vec{k}} \hat{\rho}_{-\vec{k}} \rangle = \frac{1}{N\mathcal{Z}} \int dR \rho(R, R, \beta) \left(\sum_{i=1}^N e^{-i\vec{k} \cdot \vec{r}_i} \right) \left(\sum_{i=1}^N e^{i\vec{k} \cdot \vec{r}_i} \right) \quad . \quad (7.79)$$

Using the Euler identities, the static structure factor can be expressed in a form that is computable by different Monte Carlo methods

$$S(\vec{k}) = \frac{1}{NM} \left\langle \sum_{i \neq j}^N \sum_{m=1}^M \left[\cos(\vec{k} \cdot \vec{r}_i^m) \cos(\vec{k} \cdot \vec{r}_j^m) + \sin(\vec{k} \cdot \vec{r}_i^m) \sin(\vec{k} \cdot \vec{r}_j^m) \right] \right\rangle \quad .$$

where we have averaged over the M equivalent timeslices as before. As in the previous case, in PIMC the sum over m covers all the timeslices; in PIGS, this sum must be intended only over the central timeslices, where Eq. (7.67) gives an accurate description of the ground state.

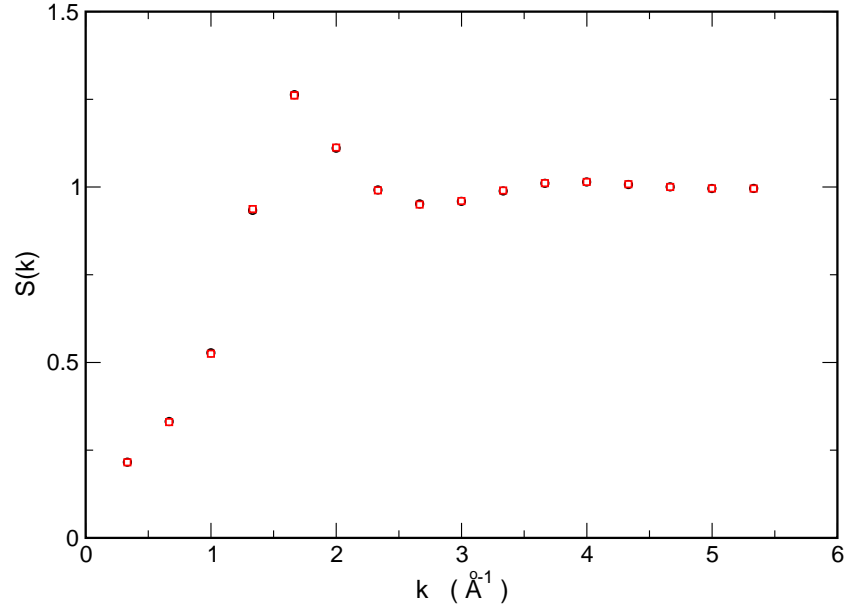


Figure 7.11: PIGS computation of the static structure factor along the axis direction of the simulation box. The system is two-dimensional and consists of $N = 16$ atoms of ${}^4\text{He}$ at a density $\rho = 0.045 \text{ \AA}^{-2}$, interacting with the Aziz potential described in Ref. [7]. The trial wave function is $|\Psi_T\rangle = 1$, the total projection time $\tau = 0.5 \text{ K}^{-1}$ and the averages were taken in the imaginary-time interval $0.2 \text{ K}^{-1} - 0.3 \text{ K}^{-1}$. Red squares are obtained with an 8-th order multi-product expansion (see Appendix B) at a timestep $6\delta\tau = 1/80 \text{ K}^{-1}$. Black circles are obtained with the primitive approximation at a timestep $\delta\tau = 1/480 \text{ K}^{-1}$.

It must be remarked that in a QMC simulation the simulation box has finite dimensions that in the case of d dimensions are (L_0, \dots, L_d) . This implies that the wave vectors that are accessible by the simulation are of the form $\vec{k} = \left(\frac{2\pi}{L_0}n_0, \dots, \frac{2\pi}{L_d}n_d\right)$, with $n_0, \dots, n_d \in \mathbb{I}$. An example of static structure factor is shown in Fig. 7.11

Imaginary-time correlation functions

The static structure factor is also called ‘density-density correlation function’. In general, a correlation function between two operators \hat{A} and \hat{B} is a quantum average

$$c_{AB} = \langle \hat{A}\hat{B} \rangle . \quad (7.80)$$

In particular, the operators \hat{A} and \hat{B} can be evaluated at different imaginary-times (different time-sectors) and this is an imaginary-time correlation function. A significant example of imaginary-time correlation function is the density-density one:

$$F(\vec{k}, \tau) = \frac{1}{N} \langle \hat{\rho}_{\vec{k}}(0) \hat{\rho}_{-\vec{k}}(\tau) \rangle \quad (7.81)$$

that for $\tau = 0$ reduces to the static structure factor. This function is related to the dynamical structure factor of the system by a Laplace transform and thus contains informations about the excitations of the system. However, these informations are accessible from Eq. (7.81) only by solving a numerical inverse Laplace transform; this operation is carried out on a function $F(\vec{k}, \tau)$ which is known only for some imaginary-time τ_m and with a statistical uncertainty. In these conditions, the inversion of the Laplace transform is an ill-posed problem. Methodologies to face those problems have been implemented by many research groups[12].

One body density matrix

An important quantity to sample is the one-body density matrix (OBDM) because it is strictly connected to the Bose Einstein condensation (BEC).

BEC can be defined as a macroscopic occupancy of a given quantum state. The simple BEC occurring in ^4He may be described by a momentum distribution of the form

$$n(\vec{p}) = N_0\delta(\vec{p}) + \tilde{n}(\vec{p}) \quad . \quad (7.82)$$

The OBDM of the ground state $|0\rangle$ of the system is

$$\rho_1(\vec{r}, \vec{r}') = \langle 0 | \hat{\Psi}^\dagger(\vec{r}) \hat{\Psi}(\vec{r}') | 0 \rangle \quad . \quad (7.83)$$

The Fourier transform of this equation gives the momentum distribution $n_{\vec{p}}$ of the system at its ground state:

$$n_{\vec{p}} = \langle 0 | \hat{a}_{\vec{p}}^\dagger \hat{a}_{\vec{p}} | 0 \rangle \quad (7.84)$$

$$\hat{a}_{\vec{p}} = \frac{1}{(2\pi\hbar)^{\frac{3}{2}}} \int d\vec{r} e^{\frac{i}{\hbar}\vec{p}\cdot\vec{r}} \hat{\Psi}(\vec{r}) \quad . \quad (7.85)$$

Placing Eq. (7.85) in Eq. (7.84) yields

$$\begin{aligned} n_{\vec{p}} &= \frac{1}{(2\pi\hbar)^{\frac{3}{2}}} \int d\vec{r} d\vec{r}' e^{-\frac{i}{\hbar}\vec{p}\cdot(\vec{r}-\vec{r}')} \langle 0 | \hat{\Psi}^\dagger(\vec{r}) \hat{\Psi}(\vec{r}') | 0 \rangle = \\ &= \frac{1}{(2\pi\hbar)^{\frac{3}{2}}} \int d\vec{r} d\vec{r}' e^{-\frac{i}{\hbar}\vec{p}\cdot(\vec{r}-\vec{r}')} \rho_1(\vec{r}, \vec{r}') = \\ &= \frac{1}{(2\pi\hbar)^{\frac{3}{2}}} \int d\vec{t} d\vec{s} e^{-\frac{i}{\hbar}\vec{p}\cdot\vec{s}} \rho_1\left(\vec{t} + \frac{\vec{s}}{2}, \vec{t} - \frac{\vec{s}}{2}\right) \end{aligned} \quad (7.86)$$

where $\vec{s} = \vec{r} - \vec{r}'$ and $\vec{t} = (\vec{r} + \vec{r}')/2$. If the system is uniform and isotropic, the OBDM depends only on $s = |\vec{s}|$, and in the thermodynamic limit

$$n_{\vec{p}} = \frac{V}{(2\pi\hbar)^3} \int d\vec{s} e^{-\frac{i}{\hbar}\vec{p}\cdot\vec{s}} \rho_1(s) \quad . \quad (7.87)$$

If the momentum distribution in Eq. (7.82) is anti-transformed to coordinates, an OBDM with unvanishing tail at high s is obtained. An OBDM that displays such asymptotic behavior, that is $\lim_{s \rightarrow \infty} \rho_1(s) = n_0 > 0$, has an off-diagonal long range order; if that function is normalized so that $\rho_1(0) = 1$, n_0 corresponds to the fraction of BEC.

The OBDM in the path integral notation is

$$\rho_1^{PIGS}(\vec{r}, \vec{r}') = \frac{V}{\mathcal{N}} \int dR_1 dR_M d\vec{r}_2^{M/2} \dots d\vec{r}_M^{M/2} \Psi_T(R_1) G(R_1, R_{M/2}, \tau/2) \times \\ \times G(R'_{M/2}, R_M, \tau/2) \Psi_T(R_M) \quad (7.88)$$

where $R_m = (\vec{r}, \vec{r}_2^m, \dots, \vec{r}_N^m)$, $R'_m = (\vec{r}', \vec{r}_2^m, \dots, \vec{r}_N^m)$ and $dR_m = \prod_{i=1}^N d\vec{r}_i^m$. In the PIMC case, an analogous procedure gives

$$\rho_1^{PIMC}(\vec{r}, \vec{r}') = \frac{V \int d\vec{r}_2 \dots d\vec{r}_N G(R, R', \beta)}{\mathcal{Z}} \quad (7.89)$$

In the classical isomorphism, the i -th polymer has been split: if the original polymer had M beads, the bead at a position j is removed and two new beads are inserted. In PIGS j should correspond to an imaginary-time projection large enough to have an accurate description of the ground state; in PIMC j can be anywhere in the path integral. These beads, \vec{r} and \vec{r}' , are not linked each other but are respectively the last and the first timeslice of the new open polymer that would appear. In the PIMC case, this will be a single open polymer with extremities \vec{r} and \vec{r}' ; in the PIGS case two half polymers will appear, with extremities \vec{r}_i^1, \vec{r} and \vec{r}', \vec{r}_i^M .

If the system is homogeneous, ρ_1 depends only on the distance $r = |\vec{r} - \vec{r}'|$; the OBDM is then sampled making an histogram of the relative distance that the two newly created beads have at every MCS. This histogram should be normalized so that $\rho_1(r=0) = 1$; this is done after the QMC evaluation of ρ_1 with a Gaussian fit of the small r part of $\rho_1(r)$. In some cases, this might not be the optimal choice for the normalization: the Worm algorithm, described in Sec. 7.1.6, can provide an *a priori* normalization of the OBDM with a QMC evaluation of $\mathcal{N}(\mathcal{Z})$. As example we show in Fig. 7.12 the one body density matrix for a two-dimensional system of ^4He . We point out that in the PIMC case, the sampling of permutations is crucial to obtain off diagonal long range order: permuting ring polymers with the open polymer will result in a bigger open polymer that allows its extremities to get far away each other, eventually contributing to a non vanishing tail in the OBDM. In PIGS, permutations will yield simply other open polymers and in most situations are not essential; however, there are cases in which permutations are essential in order to obtain an ergodic sampling of the configurations; we have indeed shown an example in Sec. 2.1.1 when we studied, with PIGS, the condensate fraction of ^4He with a particular choice of Ψ_T : a Gaussian wave function centered on the equilibrium positions of solid HCP ^4He ; this is a very particular case in which the trial wave function introduces correlations that constrain the terminal beads of the polymer to arbitrary positions. In this context, single polymer moves will have the same

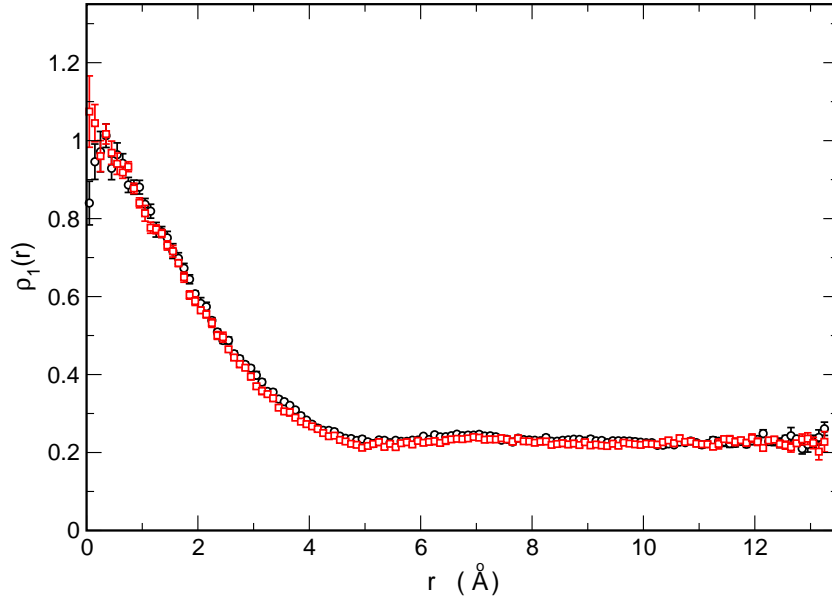


Figure 7.12: PIGS computation of the one body density matrix of a 2D system of $N = 16$ atoms of ${}^4\text{He}$ at a density $\rho = 0.045 \text{ \AA}^{-2}$, interacting with the Aziz potential described in Ref. [7]. The trial wave function is $|\Psi_T\rangle = 1$ and the total projection time $\tau = 0.5 \text{ K}^{-1}$. Red squares are obtained with an 8-th order multi-product expansion (see Appendix B) at a timestep $6\delta\tau = 1/80 \text{ K}^{-1}$. Black circles are obtained with the primitive approximation at a timestep $\delta\tau = 1/480 \text{ K}^{-1}$. The simulation box is a square of side L ; the radial distribution function has been computed also in the range $(L/2; L\sqrt{2})$. The normalization constant has been computed with the Worm algorithm (see Sec. 7.1.6).

pathology of the PIMC case: the extremities of the two half polymers are pinned, as consequence a move that would increase the distance between \vec{r} and \vec{r}' will be soon rejected by the stretching of the kinematic correlations; a permutation with another polymer, on the other hand, will allow the sampling of long-range order exactly as in the PIMC case.

In some situations, the OBDM decays exponentially; this is typical in most solid systems. In such contexts, a common way used to sample the OBDM at large distances r is with the introduction of a repulsive factor $f(r)$ in Eq. (7.88) (or Eq. 7.89 for PIMC)

$$f(r) = \frac{1}{1 + Ae^{-Br^2} + Ce^{-Dr}} \quad (7.90)$$

The parameters B and D are tuned to fit the exponential decay of the OBDM whereas A and C determine the strength of the repulsive factor. The repulsive factor is aimed to modify the probability densities (7.88) and (7.89) to a roughly uniform probability density $\tilde{\rho}(r)$ that is easier to sample. Once the histogram of $\tilde{\rho}(r)$ has been obtained,

the OBDM $\rho(r)$ is recovered with a reweighting of $\tilde{\rho}(r)$: each histogram bin $(\tilde{\rho}(r_i), r_i)$ is divided by the quantity $f(r_i)$.

Superfluidity

It has been derived in Ref. [1] that the superfluid density of a system can be expressed through the *winding number* \vec{W} ,

$$\frac{\rho_s}{\rho} = \frac{\langle \vec{W}^2 \rangle}{2\lambda\beta N} \quad (7.91)$$

and the winding number \vec{W} is defined by

$$\vec{W} = \frac{1}{L} \sum_{i=1}^N \int_0^\beta dt \left[\frac{d\vec{r}_i(t)}{dt} \right] \quad (7.92)$$

In the path integral notation, the discretized expression for Eq. (7.92) becomes

$$\vec{W} = \frac{1}{L} \sum_{m=1}^M \sum_{i=1}^N (\vec{r}_i^m - \vec{r}_i^{m+1}) \quad (7.93)$$

where L is the late of the simulation box, $\vec{r}_i^{M+1} = \vec{r}_{\hat{P}_1 i}^1$ and \hat{P}_1 the permutation operator introduced for the sampling of the Bose symmetry. The winding number represents the number of polymers that wind around the periodic boundaries of the simulation box. Averaging over the d spatial dimensions, the winding number estimator in periodic boundaries conditions is

$$\frac{\rho_s}{\rho} = \frac{\langle \vec{W}^2 \rangle}{2d\lambda\beta N} \quad (7.94)$$

Superfluid density at $T = 0$ K At zero temperature the superfluid fraction can be obtained with the center of mass diffusion *in imaginary-time*[13]. Eq. (7.94) in fact can be viewed as the ratio between the diffusion constant D_c of the center of mass of the system and the diffusion constant of the non-interacting gas, $D_0 = \hbar^2/2m$. The diffusion of the center of mass is obtained from the long τ limit of this relation

$$D_c = \lim_{\tau_x \rightarrow \infty} \frac{N}{4} \frac{\left\langle \left[\vec{R}_{CM}(\tau_x) - \vec{R}_{CM}(0) \right]^2 \right\rangle}{\tau_x} \quad (7.95)$$

where the center of mass at a discrete imaginary time $\tau = md\tau$ is $\vec{R}_{CM}(\tau) = \sum_{i=1}^N \vec{r}_i^m / N$.

The superfluid density becomes

$$\frac{\rho_s}{\rho} = \frac{D_c}{D_0} = \lim_{\tau \rightarrow \infty} \frac{N}{4\lambda} \frac{\left\langle \left[\vec{R}_{CM}(\tau) - \vec{R}_{CM}(0) \right]^2 \right\rangle}{\tau} . \quad (7.96)$$

In a PIGS calculation one has to make some considerations: first, this estimator can be applied only in an interval of imaginary-time $[\tau_0, \tau - \tau_0]$ so that, in order to achieve long- τ convergence in Eq. (7.96) one has to employ sufficiently long imaginary-time projections; secondarily, the PIGS method does not explicitly fix the center of mass of the system and thus Eq. (7.96) cannot be used when the center of mass of the system is allowed to drift; this happens, for instance, in bulk homogeneous systems, where the system can translate freely in the simulation box: due to the property of PIGS to give an unbiased sampling, any correlations from the trial wave function that would eventually fix the center of mass is removed by the quantum imaginary-time evolution. If the center of mass of the system is allowed to drift, Eq. (7.96) will then contain an unphysical contribution that is usually difficult to consider.

7.1.6 The Worm algorithm

Here we present the Worm algorithm in the Canonical ensemble. This method offers an enhanced permutation sampling and also a way to compute, *within the same simulation*, both diagonal and off-diagonal properties of the system under study. Differently from the worm in the Grand Canonical ensemble, this method can also be applied in PIGS without any further adaptation: the Worm algorithm in the Canonical ensemble has not moves that create, destroy or change the length in imaginary-time of the polymers; these moves, in fact, would not be of easy interpretation in the context of quantum evolution in imaginary-time; Canonical Worm is based on moves that in PIGS can be applied at the time-slice at position $M/2$, and in PIMC can be applied anywhere in the path integral. The space of configurations that is sampled by Metropolis is enlarged by including also configurations with one open polymer, see Fig. 7.13; this polymer is called “worm”. A configuration with a worm is called “off-diagonal” (in worm notation: G sector) whereas a configuration without worm is a “diagonal” (Z sector) configuration. Starting from a polymer i , defined by the set of beads $\{\vec{r}_i^j\}_{j=1}^M$, where eventually $\vec{r}_i^1 = \vec{r}_{\hat{P}_i}^M$, a worm at position m is constructed with the following operations:

- Remove the kinetic correlation between \vec{r}_i^{m-1} and \vec{r}_i^m
- Add a bead \vec{r}_i^ν that is linked by a kinetic correlation only with its previous bead, \vec{r}_i^{m-1}
- The beads \vec{r}_i^ν and \vec{r}_i^m are the two worm extremities on which off-diagonal properties such as the one body density matrix can be computed.

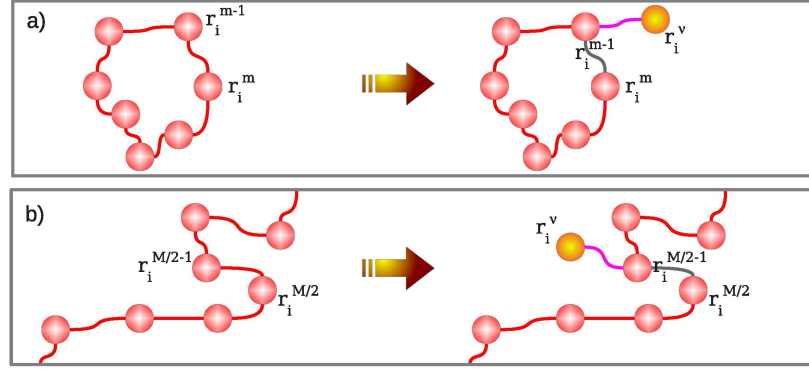


Figure 7.13: The worm in PIMC (a) and in PIGS (b). The gray lines represent the removed kinetic correlations. The worm in PIGS originates two half polymers that are not connected each other; in PIMC, instead, it originates an open polymer.

In PIMC the timeslice m can be anywhere between 1 and M because any time sector is an equivalent representation of the system; in PIGS m should be in the time sector range in which the trial wave function can be considered an accurate representation of the ground state, in our implementation of the worm algorithm in PIGS, m is fixed at the central timeslice.

The implemented worm algorithm consists of two Metropolis moves plus an extension of the Brownian bridge and an extension of the translation move which deal with the presence of the worm extremities. There are two input parameters: C and s . The parameter C sets the ratio g/z between the number of G and Z configurations that are sampled during the simulation, $g + z$ are the total MCS after the equilibration. There is not an universal relation between C and g/z but large values of C result in simulations with more off-diagonal sampling. Usually C is of the order of unity, but the best choice may vary drastically with the system under study. The parameter s is a tuning for the worm moves and specifies how many time-slices are to be involved by the swap and the open/close moves.

Open/Close These moves allow to switch from the Z sector to the G sector and vice-versa. The Open move creates a worm from a diagonal configuration while the Close move closes a worm and gives a diagonal configuration as a result. In order to maintain the detailed balance of the sampling, these moves are coupled meaning that in a MCS there is always one attempt to Open/Close and whether to Open or to Close is decided with a random number: the Open and the Close moves should always be equally probable, so, for instance, if a random number uniformly distributed between 0 and 1 is lesser than 0.5 in that MCS an Open move will be tried, otherwise a Close will be attempted, no matter whether the system is in G sector or in Z sector. The Open move is as follows

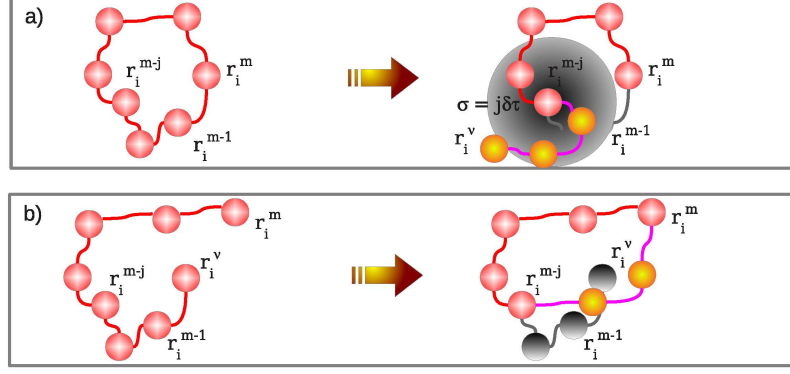


Figure 7.14: Panel a) The “open” move in the worm algorithm. The gray area on the left side represents the Gaussian probability distribution from which the coordinates of r_i^v are sampled. Panel b) The “close” move in the worm algorithm. Grey beads and lines represent the removed segment of the polymer.

- If there is already an open polymer, reject the move. Otherwise select a random integer number i between 1 and N , a random integer number j between 1 and s and a random integer number m between 1 and M .
- Create a worm in the i -th polymer at the m -th bead, the added bead \vec{r}_i^v is sampled from the probability distribution of a free particle propagator with time-step $j\delta\tau$

$$G_0(\vec{r}_i^{m-j}, \vec{r}^*, j\delta\tau) = \frac{1}{(4\pi\lambda j\delta\tau)^{-d/2}} e^{-\left[\frac{|\vec{r}^* - \vec{r}_i^{m-j}|^2}{4\lambda j\delta\tau}\right]} \quad (7.97)$$

- From the bead \vec{r}_i^{m-j} remove the beads $\vec{r}_i^{m-j+1}, \vec{r}_i^{m-j+2}, \dots, \vec{r}_i^{m-1}$ and build a discrete free-particle path to the newly created bead \vec{r}_i^v .

The probability to accept this move is

$$p_o = \min\{1, P_o\}$$

$$P_o = \frac{NC \sum_{l=m-j}^m [U(R_l^{new}, R_{l+1}^{new}) - U(R_l^{old}, R_{l+1}^{old})]}{VG_0(\vec{r}_i^{m-j}, \vec{r}_{\hat{P}_i}^{m+1}, j\delta\tau)} \quad (7.98)$$

The Close move is as follows

- If the configuration is diagonal, reject the move. Otherwise there is a worm, say in the polymer i at the bead m . Select a random integer number j between 1 and s
- Remove the worm extremity \vec{r}_i^v that is linked by a kinetic term only to its previous bead \vec{r}_i^{m-1}

- Replace the beads between \vec{r}_i^{m-j} and \vec{r}_i^m , with a free particle path

The probability to accept the move is

$$p_c = \min \{1, P_c\}$$

$$P_c = \frac{V}{NC} \sum_{l=m-j}^m [U(R_l^{new}, R_{l+1}^{new}) - U(R_l^{old} - R_{l+1}^{old})] \cdot G_0 \left(\vec{r}_i^{m-j}, \vec{r}_{\hat{P}_i}^{m+1}, j\delta\tau \right) \quad (7.99)$$

These moves can be optimized in term of computing efficiency with an automatic rejection whenever the distance between \vec{r}_i^{m-j} and $\vec{r}_{\hat{P}_i}^m$ is such that the quantity

$$\frac{|\vec{r}_i^{m-j} - \vec{r}_{\hat{P}_i}^m|^2}{4\lambda j\delta\tau} \quad (7.100)$$

is larger than some arbitrary quantity of order unity. Our choice was to set it equal to 4. This avoid very small acceptance rates when the worm extremities are far away. In order to maintain the detailed balance, this kinetic test must be applied both to the Open and the Close moves.

Swap This move is attempted only in the off-diagonal sector and implements the sampling of permutations. Consider a configuration in G sector with a worm in the i -th polymer at bead m .

- Select a random integer j between 1 and s
- Select a bead $\vec{r}_{i_k}^{m+j+1}$ with probability

$$P_{i_k} = G_0 \left(\vec{r}_i^\nu, \vec{r}_{i_k}^{m+j+1}, j\delta\tau \right) / \Sigma_T \quad (7.101)$$

$$\Sigma_T = \sum_{n=1}^N G_0 \left(\vec{r}_i^\nu, \vec{r}_n^{m+j+1}, j\delta\tau \right) \quad (7.102)$$

- Evaluate the quantity

$$\Sigma_K = \sum_{n=1}^N G_0 \left(\vec{r}_i^{m+1}, \vec{r}_n^{m+j+1}, j\delta\tau \right) \quad (7.103)$$

- Consider the bead $\vec{r}_{i_k}^{m+j+1}$ and insert a new bead $\vec{r}_{\hat{P}_{i_k}}^\nu = \vec{r}_{\hat{P}_{i_k}}^m$ that is connected by a kinetic term only to its previous bead.
- Replace j beads of the polymer i_k , namely $\vec{r}_{i_k}^{m+1}, \vec{r}_{i_k}^{m+2}, \dots, \vec{r}_{i_k}^{m+j}$ with a Brownian bridge starting from \vec{r}_i^ν and ending at $\vec{r}_{i_k}^{m+j+1}$. With this operation, the bead \vec{r}_i^ν is no longer a worm end: the Brownian bridge swaps the polymer i with the polymer i_k and the new worm extremities become $\vec{r}_{i_k}^\nu$ and \vec{r}_i^m .

The probability to accept a swap move is

$$P_{sw} = \min \left\{ 1, \frac{\Sigma_T}{\Sigma_K} e^{\sum_{l=m}^{m+j} [U(R_l^{new}, R_{l+1}^{new}) - U(R_l^{old}, R_{l+1}^{old})]} \right\} . \quad (7.104)$$

A remark is necessary here: the interpolymer correlations in the time sector $(m, m+1)$, namely $U(R_m, R_{m+1})$ must take into account the worm extremities $\vec{r}_{\hat{P}i}^\nu$ and \vec{r}_i^m . The worm extremities contribute to the interpolymer correlations like the other beads but with a weight factor of 0.5. Using a symmetrized form for the density matrix, such as Eq. (B.1) automatically gives the correct weights:

$$\begin{aligned} U(R_m, R_{m+1})_{PA} &= e^{-\frac{\delta\tau}{2} \sum_{h<k}^N v(r_{hk}^m)} e^{\frac{1}{4\lambda\delta\tau} \sum_h^N (\vec{r}_h^m - \vec{r}_h^{m+1})^2} e^{-\frac{\delta\tau}{2} \sum_{h<k} v(r_{hk}^{m+1})} \\ U(R_{m-1}, R_m)_{PA} &= e^{-\frac{\delta\tau}{2} \sum_{h<k}^N v(r_{hk}^{m-1})} e^{\frac{1}{4\lambda\delta\tau} \sum_h^N (\vec{r}_h^{m-1} - \vec{r}_h^m)^2} e^{-\frac{\delta\tau}{2} \sum_{h<k} v(\vec{r}_{hk}^m)} \end{aligned} \quad (7.105)$$

where

$$\vec{r}_h^m = \begin{cases} \vec{r}_h^m, & \text{if } h \neq \hat{P}i \\ \vec{r}_h^\nu, & \text{if } h = \hat{P}i \end{cases} \quad (7.106)$$

and

$$\tilde{r}_{hk}^m = \begin{cases} |\vec{r}_h^m - \vec{r}_k^m|, & \text{if } h \neq \hat{P}i \\ |\vec{r}_h^\nu - \vec{r}_k^m|, & \text{if } h = \hat{P}i \end{cases} . \quad (7.107)$$

The swap moves are very efficient in the permutation sampling for two reasons: first, a permutation that involves several polymers is obtained with a certain number of swaps that are more likely to be accepted; second, the Worm itself, being an open polymer, has a better probability to avoid overlaps during swap moves. The mechanism used by the Worm algorithm to sample the permutations space is depicted in Fig. 7.15; the basic idea is that two topologically different diagonal configurations are connected by at least three successful Worm moves: the open move generates an off-diagonal configuration; the swap move (or a series of swap moves) samples the permutations space and, finally, the close move returns the system to a diagonal configuration.

Brownian bridge extension The Brownian bridge in a worm computation remains unchanged; however, if the attempted reconstruction involves the worm ends, i.e. starts from a bead j_1 that is before the imaginary-time position m of the worm and ends to a bead $j_2 > m$, the reconstruction of the segment is split and the position of the worm extremities is updated:

- The first worm extremity, \vec{r}_i^ν is updated from the distribution probability

$$G_0(\vec{r}_i^{j_1}, \vec{r}^*, (m - j_1)\delta\tau) = \frac{1}{(4\pi\lambda(m - j_1)\delta\tau)^{-d/2}} e^{\left[\frac{(\vec{r}^* - \vec{r}_i^{j_1})^2}{4\lambda(m - j_1)\delta\tau} \right]} . \quad (7.108)$$

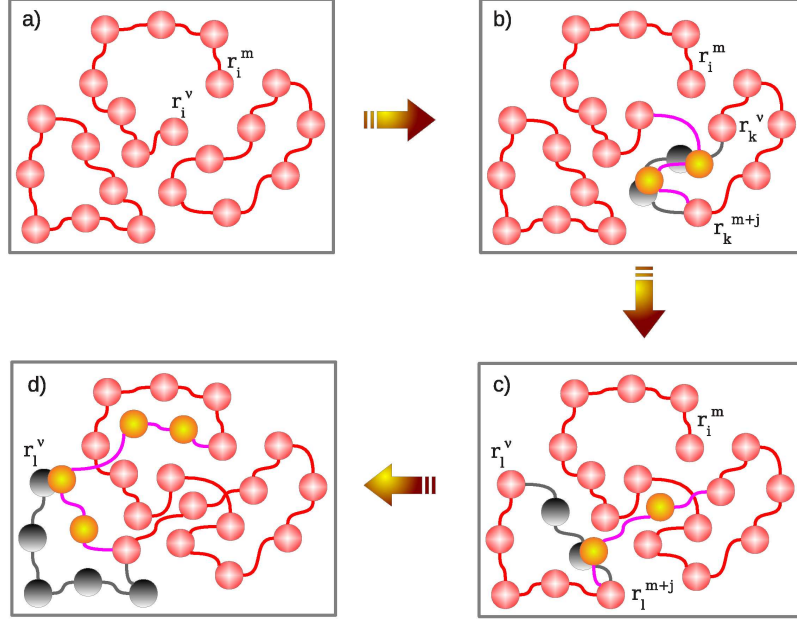


Figure 7.15: The sampling of permutations in the Worm algorithm: from an off-diagonal configuration (a), the first swap generates an open polymer of length 2β (b). Another successful swap results in a configuration with a polymer of length 3β (c); at this point, a successful close move yield a diagonal configuration with a ring polymer of length 3β (d). Grey beads and lines represent the removed segment of the polymer.

- The beads $\vec{r}_i^{j_1+1}, \vec{r}_i^{j_1+2}, \dots, \vec{r}_i^{m-1}$ are updated with a Brownian bridge that starts from $\vec{r}_i^{j_1}$ and ends to the freshly updated bead \vec{r}_i^ν
- The second worm extremity, \vec{r}_i^m is updated from the distribution probability

$$G_0(\vec{r}^*, \vec{r}_i^{j_2}, (j_2 - m)\delta\tau) = \frac{1}{(4\pi\lambda(j_2 - m)\delta\tau)^{-d/2}} e^{\left[-\frac{(\vec{r}_i^{j_2} - \vec{r}^*)^2}{4\lambda(j_2 - m)\delta\tau}\right]} \quad (7.109)$$

- The beads $\vec{r}_i^{m+1}, \vec{r}_i^{m+2}, \dots, \vec{r}_i^{j_2-1}$ are updated with a Brownian bridge that starts from the second worm extremity \vec{r}_i^m and ends at \vec{r}_i^ν

The new position of every bead is sampled here with a free particle propagator, as consequence the probability to accept this move is the same of that of a Brownian bridge between j_1 and j_2 that is expressed in Eq. (7.57) with $U(R_{m-1}, m)$ and $U(R_m, R_{m+1})$ defined as in Eq. (7.105).

Translation move extension The translation move for polymers with a worm has been extended as follows. In the PIGS case, a polymer i with Worm extremities $\vec{r}_{i_{old}}^\nu$ and $\vec{r}_{i_{old}}^m$ is defined by a set of coordinates $S = (\vec{r}_{i_{old}}^1, \dots, \vec{r}_{i_{old}}^\nu, \vec{r}_{i_{old}}^m, \dots, \vec{r}_{i_{old}}^M)$. Here,

for a polymer without worm, we define $\vec{r}^\nu = \vec{r}^m$. The translation of this polymer is parameterized by two displacement vectors \vec{d}_1, \vec{d}_2 ; from S , the move will generate a new polymer $S^{new} = (\vec{r}_{i_{new}}^1 = \vec{r}_{i_{old}}^1 + \vec{d}_1, \dots, \vec{r}_{i_{old}}^\nu + \vec{d}_1, \vec{r}_{i_{old}}^m + \vec{d}_2, \dots, \vec{r}_{i_{old}}^M + \vec{d}_2)$. The probability to accept the move becomes

$$a(\{R\}_{new}) = \min(1, P_{tr})$$

$$P_{tr} = A_1 \cdot A_2 \quad (7.110)$$

where A_1 and A_2 are the probabilities to accept the translations of the two half polymers $S_1 = (\vec{r}_{i_{old}}^1, \dots, \vec{r}_{i_{old}}^\nu)$ and $S_2 = (\vec{r}_{i_{old}}^m, \dots, \vec{r}_{i_{old}}^M)$; namely:

$$V(R_{m_{new}(old)}) := \sum_{k \neq i} v(|\vec{r}_{i_{new}(old)}^m - \vec{r}_k^m|) \quad (7.111)$$

$$A_1 = \frac{\Psi_T(R_{1_{new}}) e^{-\frac{\delta\tau}{2}V(R_{1_{new}})} e^{-\delta\tau V(R_{2_{new}})} \dots e^{-\frac{\delta\tau}{2}V(R_{\nu_{new}})}}{\Psi_T(R_{1_{old}}) e^{-\frac{\delta\tau}{2}V(R_{1_{old}})} e^{-\delta\tau V(R_{2_{old}})} \dots e^{-\frac{\delta\tau}{2}V(R_{\nu_{old}})}} \quad (7.112)$$

$$A_2 = \frac{e^{-\frac{\delta\tau}{2}V(R_{m_{new}})} e^{-\delta\tau V(R_{(m+1)_{new}})} \dots e^{-\frac{\delta\tau}{2}V(R_{M_{new}})} \Psi_T(R_{M_{new}})}{e^{-\frac{\delta\tau}{2}V(R_{m_{old}})} e^{-\delta\tau V(R_{(m+1)_{old}})} \dots e^{-\frac{\delta\tau}{2}V(R_{M_{old}})} \Psi_T(R_{M_{old}})} \quad (7.113)$$

In the PIMC case, a ring polymer i with Worm extremities $\vec{r}_{i_{old}}^\nu$ and $\vec{r}_{i_{old}}^m$ becomes an open polymer. The translation in this case has only one parameter \vec{d} , so that if the polymer is defined by $S = (\vec{r}_{i_{old}}^1, \dots, \vec{r}_{i_{old}}^\nu, \vec{r}_{i_{old}}^m, \dots, \vec{r}_{i_{old}}^M)$, the new polymer will be $S^{new} = (\vec{r}_{i_{old}}^1 + \vec{d}, \dots, \vec{r}_{i_{old}}^\nu + \vec{d}, \vec{r}_{i_{old}}^m + \vec{d}, \dots, \vec{r}_{i_{old}}^M + \vec{d})$. The probability to accept this move is

$$a(\{R\}_{new}) = \min(1, P_{tr})$$

$$P_{tr} = \frac{e^{-\delta\tau V(R_{1_{new}})} \dots e^{-\frac{\delta\tau}{2}V(R_{\nu_{new}})} e^{-\frac{\delta\tau}{2}V(R_{m_{new}})} e^{-\delta\tau V(R_{(m+1)_{new}})} \dots e^{-\delta\tau V(R_{M_{new}})}}{e^{-\delta\tau V(R_{1_{old}})} \dots e^{-\frac{\delta\tau}{2}V(R_{\nu_{old}})} e^{-\frac{\delta\tau}{2}V(R_{m_{old}})} e^{-\delta\tau V(R_{(m+1)_{old}})} \dots e^{-\delta\tau V(R_{M_{old}})}} \quad (7.114)$$

Particular care must be taken when applying the translation move to a PIMC configuration that has permutations. In this case, all the polymers that contribute to a permutation loop are translated by the same displacement vector \vec{d} ; the probability to accept such a move is of the form of Eq. (7.114) but the correlation $V(R_m)$ must take into account not only the i -th polymer but also the other polymers involved in the translation: let the polymers in the permutation loop be (i_1, i_2, \dots, i_H) and the remaining polymers the elements of the set W_{rem} ; then, considering that the translation does not change the correlations between these polymers,

$$V(R_m) := \sum_{k \in W_{rem}} \sum_{l=1}^H v(|\vec{r}_{i_l}^m - \vec{r}_k^m|) \quad (7.115)$$

Normalization of the One Body Density Matrix The Worm algorithm provides also a way to compute the correct normalization of the OBDM. We focus here

on the PIMC case, the PIGS case is analogous; the OBDM is defined by Eq. (7.89). This probability density is sampled in the G sector. The normalization of Eq. (7.89) is the partition function \mathcal{Z} ; \mathcal{Z} corresponds to Eq. (7.89) with $\vec{r} = \vec{r}'$; in the case of an homogeneous system, this is equivalent to the sampling of $\rho_1(r = |\vec{r} - \vec{r}'| = 0)$; within the Worm algorithm this quantity is related to the probability to switch from Z to G . For an homogeneous system, the OBDM $\rho_1(r)$ is the histogram of the distance between the two worm extremities, \vec{r}_i^ν and \vec{r}_i^m , normalized as follows:

$$\rho_1(r) = \frac{\langle \delta(r - |\vec{r}_i^\nu - \vec{r}_i^m|) \rangle}{V_{shell}(r) z C \rho} \quad (7.116)$$

where C is the Worm parameter previously introduced, ρ is the density of the system, z is the number of Monte Carlo steps in the Z sector. The Monte Carlo average $\langle \dots \rangle$ in this context is the histogram of the distance $|\vec{r}_i^\nu - \vec{r}_i^m|$, each bin of the histogram has a width dr and is divided by the volume of the spheric shell $V_{shell}(r) = V(r+dr) - V(r)$.

The introduction of a repulsive factor such as (7.90) does not preserve the Worm normalization. This happens because the repulsive factor interferes with the probability to switch from the Z sector to the G sector and *vice versa*. A workaround is to use a repulsive factor $f_w(r)$ that goes to unity for $r = 0$: with this repulsive factor, in fact, when $\vec{r} = \vec{r}'$ one obtains again the partition function \mathcal{Z} . A straightforward adaptation of the repulsive factor (7.90) that has been used in this work is the following

$$f_w(r) = \frac{1 + A + C}{1 + Ae^{-Br^2} + Ce^{-Dr}} \cdot \quad (7.117)$$

Bibliography

- [1] D.M. Ceperley, *Rev. Mod. Phys.* **67**, 279 (1995).
- [2] P. Baldi, in *Calcolo delle probabilita'*, Ed. McGrawHill.
- [3] R. P. Feynman and A. R. Hibbs, in *Quantum Mechanics and Path Integrals* Ed. McGraw-Hill, (1965), p. 292-293.
- [4] D. Frenkel and B. Smit, in *Understanding molecular simulation*, Academic press edition, (New York, 2002).
- [5] M.H. Kalos and P. A. Whitlock, in *Monte Carlo methods*, Ed. Wiley and Sons (2008).
- [6] N. Metropolis, A. W. Rosenbluth, M. N. Rosenbluth, A. H. Teller and E. Teller, *J. Chem. Phys.* **21** 1087(1953).
- [7] R.A. Aziz, V.P.S. Nain, J.S. Carley, W.L. Taylor and G.T. McConville, *J. Chem. Phys.* **70**, 4330 (1979).
- [8] W. Rudin, in *Functional analysis*, Ed. McGrawHill, (1973).
- [9] G. E. P. Box and M. E. Muller, *Ann. Math. Statist.* **29**, 610 (1958).
- [10] M. Boninsegni, *J. Low. Temp. Phys.* **141**, 27 (2005).
- [11] P. A. Fernandes, A. P. Carvalho and J. P. Prates Ramalho , *J. Chem. Phys.* **103**, 5720 (1995).
- [12] M. Caffarel and D. M. Ceperley, *J. Chem. Phys.* **97**, 8415 (1992) - Average spectrum method; U. Wagner and A. L. J. Geyer, *Biometrika* **82**, 887 (1995) - Maximum entropy method; E. Vitali, M. Rossi, L. Reatto and D. E. Galli, *Phys. Rev. B* **82**, 174510 (2010) - GIFT method.
- [13] S. Zhang, N. Kawashima, J. Carlson and J. E. Gubernatis, *Phys. Rev. Lett.* **74**, 1500 (1995).

Appendix A

Estimators

Here follows the derivation of some estimators with a fourth-order approximation of the propagator.

We consider the Pair Suzuki (PS) approximation:

$$G(R_m, R_{m+1}, \tau) = \frac{1}{(4\pi\lambda\tau)^{Nd}} \int \prod_{i=1}^N d\vec{r}_i^* \exp^{-\frac{1}{4\lambda\tau} \sum_{i=1}^N \left[(r_i^m - r_i^*)^2 + (r_i^* - r_i^{m+1})^2 \right]} \exp^{-\frac{\tau}{3} \sum_{i < j}^N [v_e(r_{ij}^m) + 4v_e(r_{ij}^*) + v_e(r_{ij}^{m+1})]} \quad (\text{A.1})$$

where $r_{ij}^m = |\vec{r}_i^m - \vec{r}_j^m|$ is the distance between the i -th bead and the j -th bead at an imaginary-time defined by the index m ; N is the particles number, d is the dimensionality of the system, $2M$ is the effective¹ beads number, $\lambda = \frac{\hbar^2}{2m}$, $\tau = \frac{\beta}{2M}$ and

$$v_e(r) = v(r) + \frac{2}{3}\alpha\tau^2\lambda \left(\frac{\partial v(r)}{\partial r} \right)^2 \quad (\text{A.2})$$

$$v_c(r) = v(r) + \frac{1}{3}(1 - \alpha)\tau^2\lambda \left(\frac{\partial v(r)}{\partial r} \right)^2 \quad (\text{A.3})$$

We remark that (A.1) is the Green's function that involves two adjacent *real* timeslices, thus the integration variables $\{\vec{r}_i^*\}$ represent the fictitious bead required by the PS approximation.

A.0.7 Total Energy

The thermodynamic estimator for the total energy is defined as follows

$$E = -\frac{1}{2ZM} \frac{\partial Z}{\partial \tau} \quad (\text{A.4})$$

¹With the parameter α set to zero, the odd timeslices are those which describe the system, the even timeslices are the fictitious beads used to express the fourth-order approximation of the Green's function

where Z is the partition function,

$$Z = \text{tr} \{ \hat{\rho} \} = \int dR^1 \dots dR^M \prod_{m=1}^{M-1} G(R^m, R^{m+1}, \tau) \quad (\text{A.5})$$

The imaginary-time derivative applied to the productory in (A.5) yields a sum of M terms that may be viewed as the energy evaluated at an imaginary-time sector. The τ derivative applied to (A.1) gives three terms: the first comes from the normalization of the kinetic part, the second from the gaussian which expresses the kinetic propagator and the last one from the term involving the inter-polymer correlations. After some straightforward algebra, one finds

$$E^m = \left\langle \frac{Nd}{2\tau} - \frac{1}{4\lambda\tau^2} \sum_{i=1}^N \frac{(\vec{r}_i^m - \vec{r}_i^*)^2 + (\vec{r}_i^* - \vec{r}_i^{m+1})^2}{2} + \frac{\partial}{\partial\tau} \frac{\sum_{i<j}^N \frac{\tau}{3} [v_e(r_{ij}^m) + 4v_c(r_{ij}^*) + v_e(r_{ij}^{m+1})]}{2} \right\rangle \quad (\text{A.6})$$

A.0.8 Kinetic Energy

The thermodynamic estimator for the kinetic energy is defined by the following formula

$$K = \frac{m}{\beta Z} \frac{\partial Z}{\partial m} = -\frac{\lambda}{\beta Z} \frac{\partial Z}{\partial \lambda} \quad (\text{A.7})$$

The arguments of the previous paragraph apply here too, resulting in the following expression

$$K^m = \left\langle \frac{Nd}{2\tau} - \frac{1}{4\lambda\tau^2} \sum_{i=1}^N \frac{(\vec{r}_i^m - \vec{r}_i^*)^2 + (\vec{r}_i^* - \vec{r}_i^{m+1})^2}{2} + \frac{\lambda}{\tau} \frac{\partial}{\partial\lambda} \frac{\sum_{i<j}^N \frac{\tau}{3} [v_e(r_{ij}^m) + 4v_c(r_{ij}^*) + v_e(r_{ij}^{m+1})]}{2} \right\rangle \quad (\text{A.8})$$

A.0.9 Pressure

The thermodynamic estimator for the pressure is obtained from a volume derivative of the partition function:

$$P(N, V, \beta) = \frac{1}{\beta Z} \frac{\partial Z(N, V, \beta)}{\partial V} \quad (\text{A.9})$$

In order to compute this volume derivative from (A.5) one has to perform the following change of variables

$$\vec{r} = V^{\frac{1}{d}} \tilde{r} \Rightarrow d\vec{r} = dx dy dz = V d\tilde{r} \quad (\text{A.10})$$

The estimator is composed of three terms, the first arises from a factor V^{2NM} coming from the Jacobian transformation of the differentials $d\vec{r}_i^m$, the second is the derivative applied to the kinetic factor of the propagator and the last one comes from the inter-polymer correlations part. Shifting back to the former integration variables, one obtains

$$P^m = \left\langle \frac{\rho}{\tau} - \frac{1}{2\lambda\tau^2 V d} \sum_{i=1}^N \frac{[(\vec{r}_i^m - \vec{r}_i^*)^2 + (\vec{r}_i^* - \vec{r}_i^{m+1})^2]}{2} - \frac{1}{6Vd} \sum_{i<j} r_{ij} \left[\frac{\partial v_e}{\partial r} \Big|_{r_{ij}^m} + \frac{\partial 4v_c}{\partial r} \Big|_{r_{ij}^*} + \frac{\partial v_e}{\partial r} \Big|_{r_{ij}^{m+1}} \right] \right\rangle \quad (\text{A.11})$$

A.0.10 T=0 limit

Even though the previously introduced estimators are derived from a finite-temperature background, it can be shown that they are valid also in the zero temperature limit. Let's show this for the Hamiltonian operator

$$\begin{aligned} \langle \Psi_0 \hat{H} \Psi_0 \rangle &= - \lim_{\beta \rightarrow \infty} \frac{\partial}{\partial \beta} \log \int dR^1 dR^{2M} \Psi_T(R^1) G(R^1, R^{2M}, \beta) \Psi_T(R^{2M}) = \\ &= - \lim_{\beta \rightarrow \infty} \frac{1}{\mathcal{N}} \int dR^1 dR^{2M} \Psi_T(R^1) \frac{\partial G(R^1, R^{2M}, \beta)}{\partial \beta} \Psi_T(R^{2M}) \end{aligned} \quad (\text{A.12})$$

Because of the formal similarities between PIGS and PIMC, chosen a large enough imaginary-time β , this expression evaluated at the central timeslices expresses a zero-temperature quantum average.

A.0.11 Virial Energy Estimator

Eq. (A.6), such as any estimator involving the Kinetic Energy, contains an highly fluctuating term which comes from the derivative applied to the kinetic part of the propagator. This results in a variance of the averages that increases with the beads number M . The virial estimator provides a way to get rid of these fluctuations. Let's derive it for the total energy estimator. Consider the quantity

$$E_{1,L+1} = \left\langle \frac{NLd}{2\tau} - \frac{M}{2} \alpha + \frac{\partial \tilde{U}}{\partial \tau} \right\rangle \quad (\text{A.13})$$

where

$$\alpha = \sum_{m=1}^L \frac{\sum_{i=1}^N \left[(\vec{r}_i^m - \vec{r}_i^*)^2 + (\vec{r}_i^* - \vec{r}_i^{m+1})^2 \right]}{4\lambda\tau^2 M} \quad (\text{A.14})$$

$$\tilde{U} = \sum_{m=1}^L \sum_{i<j}^N \frac{\tau}{3} \left[v_e(r_{ij}^m) + 4v_c(r_{ij}^*) + v_e(r_{ij}^{m+1}) \right] \quad (\text{A.15})$$

The quantity $E_{1,L+1}$ represents L times the total energy of the system, where L is a parameter arbitrarily chosen between 1 and M . For simplicity, let's rewrite the definitions of α and U in a more treatable way:

$$\alpha = \sum_{m=1}^{2L} \frac{\sum_{i=1}^N (\vec{r}_i^m - \vec{r}_i^*)^2}{4\lambda\tau^2 M} \quad (\text{A.16})$$

$$\tilde{U} = \sum_{m=1}^{2L} U(R^m, R^{m+1}) \quad (\text{A.17})$$

where now the index m denotes every beads, both physical and fictitious, and

$$U^*(r^m, r^{m+1}) = v_e(r_{ij}^m) + 2v_c(r_{ij}^{m+1}) \quad m \text{ odd} \quad (\text{A.18})$$

$$U^*(r^m, r^{m+1}) = 2v_c(r_{ij}^m) + v_e(r_{ij}^{m+1}) \quad m \text{ even} \quad (\text{A.19})$$

$$U(R^m, R^{m+1}) = \sum_{i<j}^N U^*(r_{ij}^m, r_{ij}^{m+1}) \quad (\text{A.20})$$

Now define $dR^m = \prod_{i=1}^N d\vec{r}_i^m$, $(R^m - R^n) = \sum_{i=1}^N (\vec{r}_i^m - \vec{r}_i^n)$, $\frac{\partial}{\partial R^m} = \sum_{i=1}^N \frac{\partial}{\partial \vec{r}_i^m}$ and consider the quantity

$$G = \frac{\int dR^2 \dots dR^{2L} \sum_{m=2}^{2L} (R^m - R^1) \left(-\frac{1}{\beta}\right) \frac{\partial}{\partial R^m} \exp^{-\beta g}}{\int dR^2 \dots dR^{2L} \sum_{m=2}^{2L} \exp^{-\beta g}} \quad (\text{A.21})$$

$$(\text{A.22})$$

with $g = \alpha + \frac{\tilde{U}}{\beta}$. If we make a change of integration variables, namely $\delta^m = R^m - R^{m-1}$, eq. (A.21) becomes

$$G = \frac{\int d\delta^2 \dots d\delta^{2L} \sum_{m=2}^{2L} \delta^m \left(-\frac{1}{\beta}\right) \frac{\partial}{\partial \delta^m} \exp^{-\beta g}}{\int dR^2 \dots dR^{2L} \sum_{m=2}^{2L} \exp^{-\beta g}} \quad (\text{A.23})$$

The integral at the numerator of (A.23) can be computed by parts. The surface term vanishes if $\tau\lambda \ll V^{\frac{2}{d}}$, thus

$$G = \frac{1}{\beta} \sum_{m=2}^{2L} \left\langle \frac{\partial \delta^m}{\partial \delta^m} \right\rangle = \frac{N(2L-1)d}{\beta} \quad (\text{A.24})$$

The quantity in the RHS of (A.21) can be expressed by explicitly computing the derivative over the positions

$$G = \left\langle \sum_{m=2}^{2L} (R^m - R^1) \frac{\partial \alpha}{\partial R^m} \right\rangle + \left\langle \frac{1}{\beta} \sum_{m=2}^{2L} 2L (R^m - R^1) \frac{\partial u}{\partial R^m} \right\rangle \quad (\text{A.25})$$

The first term on the RHS, after some algebra, becomes

$$\sum_{m=2}^{2L} (R^m - R^1) \frac{\partial \alpha}{\partial R^m} = 2\alpha + \frac{1}{4\lambda\tau^2 M} (R^{2L} - R^{2L+1}) (R^{2L+1} - R^1) \quad (\text{A.26})$$

Equating both (A.24) and (A.25) and using (A.26), the quantity α may be re-expressed as

$$\alpha = \frac{N(2L-1)d}{2\beta} - \frac{1}{8\lambda\tau^2 M} (R^{2L} - R^{2L+1}) (R^{2L+1} - R^1) - \frac{1}{2\beta} \sum_{m=2}^{2L} (R^m - R^1) \frac{\partial \tilde{U}}{\partial R^m} \quad (\text{A.27})$$

Substituting α in eq. (A.13) we finally obtain the virial estimator for the total energy per particle:

$$E_{virial} = \left\langle \frac{d}{2\tau} + \frac{1}{4\lambda\tau^2 N} \sum_{i=1}^N (\bar{r}_i^{2L} - \bar{r}_i^{2L+1}) (\bar{r}_i^{2L+1} - \bar{r}_i^1) + \frac{1}{2\tau N} \sum_{m=2}^{2L} \sum_{i < j 1}^N (\bar{r}_i^m - \bar{r}_j^m) \cdot \frac{\partial U^*(r_{ij}^m, r_{ij}^{m+1})}{\partial \bar{r}_i^m} + \frac{2}{N} \sum_{m=1}^{2L} \frac{\partial U(R^m, R^{m+1})}{\partial \tau} \right\rangle \quad (\text{A.28})$$

This estimator may be used also in the zero temperature limit if one performs the following substitutions: $R^1 \rightarrow R^\Gamma$, $L \rightarrow \tilde{L}$, $\sum_{m=1}^{2L} \rightarrow \sum_{m=\Gamma}^{\Gamma+2\tilde{L}}$ and $\sum_{m=2}^{2L} \rightarrow \sum_{m=\Gamma+1}^{\Gamma+2\tilde{L}}$, where Γ represents the index of the first time-sector that can be considered a ground-state description of the system and \tilde{L} is an arbitrary number between 1 and the number of physical timeslices available for the evaluation of ground-state expectation values.

Appendix B

Higher order approximations for the density matrix

In this appendix we show approximations for the small imaginary–time density matrix that go beyond the Primitive Approximation (PA) introduced in Eq. (2.16). We have already shown the “Pair” Suzuki (PS) approximation in Sec. 2.1, we will show now the Pair Product approximation (PPA) and the Multi Product Expansion (MPE). The MPE and the PS, as well as the Primitive Approximation, have the advantage to be analytic and thus estimators can be derived exactly; the PPA on the other hand is numerical and only a restricted set of estimators, such as those diagonal on the coordinate representation and the one body density matrix, can be simply derived. The PPA, however, requires fewer imaginary–time projection than the other two and this feature could be useful in some contexts.

As mentioned before, given the Hamiltonian $\hat{H} = \hat{T} + \hat{V}$, one has to use a small imaginary–time approximation of the propagator $e^{-\delta\tau\hat{H}}$ in order to obtain an analytic expression for $G(R, R', \delta\tau) = \langle R | e^{-\delta\tau\hat{H}} | R' \rangle$. The simplest approximation is the PA

$$G_2(R_i, R_j, \delta\tau) = e^{-\frac{\delta\tau}{2}\hat{V}_i} e^{-\delta\tau\hat{T}} e^{-\frac{\delta\tau}{2}\hat{V}_j} \quad (\text{B.1})$$

which is correct up to second–order in $\delta\tau$; this approximation is obtained by ignoring the commutator $[\hat{T}, \hat{V}]$ when factorizing the Hamiltonian. The effective potential $U(R_m, R_{m+1}, \delta\tau)$ for the beads represented with the PA is

$$U(R_m, R_{m+1}, \delta\tau) = \frac{\delta\tau}{2} [V(R_m) + V(R_{m+1})] \quad (\text{B.2})$$

so that the density matrix takes the form

$$G(R_m, R_{m+1}, \delta\tau) = G_0(R_m, R_{m+1}, \delta\tau) e^{-U(R_m, R_{m+1}, \delta\tau)} \quad (\text{B.3})$$

where G_0 is the density matrix for free particles

$$G_0(R_m, R_{m+1}, \delta\tau) = \langle R_m | e^{-\delta\tau\hat{T}} | R_{m+1} \rangle \quad (\text{B.4})$$

B.0.12 The Pair Product

Following Ref. [1], the PPA is a decomposition of the density matrix in which the effective potential is written as:

$$U(R_m, R_{m+1}, \delta\tau) = \sum_{i < j} u_2(\vec{r}_m^i - \vec{r}_m^j, \vec{r}_{m+1}^i - \vec{r}_{m+1}^j, \delta\tau) \quad (\text{B.5})$$

where \vec{r}_m^i is the position of the i -th particle at a timestep $\tau_m = m\delta\tau$. u_2 is the exact effective potential for two atoms. This approximation states that, if the imaginary time is sufficiently small, the many-body propagator can be described as a product of two-body propagators. The density matrix for two particles can be obtained with different methods. For instance, one can use the matrix-squaring method; this is shown in detail in Ref. [1] and we limit here to state the final result for the two-body effective potential,

$$u_2(\vec{r}_1, \vec{r}_2, \delta\tau) = \frac{u_0(\vec{r}_1, \delta\tau) + u_0(\vec{r}_2, \delta\tau)}{2} + \sum_{k=1}^n \sum_{j=0}^k u_{kj}(q, \delta\tau) z^{2j} s^{2(k-j)} \quad (\text{B.6})$$

where $q = (|\vec{r}_1| + |\vec{r}_2|)/2$, $s = |\vec{r}_1 - \vec{r}_2|$ and $z = |\vec{r}_1| - |\vec{r}_2|$. The first term is the effective potential of the PA and the functions u_{kj} are off-diagonal terms that are obtained from the partial wave expansion of the two-particles propagator. These off-diagonal terms are usually obtained by numerical means and an analytic description of the pair density matrix is not available.

B.0.13 The Multi Product Expansion

From Eq. (B.1), the $2n$ -th order multi-product expansion is built with the following relation

$$G_{2n}(\delta\tau) = \sum_{i=1}^n c_i G_2^{k_i}(\delta\tau/k_i) \quad (\text{B.7})$$

$$c_i = \prod_{j=1(\neq i)}^n \frac{k_i^2}{k_i^2 - k_j^2} \quad (\text{B.8})$$

Let's focus on the case $n = 4$. Following ref [2], the convenient choice for $\{k_i\}$ that yields an eight order multi-product approximation suitable for PIGS calculations is $\{k_i\} = \{1, 2, 3, 6\}$. This, infact, produces elements $G_2^{k_i}$ with time-steps $\delta\tau/k_1$ that have a common divisor $\delta\tau/6$; these elements can thus be represented by a path integral with a time-step $\delta\tau/6$. This choice for $\{k_i\}$, combined with Eq. B.7, gives

the definition of the propagator used in Sec. 5

$$\begin{aligned}
G_8(\{R_i\}_{i=1}^7, 6\delta\tau) &= G_0(1, 2, \delta\tau) \dots G_0(6, 7, \delta\tau) \times \\
&\left[\frac{54}{35} e^{-\frac{\delta\tau}{2}\hat{V}_1} e^{-\delta\tau\hat{V}_2} e^{-\delta\tau\hat{V}_3} e^{-\delta\tau\hat{V}_4} e^{-\delta\tau\hat{V}_5} e^{-\delta\tau\hat{V}_6} e^{-\frac{\delta\tau}{2}\hat{V}_7} \right. \\
&\quad - \frac{27}{40} e^{-\delta\tau\hat{V}_1} e^{-2\delta\tau\hat{V}_3} e^{-2\delta\tau\hat{V}_5} e^{-\delta\tau\hat{V}_7} \\
&\quad + \frac{2}{15} e^{-\frac{3}{2}\delta\tau\hat{V}_1} e^{-3\delta\tau\hat{V}_4} e^{-\frac{3}{2}\delta\tau\hat{V}_7} \\
&\quad \left. - \frac{1}{840} e^{-3\delta\tau\hat{V}_1} e^{-3\delta\tau\hat{V}_7} \right] \tag{B.9}
\end{aligned}$$

where G_0 has been defined in Eq. (B.4).

Bibliography

- [1] D. M. Ceperley, *Rev. Mod. Phys.* **67** 279(1995).
- [2] R. E. Zillich, J. M. Mayrhofer and S. A. Chin, *J. Chem. Phys.* **132**, 044103 (2010).